

# Modeling of a Vanadium Redox Flow Battery Electricity Storage System

THÈSE N° 4277 (2009)

PRÉSENTÉE LE 24 AVRIL 2009

À LA FACULTÉ SCIENCES ET TECHNIQUES DE L'INGÉNIEUR

LABORATOIRE D'ÉLECTRONIQUE INDUSTRIELLE

PROGRAMME DOCTORAL EN ENERGIE

ÉCOLE POLYTECHNIQUE FÉDÉRALE DE LAUSANNE

POUR L'OBTENTION DU GRADE DE DOCTEUR ÈS SCIENCES

PAR

Christian BLANC

acceptée sur proposition du jury:

Prof. J. R. Mosig, président du jury

Prof. A. Rufer, directeur de thèse

Prof. D. Hissel, rapporteur

Dr M. Schreiber, rapporteur

Dr J. Van Herle, rapporteur



ÉCOLE POLYTECHNIQUE  
FÉDÉRALE DE LAUSANNE

Suisse  
2009





---

A mes parents,  
pour toutes les opportunités  
qu'ils m'ont offertes.



---

“ *There are many ways of going forward,  
but only one way of standing still.* ”  
— FRANKLIN D. ROOSEVELT  
1882-1945



---

# Remerciements

---

Ce travail sur la modélisation d'un électrolyseur réversible est le fruit de belles années passées au sein du laboratoire d'électronique industrielle (LEI) où j'ai eu la chance de participer à de nombreux et variés projets. Je tiens à remercier chaleureusement le Professeur Alfred Rufer de m'avoir accueilli dans son équipe et pour la confiance qu'il m'a témoignée. Je resterai longtemps impressionné par l'étendue de ses connaissances aussi bien scientifiques et techniques que politiques et culturelles.

Mes remerciements vont aussi aux membres du jury, les Professeurs Daniel Hissel et Juan Mosig ainsi que les Dr. Martha Schreiber et Dr. Jan Van Herle, pour avoir accepté de juger ce travail et d'avoir pris le temps d'évaluer ce mémoire.

Je remercie également un ancien membre du LEI, le Dr. Félix Grasser qui m'a introduit, avec les membres du groupe piles à combustible du LENI, à l'électrochimie au travers de leurs travaux sur les piles à combustible. Au sein du LENI, je pense particulièrement aux Dr. Jan Van Herle, Dr. Diego Larrain et Dr. Nordahl Autissier.

Ce manuscrit n'aurait pas sa forme actuelle sans la lecture attentive du Dr. Philippe Barrade, envers qui je resterai éternellement redevable d'un *R* depuis mon impardonnable faute de frappe lors de mon travail de diplôme. A nouveau, je le remercie pour les pensées positives qu'il sait insuffler pendant les moments d'errements et de doute.

Mes remerciements vont aussi à mon collègue de bureau, Yves Birbaum,

---

pour nos longues discussions, son inestimable aide technique qu'il m'a apportée dans mes projets ainsi que pour sa délicieuse bière. Je pense également à tous mes collègues anciens et présents du LEI. Je n'oublierai pas nos nombreuses fondues et raclettes ainsi que l'atmosphère conviviale qui a plané sur le LEI. Vous me manquerez.

Une pensée particulière est destinée à mes parents, Marlis et Jean-Claude, pour le soutien qu'ils m'ont apporté depuis mes premiers jours.

Je pense également à tous mes amis qui m'ont accompagné durant toutes ces années. Je les remercie pour leurs soutien et encouragements ainsi que tous les bons moments passés ensemble.

Mes dernières pensées vont à Laetitia pour son soutien inconditionnel et sa patience durant ces derniers mois. Je t'aime si fort !

Christian Blanc  
Décembre 2008

---

# Résumé

---

Le stockage de l'électricité est appelé à jouer un rôle croissant dans l'économie électrique. En effet, la dérégulation et la déréglementation sont en train de modifier en profondeur l'industrie électrique européenne. Les avantages des systèmes de stockage sont nombreux : gestion de l'offre et de la demande, gestion de l'énergie, qualité de l'électricité, intégration des énergies renouvelables, etc. Depuis l'apparition de l'électricité, de nombreux systèmes de stockage ont été développés ; ces systèmes sont basés sur la mécanique, l'électricité ou l'électrochimie. Pour les installations de grandes puissances, les systèmes de pompes et turbinages sont les plus répandus. Malheureusement, les emplacements adéquats et disponibles sont de plus en plus rares aujourd'hui. Evidemment, d'autres techniques ont été développées : les volants cinétiques, le stockage par air comprimé, les supercondensateurs, les inductances supraconductrices ou encore les batteries avancées. Parmi elles, les électrolyseurs réversibles ont un potentiel certain dans le domaine du stockage stationnaire de puissance.

Dans le cadre de ce travail ambitieux, un modèle original et multiphysique d'un électrolyseur réversible au vanadium a été réalisé sur la base des principes d'électrochimie, de thermodynamique et de mécanique des fluides. En effet, l'énergie est stockée par une réaction électrochimique dans l'électrolyte qui est pompé depuis le réservoir jusqu'à la pile. Ainsi, ce système de stockage offre une modularité entre la puissance disponible et l'énergie stockée.

Dans un premier temps, un modèle électrochimique de la pile a été réalisé sur la base des principes de l'électrochimie. Ce modèle détermine tout

---

d'abord la tension d'équilibre à partir des concentrations de vanadium ; à cette valeur doit être soustrait les surtensions d'activation, de concentration, les pertes ohmiques et ioniques. Les concentrations dans le réservoir sont déterminées en tout temps ainsi que leurs variations à l'intérieur des cellules en fonction du courant et du flux d'électrolyte. Un modèle simplifié des pertes électrochimiques est également proposé.

Les performances électrochimiques de l'électrolyseur sont ensuite établies à travers la simulation d'un système isolé composé d'un électrolyseur, d'un panneau solaire et d'une charge. Le modèle permet de déterminer les flux de puissance, la tension de l'électrolyseur ainsi que les concentrations de vanadium sur une période de 24 heures. Une série de charge et décharge à courant ou puissance constant nous a permis d'établir les rendements électrochimiques de l'électrolyseur.

Les propriétés de l'électrolyte sont ensuite brièvement discutées ; en particulier leur dépendance vis-à-vis de la composition de l'électrolyte. En effet, la viscosité et la densité sont des variables importantes du modèle mécanique développé dans la suite de ce travail.

Afin de déterminer les pertes mécaniques liées à la circulation de l'électrolyte, un modèle basé sur la mécanique des fluides est proposé. Ce modèle comporte une partie analytique qui détermine les chutes de pression à l'intérieur des tuyaux et réservoirs ainsi qu'une partie numérique. En effet, la complexité du circuit hydraulique à l'intérieur de la pile ne permet pas une description analytique ; c'est pourquoi un modèle basé sur la méthode des éléments finis est utilisé. Il est ainsi possible de déterminer la puissance mécanique nécessaire au fonctionnement de l'électrolyseur.

Ces deux modèles sont ensuite assemblés afin de former le modèle complet du système de stockage. Il permet alors de comparer les performances de différents modes de fonctionnement. En effet, il existe à courant constant un débit qui permet d'optimiser le rendement de l'électrolyseur. Une nouvelle série de charges et décharges permet d'établir le rendement de ces modes de fonctionnement. Ensuite, le mode de fonctionnement à puissance constante est également abordé en détail et finalement un point de fonctionnement optimal est mis en évidence.

## Mots clés

Electrolyseur réversible au vanadium, modélisation, stockage de l'électricité, électrochimie, mécanique des fluides, optimisation



---

# Summary

---

Today, the electricity industries are facing new challenges as the market is being liberalized and deregulated in many countries. Electricity storage is undoubtedly a disruptive technology that will play, in the near future, a major role in the fast developing distributed generations network. Indeed, electricity storage has many potential applications: management of the supply and demand of electricity, power quality, integration of renewable sources, improvement of the level of use of the transport and distribution network, etc. Over the years, many storage technologies have been investigated and developed, some have reached the demonstrator level and only a few have become commercially available. The pumped hydro facilities have been successfully storing electricity for more than a century; but today, appropriate locations are seldom found. Electrochemical storage is also an effective means to accumulate electrical energy; among the emerging technologies, the flow batteries are excellent candidates for large stationary storage applications where the vanadium redox flow battery (VRB) distinguishes itself thanks to its competitive cost and simplicity.

In this ambitious work that encompasses the domains of electricity, electrochemistry and fluid mechanics, we have proposed a novel multiphysics model of the VRB. This model describes the principles and relations that govern the behaviour of the VRB under any set of operating conditions. Furthermore, this multiphysics model is a powerful means to identify and quantify the sources of losses within the VRB storage system; indeed, one of the purposes of this study is to propose strategies of control and operation for a greater effectiveness of the overall storage system.

The electrochemical model is based on the electrochemical principles and

---

the study of the VRB chemistry; this model determines the equilibrium voltage from the vanadium concentrations, and the associated activation, concentration, ohmic and ionic overpotentials. Furthermore, the vanadium concentrations within the tank and the stack are constantly determined as a function of the current and the electrolyte flowrate. A simplified model of the internal loss is also proposed.

The electrochemical performance was then established through the simulation of a stand alone system composed of a solar source, a VRB and a load. The model determines the stack voltage, the power flows and the vanadium concentrations over a 24 h period. Furthermore, the model was successfully compared with experimental data through a series of charge and discharge cycles at constant currents.

Thereafter, the properties of the electrolyte are briefly investigated: in particular their dependence upon the electrolyte composition. Indeed, the viscosity and the density are important parameters of the mechanical model.

In order to analyse the battery performance, a mechanical model has been proposed to determine the mechanical power required to flow the electrolytes. This model based on fluid mechanics has an analytical part that predicts the pressure drop within the pipes and the tanks, and a numerical part. Indeed, the stack geometry is so complex that it can not be described analytically; therefore, a numerical model based on finite element method (FEM) is proposed. Hence, the mechanical power necessary to the battery operation is obtained at any operating conditions.

The electrochemical and the mechanical models are finally assembled to form the original multiphysics model of the VRB. This model provides a good insight of the battery operation and offers a powerful means to enhance the battery performance. Indeed, there is at constant current an optimal flowrate that maximizes the efficiency. A second series of charge and discharge cycles has determined the efficiency of different control strategies. Finally, the battery operations at constant power were also discussed in details and an optimal operating point has been highlighted.

## **Keywords**

Vanadium redox flow battery, flow battery, electricity storage, modeling, electrochemistry, fluid mechanics, optimization

---

# Contents

---

<b>Remerciements</b>	<b>v</b>
<b>Résumé</b>	<b>vii</b>
<b>Summary</b>	<b>ix</b>
<b>Nomenclature</b>	<b>xvii</b>
<b>1. Electricity Storage: Why and How?</b>	<b>1</b>
1.1. A Trend Towards Electricity Storage . . . . .	1
1.2. The Benefits of Electricity Storage . . . . .	3
1.2.1. Bulk Electricity Price Arbitrage . . . . .	4
1.2.2. Electricity Demand Management at Customer Level . . . . .	4
1.2.3. Ancillary Services . . . . .	5
1.2.4. Generation Capacity Upgrade Deferral . . . . .	7
1.2.5. Transmission and Distribution Support . . . . .	7
1.2.6. Electric Service Reliability and Power Quality . . . . .	8
1.2.7. Renewable Capacity Firming and Energy Time-Shift . . . . .	9
1.3. How to Store Electricity . . . . .	9
1.3.1. Mechanical Storage Systems . . . . .	10
1.3.2. Electrical Storage Systems . . . . .	15
1.3.3. Electrochemical Storage Systems . . . . .	17

1.4. Technology Comparisons . . . . .	24
1.4.1. Power and Discharge Time Ratings . . . . .	25
1.4.2. Capital Cost . . . . .	27
1.4.3. Efficiency and Lifetime . . . . .	31
1.5. The Vanadium Redox Battery . . . . .	33
1.5.1. VRB Installations . . . . .	36
1.5.2. Other Flow Batteries . . . . .	40
1.6. Motivation of the Present Work . . . . .	41
1.7. Structure of the Present Work . . . . .	42
<b>2. Electrochemistry of the Vanadium Redox Batteries</b>	<b>45</b>
2.1. Introduction . . . . .	45
2.2. Generalities about Electrochemistry . . . . .	47
2.2.1. Molality and Molarity . . . . .	48
2.2.2. Chemical Equilibrium and Activity . . . . .	48
2.2.3. Redox Chemistry . . . . .	50
2.2.4. Gibbs Free Energy and Nernst Equation . . . . .	51
2.3. All-Vanadium Battery Reaction . . . . .	54
2.3.1. Application of the Nernst Equation to the VRB . . . . .	55
2.3.2. Standard Potential . . . . .	58
2.3.3. Full Ionic Equations . . . . .	63
2.3.4. State of Charge . . . . .	66
2.3.5. Numerical Example of the Cell Voltage . . . . .	66
2.4. Overpotentials, Ohmic and Ionic Losses . . . . .	68
2.4.1. Activation Overpotential . . . . .	68
2.4.2. Concentration Overpotential . . . . .	78
2.4.3. Ohmic and Ionic Overpotentials . . . . .	82
2.5. Electrochemical Stack Model . . . . .	84
2.6. Summary . . . . .	85
<b>3. Electrochemical Model of a Vanadium Redox Stack</b>	<b>89</b>
3.1. Introduction . . . . .	89
3.2. Concentration of the Vanadium Ions . . . . .	90
3.2.1. Electrons Exchange Rate . . . . .	91
3.2.2. Input, Output and Average Concentrations of Vanadium Ions . . . . .	93
3.2.3. Observation of the Concentration . . . . .	100
3.3. Proton Concentration in the Catholyte . . . . .	101

3.4. Internal Losses . . . . .	102
3.5. Response Time . . . . .	107
3.6. Augmented and Simplified VRB Model . . . . .	107
3.7. Energy Density . . . . .	109
3.8. Efficiencies . . . . .	110
3.9. Simulation of a Small Stand Alone System . . . . .	112
3.10. Charge and Discharge Cycles . . . . .	117
3.10.1. Constant Current . . . . .	118
3.10.2. Constant Power . . . . .	121
3.11. Power Density and Efficiency . . . . .	122
3.12. Effects of the Operating Conditions . . . . .	125
3.13. Summary . . . . .	128
<b>4. Electrolyte Properties</b>	<b>131</b>
4.1. Introduction . . . . .	131
4.2. Electrolyte Preparation . . . . .	132
4.3. Density . . . . .	134
4.3.1. Density of $V^{2+}$ and $V^{3+}$ Solutions . . . . .	135
4.3.2. Influence of the Sulphuric Acid Concentration and of the Temperature . . . . .	136
4.3.3. Empirical Model . . . . .	137
4.3.4. Density of $V^{4+}$ and $V^{5+}$ Solutions . . . . .	138
4.4. Viscosity . . . . .	138
4.4.1. Viscosity of $V^{2+}$ and $V^{3+}$ Solutions . . . . .	139
4.4.2. Viscosity of $V^{4+}$ and $V^{5+}$ Solutions . . . . .	140
4.4.3. Empirical Model . . . . .	141
4.4.4. Effect of the Temperature . . . . .	143
4.4.5. Effect of the Sulphuric Acid Concentration . . . . .	143
4.5. Electrolyte Stability . . . . .	143
4.6. Summary and Outlook . . . . .	146
<b>5. Fluid Mechanics Applied to the Vanadium Redox Flow Batteries</b>	<b>149</b>
5.1. Introduction . . . . .	149
5.2. Construction of a Stack . . . . .	150
5.3. Generalities about Fluid Mechanics . . . . .	153
5.3.1. Reynolds Number . . . . .	153
5.3.2. Bernoulli's Principle . . . . .	155
5.3.3. The First Law of Thermodynamics . . . . .	156

5.3.4.	The Extended Bernoulli's Equation . . . . .	157
5.3.5.	Head Loss Due to Friction . . . . .	159
5.3.6.	Minor Losses . . . . .	161
5.3.7.	Pump Power . . . . .	166
5.4.	Analytical Model of the Hydraulic Circuit . . . . .	167
5.5.	Stack Hydraulic Model . . . . .	168
5.5.1.	The Flow Resistance, an Analogy with the Ohm's Law . . . . .	171
5.5.2.	Hydraulic Resistance of a Stack . . . . .	172
5.5.3.	The Peclet Number and its Effects . . . . .	178
5.5.4.	Validation of the Stack Decomposition . . . . .	181
5.5.5.	The Effect of the Density on the Flow Resistance . . . . .	182
5.5.6.	The Effect of the Viscosity on the Flow Resistance . . . . .	184
5.6.	Mechanical model of the VRB . . . . .	185
5.7.	Summary and Outlook . . . . .	187
<b>6.</b>	<b>The Multiphysics Model and Energetic Considerations</b>	<b>193</b>
6.1.	Introduction . . . . .	193
6.2.	Multiphysics System Model . . . . .	195
6.3.	Energetic Considerations at Constant Current . . . . .	198
6.3.1.	Maximal Flowrate . . . . .	200
6.3.2.	Minimal Flowrate . . . . .	201
6.3.3.	Optimal Flowrate . . . . .	210
6.3.4.	Charge and Discharge Cycle at Constant Current . . . . .	216
6.4.	Energetic Considerations at Constant Power . . . . .	220
6.4.1.	Constant Stack Power . . . . .	220
6.4.2.	Constant Battery Power . . . . .	222
6.5.	Summary . . . . .	226
<b>7.</b>	<b>Epilogue</b>	<b>229</b>
7.1.	Overview and Contributions . . . . .	229
7.2.	Perspectives and Future Developments . . . . .	232
<b>A.</b>	<b>Finite Element Analysis</b>	<b>233</b>
A.1.	Simulation of a Channel . . . . .	233
A.1.1.	Analytical Model . . . . .	234
A.1.2.	Finite Element Model . . . . .	235

<b>B. Vanadium Redox Flow Auxiliaries Hydraulic Circuit</b>	<b>241</b>
<b>C. Miscellaneous Graphs</b>	<b>245</b>
<b>Curriculum vitae</b>	<b>263</b>





---

---

# Nomenclature

---

## Abbreviations

Symbol	Explanation
<i>CAES</i>	Compressed air energy storage
<i>CHP</i>	Combined heat and power
<i>DGU</i>	Distributed generation unit
<i>EPFL</i>	Ecole Polytechnique Fédérale de Lausanne
<i>ESS</i>	Energy storage system
<i>ESA</i>	Electricity Storage Association
<i>FB</i>	Flow battery
<i>FEM</i>	Finite element method
<i>FERC</i>	Federal Energy Regulatory Commission
<i>FP</i>	Flow plate
<i>IEA</i>	International Energy Agency
<i>LEI</i>	Laboratoire d'Electronique Industrielle
<i>M</i>	Manifold
<i>NaS</i>	Sodium sulfur
<i>NiCd</i>	Nickel-cadmium battery
<i>PEM</i>	Proton Exchange Membrane
<i>PV</i>	Photovoltaic
<i>PSB</i>	Polysulfide bromide battery
<i>NC</i>	Supercapacitor

---

<i>RDE</i>	Rotating disk electrode
<i>SCE</i>	Saturated calomel electrode
<i>SHE</i>	Standard hydrogen electrode
<i>SMES</i>	Superconducting magnetic energy storage
<i>OCV</i>	Open-circuit voltage
<i>RFB</i>	Redox flow battery
<i>T&amp;D</i>	Transport and distribution
<i>UPS</i>	Uninterruptible power supply
<i>VRB</i>	Vanadium redox battery
<i>VRF</i>	Vanadium redox flow
<i>ZBB</i>	Zinc bromine battery

---

## Constants

Symbol	Explanation	Value	Units
<i>e</i>	Elementary charge	$1.6022 \cdot 10^{-19}$	<i>C</i>
<i>F</i>	Faraday's constant	$9.6485 \cdot 10^4$	<i>C/mol</i>
<i>h</i>	Planck's constant	$6.626 \cdot 10^{-34}$	<i>J s</i>
<i>k<sub>b</sub></i>	Boltzmann's constant	$1.38066 \cdot 10^{-23}$	<i>J/K</i>
<i>N<sub>A</sub></i>	Avogadro's number	$6.0220 \cdot 10^{23}$	<i>1/mol</i>
<i>R</i>	Gas constant	8.3144	<i>J/K · mol</i>

## Roman Symbols

Symbol	Explanation	Units
<i>a<sub>i</sub></i>	Activity of species i	—
<i>c<sub>i</sub></i>	Molarity (or concentration) of species i	<i>mol/m<sup>3</sup></i>
<i>c</i>	Specific heat capacity	<i>J/kg K</i>

---

$D$	Diameter	$m$
$D_i$	Diffusion coefficient or diffusivity	$m^2/s$
$E$	Cell voltage	$V$
$E$	Electric field	$V/m$
$E$	Energy	$Wh$
$\bar{E}$	Average cell voltage	$V$
$E^\ominus$	Standard electrode potential	$V$
$E^{\ominus'}$	Formal electrode potential	$V$
$E_0$	Nernst potential	$V$
$\Delta E_{int}$	Internal energy	$J$
$E_f$	Friction loss	$J$
$e_f$	Friction loss per mass unit	$m^2/s^2$
$e_{int}$	Internal energy per mass unit	$m^2/s^2$
$E_m$	Minor loss	$J$
$e_m$	Minor loss per mass unit	$m^2/s^2$
$f$	Friction factor	$-$
$g$	Gravitational acceleration	$m/s^2$
$G$	Conductance	$S$
$\Delta G$	Molar Gibbs free reaction enthalpy	$J/mol$
$\Delta G_{act}^\ominus$	Standard Gibbs energy of activation	$J/mol$
$h_f$	Head loss due to friction	$m$
$h_m$	Head loss due to minor loss	$m$
$h_{mesh}$	local mesh diameter	$m$
$h_w$	Head due to work	$m$
$\Delta H_r$	Reaction enthalpy	$J$
$\Delta H$	Change in enthalpy	$J$
$h$	Enthalpy per mass unit	$m^2/s^2$
$\Delta H_r^\ominus$	Molar reaction enthalpy at standard conditions	$J/mol$
$I$	Current	$A$
$I_{leak}$	Leakage current	$A$
$J_{diff}$	Diffusion flux	$mol/m^2s$
$K_L$	Loss coefficient	$-$
$\Delta K$	Change in kinetic energy	$J$
$k$	Kinetic energy per mass unit	$m^2/s^2$
$k_a$	Anodic rate constant	$m/s$
$k_c$	Cathodic rate constant	$m/s$

---

$L$	Length	$m$
$m$	Mass	$kg$
$m$	Molality	$mol/kg$
$M_i$	Molar mass of species $i$	$kg/mol$
$n$	Number of moles of electrons exchanged in a reaction	—
$\dot{N}_i$	Molar flowrate of species $i$	$mol/s$
$p$	Pressure	$Pa$
$\Delta p$	Pressure drop	$Pa$
$P$	Power	$W$
$Q$	Electrolyte flowrate	$m^3/s$
$Q_c$	Charge	$C$
$Q_{heat}$	Heat added to the system	$J$
$q_{heat}$	Heat transfer per mass unit	$m^2/s^2$
$R$	Ohmic resistance	$\Omega$
$R_A$	Area resistivity	$\Omega\ cm^2$
$\tilde{R}$	Hydraulic resistance	$Pa\ s/m^3$
$r$	Radius	$m$
$Re$	Reynolds number	—
$S$	Entropy	$J/K$
$\Delta S_r^\ominus$	Molar reaction entropy at standard conditions	$J/K\ mol$
$SoC$	State of charge	—
$t$	Time	$s$
$T$	Temperature	$K$
$U$	Voltage	$V$
$U$	Energy density	$Wh/l$
$\Delta U_{en}$	Change in potential energy	$J$
$u_{en}$	Potential energy per mass unit	$m^2/s^2$
$u$	Electric mobility	$m^2/Vs$
$\tilde{u}_i$	Electrochemical mobility	$m^2/Js$
$V$	Volume	$m^3$
$V_s$	Velocity	$m/s$
$\mathcal{V}$	Molar volume	$m^3/mol$
$W$	Work done to the system	$J$
$w$	Work done to the system per mass unit	$m^2/s^2$
$x_i$	Molar fraction	—

---

---

## Greek Symbols

Symbol	Explanation	Units
$\alpha$	Charge transfer coefficient	—
$\gamma_i$	Activity coefficient of the species i	—
$\gamma$	Specific weight ( $\gamma = \rho g$ )	$N/m^3$
$\mu_i$	(Dynamic) viscosity of species i	$N\ s/m^2$
$\nu_i$	Kinematic viscosity of species i	$m^2/s$
$\nu$	Reaction rate	$mol/m^2\ s$
$\rho_i$	Density	$kg/m^3$
$\sigma$	Specific conductivity	$S/m$
$\tau$	Shear stress	$N/m^2$

## Indices

Symbol	Explanation
$\ominus$	Standard conditions
$\uparrow$	Species with an increasing concentration
$\downarrow$	Species with a decreasing concentration
<i>act</i>	Activation
<i>conc</i>	Concentration
<i>eq</i>	Equilibrium conditions
<i>i</i>	Species (i.e. $V^{2+}$ , $VO_2^+$ , etc.)
<i>O</i>	Pertaining to species Ox in $Ox + ne \rightleftharpoons Red$
<i>R</i>	Pertaining to species Red in $Ox + ne \rightleftharpoons Red$



# Electricity Storage: Why and How?

---

## 1.1. A Trend Towards Electricity Storage

Liberalization and deregulation in the electricity industry bring new challenges. Large centralized power plants will be complemented by distributed generation; the increasing amounts of distributed generation will require changes in the technology managing the transmission and distribution of electricity. Thus there will be a growing need for network operators to manage more actively the network: electricity storage system (ESS) will be a major tool for this purpose.

Distributed generation is a new trend in the generation of heat and electrical power; it refers to the placement of individual, smaller sized electric generation units at residential, commercial and industrial sites (Fig. 1.1). Examples of distributed generation units (DGU) are small gas turbines, fuel cells, photovoltaic (PV) cells and wind turbines. In the case of gas turbines and fuel cells, the heat that would normally be lost as a waste of energy can easily be harnessed to perform other functions, such as powering a boiler or space heating: this is known as combined heat and power (CHP) system.

Distributed generation systems with CHP can be very efficient, using up to 90% of the potential energy in the fuel they consume. And the shortened distance between the generation and the consumer diminishes the transport losses. On the other hand, the load of a centralized struc-

## 1.1. A TREND TOWARDS ELECTRICITY STORAGE

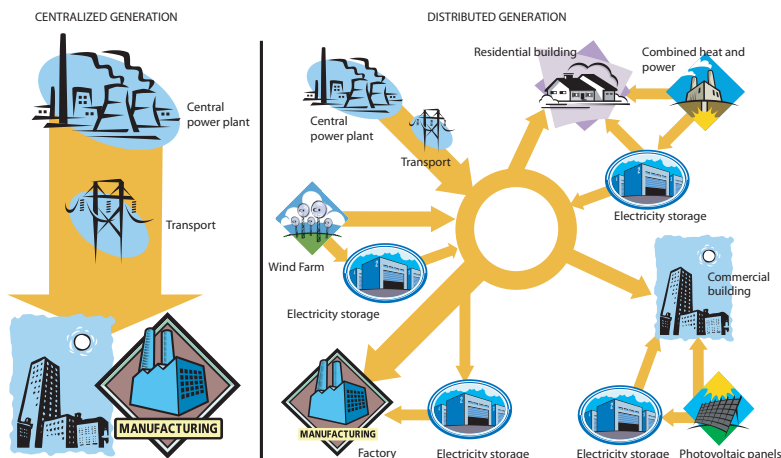


Figure 1.1.: Today's centralised generation vs. tomorrow's distributed generation.

ture changes slowly, thanks to the averaging effect of a large amount of consumers. This is not the case in a distributed structure, where fewer consumers are connected to a single generation units; this load can impose large and fast power fluctuations. Because production has to always equal the consumption, the generation unit needs to quickly follow the load. Thus, the power quality will be strongly affected by generation unit not able to follow the fast changing load. Once again, ESS will play a major role in increasing the power quality [1, 2].

High efficiency is achievable when the generator runs at nominal power: partial load results in low efficiency and high emission of pollutants. ESS levels the load by absorbing or furnishing power to the network; thus, generators are working at their nominal power and the fluctuation of the load is absorbed by the ESS.

Renewable energies such as wind turbines and PV cells have a fluctuating power output due to the variability of the wind speed or sun intensity. The utilization of such energy sources requires suitable energy storage systems since the offer and the demand of energy are more or less uncorrelated. Renewable energy sources integrating an ESS have a stability equal



to conventional systems: the economical value of the energy is strongly increased by this high availability.

Indeed, renewable sources with prediction errors and variable production, like wind and solar power, are not dispatchable and must run when available; the power from these sources is generally sold to grid operators for less than power available on demand. As renewable supplies become increasingly popular, this difference in price opens an increasingly large economical opportunity for ESS.

ESS bring additional benefits to the network such as bulk electricity price arbitrage, ancillary services, transmission support, demand charge management, and many more discussed in the next section.

Economically, the large domain of applications offers many opportunities for innovative technologies; the ESS market has been estimated at 60 billions dollars [3].

### 1.2. The Benefits of Electricity Storage

Energy storage became a major concern with the introduction of electricity. Unlike the other common power sources, such as natural gas, coal or petroleum, electricity has to be used whenever it is generated. This means that changes in demand are difficult to deal with, without either cutting supplies at times, or having expensive excess capacities (spinning reserve).

ESS have a wide range of potential applications: an application is defined as a specific way that energy storage is used to satisfy a specific need [2, 4]. The main applications are introduced in this section.

Over short time periods, the requirement is essentially power quality control. Energy storage system can rapidly absorb or generate reactive power to maintain transmission system voltages stability. They also provide spinning reserve to maintain the system frequency.

Over longer periods of time, the requirements become those of energy management (arbitrage) or provision of a contingency against an undesired event. Energy storage can be used to provide real power in the case of transport and distribution (T&D) failure or to energize part of a grid without outside assistance after a blackout has occurred.

Increased active management will bring additional benefits for consumers in terms of the introduction of greater choice with regard to energy supply services and greater competition. However, the switch to more active management may be a difficult one; distribution networks are a natural

## 1.2. THE BENEFITS OF ELECTRICITY STORAGE

---

monopoly and are thus tightly regulated to ensure that they do not draw excess profits at the expense of the consumer.

### 1.2.1. Bulk Electricity Price Arbitrage

Arbitrage is a business operation involving the purchase of foreign exchange, gold, financial securities, or commodities in one market and their almost simultaneous sale in another market, in order to profit from price differentials existing between the markets [5].

Hence, arbitrage applied to the electricity market involves the purchase of inexpensive electricity available during periods of low demand and its resale during period of strong demand and higher price. In consequence, ESS balance the fluctuations between the supply and the demand of electricity.

And since the price differential happens everyday, daytime electricity is always more expensive than nighttime electricity, therefore bulk electricity price arbitrage is almost a risk-free operation if the price differential is larger than the storage cost.

### 1.2.2. Electricity Demand Management at Customer Level

Electric utilities often charge their commercial and industrial customer a demand charge associated with a given peak load (kW). In order to reduce their overall cost, energy end-users can use an ESS to reduce their peak load, and thus, the associated demand charge.

This first application is called peak shaving and consists of storing electricity during low demand period and using it during the peak period to reduce the peak height. Peak shaving is illustrated in Fig. 1.2.

On a shorter and more repetitive time scale, peak shaving can be applied to the transportation systems. Indeed, ESS can smooth the short bursts of power on the distribution network produced when electrical vehicles brake or accelerate; in addition, elevators are also good candidates for this type of applications [6].

The second type of electricity demand management is the time-of-use electricity cost management. In fact, electricity prices are divided into categories (off-peak, mid-peak and on-peak) with different prices for different periods. In the same way as bulk electricity arbitrage, but at a smaller scale, end-users can take advantage of the price differential by

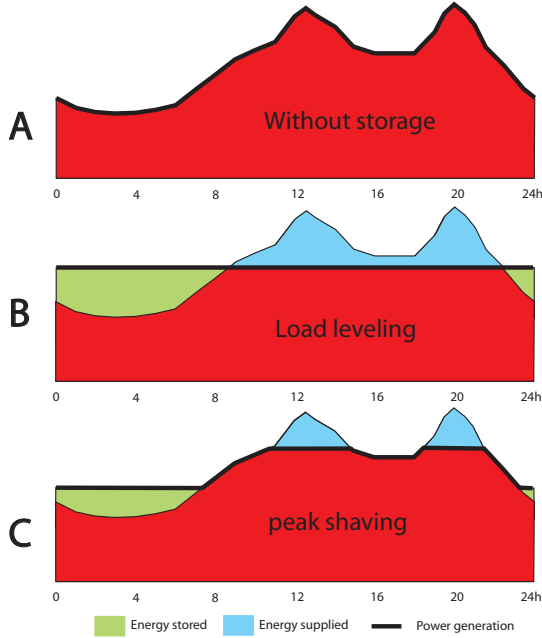


Figure 1.2.: Load profiles (A) without storage, (B) with load leveling and (C) peak shaving.

storing electricity during off-peak period: load leveling is a good example of time-of-use cost management and is illustrated in Fig. 1.2.

### 1.2.3. Ancillary Services

Ancillary services are those functions performed by the equipment and people that generate, control and transmit electricity in support of the basic services of generating capacity, energy supply and power delivery [7]. The *Federal Energy Regulatory Commission* (FERC) defines such services as those services necessary to support the delivery of electricity from seller to purchaser while maintaining the integrity and reliability of the

interconnected transmission system [2].

FERC has defined a list of key ancillary services [2, 7] for bulk-power reliability and support of commercial transactions. Naturally, ESS are able to provide many of those services. And thus, their economical values are greatly enhanced from this large range of potential services. Ancillary services that ESS can provide are given below:

- ***Reactive supply and voltage control***: The injection or absorption of reactive power to maintain the transmission system voltages within the required ranges.
- ***Regulation***: Minute-by-minute generation/load balance within a control area to meet standards.
- ***Spinning reserve***: Generation capacity that is synchronized to the grid but unloaded and that can respond immediately to compensate for generation or transmission outages.
- ***Supplemental reserve***: Generation capacity that may be off-line or curtailable load that can respond within 10 minutes to compensate for generation or transmission outages.
- ***Load following***: Meeting hour-to-hour and daily load variations.
- ***Energy imbalance***: Correcting for mismatches between actual and scheduled transactions on an hourly basis.
- ***Backup supply***: Generation available within an hour, for backing up reserves or for commercial transactions.
- ***Real power loss replacement***: Generation that compensates for losses in the transport and distribution (T&D) system.
- ***Black start***: Ability to energize part of a grid without outside assistance after a blackout has occurred.
- ***Network stability***: Real-time response to system disturbances to maintain system stability or security.

Other non-related to energy storage ancillary services are the system control and the dynamic scheduling.

#### 1.2.4. Generation Capacity Upgrade Deferral

Whenever the capacity of electric generation becomes tight, ESS can be used to defer and/or reduce the need to install a new generation unit in a certain area. Indeed, storage is used in lieu of adding generation capacity as it is illustrated in Fig. 1.3. Additional benefits of the storage solution are a better utilization of the capacity of the generation unit and probably a higher efficiency.

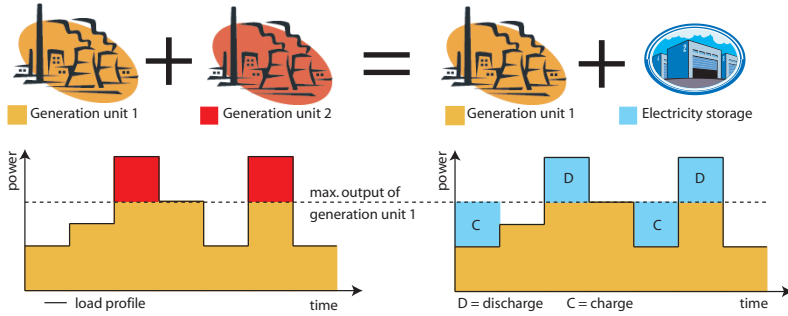


Figure 1.3.: Generation capacity upgrade deferral. Left, the load is met with an additional generation unit. Note that this second unit is seldom in service. Right, the generation unit is supplemented with an ESS allowing a better utilization of the generation capacity.

#### 1.2.5. Transmission and Distribution Support

In many areas, transmission capacities are not keeping pace with the growth in peak electricity demand so the T&D systems are becoming congested. The construction of an additional power line could be cancelled or postponed following the same approach than for the generation capacity. Indeed, the installation of an ESS downstream from the overloaded T&D line will relieve the power line during period of congestion by storing a part of the transported energy during a period of low demand. This is illustrated in Fig. 1.4.

Furthermore, ESS reduce the requirements of transmission capacity since networks are designed and built to carry the expected peak load,

## 1.2. THE BENEFITS OF ELECTRICITY STORAGE

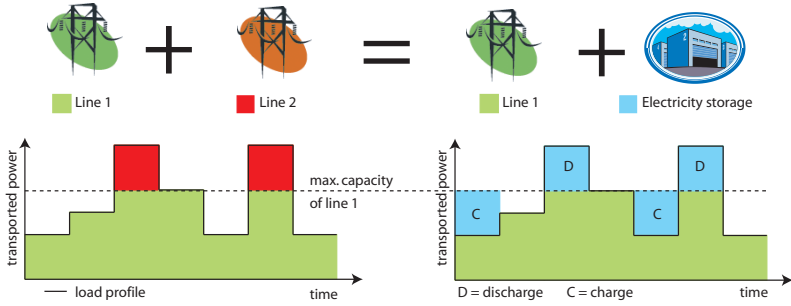


Figure 1.4.: Transmission upgrade deferral with the addition of a second line (left) or an ESS (right).

which often only exists for a small part of the annual operating cycle. Thus, the utilization of assets is increased with ESS.

Finally, ESS may be used to improve the transmission and distribution systems performance by compensating for electrical anomalies and disturbances such as voltage sag, unstable voltage and presence of sub-synchronous resonance. The result is a more stable system.

### 1.2.6. Electric Service Reliability and Power Quality

Electric service reliability and power quality are two important applications at the customer level.

#### Reliability

Customers expecting a highly reliable electric service might consider an ESS to protect themselves against a complete power outage. In that event, the storage system provides enough energy either to:

- ride through outages of extended duration
- complete an orderly shutdown of processes
- transfer to on site resources

### Power Quality

A high power quality can be achieved with an ESS that protects the loads downstream against short duration events which affect the quality of power. Some manifestations of poor power quality include:

- variations in voltage magnitude
- frequency variations
- low power factor (voltage and current excessively out of phase)
- harmonics (currents or voltages at frequencies other than the primary frequency)
- interruptions in service, of any duration, from a fraction of a second to minutes

#### 1.2.7. Renewable Capacity Firming and Energy Time-Shift

On the open market, a producer offers a certain amount of renewable power for a certain period of time. Since this is a firm offer, a penalty is due when the producer is not able to supply the power; the producer sometimes protects himself with a backup generation unit. The *International Energy Agency* (IEA) has found that, in some extreme cases, for every 100 MW of wind power, 100 MW of fossil, nuclear or hydroelectric power is needed as backup to run the transmission grids reliably [8]. Obviously, ESS are excellent candidate for this backup task.

Furthermore, an ESS might be charged with energy from renewable sources during periods when demand for electricity is low (and thus its value). In that case, the ESS time-shifts the energy delivery and thus, allows the producer to sell firm *green* power at a generally premium rate.

### 1.3. How to Store Electricity

In the previous sections, we have been through the wide spectrum of ESS applications, we are now ready to explore the different means to store electricity. Over the years, many energy storage technologies have been developed; some, like the pumped hydro facilities, with great success while others are still struggling to breakthrough.

### 1.3. HOW TO STORE ELECTRICITY

---

All have different characteristics, their own advantages and disadvantages depending on the considered applications. These technologies can be divided in three main categories:

- mechanical storage systems
- electrical storage systems
- electrochemical storage systems

We will discuss these categories in the following sections while keeping in mind that we are considering power applications.

#### 1.3.1. Mechanical Storage Systems

Watermills were used by Greeks and Romans to harvest the mechanical power of water; later, system of reservoirs and dams were built to store and release water whenever it was needed; later flywheels were added to smooth the output power.

Modern mechanical storage systems are based on the same ideas; indeed, the potential energy of water is used in pumped hydro facilities, the flywheels employ kinetic energy and compressed air energy storage systems take advantage of pneumatic energy. These modern technologies are described in the next three sections.

#### Pumped Hydro Facilities

Potential energy storage systems are today the most widespread ESS in use for power network applications. Worldwide, there are 285 pumped hydro power plants installed, representing a total installed power of 75 GW [9] which is about 3% of the global generation capacity. Their main applications are for energy management, frequency control and provision of reserve.

Pumped hydro was first used in Italy and Switzerland in the 1890's; by 1933 reversible pump-turbines with motor-generators were available. Today, adjustable speed machines are used to improve the efficiency.

Pumped hydro facilities are available at almost any scale with discharge times ranging from several hours to a few days and their efficiencies are in the 70% to 85% range. In addition, they are characterized by long construction time and high capital cost.



One of the major problems related to building new storage installations is of ecological nature. Indeed, appropriate locations are seldom found; therefore, the trend is actually to upgrade existing installations with existing cascaded basins. These facilities are complemented with new pump/turbines, enabling a bidirectional pump-storage operation of several hundreds MW. For example, two major upgrade projects are envisioned in Switzerland: *Linth Limmern* and *Nant-de-Dranse* [1].

The pumped hydro facilities consist of two water reservoirs separated vertically (Fig. 1.5) and use a basic principle: electricity is stored by pumping water from the lower reservoir into the upper reservoir and is generated when the water flow is reversed. Some conventional dam hydro plants have a storage capability and can be dispatched as virtual pumped hydro facilities by deferring the output until needed.

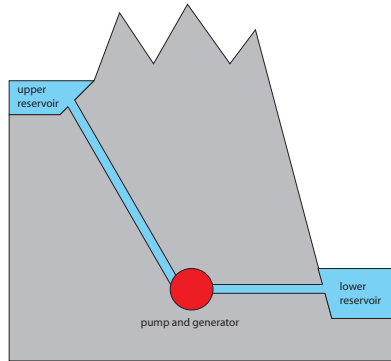


Figure 1.5.: Principles of a pumped hydro plant.

Unusual techniques such as open sea facilities or underground pumped storage have also been investigated; underground installations use flooded mine shaft or other cavities as reservoir. A demonstrator of the open sea technology has been built in Japan in 1999 and uses the sea as the lower reservoir [10].

#### Flywheels

Modern flywheels, like those installed on ancient watermills, are made of massive rotating cylinders that store kinetically the energy. The main differences being the spinning velocity, more than 20'000 rpm for modern technologies, and strong materials, such as steel or composite materials, that have replaced earlier materials.

Flywheels are connected to a motor/generator that, through some power electronics, interacts with the utility grid (Fig. 1.6). A low vacuum environment and magnetic bearings are used to reduce the drag and wear, thus increasing the efficiency and lifetime.

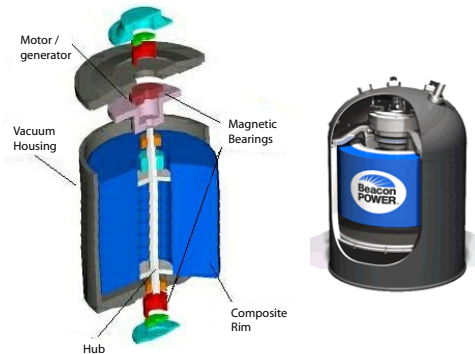


Figure 1.6.: Components of a flywheel (sources: [11] and [12]).

Advantages of flywheels are high efficiency, low maintenance, long life (20 years or 30'000 cycles) and environmentally friendly material. Flywheels applications are mainly focused on energy storage during a short time (bridging of voltage sags, smoothing a load profile, constant power output of wind turbines).

Today, 2kW, 6 kWh systems are deployed for uninterruptible power supply (UPS) applications. In the future, a flywheel farm approach may

provide a solution for frequency regulation on the electricity grid [11].

#### Compressed Air Energy Storage

Compressed air energy storage (CAES) is the last family of mechanical storage system introduced in this work; the idea of a pneumatic motor appears with the industrial revolution, but we had to wait until the second half of the twentieth century to see the first application of electricity storage.

The working principle of CAES is simple: basically, a pneumatic motor compresses the air inside an air tank to charge the CAES and electricity is produced when air is released through the pneumatic motor driving a generator. True CAES systems, as opposed to CAES coupled with a gas turbine, are based on thermodynamics, especially the isothermal cycle. They are currently developed at the *Laboratoire d'Electronique Industrielle* (LEI) (Fig. 1.7) combined with a supercapacitive auxiliary storage device [13].

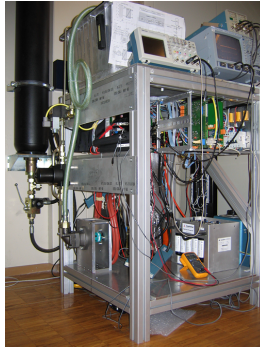


Figure 1.7.: Experimental setup of the hydraulic/pneumatic storage facility (LEI, EPFL).

Economically, a comparison based on the Golden Valley NiCd batteries storage system (40 MW, 13.3 MWh) found that CAES (air tank) is three times cheaper than lead-acid batteries storage (9.91 M€ instead of 30 M€) [14]. Moreover, CAES is environmentally friendly as it contains no toxic material.

### 1.3. HOW TO STORE ELECTRICITY

---

CAES is also a sustainable technology from which developing countries will particularly benefit when coupled with a renewable source. Indeed, CAES maintenance is low and its lifetime is long even under heavy environmental conditions. Actually, the lead-acid batteries installed in Africa with PV generation have a very short lifetime (sometimes less than 1 year), making their operating cost very high for these small communities.

#### CAES Coupled with a Gas Turbine

There is a second category of CAES coupled with a gas turbine which is not truly an energy storage: it is a peaking gas turbine power plant that consumes less than 40% of the gas used in a conventional gas turbine to produce the same amount of electricity. Unlike conventional gas turbines, where roughly 66% of their input fuel is used to compress air at the time of generation, low-cost electricity is used to pre-compress air into an underground cavern. During the generation phase, the pre-compressed air is preheated through a heat recuperator, then mixed with gas and burned to feed the turbine in order to produce electricity during peak demand (Fig. 1.8).

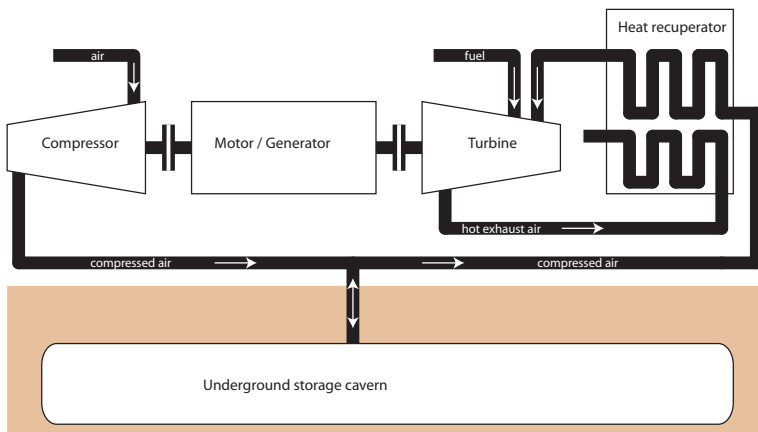


Figure 1.8.: Principle of a CAES coupled with a gas turbine.

Their advantages are long time (more than one year) energy storage and a relatively fast start-up time (9 to 12 min) which makes them suitable for grid operation. Their main drawback is their reliance on a particular geological structure, which substantially limits the usability of this storage system [14].

The first commercial CAES is a 290 MW unit built in Hundorf, Germany in 1978. The second commercial CAES is a 110 MW unit built in McIntosh, Alabama in 1991. The construction took 30 months and cost \$65M (\$590/kW) [11]. An additional 2700 MW facility was planned in Norton, Ohio.

### 1.3.2. Electrical Storage Systems

Previously, we have seen that the mechanical storage systems are based on simple principles; in the next sections, we will see that this is also the case for the electrical storage systems. Recently, new storage technologies have emerged, thanks to breakthroughs in superconductivity and material science. Simplicity comes from the fact that they are based on two of the main passive electrical components: capacitors and inductors.

Indeed, superconductivity enables the storage of electricity in the magnetic field of large inductors with minimal loss, and new materials have enabled the emergence of capacitors with extraordinarily high capacitances: the supercapacitors are able to store large amount of electrostatic charges.

#### Superconducting Magnetic Energy Storage

Superconducting magnetic energy storage (SMES) systems store energy in the magnetic field, created by the flow of direct current, of a large superconducting coil. At low temperature, the current encounters almost no resistance in superconducting materials: this enable the coil to carry large current with very low loss for long period of time. The major loss during storage is the energy required to maintain the superconducting coil at low temperature [15]. Fast response capability of SMES makes them commonly devoted to improving power quality. SMES is currently used for short duration energy storage.

Low temperature SMES (2 kW, 8 s) cooled by liquid helium are commercially available. Larger facilities have been built in the US up to 2.5 MW [17]. High temperature SMES cooled by liquid nitrogen is still in the development stage and may become a viable commercial ESS in the future.



Figure 1.9.: 200 kW, 8 s SMES (source: [16]).

SMES operation and lifetime are not influenced by the number of duty cycles or the depth of discharge. High overall efficiency (about 90%) has been reported in [18]. One of the major remaining problems is still its price.

#### **Supercapacitor**

The supercapacitor (SC) possess a very high capacitance, up to several thousands Farads, in a small package. SC can deliver high power in a very short time, but their amount of energy stored is low. In a way, SC bridges the gap between classical capacitors and batteries in terms of power and energy density.

SC is an electrochemical double layer capacitor consisting of two electrodes immersed into an electrolyte and separated by a separator [20]. Although the double layer is formed through the movement of anions and cations in the electrolyte (Fig. 1.11), we distinguish the supercapacitors from the electrochemical storage systems discussed in the next sections because no electrochemical reaction occurs in the supercapacitors. Indeed, the energy storage is by means of an electrostatic charge, purely physical and highly reversible like a conventional capacitor.

Unlike the electrochemical battery, there is very little wear and tear induced by cycling and age does not affect SC much: SC can withstand over a million of charge and discharge cycles [19]. A single SC has a typical



Figure 1.10.: 3000 F supercapacitor and supercapacitor modules (source: [19]).

voltage of a few volts; to operate at higher voltages, SC are connected in series. On a string of more than three capacitors, voltage balancing is required to prevent any cell from reaching overvoltage.

SC are not intended to replace batteries, but to complement them in handling their disadvantages in power delivery. They are ideal for applications requiring high peak power discharge for a few milliseconds up to several minutes. Examples of SC applications are: bridging short power interruptions (UPS), improving the current handling of a battery or a generator (SC can reduce the fuel consumption of a diesel train by 44% [21]), energy feeders for weak networks (for example trolley-buses supply [22, 23]) and many more.

### 1.3.3. Electrochemical Storage Systems

In 1800, Alessandro Volta invented the first modern electric battery: the voltaic pile. Since then, much progress has been made, batteries have evolved from non-rechargeable primary cells to rechargeable secondary cells. Today, electrochemistry is commonly used to store electricity in consumer electronics; moreover, larger power applications based on advanced batteries have been developed and successfully implemented.

Batteries are the core of the electrochemical storage systems; they consist of two types of electrochemical devices: galvanic cells and flow cells. Over the years, many designs have been proposed using different chemicals. Each design has its own advantages and drawbacks. In the next sections, we will discuss first some common galvanic batteries and then

### 1.3. HOW TO STORE ELECTRICITY

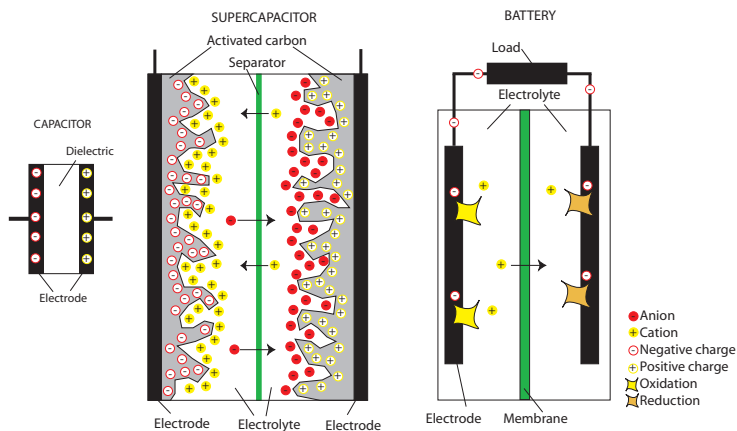


Figure 1.11.: Principles schematics of a capacitor, a supercapacitor and a battery. In the capacitor, the charges are simply stored in two electrodes separated by a dielectric material. In the supercapacitor, the charges are stored in porous activated carbon and, together with the ions dissolved in the electrolyte, they create the electrolytic double layers. In the conventional battery, the electrons are stored in the electrode material through an electrochemical reaction. The reduction and oxidation reactions are discussed in more detail in section 2.2.3.

present the flow batteries.

In general, batteries and advanced batteries can respond to changes in power demand within microseconds. Batteries usually have low standby losses and can have high energy efficiency, depending on the application and the details of the operation. However, most batteries contain toxic materials; hence their ecological impact from uncontrolled disposal must always be considered.

#### Lead-Acid Batteries

Lead-acid is one of the oldest and most developed battery technologies; it was invented by the French physician Gaston Planté in 1859. Materially, lead-acid batteries consist of a series of cells connected together, each cell





Figure 1.12.: Alessandro Volta 1745 - 1827 (source: [24]).

having a 2.1 V nominal voltage. A cell is made of two electrodes, one of lead metal ( $Pb$ ) and the other of lead oxide ( $PbO_2$ ), placed in a sulphuric acid electrolyte ( $H_2SO_4$ ). These batteries have an energy density around 35-55 Wh/kg.

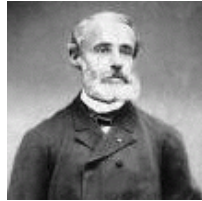


Figure 1.13.: Gaston Planté 1834-1889 (source: [24]).

Lead-acid batteries are a low cost and popular storage choice for power quality, UPS and some spinning reserve applications. Its application for energy management, however, has been very limited due to its short cycle life and its inability to withstand deep discharges. Nevertheless, they have been used in a few commercial and large-scale energy management applications: the largest ones are a 10 MW, 40 MWh system in Chino, California, built in 1988 (Fig. 1.14) and a 20 MW, 14 MWh system installed in Puerto Rico in 1994. Lead-acid are relatively inexpensive to purchase but their operational costs can be high due to frequent maintenance and replacement of cells [25].

Indeed, a full discharge causes extra strain, and each cycle robs the battery of a small amount of capacity. Depending on the depth of discharge

### 1.3. HOW TO STORE ELECTRICITY

---



Figure 1.14.: 10 MW, 40 MWh lead-acid storage system in Chino, California (source: [11]).

and operating temperature, lead-acid provides between 200 to 1800 charge and discharge cycles [13, 26]. But fortunately, they have a good electrical efficiency, 75 to 80% [27].

#### Sodium Sulphur Batteries

The sodium sulphur (NaS) technology was introduced in the 70s. At that time, it was an attractive candidate for electric vehicle applications and for large scale energy storage applications [28]. The market for the electric vehicles vanishes in the mid-90s when economical analyses have shown that the customers were not ready to purchase expensive pure battery-powered vehicles in high volume. However, development of this technology for stationary applications is still underway [27].

NaS battery consists of sulphur at the positive electrode, sodium at the negative electrode as active materials, and  $\beta$  alumina (a sodium ion conductive ceramic) which separates both electrodes (Fig. 1.15). This hermetically sealed battery is operating at high temperature 290-380°C , and its cell voltage is approx. 2 V at 300 °C.

The efficiency of the NaS system is 75% and its lifetime is assumed to be 15 years or 2500 cycles [27, 29]. Actually, a NaS cell has an energy density of 341 Wh/l and a module has a density of 145 Wh/l [30], this is 3-4 times higher than lead-acid batteries.

Load leveling, power quality and UPS are typical applications of the NAS battery. This technology has been demonstrated at over 30 sites in Japan totalling more than 20 MW [11]. The largest NaS installation is a 6 MW, 8 h unit for Tokyo Electric Power Company.

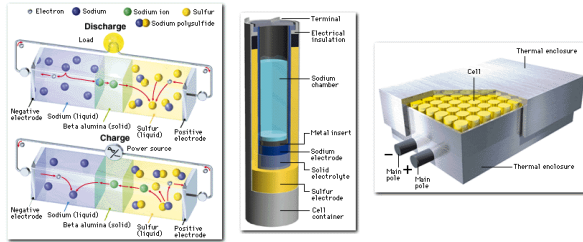


Figure 1.15.: Principle of NaS battery, NaS cell and NaS battery module (source: [29]).

### Lithium-Ions Batteries

Pioneer work with the lithium battery began in 1912 under the direction of Gilbert Lewis but the first non-rechargeable lithium batteries did not become commercially available until the early 1970s. We had to wait until the early nineties to see the first commercial rechargeable lithium-ion (Li-ion) battery and a few years later the first Li-ion polymer battery.



Figure 1.16.: Gilbert Newton Lewis 1875-1946 (source: [24]).

Lithium is the lightest metal and has the greatest electrochemical potential. Hence, Li-ion batteries have a high open circuit voltage in comparison to aqueous batteries, i.e. the average cell voltage is 3.6 V. Furthermore, Li-ion batteries provide the largest energy density (300 - 400 Wh/l, 130 Wh/kg); this is typically 5 times greater than the standard lead-acid batteries. Moreover, they have a long life cycle, 2500 cycles at an 80%

depth of discharge [31, 32].

Nonetheless, mistreatments, such as overcharge or perforation, may cause the batteries to explode. In that aspect, Li-ion polymer are more robust than Li-ion batteries; their energy density is also higher.

While Li-ion batteries took over 50% of the small portable market in a few years, there are some challenges for making large-scale Li-ion batteries. The main hurdle is the high cost (above \$600/kWh) due to special packaging and internal overcharge protection circuits.

#### **Metal-Air Batteries**

The last galvanic batteries introduced in this work are the metal-air batteries. They have a high energy density and are relatively inexpensive to produce. Zinc, aluminium and lithium are common electrode materials for metal-air batteries.

Zinc-air batteries have received the most attention due to their stability and electropositivity. Zinc-air has an energy density of 130-180 Wh/kg or 130-160 Wh/l [27], a density comparable to the NaS batteries.

While the metal-air batteries are environmentally benign, they have a huge disadvantage compared to other batteries: their energy efficiency is low, around 50%. This comes from the difficulty to recharge these batteries.

Another major issue is their short lifetime, 400 h or a few hundred cycles. It is worthwhile to note that the metal-air batteries can be mechanically recharged: the consumed metal being replaced, but this has no practical value for electricity storage.

In conclusion, while the high energy density and low cost of metal-air batteries may make them ideal for many primary battery applications, the electrical rechargeability feature of these batteries needs to be developed further before they can compete with other rechargeable battery technologies.

#### **Flow Batteries**

Flow batteries (FB) are the second category of electrochemical storage systems; they are large energy storage devices that have a wide range of potential applications in a distributed generation network. In the 70s, NASA started to work on redox flow batteries (RFB) with the aim to develop stationary energy storage applications [27, 33].

The term redox battery is used for electrochemical systems where the oxidation and reduction reactions involve only ionic species in solution and where the reactions take place on inert electrodes. FB differ from conventional batteries in two ways:

- the reaction occurs between two electrolytes, rather than between an electrolyte and an electrode. Therefore, no electro-deposition or loss in electroactive substances takes place when the battery is repeatedly deeply cycled.
- Electrolytes are stored in external tanks and are circulated through the cell stack.

FB are essentially comprised of two key elements (Fig. 1.17): the cell stacks, where chemical energy is converted to electricity in a reversible process, and the tanks of electrolytes where energy is stored. These two elements are supplemented with the circulation and control systems that respectively flows the electrolytes from the tanks to the electrochemical cells and supervises the operation of the storage system.

An individual cell consists of a negative electrode and a positive electrode separated by an ion exchange membrane. The electrolyte contains one or more dissolved electroactive species. Important features of the FB are the electrodes that do not take part in the reactions. Thus, there is no loss of performance, as it is the case in most rechargeable batteries, from repeated cycling that causes the deterioration of the electrode material.

The most significant feature of the FB is maybe the modularity of their power (MW) and energy (MWh) ratings which are independent of each other. In fact, the power is defined by the size and number of cells whereas the energetic capacity is set by the amount of electrolyte stored in the reservoirs. Therefore, FB can be optimized for either energy and/or power delivery.

Further advantages are quick response times, a characteristic that they share with other galvanic batteries and long life cycle, around 10'000 cycles. FB are normally considered for large stationary applications, ranging from a few kW to MW, in particular load leveling, peak shaving, power quality, renewable energy storage and UPS.

FB are categorized by the chemistry of the electrolytes. Over the past thirty years, several chemical couples have been investigated: Vanadium Redox, Zinc Bromine, Polysulphide Bromide and Cerium/Zinc. Some of

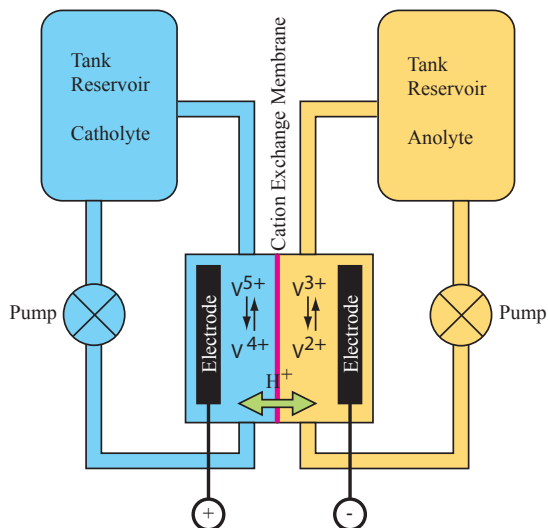


Figure 1.17.: The schematics of the vanadium redox flow battery.

these technologies are now available commercially and some are just emerging from development. M. Bartolozzi has done an historical bibliography of the development of redox flow batteries [33].

### 1.4. Technology Comparisons

We have seen in the previous sections that many storage technologies are available today to cover the wide spectrum of storage applications. But the comparison of these various technologies is difficult because they all have their own advantages and disadvantages, and to complicate this a little more, these qualities depend on the considered application. Nevertheless, three comparisons are presented in this work based on three important characteristics:

- Power and discharge time ratings

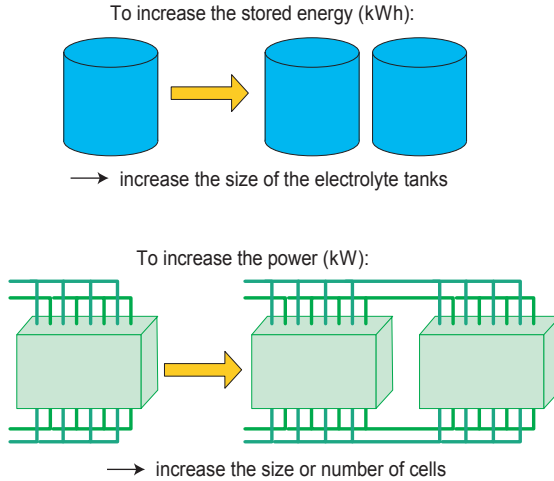


Figure 1.18.: Flow batteries energy and power modularity.

- Capital cost
- Efficiency and lifetime

### 1.4.1. Power and Discharge Time Ratings

The storage technologies available today cover a wide range of power and discharge time rating: from a few kW to a thousand of MW and from seconds to days. This section gives a hint on their ratings that are shown in Fig. 1.19. The technologies can be classified in two categories based on the discharge time:

1. **Short discharge time:** Power quality and UPS are typical short discharge time applications. Supercapacitors, flywheels and SMES are able to provide almost instantly large quantity of energy during periods of time ranging from seconds to minutes. Furthermore, they can withstand the large number of duty cycles imposed by power quality applications.

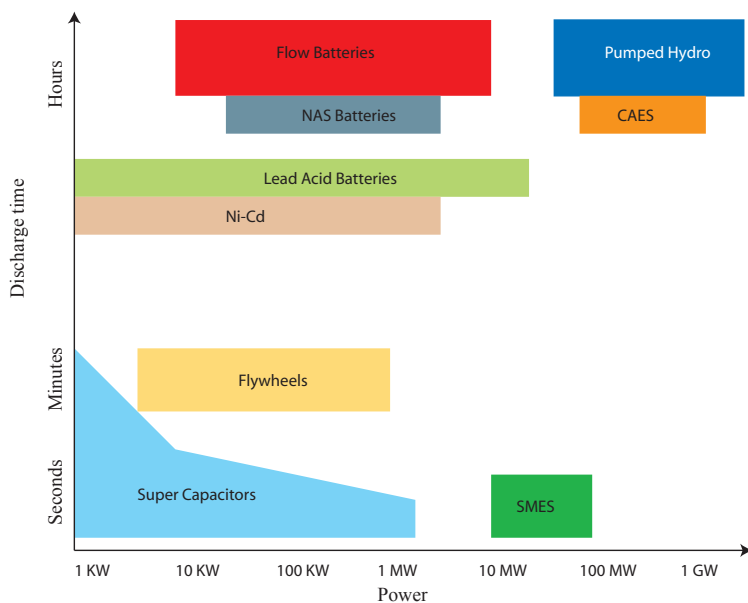


Figure 1.19.: System power ratings vs. discharge time at rated power.

2. **Long discharge time:** Power management is the typical long discharge time application. Flow batteries, CAES and hydro power can store large quantity of energy for very long period of time. Classic batteries are often used for shorter discharge time applications. Note that advanced batteries can also provide power quality and UPS services.

Although some storage technologies can operate in both storage ranges, it would not always be an economical solution.



### 1.4.2. Capital Cost

Capital cost is probably one of the most important characteristics<sup>1</sup>, along with the potential benefits, for the market acceptance of a new storage technology. The cost profile of storage technologies depends on the power and energy rating, and a balance has to be achieved between the cost and the benefits. Therefore, a technical and economic analysis is required to assess the cost of the storage system as the final cost and future benefits depend on the considered applications and on the chosen technology.

We will introduce here some notions about the total ownership cost, then compare the cost of various technologies and finally detail the capital cost of a 2 kW, 30 kWh VRB.

A cost assessment of an ESS must at least include the three following economic parameters and then compare them with the revenue from the considered storage applications:

- **Capital cost** is the total cost needed to construct or purchase the storage equipment. It includes the cost of financing.
- **Operating and maintenance cost** might have a significant impact on the total ownership cost.
- **Lifetime** is also an economic parameter because equipments with short lifetime need to be replaced more often.

Note that the costs are changing as the technologies evolve, some are already mature, like the lead acid batteries, and other are still under development. The costs of these technologies are expected to decrease when produced at larger scale.

The *Electricity Storage Association* (ESA) compiled a chart of the specific cost per power unit and energy unit of various storage technologies. The cost ranges in Fig. 1.20 include approximate values in 2002 and the expected mature values. The battery costs have been adjusted to exclude the cost of power conversion electronics and the cost per unit of energy has been divided by the storage efficiency [11].

---

<sup>1</sup> Although the network stability might increase in importance as the network becomes more and more decentralised and congested.

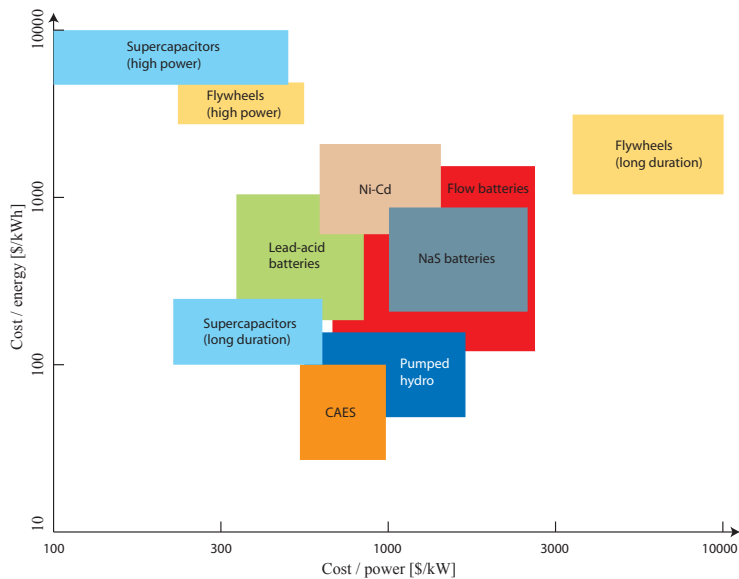


Figure 1.20.: Specific cost per power unit and energy unit for different electricity storage systems. These costs are changing as they evolve. The cost ranges in this chart include approximate values in 2002 and the expected mature values in a few years [11].

### One MW Storage System Cost Comparison

The capital cost depends on the ESS capacity, in particular on its maximum power output (kW) and its energy storage capability (kWh). An estimation of the specific cost per power unit and per energy unit is given in Tab. 1.1. These costs are for installations in the range of a few dozen to a few hundreds of kWh for the lead acid and NiCd batteries and of a few MW, 8 to 12 h for the NaS and VRB batteries [34].

The capital cost comparison of the four technologies is presented in Fig. 1.21; the costs of a 1 MW ESS as a function of the energetic capability are calculated from the specific cost given in Tab. 1.1.

	NaS	VRB	Lead Acid	NiCd
Specific cost per power unit [€/kW ]	300	426	0	0
Specific cost per energy unit [€/kWh]	192	100	225	1500

Table 1.1.: Specific cost per power unit or energy unit for different electricity storage systems. These costs are for installations in the range of a few dozen to a few hundreds of kWh for the lead acid and NiCd batteries and of a few MW, 8 to 12h for the NaS and VRB batteries [34].

The two most cost effective technologies are the lead acid battery and the VRB, depending on the amount of stored energy. The lead acid battery is competitive for small amount of stored energy, and then strongly penalized at larger amount for the dependence between its power rating and its energy storage capability.

On the other hand, the VRB is penalized by the cost of the stack designed to meet the power requirement and becomes very attractive at larger storage capacity, thanks to its modularity (see Fig. 1.18).

However, the choice of a specific technology must not only rely on the capital cost, but also on the technology efficiency, operating and maintenance cost, and lifetime. Economical success of a project depends also on the intended applications and the economical environment.

### Capital Cost of a 2 kW, 30 kWh Vanadium Redox Battery

To conclude this section on the capital cost, the detailed cost of a 2 kW, 30 kWh VRB based on an annual production of 1700 units, compiled by Joerissen and al. in [35], are given in Tab. 1.2. The characteristics of this battery are the following: 32 cells of 1100 cm<sup>2</sup>, a current density of 52 mA/cm<sup>2</sup> and an electrode area of 1.75 m<sup>2</sup>/kW.

The electrolyte is the most expensive part of the battery, representing more than half of its price. Unfortunately, the vanadium pentoxide  $V_2SO_4$  is also used in the production of steel and its price is likely to follow the rise of the raw materials market.

#### 1.4. TECHNOLOGY COMPARISONS

---

	Quantity	Cost per unit	Cost [€]
Activation felt	3.5 m <sup>2</sup> /kW	50 €/m <sup>2</sup>	350
Bipolar plates		65 €/kW	130
Flow frames, etc.		435 €/kW	870
Separator	2.1 m <sup>2</sup> /kW	25 €/m <sup>2</sup>	105
V <sub>2</sub> O <sub>5</sub>	1800 kg	13.6 €/kg	2448
Electrolyte preparation	for 1800 kg of V <sub>2</sub> O <sub>5</sub>	3 €/kg	540
Tanks	2 of 5500 l	185 €	370
Pumps	2	160 €	320
Battery management system	1	500 €	500
Total cost			5633

Table 1.2.: Cost estimation for a 2 kW, 30 kWh VRB system based on an annual production of 1700 units. The characteristics of this battery are: 32 cells of 1100 cm<sup>2</sup>, current density 52 mA/cm<sup>2</sup>, electrode area 1.75 m<sup>2</sup>/kW and V<sub>2</sub>O<sub>5</sub> energy density 6.0 kg/kWh [35].

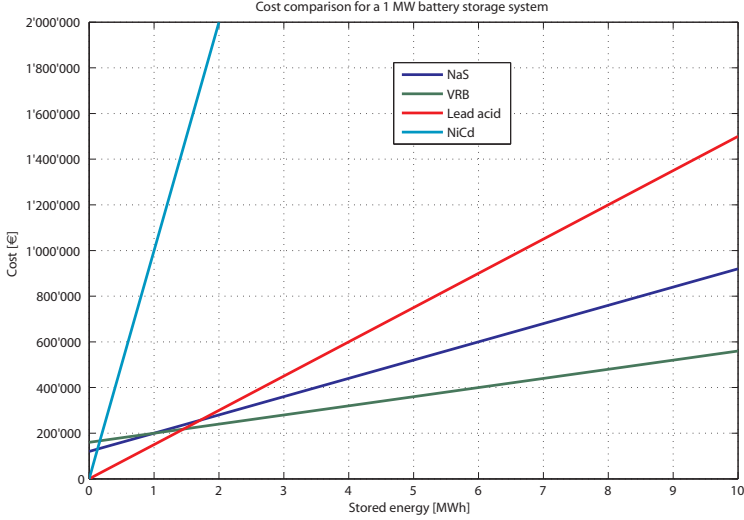


Figure 1.21.: Capital cost comparison for a 1 MW electricity storage system using the specific costs from Tab. 1.1.

### 1.4.3. Efficiency and Lifetime

Finally, comparing the efficiency and the lifetime is a tricky task because they are strongly influenced by the operating condition of the battery. For example, deep discharge and harsh environment, among other factors, tend to reduce the lifetime and the efficiency, but some technologies are less sensible than others.

The efficiency is also altered by the charge and discharge mode, a gentle cycle often has a better efficiency than a deep discharge at full power, but once again, this is not true for all technologies: SMES need a constant power to refrigerate its coil, negatively affecting its efficiency at low power and low duty cycle.

Fig. 1.22 shows the efficiency and the lifetime for different storage technologies. Conventional batteries like the lead acid batteries and NaS batteries, have shorter lifetime because their electrodes are participating in the redox reaction and therefore wear out faster than other technologies.

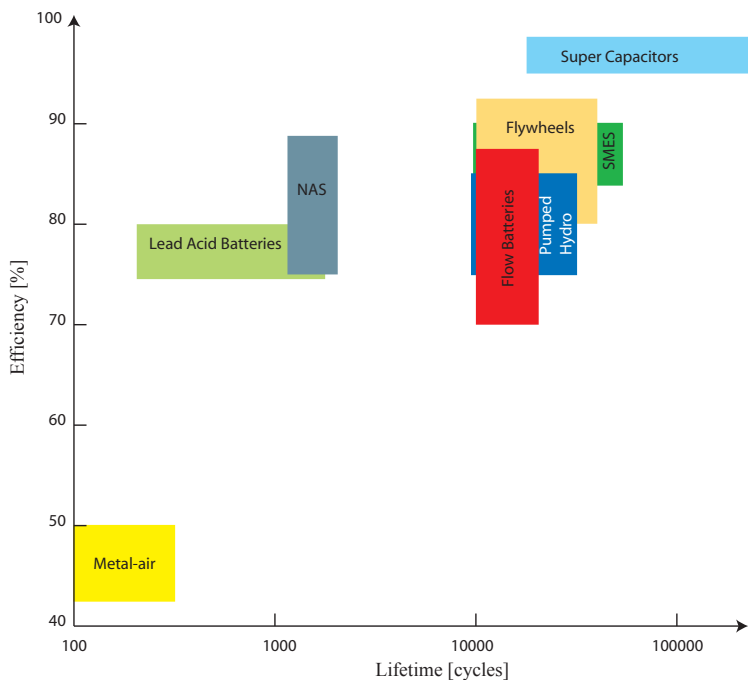


Figure 1.22.: Efficiency and lifetime comparison.

Although the supercapacitors have the highest efficiency and lifetime, they do not qualify for most of the applications due to their low amount of energy stored. In fact, they are often an ideal complement to other technologies in handling their disadvantages in power delivery.

The efficiency and lifetime both affect the overall cost of a storage system. Indeed, low lifetime technologies are worn out faster and need to be replaced more often, thus increase the operating cost. The same conclusion is drawn for low efficiency applications where the effective energy cost increases as only a fraction of the stored energy is utilized.

## 1.5. The Vanadium Redox Battery

We have seen through the previous sections that flow batteries are excellent candidates for large stationary storage applications. In this section, we introduce in more details the vanadium redox (flow) battery because we believe this technology has the best chance among the FB family to be widely adopted. Indeed, the VRB distinguishes itself thanks to its very competitive cost and its simplicity; the simplicity comes from the fact that the VRB deploys the same electrolyte in both half-cells. Furthermore, we will see in section 1.5.2, that some of the other FB employ toxic materials, require a recirculating pump to homogenize the electrolyte or even deposit materials on the electrode, thus limiting its energetic capacity. Therefore, we have selected the VRB in this work for a deeper investigation on its operating principles.

The VRB was developed at the University of New South Wales, Australia by Maria Skyllas-Kazacos and co-workers [36, 37]. It employs vanadium redox couples in both half-cells, thereby eliminating the problem of cross contamination by diffusion of ions across the membrane. The VRB exploits the ability of vanadium to exist in 4 different oxidation states, and uses this property to make a battery that has just one electroactive element instead of two.

A VRB consists of an assembly of power cells, each of which contains two half-cells that are separated by an ion permeable membrane. In the half-cells, the electrochemical reactions take place on inert carbon felt electrodes from which the current is collected. The balance of components required for the VRB consists of pipes and pumps to flow the electrolytes from the tanks to the stack. The schematic of the VRB is shown in Fig 1.17.

The electrolyte is a solution of vanadium mixed with a dilute sulphuric acid; this acidic solution has the same acidity as a conventional lead-acid battery. And unlike lead-acid systems, the VRB electrolyte has an indefinite life span and is reusable.

In more details, the electrolyte is an aqueous solution of sulphates of vanadium which is circulated from the tanks to the half-cells: the positive half-cells contain  $VO_2^+$  ( $V^{5+}$ ) and  $VO^{2+}$  ( $V^{4+}$ ) ions and the negative half-cells contain  $V^{3+}$  and  $V^{2+}$  ions. The electrolytes are typically prepared by a number of processes, that include the preparation of a vanadyl sulphate  $VOSO_4$  solution and the electrolytic reduction and/or oxidation of the

vanadium ions. The solution remains thereafter strongly acidic.

When charged electrolyte is flowed through the stack, an electrochemical redox reaction occurs and electrons are released during the  $V^{2+}$  oxidation in the anolyte. Then, these electrons are collected by the anode and transferred to the cathode, creating thus a direct current that flows through an external load. Finally, the electrons are accepted in the catholyte by the  $V^{5+}$  ions that are reduced in the process.

To charge the battery, the flow of electrons is reversed by an external source. By doing so, the reactions are reversed in both sides.

### Advantages and Disadvantages of VRB

Redox flow batteries (RFB) have many advantages when compared to ordinary batteries: RFB have a storage capacity independent of the battery power. They require low maintenance and are tolerant to deep discharge without any risk of damage. They also have a quick response time, an advantage in common with nearly all secondary batteries.

Furthermore, no solid state electrochemical reactions are involved and, as a consequence, the lifetime is very long compared to galvanic batteries. 10'000 charge and discharge cycles have been demonstrated [38], this corresponds to a 7-15 years lifetime. The efficiency belongs also in the advantages list of the VRB with a net efficiency as high as 85% [39].

As an environmentally friendly energy storage technology, the VRB is characterized by a low ecological impact: indeed, it does not rely on toxic substances such as lead, zinc or cadmium, like many other conventional energy storage systems do. C. Rydh found that the environmental impact was lower for the VRB than for the lead-acid battery [26].

The use of aggressive chemical solutions, which can have an impact on the environment, is a disadvantage for certain types of RFB. Fortunately, the VRB electrolyte is composed of vanadium dissolved in a sulphuric acid solution, an acid widely used and well known in other industries. Furthermore, because the electrolyte does not degrade, it can be easily recycled in a new VRB system.

Finally, the main disadvantage is the energy density that is low compared to other electrochemical batteries (15-30 Wh/l and 20-25 Wh/kg), this is due to the limited solubility of the active materials. But this low density is often not a drawback for stationary applications.



VRB characteristics are summarized in Tab. 1.3 and compared with the lead-acid battery.

	Vanadium Battery	Lead-acid battery
Specific energy	20-25 Wh/kg 30 Wh/l	37 Wh/kg
Efficiency <sup>a</sup>	70-88% <sup>b</sup>	70-80%
Life-cycle <sup>c</sup>	10'000-16'000 cycles	200-1500 cycles
Response time	350 $\mu$ s	
Operating temperature	10 to 45°C <sup>d</sup>	-10 to 40°C

<sup>a</sup>Pumped hydro have an efficiency of 70-80%, Metal-Air batteries 50%, NaS Batteries 89%, others advanced batteries 90-95% and supercapacitors 93-98% [13].

<sup>b</sup>70% system efficiency and 84% battery efficiency [39] or 82% battery efficiency and overall efficiency as low as 65% including pump and inverter loss [40].

<sup>c</sup>Pumped hydro life-cycle is 75 years, compressed air storage 40 years, Metal-Air batteries 100-200 cycles, NaS Batteries 2000-3000 cycles, others advanced batteries 500-1500 cycles and supercapacitors 10'000-100'000 cycles [13].

<sup>d</sup>[41] claims that the battery can be operated over the temperature range -5 to 99°C

Table 1.3.: VRB and lead-acid characteristics.

## Vanadium

The name vanadium comes from Vanadis, a goddess of beauty and fertility in the Scandinavian mythology, because the element has beautiful multicoloured chemical compounds.

Vanadium was originally discovered by Andrés Manuel del Río, a Spanish mineralogist, at Mexico City in 1801, who called it *brown lead* (see Fig. 1.23). A French chemist incorrectly declared that del Río's new element was only impure chromium. Del Río thought himself to be mistaken and accepted the statement of the French chemist.

In 1831, Nils Sefström, a Swedish chemist, rediscovered vanadium in a new oxide he found while working with some iron ores. He named it vanadium in honour of Vanadis.

Vanadium is a soft and ductile silver-grey metallic element. Its common oxidation states include +2, +3, +4 and +5. Vanadium itself may be soft in its pure form, but when it is alloyed with other metals like iron,



Figure 1.23.: Brown lead, currently named vanadinite, an ore of vanadium and lead (source: [42]).

it hardens and strengthens them dramatically. Approximately 80% of vanadium produced is used in the production of steels and alloys.

Vanadium is not found unbound in nature but it does occur in about 65 minerals. Russia and South Africa are the world's largest producers of vanadium. Large reserves are also found in the U.S., Canada, and China.

### Sulphuric Acid

Sulphuric acid,  $H_2SO_4$ , is a strong mineral acid. It is soluble in water at all concentrations. The old name for sulphuric acid was oil of vitriol. The discovery of sulphuric acid is credited to the 9th century Islamic physician and alchemist Ibn Zakariya al-Razi.

Sulphuric acid is widely used in many industries (fertilizer, textile, petroleum, chemicals, ...) and was the most produced chemical in the US with an annual production of 43'200'000 t in 1995 [43].

#### 1.5.1. VRB Installations

The selection of VRB installations presented in this section reflects some of their potential applications: wind power stabilization, new transmission line deferral, load leveling, emissions reduction and powering stand alone remote installation. Finally, Tab. 1.4 gives a list of VRB facilities installed around the world.



Figure 1.24.: Ibn Zakariya al-Razi (865 - 925) treating a patient (source: [24]).

### Tomamae Wind Villa Farm

The Tomamae Wind Villa farm is built on the island of Hokkaido, Japan, and consists of 19 turbines, corresponding to a total capacity of 30 MW. The fluctuation of the power output due to the wind variability might cause frequency instability and, in some place, limits the penetration level of wind generation. To mitigate this problem, it has been decided to install an ESS in order to improve the power quality [48, 49].

Therefore, a 4 MW, 6 MVA, 1.5 h VRB system has been installed at the Tomamae Wind farm; and since 2005, it successfully smoothes the power output and enables the supply of firm power to the network.

### Castle Valley

Castle Valley is a Southeast Utah isolated rural community bordering the Arches National Park; the power line that feeds this environmentally sensitive area has to traverse great distances. And lately, reliability and power quality issues arise because the line capacity did not keep pace with the increasing demand.

The Castle Valley VRB-ESS (Fig. 1.25) was built in order to defer the construction of a new \$5 million power line and avoid the lengthy permitting process required in this scenic area. This 250 kW, 350 kVA, 8 h VRB-ESS was commissioned in 2004 and has since effectively relieved the congested power line: the system is charged overnight and discharged

during the peak period. In addition, the power factor improvement has reduced the line loss by 40 kW [50, 51].

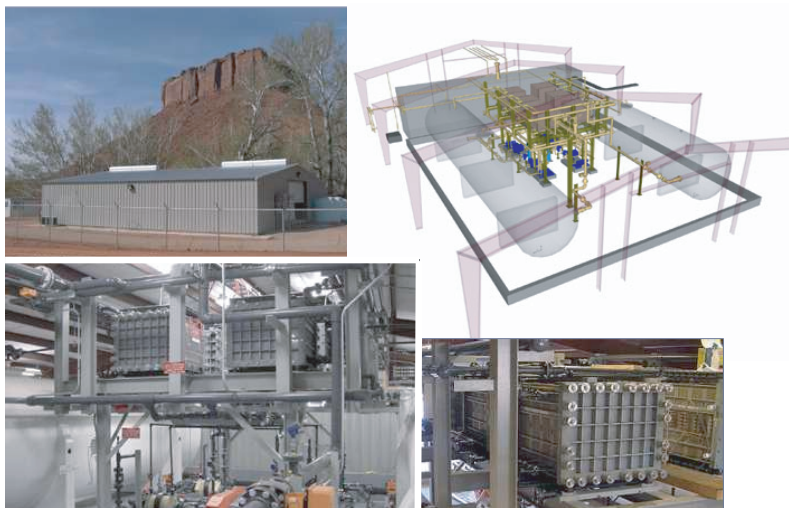


Figure 1.25.: Castle Valley VRB-ESS (source: [52]).

### King Island Wind Farm

King Island is one of the Tasmanian islands situated north of Tasmania mainland; it is not connected to the Tasmanian network and relied mainly on diesel generators for its electricity until the wind farm expansion. The power station has three diesel generators, totalling 3.2 MW, and is using approximately three million litres of diesel each year.

A 2.45 MW wind farm has been installed along with a VRB-ESS 200 kW, 4h, with the objectives to produce 45-50 % of the island consumption from wind energy and to reduce the diesel consumption by one third. Thus reducing  $CO_2$  emission by 3000 tonnes each year [45].

This VRB-ESS has allowed the island to boost its wind power production by smoothing out the wind variability and also providing additional

services in power quality and reliability.

### Leobersdorf VRB

The Leobersdorf VRB-ESS is a relatively small installation compared to the previous ones. The system is composed of a 1 kW, 50 kWh VRB supplied by a 1.1 kW photovoltaic source and a 1 kW wind turbine [46]. In this last example of potential application, the VRB is used to power a remote installation that is not connected to the grid: in this case, a traffic display board along a highway in Austria.



Figure 1.26.: Leobersdorf VRB (source: [53]).

In 2005, this system has been operating for 12 months and experienced a wide range of temperature (average external temperature varied from  $-9$  to  $30^{\circ}\text{C}$  ). A round-trip efficiency of 70% has been found for an average daily load of 4 kWh, equivalent to 170 W continuously [54]. This efficiency drops to 50% when the load is very small: daily load of 0.9 kWh or 38 W continuously, which is quite a low load for a 1 kW battery.

### 1.5.2. Other Flow Batteries

#### Polysulphide Bromide Battery

Polysulphide bromide battery (PSB) is a FB using sodium bromide and sodium polysulphide as salt solution electrolytes. Sodium ions pass through the membrane to maintain the electroneutrality of the cell. PSB has been developed since the early 90s in the UK [27]. Although this technology is claimed to be environmentally benign [55], there is concern that toxic bromine vapour might be released in an accident.

Some multi-kW batteries have been built; Innogy has built a 100 kW stack with a 1 m<sup>2</sup> electrode area. The net efficiency of this battery is about 75%. The construction of two large (12 and 15 MW, 120 MWh) storage plants in the UK and US has been stopped due to engineering difficulties and financial constraint [56]. Active PSB development has since been abandoned.

#### Zinc Bromine Batteries

The zinc bromine battery (ZBB) is a hybrid flow battery because one of its electrodes is participating in the reaction. This technology is currently being developed primarily for stationary energy storage applications, but also for electric-vehicle applications. The system offers a good specific energy (65-84 Wh/kg) and can withstand 2000 cycles [57]. The concept of a battery based on zinc/bromine couple was patented in 1885 [27], but technical difficulties halted the development until the mid-70s.

The electrolyte is zinc bromide salt dissolved in water; during the charge, zinc is plated on the negative electrode, thus limiting the capacity of the battery. At the positive electrode, bromine is produced and forms a bromine complex that sinks down the positive electrolyte tank. During the discharge, zinc is redissolved to form zinc ions and bromide ions are formed at the positive electrode. A third pump is required to recirculate the bromine complex (Fig. 1.27). The ZBB efficiency is around 60 - 75 %.

Over the years, some multi-kWh ZBB have been built and tested. Meidisha demonstrated a 1MW, 4MWh ZBB in 1991 at Kyushu Electric Power Company. ZBB Energy is producing a 250 kW, 500 kWh storage system mounted on a trailer.

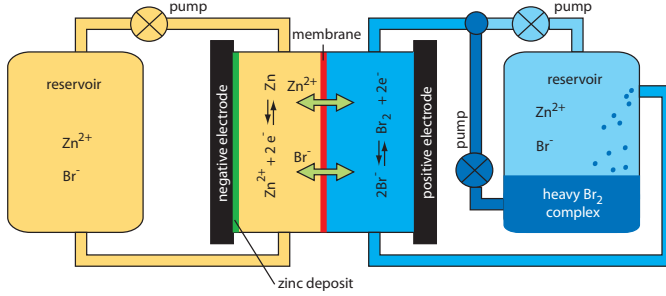


Figure 1.27.: Zinc bromine battery principles.

## 1.6. Motivation of the Present Work

Electricity storage is a disruptive technology, which can change the structure of the existing industry. Indeed, it offers alternative solution to traditional methods of improving and enhancing the network operations. Among the drivers for change in the power industry are cost reduction often based on the quest for improved efficiency, environmental considerations through the integration of renewables, power quality and reliability issues, and finally the technology itself.

Without a doubt, the vanadium redox battery is an enabling technology in electricity storage applications with many research and development opportunities for the present and the future. If the VRB technology has to be integrated in a distributed network, the storage systems have to be able to adapt to fast load changes, including transitions between the charge and discharge mode, and varying operating conditions.

In order to achieve such performance, the system's behaviour along with its interactions with the different subsystems, typically between the VRB stack and its auxiliaries (i.e. electrolyte circulation and electrolyte state of charge), and the electrical system it is being connected to have to be understood and appropriately modeled.

Once they are well understood and described in an appropriate model, it can be used to derive a control strategy for the whole VRB system that maximises or optimises the performance, the efficiency and the lifetime. Obviously, modeling a VRB is a strongly multidisciplinary project based

on electrochemistry and fluid mechanics; this represents an ambitious and formidable task for electrical engineers with little prior knowledge in these fields.

The *Laboratoire d'Electronique Industrielle* (LEI) has a strong interest in electrical power conversion and storage technologies, particularly in the context of future distributed power generation systems. Among others, S. Lemofouet has recently investigated and developed an ESS based on compressed air and supercapacitors [14], F. Grasser has developed an analytical model of a proton exchange membrane (PEM) fuel cell system [58] and C. Rivas has developed a new DC-AC power conversion strategy for use with fuel cell system [59].

Since the invention of the VRB in the 80's, electrochemists have studied the kinetics of the redox reactions [36, 37], compared various materials for the electrodes and membrane [60], optimized the composition of the electrolyte, but not much work has been done to characterise the VRB as a system component. Therefore, the goal of the present study is to elaborate a multiphysics model of the VRB ESS.

### 1.7. Structure of the Present Work

In this first chapter, we have seen that a trend toward electricity storage exists as a multi-purpose tool to improve network operations. Among the many available technologies, VRB are an attractive solution, both economically and technically, for large stationary storage applications.

Chapter 2 begins with an introduction to the electrochemical principles that govern the VRB chemical reactions. Starting from the chemical equations of the VRB reactions and with some thermodynamical principles, it details how to obtain the equilibrium voltage. When no electrical current is flowing, this equilibrium voltage depends on the state of charge and describes the voltage observed at the electrodes. Then, the deviations from the equilibrium state are described in detail; this includes the activation and concentration overpotentials, the ohmic loss and the ionic loss. A first electrochemical model is built from the relations introduced in this chapter.

Chapter 3 first deals with the variation of the vanadium and proton concentrations as a function of the operating conditions. Then a simplified model of the internal loss is proposed; together with the electrochemical model, they form the simplified and augmented model of the VRB



stack. This model is then used to simulate the behaviour of a small system comprising a photovoltaic array coupled with a 1.5 kW, 10 h VRB storage system. After the definition of the energy, coulombic and voltage efficiencies, a series of charge and discharge cycles are simulated and then compared to experimental data.

Chapter 4 focuses on the electrolyte properties. It begins with a short description of its preparation and then concentrates on two of its main characteristics: the density and the viscosity. We will see how they vary with the vanadium concentrations, the sulphuric acid concentration and the temperature. The importance of these two characteristics will appear in the next chapter.

Chapter 5 contains the relations necessary to build the mechanical model; this model determines the power required to flow the electrolytes from the pressure drops occurring in the hydraulic circuit, i.e. in the pipes, the tanks and the stack. The mechanical model is composed of two parts: an analytical model that describes the hydraulic circuit with the exception of the stack that is geometrically too complex. Therefore, a numerical model is proposed; it is based on a finite element method (FEM) analysis.

Chapter 6 assembles the multiphysics model from the electrochemical model and the mechanical model; in addition, the electrolyte properties are also included. Then different operating strategies are investigated, compared and commented; in particular, we will discuss in detail the performance of the battery at constant current and at various flowrates. We will also perform a new series of charge and discharge cycles to determine the overall battery efficiency. Finally, we will examine the battery performance at constant power and propose a method to determine the optimal operating point.

Chapter 7 presents the conclusion of this work and draw some interesting perspectives and future developments.

	Location	Rating	Year	Operator
1	Tomanae Wind farm, Japan	4MW, 6MVA, 1.5h	2005	Electric Power Development Co.
2	Castle Valley, Utah, USA	250kW, 350 kVA, 8h	2004	VRB power, PacificCorp
3	University of Stellenbosch, South Africa	250kW, 2h	2001	VRB power, Eskom [44]
4	King Island wind farm	200kW, 4h	2003	VRB power, Hydro Tasmania [44] [45]
5	Institute of Applied Energy, Japan	170kW, 6h	2001	SEI [44]
6	Totori Sanyo Electric, Japan	3MW, 1.5s	2001	SEI [44]
7	Obayashi Corp, Japan	30 kW dc, 8h	2001	SEI [44]
8	Kwansei Gakuin University, Japan	500 kW, 10h	2001	SEI [44]
9	Centro Elettrotecnico Sperimentale Italiano, Italy	42 kW, 2h	2001	SEI [44]
10	Leobersdorf, Austria	1 kW, 50 kWh	2004	En-O-De [46]
11	Risø National Laboratory, Denmark	15 kW, 120 kWh	2007	Risø National Laboratory [47]

Table 1.4.: VRB-ESS installations.

# Electrochemistry of the Vanadium Redox Batteries

---

## 2.1. Introduction

This chapter, based on electrochemical and thermodynamic principles, is focused on the chemistry of the vanadium redox battery. After a brief introduction of some general principles such as the molality, the molarity, the chemical equilibrium and the activity, we will introduce the important notion of redox chemistry and its application to the VRB. Then we will discuss the Gibbs free energy which represents the maximal amount of energy extractable from a chemical reaction, and the Nernst equation which is probably one of the most important relations of the electrochemical model. Indeed, the Nernst equation describes the equilibrium voltage.

In order to apply this powerful equation to the VRB, we must understand the chemical equation of the VRB reactions; therefore we must introduce a few relations that describe the standard potential, an ideal state where the battery is at standard conditions. Of course, we will see how to determine the standard potential from two methods: the thermodynamics and the standard reduction potentials. Then we will discuss the full ionic equations that are necessary to understand how the vanadium concentrations change during the battery operation and why the protons cross the membrane to equilibrate the charge balance. A numerical example will

then illustrate how the cell voltage changes as a function of the state of charge.

In the second part, we will explore the deviations from the equilibrium conditions; these conditions are disturbed when an electrical current flows through the cells. These deviations have the form of an overpotential; in fact, we can distinguish four types of overpotentials: the activation overpotential associated with the energy required to initiate a charge transfer, the concentration overpotential caused by the difference in electroactive species concentrations between the bulk electrolyte and the electrode surface, the ohmic and ionic overpotentials due to the electrical resistance that impedes the flow of electric charges. The overpotentials depend on the operating conditions and on the characteristics of the battery. Indeed, the design of the stack, the quality of its components (electrodes, membranes, etc.) and the composition of the electrolytes are important factors that influence the battery performance.

In the last part, the electrochemical relations introduced in the previous parts are assembled to form an analytical stack model that describes the battery behaviour; the model determines the overall stack voltage as a function of the operating conditions. The operating parameters are based on physical system inputs and are summarized in Tab. 2.1. These parameters can be divided in three categories:

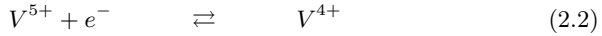
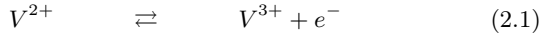
- **User parameter:** the user interacts with the battery through the electrical current  $I$ , it determines the power exchanged.
- **Internal parameters:** the vanadium concentrations  $c_{V^{2+}}$ ,  $c_{V^{3+}}$ ,  $c_{V^{4+}}$  and  $c_{V^{5+}}$  and the proton concentration  $c_{H^+}$  depend only on their initial concentrations and on the operating history of the battery, or in other words, on its actual state of charge.
- **External parameter:** the electrolyte temperature  $T$  reflects the ambient temperature, although in some circumstances, the battery operation might influence the temperature.
- **Control parameter:** the flowrate  $Q$  might be adapted to the actual operating conditions by the control system to enhance the battery performance.

Variable name	Operating parameter	Unit
$I$	Electrical current	A
$c_{V^{2+}}$	$V^{2+}$ anolyte concentration	mol/l
$c_{V^{3+}}$	$V^{3+}$ anolyte concentration	mol/l
$c_{V^{4+}}$	$V^{4+}$ catholyte concentration	mol/l
$c_{V^{5+}}$	$V^{5+}$ catholyte concentration	mol/l
$c_{H^+}$	Proton concentration in the catholyte	mol/l
$T$	Stack temperature	K
$Q$	Electrolyte flowrate	l/s

Table 2.1.: VRB operating parameters.

## 2.2. Generalities about Electrochemistry

This section focuses on some general notions that are helpful to understand the VRB chemistry. It starts with a brief definition of some units of concentration followed by the introduction of the important principle of chemical equilibrium. As an example, we introduce here the simplest chemical equations of the VRB reactions; the VRB is based on the four possible oxidation states of vanadium combined in the two electrode reactions:



→ discharge

← charge

At equilibrium, the forward reactions proceed at the same rate as the reverse reactions. To formalize this, we will introduce the equilibrium constant  $K$  and the species activities  $a_i$ . Then, we will discuss the redox chemistry that explains how the electricity is stored in the VRB.

The Gibbs free energy and the Nernst equation will conclude this section; from thermodynamical principles and the conservation of energy, they will lead to the definition of the equilibrium voltage.

### 2.2.1. Molality and Molarity

Molality and molarity are units of concentration that are particularly useful to chemists. The molality  $m$  is the number of moles of solute dissolved in one kilogram of solvent and the molarity is the number of moles of a solute dissolved in a litre of solution [61]. The molality is independent of the temperature and is defined as:

$$m_B = \frac{n_B}{n_A M_A} \quad \left[ \frac{\text{mol}}{\text{kg}} \right] \quad (2.3)$$

$$\begin{array}{lll} \text{where:} & n_A & = \text{number of mole of the solvent A} & [-] \\ & n_B & = \text{number of mole of the solute B} & [-] \\ & M_A & = \text{molar mass of A} & [\text{kg/mol}] \end{array}$$

The molar fraction  $x_b$  is defined as:

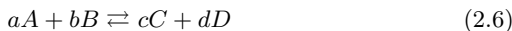
$$x_B = \frac{n_B}{n_B + n_A} \quad [-] \quad (2.4)$$

and the molarity  $c_b$  (or molar concentration) is defined as the ratio of the number of mole  $n_b$  to the volume of the solution  $V$ :

$$c_B = \frac{n_B}{V} \quad \left[ \frac{\text{mol}}{\text{l}} \right] \text{ or } [M] \quad (2.5)$$

### 2.2.2. Chemical Equilibrium and Activity

The chemical equilibrium describes the state that a system will reach *if you wait long enough* [62]. It is met when the forward chemical reactions proceed at the same rate as their reverse reactions, i.e. there are no net changes in any of the reactants ( $A$  and  $B$ ) or products ( $C$  and  $D$ ) concentrations.



where the stoichiometric factors  $a$ ,  $b$ ,  $c$  and  $d$  are introduced to maintain the composition of the reaction mixture since matter can neither be created nor destroyed by a chemical reaction.

The velocity of the reaction  $aA + bB$  or  $cC + dD$  is a function of the activities  $a_i$  of the reacting substances and, indeed, is proportional to the product of the activities, each activity being raised to a power equal to the number of moles of that substance in the reaction [63]. The equilibrium

is met when both velocities are equal; thus we can define the equilibrium constant  $K$  in the following form<sup>1</sup>:

$$K = \frac{a_C^c a_D^d}{a_A^a a_B^b} \quad [-] \quad (2.7)$$

The activity  $a_i$  is a sort of effective mole fraction and is given by the product between the mole fraction and the activity coefficient  $\gamma_i$ :

$$a_i = \gamma_i x_i \quad [-] \quad (2.8)$$

The activity coefficient  $\gamma_i$  is used to account for the effect of ionic strength on the chemical reaction. Under ideal solution conditions (very dilute solution  $< 0.01$  M), the activity coefficient tends to one and therefore the activity is given by the mole fraction [61, 63].

It is often convenient to use the scales of molality or of molarity when working with dilute solutions. Thus, the activity  $a_i$  is defined in the molarity scale as:

$$a_i = \gamma_i^c \frac{c_i}{c^\ominus} \quad [-] \quad (2.9)$$

$$\begin{aligned} \text{where: } \gamma_i^c &= \text{activity coefficient of the species } i \text{ in } [-] \\ &\quad \text{the molarity scale} \\ c^\ominus &= \text{standard molarity } (=1\text{M}) \quad [\text{mol/l}] \end{aligned}$$

Thus we can rewrite the chemical equilibrium expression<sup>2</sup> (2.6) at a constant temperature:

$$K = \frac{a_C^c a_D^d}{a_A^a a_B^b} = \frac{(\gamma_C^c)^c (\gamma_D^c)^d}{(\gamma_A^c)^a (\gamma_B^c)^b} \cdot \frac{c_C^c c_D^d}{c_A^a c_B^b} \quad [-] \quad (2.10)$$

Although  $a_A$ ,  $a_B$ ,  $a_C$  and  $a_D$  may not be identical to  $c_A$ ,  $c_B$ ,  $c_C$  and  $c_D$ , respectively, in most instances involving analytical work, little error is normally introduced by assuming that the ratios as given above are identical. However, under certain circumstances, activity should be used

---

<sup>1</sup>The activity of a pure liquid (i.e. a solvent), or a pure solid, is taken as unity.

<sup>2</sup>In order to ensure that equilibrium constants involving concentrations of reactant and product do not possess units themselves, all concentration terms in such formulae are expressed as ratios of the molarity or molality to a standard value, usually written  $m^\ominus$  or  $c^\ominus$ . It is understood that the term  $c_i$  in (2.10) really means  $\frac{c_i}{c^\ominus}$  if  $i$  is a solute [62, 64]. The mute term  $c^\ominus$  will be ignored and  $\gamma_i$  will be used instead of  $\gamma_i^c$  in the rest of this work.

in order to increase the accuracy of the calculations [63]:

$$K = \frac{a_C^c a_D^d}{a_A^a a_B^b} \cong \frac{c_C^c c_D^d}{c_A^a c_B^b} \quad [-] \quad (2.11)$$

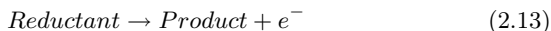
### 2.2.3. Redox Chemistry

Batteries are devices that store chemical energy and generate electricity by a redox (reduction-oxidation) reaction. Galvanic cells, fuel cells and flow cells are all based on a redox reaction. A redox reaction is a transformation of matter at the atomic level by electron transfer from one species to another. A molecule is said to be oxidized when it loses electrons. It is reduced when it gains electrons.

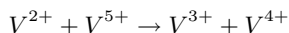
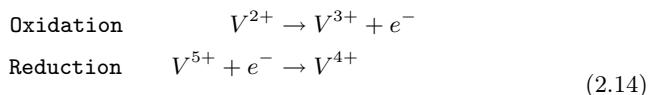
An oxidizing agent, also called an oxidant, takes electrons from another substance and becomes reduced.



A reducing agent (or reductant) gives electrons to another substance and is oxidized in the process.



In the VRB, the redox reaction is separated in two simultaneous steps occurring on both sides of the membrane (Fig. 2.1). During the discharge, electrons are removed from the anolyte and transferred through the external circuit to the catholyte. The redox reaction is in that case:



The oxidant  $V^{5+}$  takes an electron from the reductant  $V^{2+}$ . As the reaction proceeds from left to right,  $V^{5+}$  is reduced and  $V^{2+}$  is oxidized. The flow of electrons is reversed during the charge, the reduction is now taking place in the anolyte and the oxidation in the catholyte. The redox



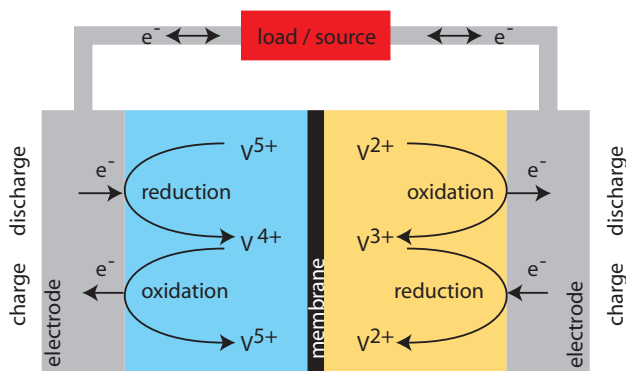
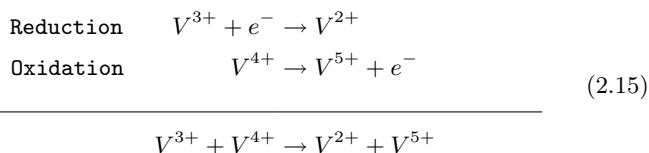


Figure 2.1.: VRB redox reaction during the charge and discharge.

reaction is then:



Because there is no net change in charge during a redox reaction, the number of electrons in excess in the oxidation reaction must equal the number consumed by the reduction reaction.

#### 2.2.4. Gibbs Free Energy and Nernst Equation

In electrochemistry, the standard electrode potential  $E^\circ$  is the measure of individual potential of any electrode at standard conditions:  $25^\circ\text{C}$ , 100 kPa and solutes at a concentration of 1 M. But in real applications, the conditions greatly differ from the standard: the concentration of the reagents and products vary in the course of the reaction and the operating temperature often differs from  $25^\circ\text{C}$ . Therefore, a relation is needed between the electrode potential  $E$  and the operating conditions: this relation is the Nernst equation.

## 2.2. GENERALITIES ABOUT ELECTROCHEMISTRY

---

The Nernst equation was discovered in 1889 by Walther Nernst (1864-1941), a Polish-German chemist who helped establish the modern field of physical chemistry with his contribution to electrochemistry, thermodynamics, solid state chemistry and photochemistry.



Figure 2.2.: Walther Nernst 1864-1941 (source: [24]).

In the 1870s, J. Willard Gibbs, an American physicist, chemist and mathematician, has defined the concepts of chemical potential and free energy. From the thermodynamics, he has stated that the maximal amount of energy that can be extracted from a chemical reaction is given by the *available energy*, now called in his honour the Gibbs free energy  $\Delta G$ :

$$\Delta G = \Delta H - T\Delta S \quad [J/mol] \quad (2.16)$$

where:	$\Delta H$	=	change in enthalpy	$[J/mol]$
	$\Delta S$	=	change in entropy	$[J/K \cdot mol]$

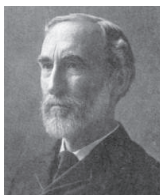


Figure 2.3.: J. Willard Gibbs 1839-1903 (source: [24]).

Complying with the law of mass action stating that the rate of a chemical reaction is directly proportional to the product of the effective concentration of each participating molecule, the thermodynamics state that for a chemical equilibrium, the Gibbs free energy  $\Delta G$  is expressed as a sum of a constant term  $\Delta G^\ominus$  that represents the free energy change for the reaction when the activity of each product and reactant is unity, and a variable term that is a function of the temperature and the equilibrium constant  $K$ :

$$\Delta G = \Delta G^\ominus + RT \ln K \quad [J/mol] \quad (2.17)$$

where  $R$  is the gas constant. When we introduce (2.10) into (2.17), we obtain:

$$\Delta G = \Delta G^\ominus + RT \ln \frac{a_C^c a_D^d}{a_A^a a_B^b} = \Delta G^\ominus + RT \ln \left[ \frac{c_C^c c_D^d}{c_A^a c_B^b} \cdot \frac{\gamma_C^c \gamma_D^d}{\gamma_A^a \gamma_B^b} \right] \quad [J/mol] \quad (2.18)$$

Then, the conservation of energy relates the change in free energy resulting from the transfer of  $n$  moles of electrons to the difference of potential  $E$ :

$$\Delta G = -nFE \quad [J/mol] \quad (2.19)$$

where  $F$  is the Faraday constant. Thereafter, we combine (2.18) and (2.19) into:

$$-nFE = -nFE^\ominus + RT \ln \left[ \frac{c_C^c c_D^d}{c_A^a c_B^b} \cdot \frac{\gamma_C^c \gamma_D^d}{\gamma_A^a \gamma_B^b} \right] \quad [J/mol] \quad (2.20)$$

which finally leads to the Nernst equation:

$$E = E^\ominus - \frac{RT}{nF} \ln \left[ \frac{c_C^c c_D^d}{c_A^a c_B^b} \cdot \frac{\gamma_C^c \gamma_D^d}{\gamma_A^a \gamma_B^b} \right] \quad [V] \quad (2.21)$$

Here  $E^\ominus$  is the standard electrode potential developed for a redox reaction where the activity of each product and reactant is unity.

The activities  $a_i$  and the activity coefficients  $\gamma_i$  are thermodynamic notions that can not be directly measured. To circumvent this limitation, the formal redox potential  $E^{\ominus'}$  has been introduced, this quantity is a measured potential and depends on the experimental conditions:

$$E^{\ominus'} = E^\ominus + \frac{RT}{nF} \ln \left[ \frac{\gamma_C^c \gamma_D^d}{\gamma_A^a \gamma_B^b} \right] \quad [V] \quad (2.22)$$

## 2.3. ALL-VANADIUM BATTERY REACTION

---

So, the activity coefficients  $\gamma_i$  are hidden and the Nernst equation (2.23) relies only on experimental quantities such as the concentrations:

$$E = E^{\ominus'} - \frac{RT}{nF} \ln \left[ \frac{c_C^c c_D^d}{c_A^a c_B^b} \right] \quad [V] \quad (2.23)$$

Note that in dilute solutions, the activity coefficients tend to unity and activities can be replaced by concentrations. In this case, the formal redox potential tends to the standard redox potential. Unfortunately, the VRB electrolyte is not a dilute solution, but a concentrated one.

## 2.3. All-Vanadium Battery Reaction

In the first part of this chapter, we have introduced some general electrochemical principles and relations; in this section, we will develop them and apply them to the all-vanadium battery. First, we will expand the chemical equations of the VRB reactions to reflect the real composition of the vanadium species; then, we will introduce the corresponding species in the Nernst equation to determine the equilibrium voltage. We will also discuss the assumption made when the activities are replaced with the concentrations.

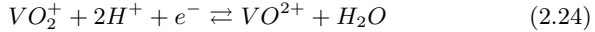
To resolve the Nernst equation, we must determine the value of the standard potential; therefore we will dedicate a section to the definition of the standard potential. Its value will be determined from the thermodynamics and from the standard reduction potentials; both methods are based on thermodynamical data available in tables. We will also shortly discuss its dependence upon the temperature.

Then, we will refine the chemical equations with the introduction of the complete ionic equations; this further step is necessary to determine the concentration of the protons in the catholyte. This concentration appears in the Nernst equation and changes as the battery operates. We will also explain why some protons cross the membrane to equilibrate the charge balance in the electrolytes.

In the last part, we will introduce a formal definition of the state of charge *SoC* and a brief numerical example will illustrate the equilibrium voltage of a single cell as a function of the vanadium concentrations.

### Chemical Equations of the VRB Reactions

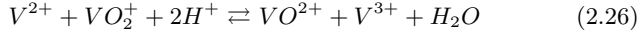
In reality, the VRB reactions are not as simple as presented in the electrochemical equations (2.14) and (2.15), or in Fig. 2.1: indeed, the vanadium ions  $V^{4+}$  and  $V^{5+}$  are in fact vanadium oxides, respectively  $VO^{2+}$  and  $VO_2^+$ . So, in order to maintain the charge balance and the stoichiometry, water molecules  $H_2O$  and protons  $H^+$  must be introduced in the cathodic reaction. Therefore, we rewrite (2.2) to take into account this new composition; the VRB reaction at the positive electrode (cathode) becomes:



At the negative electrode (anode), the water molecules and the protons do not take part in the electrochemical reaction; thus the anodic reaction stays as in (2.1):



Finally, we summarize (2.24) and (2.25) into a single VRB reaction:



We can draw a few observations about the VRB operations from the electrochemical reactions (2.24) and (2.25) that are summarized in Tab. 2.2. First, the anolyte and catholyte solutions contain respectively only  $V^{3+}$  ions (oxidation state +3) and  $VO^{2+}$  ions (oxidation state +4) at the totally discharged state. Then, when the battery is in charge, the reactions are shifted to the left and the concentration of  $V^{2+}$  ions (oxidation state +2) increases in the anolyte, at the same time, the  $V^{3+}$  concentration decreases at the same rate. Simultaneously in the catholyte, the concentration of  $VO_2^+$ -ions (oxidation state +5) increases and the  $VO^{2+}$  concentration decreases, both at the same rate as the anodic reaction.

The importance of the salt compositions introduced in Tab. 2.2 will appear in the full ionic equations discussed in section 2.3.3.

#### 2.3.1. Application of the Nernst Equation to the VRB

Now, we are ready to introduce the chemical equations (2.24) and (2.25) established in the previous section into the Nernst equation (2.21) to de-

### 2.3. ALL-VANADIUM BATTERY REACTION

Species	Salt	Battery state	Electrolyte
$V^{2+}$	$VSO_4$	Charged	Anolyte
$V^{3+}$	$0.5 V_2(SO_4)_3$	Discharged	Anolyte
$V^{4+}$ or $VO^{2+}$	$VOSO_4$	Discharged	Catholyte
$V^{5+}$ or $VO_2^+$	$0.5 (VO_2)_2SO_4$	Charged	Catholyte

Table 2.2.: The different vanadium ions, their corresponding salt, their corresponding battery state and the electrolyte where they are dissolved.

termine the equilibrium voltage  $E$  of a single cell:

$$\begin{aligned}
 E &= E^\ominus + \frac{RT}{nF} \ln \left\{ \left( \frac{c_{VO_2^+} \gamma_{VO_2^+} c_{H^+}^2 \gamma_{H^+}^2}{c_{VO^{2+}} \gamma_{VO^{2+}}} \right) \left( \frac{c_{V^{2+}} \gamma_{V^{2+}}}{c_{V^{3+}} \gamma_{V^{3+}}} \right) \right\} \\
 &= E^\ominus + \frac{RT}{nF} \ln \left\{ \frac{\gamma_{VO_2^+} \gamma_{V^{2+}} \gamma_{H^+}^2}{\gamma_{V^{3+}} \gamma_{VO^{2+}}} \cdot \frac{c_{VO_2^+} c_{V^{2+}} c_{H^+}^2}{c_{VO^{2+}} c_{V^{3+}}} \right\} \quad [V]
 \end{aligned} \tag{2.27}$$

In the case of the VRB reaction, the number of electrons  $n$  involved in (2.26) is equal to one. Obviously, the formal potential  $E^{\ominus'}$  can be used to hide the activity coefficients from (2.27):

$$E = E^{\ominus'} + \frac{RT}{F} \ln \left\{ \left( \frac{c_{VO_2^+} \cdot c_{H^+}^2}{c_{VO^{2+}}} \right)_{catholyte} \left( \frac{c_{V^{2+}}}{c_{V^{3+}}} \right)_{anolyte} \right\} \quad [V] \tag{2.28}$$

When the formal potential, which is an experimental value, is not available, the standard potential  $E^\ominus$  can be used instead if we neglect the effect of the activity coefficients  $\gamma_i$ . Indeed, the product/ratio of the  $\gamma_i$  in (2.27) can be set equal to 1 by assuming that the values of the  $\gamma_i$ , which probably deviate remarkably from 1 at the given concentrations, cancel each other approximately [65]. Thus, (2.27) can be rewritten as:

$$E = E^\ominus + \frac{RT}{F} \ln \left\{ \left( \frac{c_{VO_2^+} \cdot c_{H^+}^2}{c_{VO^{2+}}} \right)_{catholyte} \left( \frac{c_{V^{2+}}}{c_{V^{3+}}} \right)_{anolyte} \right\} \quad [V] \tag{2.29}$$

The value of the standard potential will be determined in the next section 2.3.2, it reflects the value of the cell voltage in the standard state which is a hypothetical state of an ideal solution with all activity coefficients  $\gamma_i$  equal to one and all concentrations equal to unity.

### Discussion about the Validity of the Previous Assumption

To establish the simplified Nernst equation (2.29), we have assumed that the effect of the activity coefficients  $\gamma_i$  is negligible in (2.27) because they cancel each other approximately. We will verify here this assumption, first by quantifying the contribution of the product/ratio of the activity coefficients to the equilibrium voltage and then by comparing the equilibrium voltage determined with the Nernst equation with experimental data.

So, the contribution of the activity coefficients was determined over a wide range from (2.27) and is illustrated in Fig. 2.4. We have also calculated the relative error introduced by this assumption which stays below 2% when the value of the product/ratio is bounded between 0.4 and 2.6. Therefore, we can clearly state from the observation of Fig. 2.4 that the contribution of the activity coefficients to the equilibrium voltage is negligible as long as their product/ratio is in the vicinity of one.

Although we have just seen that the activity coefficients have a negligible contribution to the equilibrium voltage if their product/ratio is close to one, we do not know yet if this is the case in reality. Therefore, we must compare our analytical model with experimental data published in the literature [65]. To do so, we have introduced into the Nernst equation (2.29) the standard potential  $E^\circ$  whose value is determined in the next section 2.3.2 and the proton concentration  $c_{H^+}$  which was determined from principles discussed in section 2.3.3. Finally, the electrolyte composition, i.e. the vanadium and proton concentrations were set to match the experimental conditions; these conditions were also reproduced in the numerical example concluding the presentation of the all-vanadium battery reaction in section 2.3.5. The comparison between the analytical model of the equilibrium voltage and experimental data is shown in Fig. 2.5.

We observe in Fig. 2.5 that the difference between the analytical and experimental data stays around or below 3% with the exception of both extremities of the graph. Indeed when the battery is fully charged, the difference climbs around 4% but the situation worsens when the battery becomes discharged, the difference quickly increases as the cell voltage

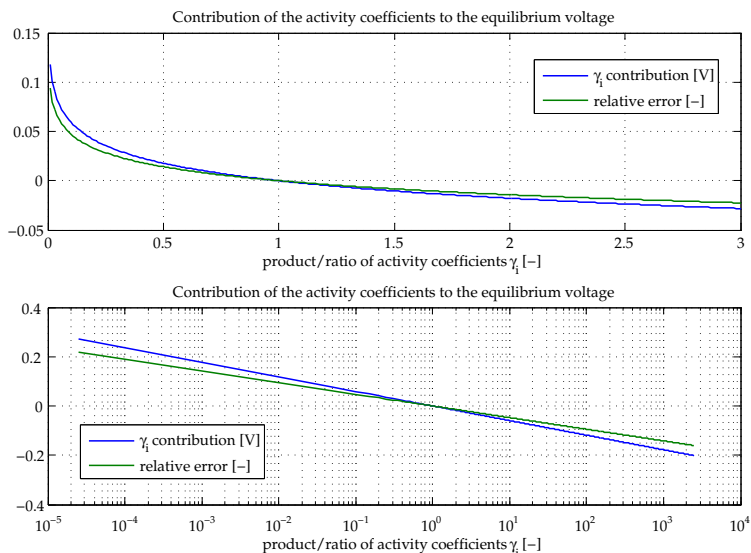


Figure 2.4.: Sensitivity analysis of the contribution of the activity coefficients  $\gamma_i$  to the equilibrium voltage (2.27) and relative errors introduced by their omission as a function of the product/ratio of  $\gamma_i$ .

drop. There is no easy explanation for this phenomenon probably due to the complexity of the vanadium electrochemical reactions at those high concentrations. Nevertheless, our assumption is acceptable since the difference is small for the majority of the battery operating range; furthermore the battery is seldom operated at these extreme states of charge where the difference increases.

### 2.3.2. Standard Potential

In the previous section, we have established the equilibrium voltage of a VRB cell (2.29) and examined its validity; but we did not explain how certain values or parameters are obtained. We are about to fill this gaps in the next few sections; here, we will define the standard potential  $E^\ominus$ , an



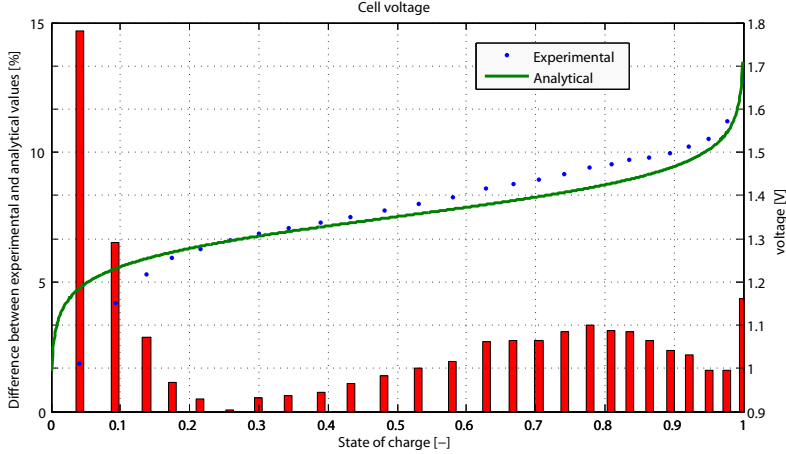


Figure 2.5.: Comparison between the simplified Nernst equation (2.29) and the experimental data published in [65]. The red bars represent the difference between the analytical and experimental data.

ideal state where the battery is at standard conditions: vanadium species at a concentration of 1 M, all activity coefficients  $\gamma_i$  equal to one and a temperature of 25°C . In the next sections, we will see how to determine the proton concentration from the full ionic equations and how to determine the state of charge.

The standard potential is an important parameter in the Nernst equation because it expresses the reaction potential at standard conditions; the second term in the Nernst equation is an expression of the deviation from these standard conditions. Together, they determine the equilibrium cell voltage under any conditions.

In this section, we will introduce two methods to find the value of  $E^\ominus$ ; the first is derived from the thermodynamical characteristics of the elements involved in the VRB reactions and the second is a combination of the standard reduction potentials of the two half-cell reactions. Both methods employ empirical parameters found in electrochemical tables.

### From the Thermodynamics

This first method is based on thermodynamical principles introduced in section 2.2.4, namely the Gibbs free enthalpy  $\Delta G$  and the conservation of energy. We introduce here the standard Gibbs free enthalpy of reaction  $\Delta G^\ominus$  which represents the change of free energy that accompanies the formation of 1 M of a substance from its component elements at their standard states: 25°C , 100 kPa and 1 M [66]:

$$\Delta G^\ominus = \Delta H_r^\ominus - T\Delta S_r^\ominus \quad [kJ/mol] \quad (2.30)$$

where the standard reaction enthalpy  $\Delta H_r^\ominus$  is the difference of molar formation enthalpies between the products  $\Delta H_{f,product}^\ominus$  and the reagents  $\Delta H_{f,reagent}^\ominus$ :

$$\Delta H_r^\ominus = \sum_{products} \Delta H_{f,product}^\ominus - \sum_{reagents} \Delta H_{f,reagent}^\ominus \quad [kJ/mol] \quad (2.31)$$

and the standard reaction entropy  $\Delta S_r^\ominus$  is the difference of molar formation entropies between the products  $S_{f,product}^\ominus$  and the reagents  $S_{f,reagent}^\ominus$ :

$$\Delta S_r^\ominus = \sum_{products} S_{f,product}^\ominus - \sum_{reagents} S_{f,reagent}^\ominus \quad [J/mol \cdot K] \quad (2.32)$$

Then, when we introduce the thermodynamical data from Tab. 2.3 into (2.31), the standard reaction enthalpy  $\Delta H_r^\ominus$  of the VRB reaction (2.26) becomes:

$$\begin{aligned} \Delta H_r^\ominus &= \Delta H_{f,VO^{2+}}^\ominus + \Delta H_{f,V^{3+}}^\ominus + \Delta H_{f,H_2O}^\ominus \\ &\quad - \Delta H_{f,V^{2+}}^\ominus - \Delta H_{f,VO_2^+}^\ominus - 2\Delta H_{f,H^+}^\ominus \\ &= -155.6 \text{ kJ/mol} \end{aligned} \quad (2.33)$$

and similarly, the standard reaction entropy  $\Delta S_r^\ominus$  is obtained when these thermodynamical data are introduced into (2.32):

$$\begin{aligned} \Delta S_r^\ominus &= S_{f,VO^{2+}}^\ominus + S_{f,V^{3+}}^\ominus + S_{f,H_2O}^\ominus \\ &\quad - S_{f,V^{2+}}^\ominus - S_{f,VO_2^+}^\ominus - 2S_{f,H^+}^\ominus \\ &= -121.7 \text{ J/mol} \cdot K \end{aligned} \quad (2.34)$$

Formula	State	$\Delta H_f^\ominus$ [kJ/mol]	$\Delta G_f^\ominus$ [kJ/mol]	$S_f^\ominus$ [J/mol · K]
$V^{2+}$	aq	(-226)	-218	(-130)
$V^{3+}$	aq	(-259)	-251.3	(-230)
$VO^{2+}$	aq	-486.6	-446.4	-133.9
$VO_2^+$	aq	-649.8	-587.0	-42.3
$H_2O$	aq	-285.8	-237.2	69.9
$H^+$	aq	0	0	0

Table 2.3.: Thermodynamical data for some vanadium compounds at 298.15 K. Values in parentheses are estimated [66, 67].

Finally, the conservation of energy relates the standard Gibbs free enthalpy of reaction  $\Delta G^\ominus$  to the standard potential  $E^\ominus$ ; therefore, we obtain the standard potential  $E^\ominus$  when we introduce  $\Delta G^\ominus$  (2.30) with the values of the standard reaction enthalpy (2.33) and entropy (2.34) into the reformulated (2.19):

$$E^\ominus = -\frac{\Delta G^\ominus}{nF} = -\frac{\Delta H_r^\ominus - T\Delta S_r^\ominus}{nF} \quad [V] \quad (2.35)$$

So, we have determined from the thermodynamical principles that the standard potential  $E^\ominus$  is 1.23 V at 25°C .

### Temperature Dependence

We make here a short digression to consider the temperature dependence of the standard potential; indeed, the standard potential depends on the temperature as it is illustrated in Fig. 2.6. Furthermore, we can determine the change in  $E^\ominus$  from (2.35):

$$\frac{\partial E^\ominus}{\partial T} = -\frac{1}{nF} \left( \frac{\partial \Delta G^\ominus}{\partial T} \right) \cong \frac{\Delta S_r^\ominus}{nF} = -1.26 \text{ [mV/K]} \quad (2.36)$$

Experimentally, Heintz and Illenberger [65] have highlighted this linear relationship between the standard potential  $E^\ominus$  and the temperature.

## 2.3. ALL-VANADIUM BATTERY REACTION

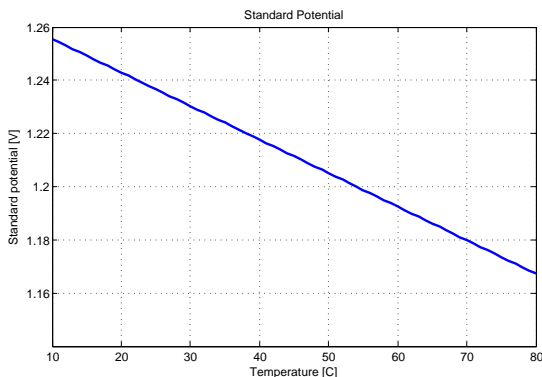
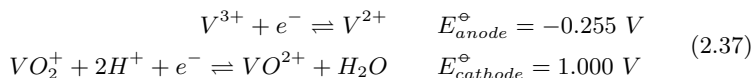


Figure 2.6.: Standard potential (2.35) as a function of temperature.

They have found a negative slope of -1.62 mV/K between 5°C and 50°C ; this is slightly higher than the theoretical value of -1.26 mV/K.

### From the Standard Reduction Potentials

The second method to determine the standard potential  $E^\ominus$  is based on the standard reduction potential which represents the tendency of a chemical species to acquire electrons and thereby be reduced. These potentials are available in electrochemical tables and can be represented in a potential diagram (Fig. 2.7). In the case of the VRB, we can determine the standard reduction potentials of the two redox couples; the two electrode potentials,  $E_{anode}^\ominus$  and  $E_{cathode}^\ominus$  have the following values<sup>3</sup>:



<sup>3</sup>The standard potential for the anodic reaction  $E_{anode}^\ominus$  has also been reported to be -0.24 V in [68] and measurements in 0.5 and 3M  $H_2SO_4$  solutions of -0.258 V and -0.291 V have been reported in [69]. For the cathodic reaction, the standard potential  $E_{cathode}^\ominus$  has also been reported to be as low as 0.991 V in [35, 70] and as high as 1.004 V [69]. Experimental measurements in 1 and 3M  $H_2SO_4$  solutions of 1.008 V and 1.103 V have been reported in [69].

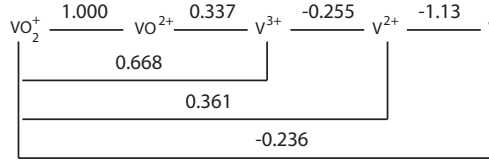


Figure 2.7.: Potential diagram for the vanadium species in strongly acidic solutions [67]. The values are given in V.

Note that the electrode potentials  $E_{anode}^\ominus$  and  $E_{cathode}^\ominus$  are valid for a given temperature<sup>4</sup>; therefore, this second method is only able to determine the standard potential  $E^\ominus$  at this temperature. The standard potential is given from the difference between the cathode potential  $E_{cathode}^\ominus$  and the anode potential  $E_{anode}^\ominus$ :

$$E^\ominus = E_{cathode}^\ominus - E_{anode}^\ominus = 1.255 \text{ V} \quad (2.38)$$

To conclude this section, we can state that the two above methods give similar results for the standard potential  $E^\ominus$ , at 25°C, the difference is below 2%; but the thermodynamical method is able to determine  $E^\ominus$  at any temperature. Furthermore, we will observe in the sections 2.3.5 and 3.3 that the open circuit cell voltage (OCV) at a 50% state of charge is often found to be higher than the standard potential (see Fig. 2.9 and 3.8); we can explain this by the high sulphuric acid concentration, inducing a high proton concentration, and by the high vanadium ion concentrations.

### 2.3.3. Full Ionic Equations

At the beginning of this section 2.3, we have established the chemical equations of the VRB reactions (2.24), (2.25) and (2.26); unfortunately, these equations do not reflect exactly the phenomena happening in the cells. Indeed, the VRB electrolytes contain not only vanadium ions at different oxidation states, but also protons  $H^+$  and sulphate ions  $\text{SO}_4^{2-}$  that are only partially represented in the chemical equations; these ions are called spectator ions and do not take an active part in the reaction. But these spectator ions are important to respect the law of conservation of mass

<sup>4</sup>in this case, standard reduction potentials are given at 25°C.

and the charge balance in both electrolytes. Therefore, we introduce here the complete ionic equations that will help us understand the variations of the proton concentrations and why some protons  $H^+$  cross the membrane to balance the charge in the electrolytes.

To determine the full anodic equation, we introduce the salts corresponding to the vanadium species (see Tab. 2.2) and the sulphuric acid<sup>5</sup>  $H_2SO_4$  into the net ionic equation (2.25); in the electrolyte, these salts are dissociated and similar ions are then grouped together:

$$\begin{aligned}
 & V^{3+} + e^- \\
 & \equiv 0.5 V_2(SO_4)_3 + a H_2SO_4 + e^- \\
 & \equiv (V^{3+} + (1.5 + a) SO_4^{2-} + 2a H^+ + e^-) \\
 & \quad \downarrow \text{CHARGE} \\
 & V^{2+} \\
 & \equiv VSO_4 + b H_2SO_4 \\
 & \equiv V^{2+} + (1 + b) SO_4^{2-} + 2b H^+
 \end{aligned} \tag{2.39}$$

Using the law of conservation of mass that states that the mass of a closed system remains constant, i.e. in chemical reactions or equations no atom may be created or destroyed, we know that the quantity of sulphate  $SO_4^{2-}$  must remain constant, therefore:

$$b = 0.5 + a \tag{2.40}$$

A careful examination of (2.39) reveals that the quantity of protons  $H^+$  is increased by 1 M during the reduction of 1 M of vanadium  $V^{3+}$ . Fortunately, we will soon discover that the cathodic reaction produces an extra mole of  $H^+$  during the oxidation of 1 M of  $VO^{2+}$ . Therefore, if the protons are able to cross the membrane, the law of conservation of mass is respected; furthermore, the charge balance is also maintained throughout the reaction. This can be observed in Fig. 2.8 where the full ionic equations are illustrated.

Following a similar approach, we can derive the full cathodic equation

---

<sup>5</sup>The quantity of sulphuric acid depends on the electrolyte composition.

### 2.3. ALL-VANADIUM BATTERY REACTION

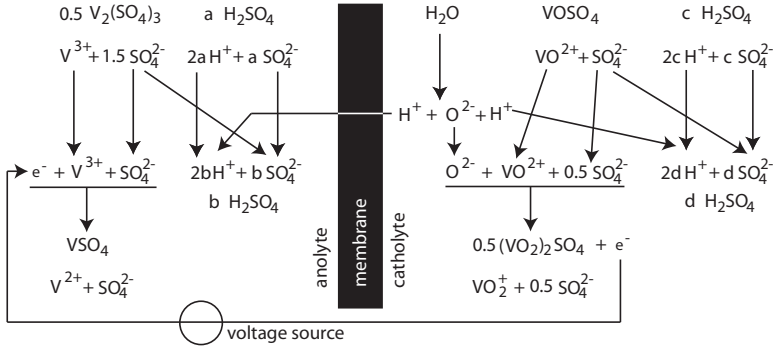


Figure 2.8.: Illustration of the full ionic equations of the VRB during the charging cycle.

from the net ionic equation (2.24):

$$\begin{aligned}
 & \text{VO}^{2+} + \text{H}_2\text{O} \\
 & \equiv \text{VOSO}_4 + c \text{ H}_2\text{SO}_4 + \text{H}_2\text{O} \\
 & \equiv \text{VO}^{2+} + (1 + c) \text{ SO}_4^{2-} + 2c \text{ H}^+ + \text{H}_2\text{O} \\
 & \quad \downarrow \text{CHARGE} \\
 & \text{VO}_2^+ + 2 \text{ H}^+ + e^- \\
 & \equiv 0.5 (\text{VO}_2)_2\text{SO}_4 + d \text{ H}_2\text{SO}_4 + \text{H}^+ + e^- \\
 & \equiv \text{VO}_2^+ + (0.5 + d) \text{ SO}_4^{2-} + 2d \text{ H}^+ + \text{H}^+ + e^-
 \end{aligned} \tag{2.41}$$

Similarly, the quantity of sulphate must remain constant and therefore:

$$d = 0.5 + c \tag{2.42}$$

Here, a close examination of (2.41) quickly reveals that the charge balance is only maintained if we remove the undesirable protons  $\text{H}^+$ ; indeed, the dissociation of the water molecules  $\text{H}_2\text{O}$  during the oxidation of 1 M of  $\text{VO}^{2+}$  produces 2 M of protons: the first is necessary to maintain the charge balance in the catholyte and the second is needed in the anolyte to equilibrate there the charge balance. Therefore, the migration of 1 M of

### 2.3. ALL-VANADIUM BATTERY REACTION

---

$H^+$  is necessary to equilibrate both electrolytes. Finally, we observe that the quantities of protons in both electrolytes are increased by 1 M (after the migration) during the oxidation of 1 M of  $V^{4+}$ ; this last observation is important to the resolution of the Nernst equation (2.29) and will be discussed in more details in section 3.3.

#### 2.3.4. State of Charge

The VRB state of charge  $SoC$  is the equivalent of a fuel gauge in a car: it is an indication of how much energy is stored in the battery.  $SoC$  varies from 0, when the battery is discharged, to 1, when the battery is fully charged. Analytically, its value is given by the concentrations of the different vanadium species.

$$SoC = \left( \frac{c_{V^{2+}}}{c_{V^{2+}} + c_{V^{3+}}} \right) = \left( \frac{c_{VO_2^+}}{c_{VO_2^+} + c_{VO_2^+}} \right) \quad [-] \quad (2.43)$$

When the total vanadium concentration  $c_{V_{total}}$  is the same in both electrolytes, the relations between the concentrations of each species can be written as:

$$c_{V^{3+}} = c_{V_{total}} - c_{V^{2+}}, \quad c_{VO_2^+} = c_{V_{total}} - c_{VO_2^+} \quad [mol/l] \quad (2.44)$$

In this case, when (2.44) is introduced into (2.43), the state of charge  $SoC$  simply becomes:

$$SoC = \left( \frac{c_{V^{2+}}}{c_{V_{total}}} \right)_{anolyte} = \left( \frac{c_{VO_2^+}}{c_{V_{total}}} \right)_{catholyte} \quad [-] \quad (2.45)$$

#### 2.3.5. Numerical Example of the Cell Voltage

We conclude this section dedicated to the VRB reactions, in particular its equilibrium voltage, with a numerical example of the relations and principles introduced previously. This example illustrates the dependence of the cell voltage upon the various vanadium species concentrations and upon the protons  $H^+$  concentration. It is important to notice that in this particular case, no electrical current is flowing through the cell; therefore, the first graph of Fig. 2.9 represents the open-circuit voltage (OCV) as a function of the state of charge  $SoC$  which is proportional to the vanadium



## 2.3. ALL-VANADIUM BATTERY REACTION

concentrations. In the next section, we will examine what happens when the equilibrium conditions are not met, i.e. when a net electrical current is observed through the electrodes.

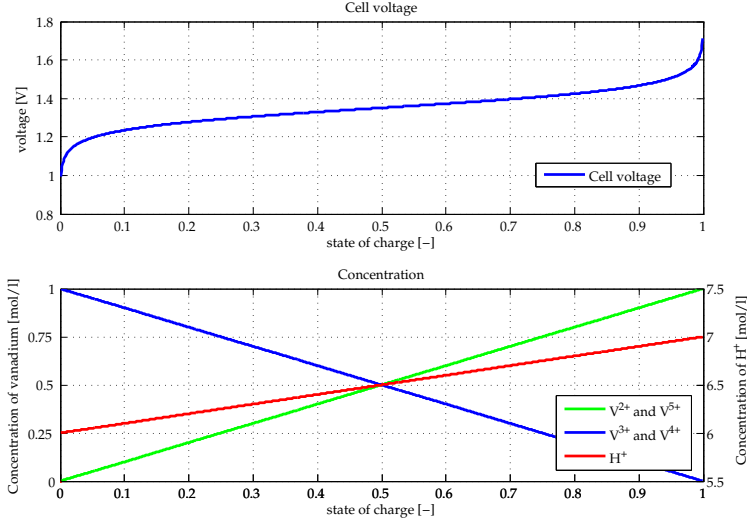


Figure 2.9.: Top: Cell voltage versus the state of charge at 25 °C . Bottom: Proton  $H^+$  and vanadium concentrations versus the state of charge at 25 °C .

The total concentration of vanadium in each electrolyte is at all time equal to 1 M in this example. The concentration of a particular species depends on the state of charge (2.43). At the discharged state, the anolyte contains 1 M of  $V^{3+}$  and the catholyte contains 1 M of  $VO^{2+}$ . Both electrolytes contain the same quantity of sulphate  $SO_4^{2-}$  (4 M) and the proton concentration in the catholyte varies from 6 M to 7 M according to the relations presented in the previous section 2.3.3.

### 2.4. Overpotentials, Ohmic and Ionic Losses

In the first part of this chapter, we have extensively discussed the VRB chemistry under equilibrium conditions, we know how to determine the equilibrium potential from the vanadium concentrations. But what happens when a current starts to flow? The equilibrium conditions are not met anymore and the cell voltage differs from the Nernst voltage. This difference represents the energy needed to force the redox reaction to proceed at the required rate and is often called overpotential, or sometimes overvoltage.

The overpotentials are electrode phenomena that may affect either or both electrodes; in fact, there are different types of overpotentials: the activation overpotential is associated with energy required to initiate a charge transfer and the concentration overpotential is caused by differences in concentration between the bulk solution and the electrode surface. The degree of polarization of an electrode varies widely; in some instances, it approaches zero and in others, it can be so large that the current becomes independent of the potential [71].

Additionally to these electrode phenomena, the material resistances that impede the flow of electrical charges also influence the cell voltage. The ohmic losses occur in the electrodes, bipolar plates, collector plates and wires whereas the ionic losses occur inside the electrolyte and in the membrane. The ohmic and ionic losses are sometimes called *IR drops*.

All these phenomena share a common characteristic: they are all amplified by the current. During the discharge, these overpotentials reduce the available voltage and in consequence the power. Furthermore, they must be compensated during the charge, i.e. an additional voltage has to be applied to maintain the reaction rate, or in other words, the current.

#### 2.4.1. Activation Overpotential

In a battery, the magnitude of the current is either limited by the rate of the mass transfer of reactants to the electrode (the concentration overpotential is discussed in the next section) or by the rate of one or both of the redox reactions, that is, by the rate of electron transfer between the reactant and the electrodes.

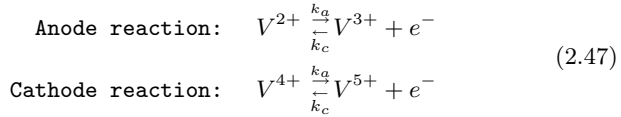
In electrochemistry, the behaviour of the electrode kinetics is influenced by the potential and the concentrations. Indeed, when an additional po-

tential, or overvoltage, is applied, the equilibrium conditions are modified and a net current is observed. This overvoltage is required to overcome the activation energy of the half reaction. The magnitude of the overpotential depends on the rate of the reaction: a slow reaction requires a larger overpotential than a fast reaction. To understand the mechanisms of the activation overpotential, let's consider a general redox reaction [61, 72]:



$$\begin{array}{lll} \text{where: } k_a & = & \text{anodic rate constant} \quad [m/s] \\ k_c & = & \text{cathodic rate constant} \quad [m/s] \end{array}$$

This general redox reaction is easily transposed to the VRB reactions:



Both the oxidation and the reduction are occurring simultaneously all the time, but not necessarily at the same rate. The rate of the forward reaction is given by  $\nu_a$  and the reverse reaction by  $\nu_c$ :

$$\begin{array}{ll} \nu_a = k_a c_R & [mol/m^2 s] \\ \nu_c = k_c c_O & [mol/m^2 s] \end{array} \quad (2.48)$$

### Under Equilibrium Conditions

At equilibrium, both the forward and backward reactions occur at the same rate and therefore no current is flowing. Under standard conditions, i.e. the bulk concentrations of the oxidised and reduced species are equal, the activation energy barrier is symmetrical as illustrated in Fig. 2.10.

In 1889, Svante Arrhenius, a Swedish physicist and chemist who was one of the founders of physical chemistry, found that a molecule must overcome an energy barrier before it can react with another molecule. The Arrhenius equation gives the relationship between the activation energy and the rate of a reaction<sup>6</sup>. At equilibrium, the anodic and cathodic rate constants are

---

<sup>6</sup> Additionally, the Arrhenius equation formulates the temperature dependence of the rate constant.

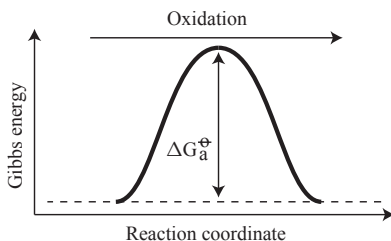


Figure 2.10.: activation barrier for a redox reaction in the standard case, i.e. the bulk concentrations of the oxidised and reduced species are equal.

given by the standard rate constant  $k^\ominus$ :

$$k^\ominus = k_a = k_c = \delta \left( \frac{k_b T}{h} \right) e^{\Delta G_{act}^\ominus / RT} \quad [m/s] \quad (2.49)$$

where:

$\delta$	=	minimum distance separating the re-	[m]
		actants from the electrode	
$k_b$	=	Boltzmann's constant	[J/K]
$h$	=	Planck's constant	[Js]
$\Delta G_{act}^\ominus$	=	standard Gibbs energy of activation	[J/mol]



Figure 2.11.: Svante A. Arrhenius 1859 - 1927 (source: [24]).

### The General Case

In the general case, where the concentrations of the oxidised and reduced species are not equal, the activation energy barrier is not symmetrical anymore (see Fig. 2.12); thus, the anodic and cathodic activation energy are also not equal anymore.

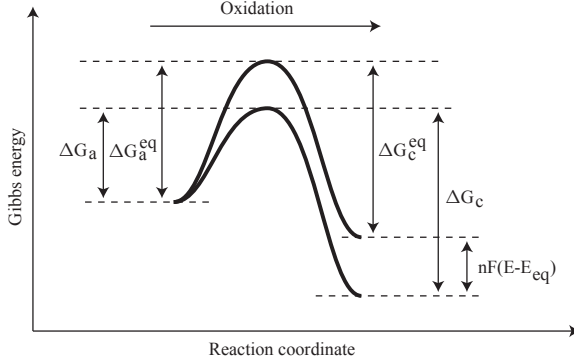


Figure 2.12.: activation barrier for an oxidation in the general case, i.e. the bulk concentrations of the oxidised and reduced species are not equal. The curve at the top is under equilibrium condition (no current) and below when an overpotential is applied.

Even so, at equilibrium, no current is flowing and the equality between the rates of oxidation and reduction (2.50) is maintained; therefore, the inequality of the surface concentrations  $c_R(0)$  and  $c_O(0)$  means that the anodic and cathodic rate constants are not equal.

$$k_a c_R(0) = k_c c_O(0) \quad [mol/m^2 s] \quad (2.50)$$

where:  $c(x)$  = concentration at the distance  $x$  from the electrode,  $x = 0$  corresponds to the electrode surface. [mol/l]

From the Arrhenius equation (2.49), we know that the electrochemical rates constant depend on the temperature  $T$  and on the Gibbs energy of activation  $\Delta G_{act}$ . Hence, a modification of  $\Delta G_{act}$  changes the reaction

rates: one being faster than the other; thus a net current appears across the electrode. This principle is illustrated in Fig. 2.12, the height of the energy barrier is reduced when the Gibbs energy of activation is decreased, favouring the oxidation over the reduction in that case.

We know from (2.19), that the Gibbs energy of activation depends on the electrode potential. So, if we change the electrode potential  $E$  from its equilibrium potential  $E_{eq}$  by an amount of  $E - E_{eq}$ , the anodic  $\Delta G_a$  and cathodic  $\Delta G_c$  activation energies become:

$$\Delta G_a = \Delta G_a^{eq} - \alpha nF(E - E_{eq}) \quad [J/mol] \quad (2.51)$$

$$\Delta G_c = \Delta G_c^{eq} + (1 - \alpha)nF(E - E_{eq}) \quad [J/mol] \quad (2.52)$$

where:  $\Delta G_{a,c}^{eq}$  = anodic and cathodic Gibbs energies of activation at equilibrium  $[J/mol]$   
 $\alpha$  = charge transfer coefficient  $[-]$

From (2.49), (2.51) and (2.52), the variation of the anodic and cathodic rate constants are expressed as a function of the electrode potential  $E$ :

$$k_a = k_a^0 e^{\alpha nFE/RT} \quad [m/s] \quad (2.53)$$

and

$$k_c = k_c^0 e^{-(1-\alpha)nFE/RT} \quad [m/s] \quad (2.54)$$

The value of the two rate constants  $k_a^0$  and  $k_c^0$  are linked to the standard rate constant  $k^\ominus$  when the electrode potential is set at the formal redox potential  $E^{\ominus'}$ . Indeed, at this potential, the activation barrier is symmetrical and the bulk concentrations are equal ( $c_R(\infty) = c_O(\infty)$ ), so from (2.50),  $E^{\ominus'}$  is the potential where the forward and backward reactions have the same value, therefore:

$$k^\ominus = k_a^0 e^{\alpha nFE^{\ominus'}/RT} = k_c^0 e^{-(1-\alpha)nFE^{\ominus'}/RT} \quad [m/s] \quad (2.55)$$

We can now express the anodic current which represents the number of electrons per second transferred from the reduced species in solution to the electrode:

$$I_a = nFAk_a c_R(0) \quad [A] \quad (2.56)$$

where  $A$  is the surface of the electrode. Assuming an excess of electrons in the electrode, we can write the cathodic current which represents the

number of electrons per second transferred toward the oxidized species in the solution from the electrode:

$$I_c = -nFAk_c c_O(0) \quad [A] \quad (2.57)$$

Finally, the sum of the anodic and cathodic currents represents the net current  $I$  flowing through the electrode:

$$\begin{aligned} I &= nFA \left[ k_a^0 c_R(0) e^{\alpha nFE/RT} - k_c^0 c_O(0) e^{-(1-\alpha)nFE/RT} \right] \\ &= nFAk^\ominus \left[ c_R(0) e^{\alpha nF(E-E^\ominus)/RT} - c_O(0) e^{-(1-\alpha)nF(E-E^\ominus)/RT} \right] \quad [A] \end{aligned} \quad (2.58)$$

Next, we want to rearrange (2.58) to express the current  $I$  as a function of the overpotential  $\eta_{act}$ , which is the difference between the equilibrium potential  $E_{eq}$  and the electrode potential  $E$  required to induce the current:

$$\eta_{act} = E - E_{eq} \quad [V] \quad (2.59)$$

Remembering that the Nernst equation (2.23) links the formal standard potential  $E^{\ominus'}$  and the equilibrium potential  $E_{eq}$ :

$$E_{eq} = E^{\ominus'} + \frac{RT}{nF} \ln \left( \frac{c_O(0)}{c_R(0)} \right) \quad [V] \quad (2.60)$$

And since equilibrium conditions apply (no current), the bulk concentrations  $c_i(\infty)$  are found at the surface of the electrode. Furthermore, we introduce (2.59) into (2.60):

$$E - E^{\ominus'} = \eta_{act} + \frac{RT}{nF} \ln \left( \frac{c_O(\infty)}{c_R(\infty)} \right) \quad [V] \quad (2.61)$$

The introduction of (2.61) into (2.58) leads to the expression of the current as a function of the overpotential  $\eta_{act}$ :

$$I = I_0 \left[ \left( \frac{c_R(0)}{c_R(\infty)} \right) e^{\alpha nF\eta_{act}/RT} - \left( \frac{c_O(0)}{c_O(\infty)} \right) e^{-(1-\alpha)nF\eta_{act}/RT} \right] \quad [A] \quad (2.62)$$

in which  $I_0$  is termed the exchange current and represents the value of either of the anodic current or the absolute value of the cathodic current

at equilibrium:

$$I_0 = nFAk^\ominus [c_R(\infty)]^{1-\alpha} [c_O(\infty)]^\alpha \quad [A] \quad (2.63)$$

### The Butler-Volmer Equation

When the mass transfer effects are negligible, i.e. when the current at the electrode is sufficiently small and/or when the solution is well stirred (or refreshed), the concentrations at the surface of the electrode remain equal to the concentrations in the bulk solution ( $c(0) = c(\infty)$ ); (2.62) becomes the *Butler-Volmer* equation, one of the most fundamental relationships of electrochemistry:

$$I = I_0 \left[ e^{\alpha n F \eta_{act} / RT} - e^{-(1-\alpha) n F \eta_{act} / RT} \right] \quad [A] \quad (2.64)$$

For large overpotential  $\eta_{act}$ , one of the exponential terms in (2.64) becomes negligible. Hence, a simple exponential relationship between the current and the overpotential is obtained in the form of a Tafel equation. For example, a large positive overpotential yields to:

$$\eta_{act} = \frac{RT}{\alpha n F} \ln(I) - \frac{RT}{\alpha n F} \ln(I_0) \quad [V] \quad (2.65)$$

### Applications to the VRB

To conclude this section dedicated to the activation overpotential, we will observe and comment typical polarization curves measured with a rotating disk electrode (RDE) against a saturated calomel electrode (SCE). The movement of the spinning electrode constantly refreshes the solution at the electrode surface; therefore the Butler-Volmer equation (2.64) is applicable in that situation. We have shown in Fig. 2.13 the polarization curves of a very dilute vanadium solution; they provide nevertheless a good overview of the VRB redox reactions. These experimental data were published by M. Gattrell and al. in [69].

First, we observe in Fig. 2.13 that the kinetics of the  $VO^{2+}/VO_2^+$  couple are slower than the  $V^{3+}/V^{2+}$  couple, i.e. a larger overpotential is needed to initiate the charge transfer. Furthermore, we also remark that the reduction of  $VO_2^+$  is slower than the reverse reaction, the  $VO^{2+}$  oxidation; this means that higher voltage losses must be expected during



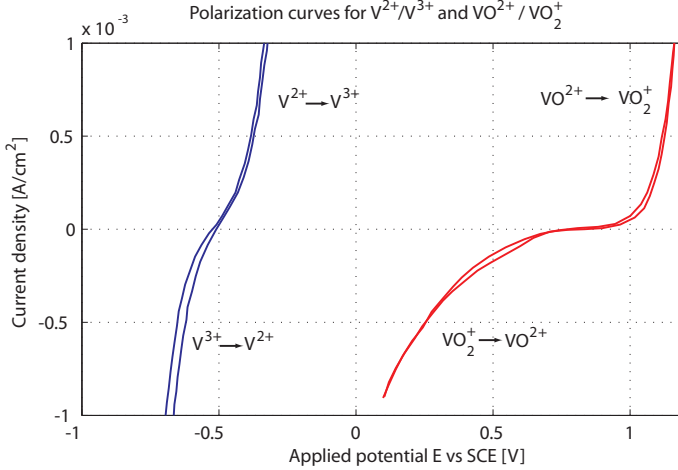


Figure 2.13.: Typical polarisation curves measured at the RDE versus a SCE. The concentrations are  $c_{V^{2+}} \cong 16$  mM,  $c_{V^{3+}} \cong 36$  mM,  $c_{VO^{2+}} \cong 31$  mM and  $c_{VO_2^+} \cong 19$  mM dissolved in 1 M  $H_2SO_4$ . Experimental data are from [69].

the discharge. This observation will become really meaningful in section 3.4 dedicated to the internal losses.

Then, we can also determine the formal electrode potential  $E^{\ominus'}$  from these polarization curves; indeed, under equilibrium conditions, the electrode potential  $E$  corrected to equimolar concentrations with the Nernst equation (2.23) and given versus the standard hydrogen electrode (SHE)<sup>7</sup> instead of the SCE, corresponds to formal electrode potential. Hence, we have for the formal anode potential  $E_{anode}^{\ominus'} = -0.26$  V and for the formal cathode potential  $E_{cathode}^{\ominus'} = 1$  V; together, they determine  $E^{\ominus'}$  which equals in that case 1.26 V.

Furthermore, we remark that the formal electrode potential  $E^{\ominus'}$  is very close to the standard potential  $E^{\ominus}$  found in section 2.3.2; this correlation

<sup>7</sup>  $E_{SHE} = E_{SCE} + 0.241$  [V]

gives us a very good confidence in the assumption made in section 2.3.1 when it was stated that the activity coefficients cancelled each other. Even in the least favourable case, we have:

$$E^{\ominus} = 1.23 \text{ V} \cong 1.26 \text{ V} = E^{\ominus'} \quad (2.66)$$

In Fig. 2.14, we compare in a Tafel plot the polarization curve of the slowest couple,  $VO^{2+}/VO_2^+$ , with the theoretical values; the theoretical curve is obtained from the Butler-Volmer equation (2.64). The value of the exchange current  $I_0$  is determined from (2.63) with the parameters found in Tab. 2.4:

$$I_0 = nFAk^{\ominus} [c_R(\infty)]^{1-\alpha} [c_O(\infty)]^{\alpha} = 5.555 \cdot 10^{-7} \text{ [A]} \quad (2.67)$$

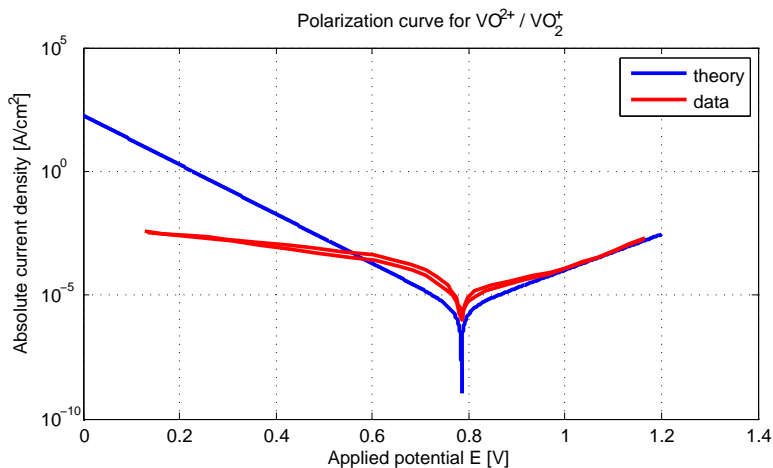


Figure 2.14.: Tafel type plot of the polarization curve for  $VO^{2+}/VO_2^+$  where  $c_{VO^{2+}} \cong 90 \text{ mM}$  and  $c_{VO_2^+} \cong 110 \text{ mM}$  dissolved in  $1 \text{ M } H_2SO_4$ . Experimental data are from [69].

But before we discuss the significant difference between the theoretical and experimental curves in Fig. 2.14, we should present the pathway of a

Symbol	Name	Value
$E^{\ominus'}$	Formal potential vs. SCE	0.781 V
$A$	Area	$0.196 \text{ cm}^2$
$k^{\ominus}$	Standard rate constant	$3 \cdot 10^{-7} \text{ cm/s}$
$c_R(\infty)$	$VO_2^-$ bulk concentration	$90 \cdot 10^{-6} \text{ mol/cm}^3$
$c_O(\infty)$	$VO_2^+$ bulk concentration	$110 \cdot 10^{-6} \text{ mol/cm}^3$
$\alpha$	Charge transfer coefficient	0.42
$T$	Temperature	293.15 K

Table 2.4.: Parameters for the Butler-Volmer and exchange current equations. These values were found in [69].

general electrode reaction illustrated in Fig. 2.15. The simplest reactions begin with the mass transfer of the reacting species from the bulk of the solution to the electrode surface; there the redox reaction takes place. Finally, the products are diffused away from the electrode surface. In more complex reactions, other process might occur such as chemical reactions, adsorptions or desorptions [72, 73].

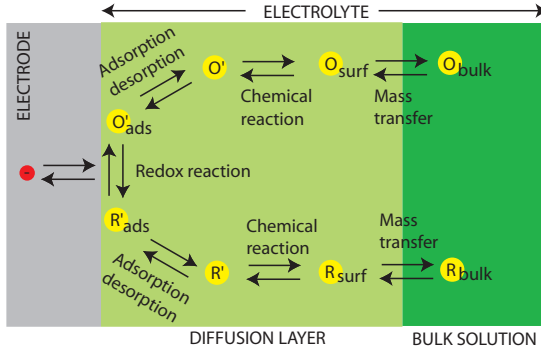
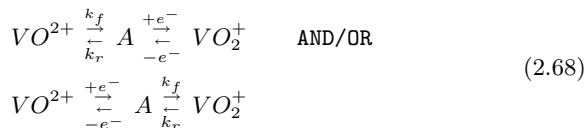


Figure 2.15.: General scheme of the processes that occur at the electrode-solution interface [72].

Hence, the significant difference observed in Fig. 2.14 suggests that the

## 2.4. OVERPOTENTIALS, OHMIC AND IONIC LOSSES

cathodic redox reactions are not a simple mechanism and that the electrons transfer is accompanied by a certain chemical step. The most probable chemical step seems to be the breaking and/or formation of the  $V - O$  chemical bond during the redox reactions between  $VO_2^+$  and  $VO^{2+}$ . The interested readers should find additional informations in [37, 69, 74]. In conclusion, the possible paths are:



In addition, we give in Tab. 2.5 some kinetic parameters of the vanadium redox reactions; these transfer coefficients  $\alpha$  and exchange currents  $I_0$  were determined by C. Fabjan and al., and published in [75]. We observe in this table that the kinetic properties depend on the electrolyte composition.

Redox couple	Concentration [mol/l]	Transfer coefficient $\alpha$ [-]	Exchange current $I_0$ [mA/cm <sup>2</sup> ]
$V^{2+}/V^{3+}$ anodic	0.5/0.25	0.26	$1.76 \cdot 10^{-3}$
$V^{2+}/V^{3+}$ cathodic	0.5/0.25	0.6	$1.00 \cdot 10^{-3}$
$V^{4+}/V^{5+}$ anodic	0.01/0.01	0.33	$1.26 \cdot 10^{-4}$
$V^{4+}/V^{5+}$ anodic	0.1/0.01	0.35	$1.79 \cdot 10^{-4}$
$V^{4+}/V^{5+}$ anodic	1.0/0.01	0.39	$6.33 \cdot 10^{-4}$

Table 2.5.: Transfer coefficients  $\alpha$  and exchange currents  $I_0$  for the vanadium redox couples at various concentrations. The electrolyte contains 2 M of  $H_2SO_4$ . These values were published in [75].

### 2.4.2. Concentration Overpotential

The concentration overpotential  $\eta_{conc}$  is caused by the difference in electroactive species concentrations between the bulk solution and the electrode surface. In an electrochemical cell, the electron transfer between a

reactive species and an electrode occurs only in a thin film (a fraction of nanometre in thickness) of solution immediately adjacent to the surface of the electrode. The different layers are illustrated in Fig. 2.16.

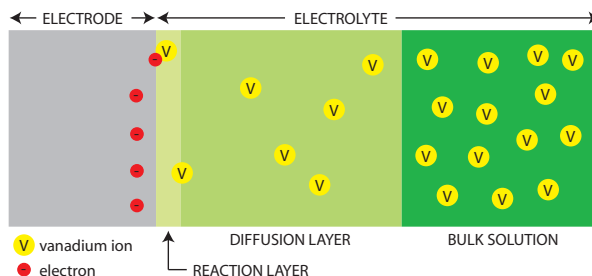


Figure 2.16.: Concentration changes in the electrolyte and the different layers.

The concentration overpotential is due to the finite rate of mass transfer from the electrolyte to the electrode surface. In order to keep the current steady, the reaction layer must be continuously replenished with fresh reactant from the bulk of the electrolyte. So, the concentration overpotential occurs when the rate of the electrochemical reaction is sufficiently rapid that the reactant species do not reach the electrode surface or that the product species do not leave the electrode fast enough. We will see in the rest of this section that the reactants and the products might be transported by three mechanisms: the diffusion, the migration and the convection.

### Diffusion

Diffusion is the spontaneous net movement of ions or molecules from the more concentrated region to the more dilute. The diffusion is due to the Brownian motion: the particles move randomly between area of high and low concentration, but because there are more particles in the high concentration region, more particles will leave it and this process ultimately leads to the disappearance of the concentration difference.

Before we introduce the Fick's first law, we must briefly define the flux of a species  $J_i$  through a unit area  $A$  (see Fig. 2.17);  $J_i$  depends on the

species concentration  $c_i$  and on its average velocity  $V_i$ :

$$J_i = c_i V_i \quad [\text{mol}/\text{m}^2 \text{ s}] \quad (2.69)$$

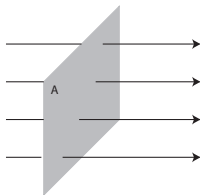


Figure 2.17.: flux through a surface  $A$ .

The Fick's first law states that the diffusion is a process driven by the concentration gradient and that the diffusion flux is directly proportional to this gradient. In the case of one-dimensional gradients, the diffusion flux  $J_{diff,i}$  is given by [61]:

$$J_{diff,i} = -D_i \left( \frac{\partial c_i}{\partial x} \right) \quad [\text{mol}/\text{m}^2 \text{ s}] \quad (2.70)$$

where  $D_i$  is the diffusion coefficient or diffusivity; this coefficient is pro-



Figure 2.18.: Adolf E. Fick 1829 - 1901 (source: [24]).

portional to the velocity of the ions or molecules, which depends on the temperature, the viscosity and the size of the particles.  $D_i$  is given by the

Stokes-Einstein equation:

$$D_i = RT\tilde{u}_i = \frac{k_b T}{6\pi\mu r} \quad [m^2/s] \quad (2.71)$$

$$\begin{array}{lll} \text{where: } \tilde{u}_i & = & \text{electrochemical mobility} & [m^2/Js] \\ \mu & = & \text{viscosity} & [Ns/m^2] \\ r & = & \text{radius of the particle} & [m] \end{array}$$

G. Oriji and al. have determined the diffusion coefficient of the vanadium species and their findings are presented in Tab. 2.6 [74] .

Species	Diffusion coefficient [ $cm^2/s$ ]	Stokes radius [nm]
$V^{2+}$	$1.1 \cdot 10^{-6}$	0.32
$V^{3+}$	$0.57 \cdot 10^{-6}$	0.32
$V^{4+}$	$1.0 \cdot 10^{-6}$	0.21
$V^{5+}$	$1.0 \cdot 10^{-6}$	0.28

Table 2.6.: Diffusion coefficient and Stokes radius for the vanadium species. Data are from [74].

### Migration

The migration is the movement of ions through a solution as a result of electrostatic attraction between the ions and the electrodes; these ions are moved under the influence of an electric field. The rate at which the ions migrate to or away from an electrode surface generally increases as the electrode potential increases; this charge movement constitutes a current, which also increases with the potential [71].

When a charged particle is under the influence of an electric field, it will accelerate until it reaches a constant drift velocity  $V_d$ :

$$V_d = uE \quad [m/s] \quad (2.72)$$

$$\begin{array}{lll} \text{where: } u & = & \text{electric mobility} & [m^2/Vs] \\ E & = & \text{electric field} & [V/m] \end{array}$$

### Convection

Reactants and products can also be transferred to or from an electrode by mechanical means. Forced convection, such as stirring or agitation, will tend to decrease the thickness of the diffusion layer at the surface of an electrode and thus decrease the concentration overpotential. Natural convection resulting from temperature or density differences also contributes to the transport of molecules to and from an electrode [71].

### Expression of the Concentration Overpotential

The concentration overpotential  $\eta_{conc}$  is by definition the difference between the Nernst potential in the bulk solution  $E_{bulk}$  and the Nernst potential at the electrode surface  $E_S$  [58] and is therefore given by the following relation derived from (2.29):

$$\eta_{conc} = E_{bulk} - E_S = \frac{RT}{F} \ln \left\{ \frac{c_{VO_2^+}(\infty)c_{H^+}(\infty)^2c_{V^{2+}}(\infty)}{c_{VO^{2+}}(\infty)c_{V^{3+}}(\infty)} \cdot \frac{c_{VO^{2+}}(0)c_{V^{3+}}(0)}{c_{VO_2^+}(0)c_{H^+}(0)^2c_{V^{2+}}(0)} \right\} [V] \quad (2.73)$$

### 2.4.3. Ohmic and Ionic Overpotentials

The ohmic and ionic overpotentials, or losses, should sound more familiar to electrical engineers than the two previous overpotentials that were clearly related to the electrochemistry; we have just seen that the activation overpotential  $\eta_{act}$  is necessary to sustain the rate of the electrochemical reaction and the concentration overpotential  $\eta_{conc}$  appears when the reactants do not reach the electrodes fast enough. The ohmic and ionic overpotentials are related to the movement of electrical charges and have some conceptual parallels with the mechanical notion of friction; they are due to the electrical resistance: a measure of the ability of an object to impede the flow of charges, electrons and/or ions.

The ohmic overpotential  $\eta_{ohm}$  within the VRB is due to the electron conduction in the carbon felt electrodes, the bipolar plates and the current collector plates; outside the battery, ohmic loss also occurs within the connecting wires. The ohmic resistance  $R_{ohm}$  is the sum of the electrical resistance of the electrodes  $R_{electrodes}$ , the bipolar plates  $R_{bipolar}$  and the



current collector plates  $R_{collector}$ . The overall ohmic losses are given by:

$$\eta_{ohm} = (R_{electrodes} + R_{bipolar} + R_{collector})I = R_{ohm}I \quad [V] \quad (2.74)$$

The electrolyte and the membrane also oppose the flow of an ionic current; this resistance is the cause of the ionic overpotential  $\eta_{ionic}$ . The resistivity of ionic liquids  $R_{electrolyte}$  varies with the salt composition and its concentration. Analogously to the ohmic resistance, the electrolyte has a conductance directly proportional to the surface of the electrodes and inversely proportional to the distance between them; the conductance  $G$  defines the electrolyte ability to conduct electricity [66, 73]:

$$G = \frac{1}{R} = \sigma \frac{A}{L} \quad [S] \quad (2.75)$$

where:	$\sigma$	=	specific conductivity	$[S/m]$
	$A$	=	cross-section	$[m^2]$
	$L$	=	length	$[m]$

The conductivity has a direct relation with the number, charge and mobility of the ions dissolved inside the electrolyte [61]:

$$\sigma = F \sum |z_i| c_i u_i \quad [S/m] \quad (2.76)$$

where  $z_i$  is the charge of the ion  $i$ . The mobility  $u_i$  is dependent on the size of the ions and their interaction with their surrounding; hence, the mobility depends on the viscosity of the solution and is therefore a function of the temperature (more details about the viscosity are given in section 4.4). The membrane separating the anolyte and the catholyte while conducting protons, has also a resistance  $R_{membrane}$  opposing the flow of charge. Thus, the overall ionic overpotential is given by:

$$\eta_{ionic} = (R_{electrolyte} + R_{membrane})I = R_{ionic}I \quad [V] \quad (2.77)$$

Thanks to the similarity between (2.74) and (2.77), we can combine the ohmic and ionic resistivities into a single resistance  $R_{tot}$ :

$$R_{tot} = R_{ohm} + R_{ionic} \quad [\Omega] \quad (2.78)$$

### External Influence on the Resistivity

Materials have an important impact on the cell resistivity and a careful selection will lead to higher performance. For example, the batteries presented in [76] have an electrode resistivity between 0.7 and 1.3  $\Omega/\text{cm}^2$ . Two membranes have been used, the first is a Selemon AMV membrane with a resistivity between 1.5 and 3  $\Omega/\text{cm}^2$  and the second is an experimental New Selemon Type II membrane with a resistivity in the vicinity of 1  $\Omega/\text{cm}^2$ . Hence, the internal losses due to the resistivity might more than double with a bad choice of materials.

## 2.5. Electrochemical Stack Model

We conclude this chapter with the electrochemical stack model that summarizes the relations introduced previously into a steady state, cell averaged and analytical stack model. This model based on building blocks predicts the stack voltage  $U_{stack}$  and the state of charge  $SoC$  as a function of the operating conditions which were summarized in Tab. 2.1. Together, these building blocks form the overall stack model as illustrated in Fig. 2.19.

In a first step, the model determines the state of charge  $SoC$  from the vanadium concentrations with (2.43); then it determines the equilibrium voltage  $E$  and the activation  $\eta_{act}$ , the concentration  $\eta_{conc}$ , the ohmic  $\eta_{ohm}$  and the ionic  $\eta_{ionic}$  overpotentials from respectively (2.29), (2.65), (2.73), (2.74) and (2.77) for a single cell. Then, these values are simply multiplied by the number of cells  $N_{cells}$  to obtain the stack equilibrium voltage  $E_{stack}$  and overpotentials. Hence, the stack voltage  $U_{stack}$  is given by the difference between  $E_{stack}$  and the sum of the overpotentials:

$$U_{stack} = N_{cell}(E - \sum \eta_i) \quad [V] \quad (2.79)$$

The dependence of the Nernst voltage, the overpotentials and the stack voltage on the operating conditions is shown in Tab. 2.7. A ‘•’ denotes a direct dependence of the variable on a given operating variable and a ‘o’ denotes an indirect dependence, i.e. the variable is calculated based on another one which itself, directly or indirectly, depends on the considered operating variable.

In the first part of chapter 3, we will explain how to determine the vana-

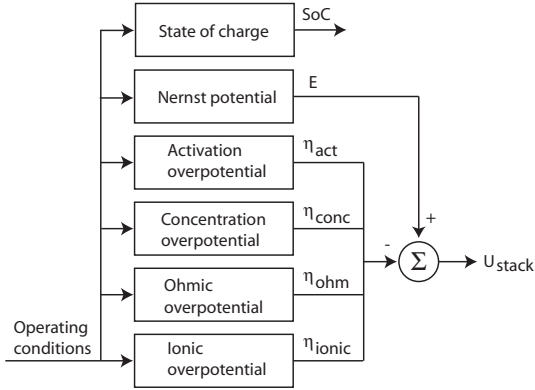


Figure 2.19.: Flowchart of the stack model. The *state of charge* is discussed in section 2.3.4, the *Nernst potential* in section 2.3.1, the *activation overpotential* in section 2.4.1, the *concentration overpotential* in section 2.4.2, the *ohmic overpotential* and the *ionic overpotential* in section 2.4.3.

dium and proton concentrations from the electrolyte composition, i.e. the battery *SoC*, the electrolyte flowrate  $Q$  and the electrical current  $I$ . Furthermore, we will also estimate the internal losses from an equivalent set of resistances; this new knowledge will enable us to augment and simplify the electrochemical stack model introduced in this chapter.

## 2.6. Summary

In the first part of this chapter, we have introduced some general electrochemical notions: molality, molarity, chemical equilibrium and activity. Then we have introduced the important principles of the redox chemistry on which the vanadium redox battery is based. We have followed our development with the introduction of the Gibbs free energy and the Nernst equation. From the chemical equations of the VRB reactions, we were able to determine the equilibrium potential  $E$  with the Nernst equation which reflects the dependence of the open-circuit voltage on the concentrations of the different vanadium species. Comparison with experimental data has shown a good correlation, except at very low state of charge *SoC*.

## 2.6. SUMMARY

Variable	$I$	$c_{V^{2+}}$	$c_{V^{3+}}$	$c_{V^{4+}}$	$c_{V^{5+}}$	$c_{H^+}$	$T$	$Q$
$SoC$		●	●	●	●			
$E$		●	●	●	●	●	●	○
$\eta_{act}$	●	●	●	●	●		●	○
$\eta_{conc}$	○	●	●	●	●		●	○
$\eta_{ohm}$	●						○	
$\eta_{ionic}$	●	○	○	○	○	○	○	
$U_{stack}$	○	○	○	○	○	○	○	○

Table 2.7.: Variables dependency on the operating conditions. ● denotes a direct dependence and ○ denotes an indirect dependence.

To solve the Nernst equation, the standard potential  $E^\ominus$  and the protons  $H^+$  concentration are required. Therefore, we have introduced two methods to determine  $E^\ominus$ , either from the thermodynamics or from the standard reduction potentials. Then, we have introduced the full ionic equations that explicitly points out the spectator ions and explains why some protons cross the membrane to equilibrate the charge balance. This first part was concluded with a numerical illustration of the cell voltage under equilibrium conditions.

After the characterization of the equilibrium conditions, we have tackled in the second part the important description of the VRB behaviour under non-equilibrium conditions; indeed, when a current  $I$  flows throughout the cell(s), the equilibrium conditions are disturbed and the cell(s) voltage  $U_{cell}$  reflects this change. The causes are multiple: activation overpotential  $\eta_{act}$ , concentration overpotential  $\eta_{conc}$ , ohmic losses  $\eta_{ohm}$  and ionic losses  $\eta_{ionic}$ .

The activation overpotential represents the potential required to initiate a net current; it modifies the electrode kinetics to favour a reaction over the other. When the mass transfer effects are negligible, we can define an exchange current  $I_0$  and then relate the current to  $\eta_{act}$  through the Butler-Volmer equation. The observation of a Tafel plot of the polarisation curve of the  $VO^{2+}/VO_2^+$  redox reactions suggests that these reactions are a complex mechanism where the electrons transfer is accompanied by a certain chemical step.

The concentration overpotential is due to the finite rate of mass trans-

fer from the bulk of the electrolyte to the electrode surface. Indeed, electroactive species must be continuously replenished, and consumed species removed, in order to keep the current  $I$  steady. The transport of reactants and products is done through three mechanisms: the diffusion, the migration and the convection. The diffusion is due to the spontaneous movement of ions from the more concentrated region to the more dilute, the migration results from an electrostatic attraction between the ions and the electrodes, and the convection transports the ions by a mechanical means such as stirring or agitation.

The ohmic and ionic overpotential are due to the VRB electrical resistance; the major contributors to the ohmic losses within the VRB are the carbon felt electrodes, the bipolar plates and the current collector plates. The ionic overpotential comes from the resistance to ions transport within the electrolyte and through the membrane.

The variables affecting the rate of an electrode reaction were nicely summarized by A. Bard and L. Faulkner in five categories that are represented in Fig. 2.20: solution variables, mass transfer variables, external variables, electrode variables and electrical variables [72]. The influence of the electrode variables like the electrode material, surface area, geometry and surface and of some solution variables like the composition of the solvent (other than the sulphuric acid) are outside the scope of this work.

This chapter was concluded with the introduction of a first electrochemical model that describes the electrochemical behaviour of the stack. This model is built with the relations introduced in this chapter and predicts the stack voltage  $U_{stack}$  as a function of the operating conditions: the vanadium concentrations  $c_{V^{2+}}$ ,  $c_{V^{3+}}$ ,  $c_{V^{4+}}$  and  $c_{V^{5+}}$ , the proton concentration  $c_{H^+}$ , the electrical current  $I$ , the temperature  $T$  and the electrolyte flowrate  $Q$ .

This first electrochemical model describes what happens at the core of VRB, it is a powerful means to apprehend the phenomena that govern and limit the performance of the battery. In the next chapter 3, we are going to simplify this electrochemical model in a more practical way; the simplification is required because many parameters are difficult to identify and often unavailable. Furthermore, we will augment the model with the addition of a model that predicts the vanadium and proton concentrations as a function of the tank concentration  $c_{tank}$ , the electrolyte flowrate  $Q$  and the current  $I$ . At that moment, we will have the whole picture of how the VRB stack operates.

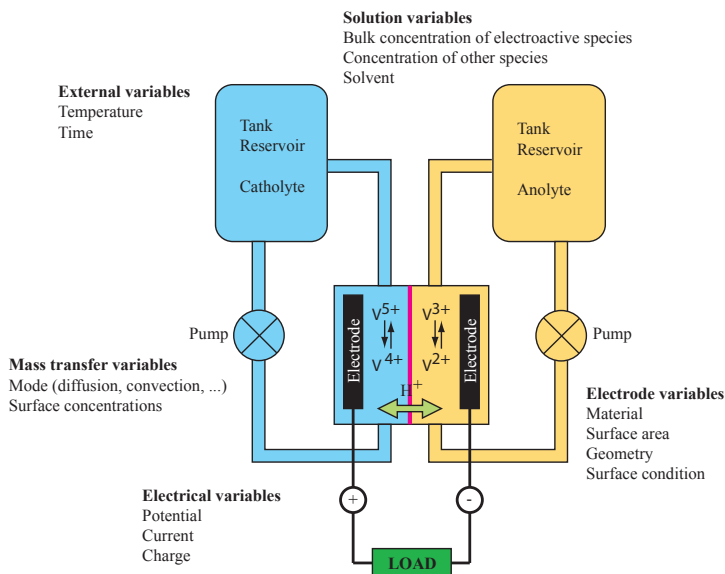


Figure 2.20.: Variables affecting the rate of the VRB redox reaction [72].

But, to correctly assess the performance of the battery, we must take into account the mechanical power required to flow the electrolyte from the tank to the stack and back to the tank. In order to achieve this goal, we will develop a hydraulic model in chapter 5 based on analytical and numerical fluid mechanics.

# Electrochemical Model of a Vanadium Redox Stack

---

## 3.1. Introduction

The main electrochemical relations governing the behaviour of the stack were introduced in the previous chapter; these relations were established to determine the stack voltage that depends, among other factors, on the vanadium concentrations. However, we have not yet described how these concentrations change when the battery is operating. Therefore, the first part of this chapter is dedicated to the description of the concentration variations.

The overpotentials and ohmic loss presented in the previous chapter required many parameters that are often unavailable; thus, a simplified model of the internal losses is introduced. Together with the relations describing the ion concentrations and the Nernst equation they form the electrochemical model of the VRB stack.

This model is then used to simulate the behaviour of a small islanded system comprising a photovoltaic source, a VRB and a typical load. From the power profile of the source and the load, the model determines the power exchanged with the battery, the stack voltage and current, and the vanadium concentrations in the tank and in the stack.

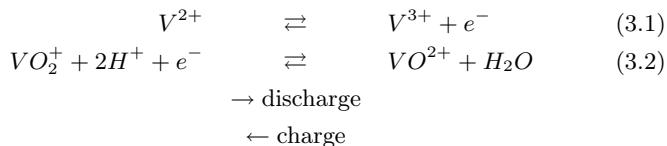
Characterizing the efficiency of a battery has always been a difficult

task as it depends strongly on its operating conditions. Therefore, we will define three types of efficiencies: energy efficiency, coulombic efficiency and voltage efficiency in order to compare the performance. Then a series of charge and discharge cycles will be performed at constant currents and at constant powers; the results are finally compared with experimental results.

We will conclude this section with a generalization of the principles introduced previously; in particular, we will discuss the effects of the efficiency on the power density and also observe the influence of the operating conditions on the stack voltage, the stack power and the internal losses.

### 3.2. Concentration of the Vanadium Ions

We remind below the two chemical equations (2.24) and (2.25) introduced in the previous chapter that characterize the VRB reaction. Clearly, we see that during the redox reactions, the vanadium ions are transformed and that some protons  $H^+$  are either produced or consumed. Therefore, the ion concentrations must change in the electrolyte to reflect these transformations which depend on how the battery is operated.



For example, when the battery is charged,  $V^{2+}$  and  $VO_2^+$  are produced and their concentrations increase; and  $V^{3+}$  and  $VO^{2+}$  are consumed and thus their concentrations diminish. This process is reversed when the battery is discharged. Tab. 3.1 summarizes the direction of the change for each species.

Obviously, the concentration changes are proportional to the reaction rate; and from the chemical equations (3.1) and (3.2), we know that an electron is produced and/or consumed each time a redox reaction occurs. Therefore, the concentration changes are also proportional to the electrical current.

So, this section starts with the introduction of the electrons exchange rate that will lead to the definition of the vanadium concentrations in the



### 3.2. CONCENTRATION OF THE VANADIUM IONS

	Charge	Discharge
$V^{2+}$	↑	↓
$V^{3+}$	↓	↑
$VO^{2+}$	↓	↑
$VO_2^+$	↑	↓

Table 3.1.: Concentration variation of vanadium ions during the charge and discharge of the VRB.

stack and in the tank. It will end with a discussion about the concentration dependence on the operating conditions, and a presentation of different means to observe the concentrations.

#### 3.2.1. Electrons Exchange Rate

According to Faraday's first law of electrolysis that states that *the mass of a substance produced at an electrode during electrolysis is proportional to the number of moles of electrons transferred at that electrode*, the quantity of vanadium ions involved in the redox reaction is directly proportional to the electrical current.

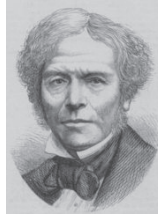


Figure 3.1.: Michael Faraday 1791-1867 (source: [24]).

This current is created by the flow of charges which can be either positive or negative. In the VRB, electrons  $e^-$  are the negative charges flowing in the external circuit and the protons  $H^+$  are the positive charges travelling inside the electrolytes and migrating through the membrane to equilibrate

### 3.2. CONCENTRATION OF THE VANADIUM IONS

---

the charge balance. The relation between the charge and the current is well known to electrical engineers and are reminded in (3.3) and (3.4):

$$i(t) = \frac{dQ_c}{dt} \quad [A] \quad (3.3)$$

and

$$Q_c = n_{e-} e = \int i(t) dt \quad [C] \quad (3.4)$$

where:	$Q_c$	=	charge	[C]
	$i$	=	current	[A]
	$t$	=	time	[s]
	$n_{e-}$	=	number of electrons	[-]
	$e$	=	elementary charge	[C]

Therefore, the number of electrons  $n_{e-}$  involved for a given current is:

$$n_{e-} = \frac{1}{eN_A} \int i(t) dt \quad [mol] \quad (3.5)$$

where  $N_A$  is the Avogadro number. Then (3.5) leads to the definition of a molar flowrate of electrons  $\dot{N}_{e-}$ :

$$\dot{N}_{e-}(t) = \frac{1}{eN_A} i(t) \quad [mol/s] \quad (3.6)$$

Hence, the electrons exchange rate is proportional to the electrical current. By convention, the current is positive during the VRB discharge in order to have a positive power delivered by the battery.

#### What Happens in a Stack?

Physically, an electron is released by the oxidation of a vanadium ion, travels through the electrodes and is captured by the reduction of another vanadium ion in the opposite half-cell. In the case of a stack composed of  $N_{cell}$  cells, the electrons travel through the bipolar electrode to the adjacent cell (Fig. 3.2). Thus, for one electron flowing through the external electrical circuit,  $N_{cell}$  redox reactions have occurred. Therefore, the total molar flowrate of electrons  $\dot{N}_{e_{tot}}$  for a stack is obtained by multiplying

(3.6) by the number of cells:

$$\dot{N}_{e_{tot}}(t) = \frac{N_{cell}}{eN_A} i(t) = \frac{N_{cell}}{F} i(t) \quad [mol/s] \quad (3.7)$$

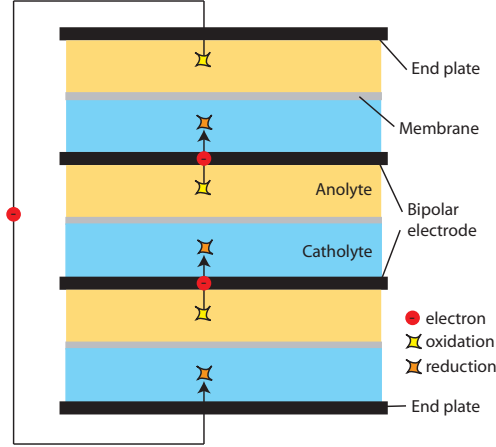


Figure 3.2.: Illustration of the redox reactions required to produce a one electron flow in a 3 elements stack during the discharge. When the battery is charged, the flow and the reactions are inverted.

### 3.2.2. Input, Output and Average Concentrations of Vanadium Ions

We know now from the previous sections that the vanadium concentrations change inside the cells when the battery is operating. Therefore, the concentrations are not uniformly distributed through the electrolyte circuit (Fig. 3.3). Indeed, four concentrations are located in the VRB: the tank concentration  $c_{tank}$ , the concentration at the cell input  $c_{in}$ , the concentration inside the cell  $c_{cell}$  and the concentration at the cell output  $c_{out}$ .

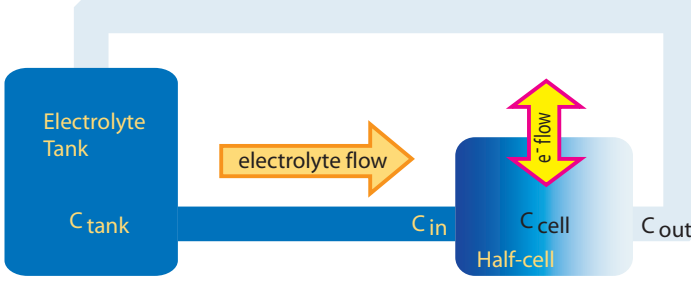


Figure 3.3.: Illustration of the hydraulic circuit (half cell) where the concentrations are shown.

#### Input and Tank Concentrations

Usually, the size of the reservoir is large compared to the electrolyte flowrate; thus the change in concentrations due to the flow of *used* electrolyte is so small that the tank concentrations are considered homogeneous. And therefore, the input concentrations  $c_{in}$  correspond exactly to  $c_{tank}$ .

The tank concentration  $c_{tank}$  reflects the past history of the battery; indeed the change in  $c_{tank}$  is proportional to the quantity of vanadium that has been transformed in the stack: this value corresponds to the quantity of electrons involves in the reaction. Therefore,  $c_{tank}$  is defined by the initial ion concentrations  $c_{tank_i}^{initial}$ , the size of the reservoir  $V_{tank}$  and the total molar flowrate of electrons  $\dot{N}_{e_{tot}}^-$ :

$$\begin{aligned} c_{in_i}(t) = c_{tank_i}(t) &= c_{tank_i}^{initial} + \frac{1}{V_{tank}} \int b \dot{N}_{e_{tot}}^-(t) dt \\ &= c_{tank_i}^{initial} + \frac{1}{V_{tank}} \int \frac{b}{F} i(t) dt \quad [mol/l] \end{aligned} \quad (3.8)$$

where  $b$  is a sign factor that reflects the direction of the reaction in accordance with Tab. 3.1:

$$b = \begin{cases} -1 & \text{for } V^{2+} \text{ and } V^{5+} \text{ ions} \\ 1 & \text{for } V^{3+} \text{ and } V^{4+} \text{ ions} \end{cases} \quad [-] \quad (3.9)$$

### How Do the Concentrations Change inside the Cell?

The vanadium concentration is one parameter, among others, on which the reaction rate depends; when the electrolyte flows through the cell, some species are depleted and others are produced along the way. Hence the concentrations and the reactions rate change (Fig. 3.4); the distribution of the reaction sites is unknown, the reactions are probably more intense at the cell input where the concentrations of electroactive species are maximal. The exact description of this phenomenon requires an extensive 3D model and is outside the scope of this work.

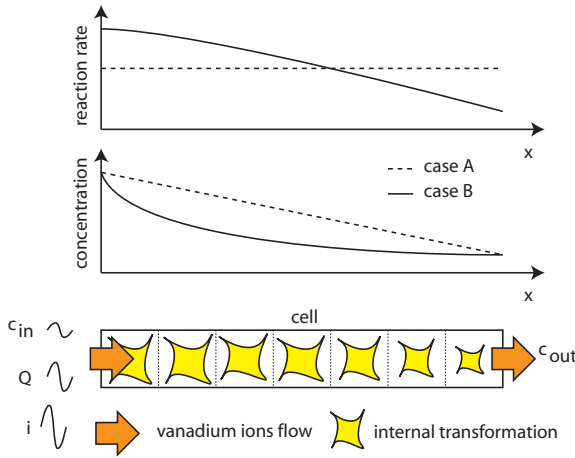


Figure 3.4.: Reaction rate and concentration as a function of the position, the electrolyte flow is in the  $x$  direction. Case A: uniform reaction rate. Case B: non uniform reaction rate. Bottom: Representation of the cell as a closed system. Vanadium ions are entering and leaving the system with the electrolyte flow; thus, their quantity is proportional to the flowrate  $Q$ , input concentration  $c_{in}$  and output concentration  $c_{out}$ . Ions are also internally transformed at a rate proportional to the current.

Fig. 3.4 illustrates the change in concentrations and reaction rate for a simple rectangular cell in the flow direction ( $x$  axis). In the first case (A), the reaction rate is constant and the concentration rate decreases linearly;

and in the second case (B), the reaction rate is maximal at the cell input and decreases rapidly as the active species are depleted. What happens in reality is somewhere in between these two cases and depends strongly on the operating conditions: a highly charged electrolyte flowing quickly will have an almost constant reaction rate as the active species concentrations stay almost constant during the cell crossing. On the contrary, a discharged electrolyte flowing slowly and encountering a high current will see its active species quickly depleted and in consequence, its reaction rate will drop.

If we consider the cell as a closed system (Fig. 3.4), the quantity of vanadium ions entering the system is easily found from the input concentration  $c_{in}$  and the electrolyte flowrate  $Q$ ; the quantity of vanadium ions produced or consumed inside the system is proportional to the current  $i$ . But how do we determine the output concentration?

We can divide the cell volume into smaller volumes that travel from the cell input to the output at a velocity imposed by the flowrate. Each volume experiences a change in vanadium concentrations depending on the instantaneous current  $i$  at each location.

So, the output concentrations  $c_{out}$  depend on the vanadium concentrations inside the cell, the quantity of vanadium flowing into the cell and the quantity transformed inside the cell at each location. Thanks to the large tank,  $c_{in}$  changes slowly and can be considered constant for the time needed by the electrolyte to cross the cell. Furthermore, the inertia of the electrolyte imposes slow change on  $Q$ , thus the only variable experiencing fast change is the current  $i$ .

#### Output Concentration

The description of the output concentration  $c_{out}$  is difficult because it depends on the electrolyte flowrate  $Q$ , the length of the hydraulic circuit and on the current  $i$  that the electrolyte encounters during the cell crossing. Since the distribution of the vanadium ions inside the cell is unknown, we decide, from the small volume point of view, to use a single volume. Thus, the model has no memory and reacts instantly to a change in the operating conditions. In that case,  $c_{out}$  is related to the electrons molar flowrate  $\dot{N}_{e_{tot}}^-$ , the electrolyte flowrate  $Q$  and on the input concentration

$c_{in}$ :

$$c_{out_i}(t) = c_{in_i}(t) + b \frac{\dot{N}_{e_{tot}}^-(t)}{Q(t)} = c_{in_i}(t) + \frac{bN_{cell}}{F} \frac{i(t)}{Q(t)} \quad [mol/l] \quad (3.10)$$

where:  $c_i$  = concentration of the different vanadium ions  $[mol/l]$   
 $Q(t)$  = flowrate of the electrolyte  $[l/s]$

For a quasi steady state, where the current and the flowrate are almost constant, the model predicts accurately the output concentrations. Unfortunately, it is not able to predict the transient behaviour when the system encounters extreme conditions such as the combination of a low flowrate, few active species and sudden current change. But when these conditions are avoided, (3.10) offers a very good insight of the battery behaviour.

#### Average Cell Concentration

We still have to establish the most important concentration: the concentration inside the cell  $c_{cell}$  that is necessary to solve the Nernst equation (2.29). Because the ion concentrations are not uniformly distributed inside the cell, we will make an approximation to determine  $c_{cell}$  from the mean value of  $c_{in}$  and  $c_{out}$ :

$$c_{cell_i}(t) = c_{av_i}(t) = \frac{c_{in_i}(t) + c_{out_i}(t)}{2} \quad [mol/l] \quad (3.11)$$

#### Another Method

A similar approach has been proposed by M. Li in [77] that describes the concentration change; as for (3.10), it considers the cell as a closed system, but also assumes, for simplicity, that the concentration inside the cell and tank are uniform and that the time delay of electrolyte flow is negligible:

$$\frac{dc_{cell_i}(t)}{dt} = \frac{bi(t)}{V_{cell}F} + \frac{Q(t)}{V_{cell}} (c_{tank_i}(t) - c_{cell_i}(t)) \quad [mol/l/s] \quad (3.12)$$

where  $V_{cell}$  is the volume of the cell. The first term represents the change due to the internal electrochemical reactions and the second term corresponds to the concentration change due to the electrolyte circulation.

Both methods give a good approximation for quasi steady state of operation, but will both struggle to accurately represent the real operating conditions in extreme cases (low flowrate, low active species concentrations and sudden current change). (3.10) has no transient state and immediately takes into account the new conditions and (3.12) will damp the concentration change and will experience a transient state which might show inaccuracy. Nevertheless, the aim here is to have a simple model that is accurate in the majority of conditions. In the rest of this work, (3.10) and (3.11) are used to describe the concentrations.

### Concentration Dependence on the Operating Conditions

How do the concentrations react to different operating conditions? That's the question we want to answer in this section. We have already stressed in the previous sections that the output concentration  $c_{out}$  and the cell concentrations  $c_{cell}$  depend on the flowrate  $Q$ , the current  $i$  and the input concentrations  $c_{in}$  as seen in (3.10) and (3.11).

We have illustrated in Fig. 3.5 the output concentration  $c_{out}$  under a wide range of operating conditions: a low input concentration (0.1 M) and a high concentration (2 M), three currents (10, 33 and 100 A) and a flowrate ranging from 0 to 0.1 l/s.

It's not obvious in Fig. 3.5, but the absolute variation of  $c_{out}$  is the same in both graphs. But, since the input concentrations are different, the change in  $c_{out}$  is important in the case of low input concentrations and negligible otherwise, except of course at low flowrate.

So, at low input concentration  $c_{in}$ , the flowrate strongly affects  $c_{out}$  which, in turn, influences the cell concentration  $c_{cell}$  and finally also influences the cell voltage. But, at high  $c_{in}$ , the flowrate has almost no effect on  $c_{out}$  above a certain threshold; this threshold is reached when the active species are almost completely depleted. Thus, for the same current, an optimal flowrate exists and depends on the electrolyte concentrations. And since  $c_{cell}$  is one of the parameters that determines the cell voltage, a good ion concentration will maintain a good battery efficiency.

In the VRB balance of plant, the pumps are the major consumer of power; therefore, a careful control of the electrolyte flowrate reduces the energy consumption and enhances the overall battery efficiency. In chapter 5, we will discuss the fluid mechanics of the VRB and determine the power needed to circulate the electrolyte at any flowrate.



### 3.2. CONCENTRATION OF THE VANADIUM IONS

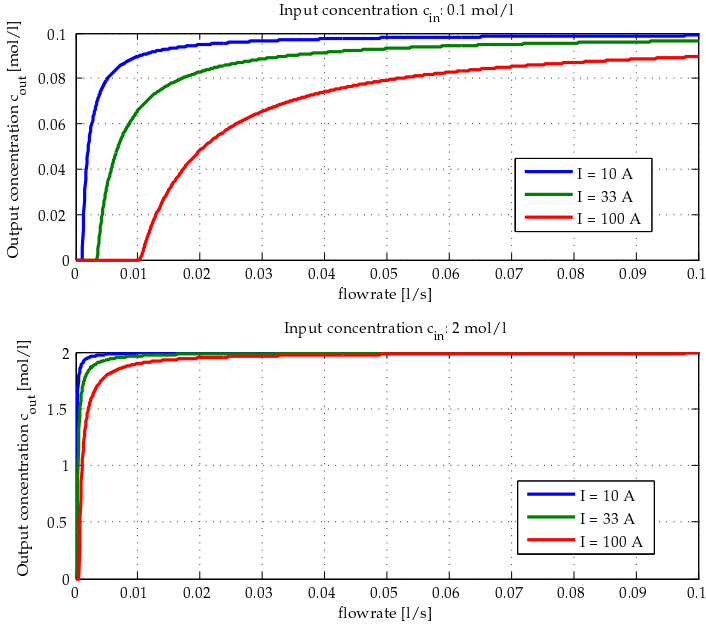


Figure 3.5.: Output concentration under various currents (10, 33 and 100 A) and flowrate. Above the input concentration is 0.1 M and below the input concentration is 2 M.

Finally, note that the ion concentrations can not be depleted below zero. Thus, there is a minimal flowrate  $Q_{min}$ , also dependent on the operating conditions (current and input concentrations), necessary to supply the required amount of electroactive species. In practice, a margin is needed because the vanadium ions and the intensity of the redox reaction are not uniformly distributed in the cell. This margin also helps to avoid side reactions when the electrolyte becomes depleted.

### 3.2.3. Observation of the Concentration

The concentrations are important internal variables that determine the state of charge  $SoC$  (2.43) and the stack voltage (2.79). It will be very convenient to be able to observe the actual concentrations in a real application. In this section, we propose two methods to do it.

The first is based on the Nernst equation (2.29) from which the vanadium ion concentrations are calculated. Indeed, under OCV conditions, there is no overpotential; thus the cell voltage depends only on the concentrations. Therefore we can determine the concentrations from a measurement of the cell voltage, if we assume that the vanadium concentrations are equal in both electrolytes. Fortunately, this is the case in VRB.

In practice, it is not possible to meet the OCV conditions which require to interrupt the current  $i$  without disturbing the battery operation. But we can circumvent this problem by diverting a small fraction of the electrolytes into a small bypass cell or stack (see Fig. 3.6). Thus, the main part of the electrolytes flows through the main stack and the battery can operate without interruption; furthermore, the bypass cell is always under OCV conditions, so the monitoring of its voltage gives an instantaneous image of the electrolyte concentrations.

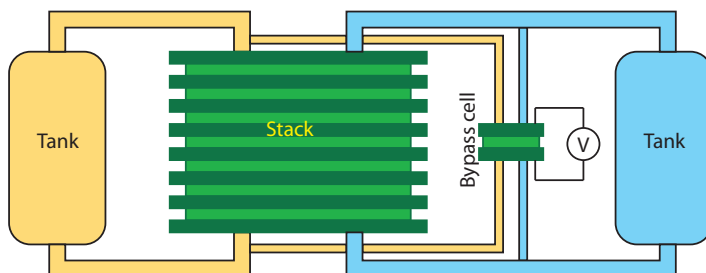


Figure 3.6.: VRB stack with a bypass cell to observe the ion concentration.

The second method comes from an interesting property of the electrolyte: its colour changes with its charge level. When fully charged, the catholyte is yellow and the anolyte is violet; when the VRB is discharged, the catholyte turns gradually blue and the anolyte turns green (see Fig. 3.7). This property can be used to estimate the state of charge

and thus the concentrations. Note that this is a more sophisticated and complex method that requires an optical cell connected to an UV-VIS spectrometer [65]. The light absorption of the electrolyte solution is measured to obtain the VRB state of charge at any time.

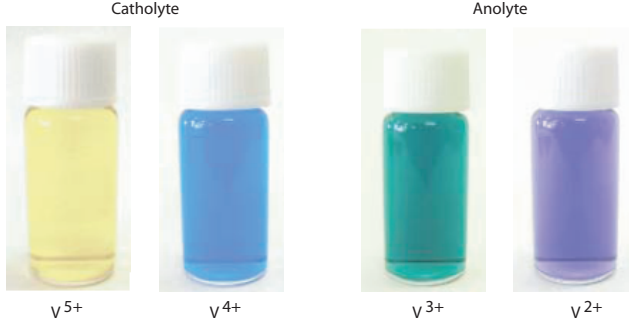


Figure 3.7.: Colour of the different vanadium ions solutions (source: [78]).

### 3.3. Proton Concentration in the Catholyte

The last unknown concentration required to solve the Nernst equation (2.29) is the proton  $H^+$  concentration in the catholyte. We have already discussed in section 2.3.3 how they are produced and consumed during the redox reactions and why they cross the membrane to balance the charge inside the cells; in particular the full ionic equations (2.39) and (2.41) define how the quantity of protons change. For example, the  $H^+$  quantity in the catholyte increases by 1 M when 1 M of vanadium  $V^{4+}$  is oxidized.

Thus, there is a direct relation between the  $H^+$  and the  $V^{4+}$  quantities from which the concentration of protons in the catholyte  $c_{H^+,catholyte}$  is derived. When the battery is discharged, the  $H^+$  concentration is set by the quantity of sulphuric acid dissolved in the electrolyte. Hence, the  $H^+$  concentration at the discharged state in the catholyte  $c_{H^+,discharged,catholyte}$  is known. So, the  $H^+$  concentration in the catholyte  $c_{H^+,catholyte}$  at any state of charge becomes:

$$c_{H^+,catholyte} = c_{H^+,discharged,catholyte} + c_{VO^{2+}} \quad [M] \quad (3.13)$$

where  $c_{VO^{2+}}$  is the concentration of  $VO^{2+}$  ions.

#### **Influence of the Proton Concentration on the Cell Voltage**

There are two main sources of protons in the VRB: the sulphuric acid  $H_2SO_4$  and the dissociation of water during the oxidation of  $V^{4+}$  ions. But we can only influence the  $H^+$  concentration with the quantity of sulphuric acid as the  $H^+$  quantity coming from the dissociation of water depends uniquely on the state of charge of the battery (see section 2.3.3 for more details).

The proton concentration  $c_{H^+}$  has a beneficial effect on the cell voltage, as it can be observed in Fig 3.8. Hence, the performance of the battery during the discharge is increased when the  $H^+$  concentration is higher; this is due to the increased power available at the same state of charge. However, this is mitigated by the higher power required during the charge. Moreover, we will see in chapter 4 that the sulphuric acid concentration influences other parameters such as the density and the viscosity of the electrolyte.

The second graph of Fig. 3.8 shows the  $c_{H^+}$  contribution to the cell voltage. This contribution is extracted from the second term of the Nernst equation (2.29); it grows logarithmically with the  $H^+$  concentration and is negative for concentration below 1 M.

### **3.4. Internal Losses**

The equilibrium voltage  $E$  is expressed by the Nernst equation (2.29) and represents the open circuit voltage (OCV). As soon as current starts to flow, equilibrium conditions are not met anymore and voltage drops occur in the cells. These losses are associated with different physical phenomena discussed in section 2.4: the activation overpotential  $\eta_{act}$  associated with the activation energy required to initiate a charge transfer, the concentration overpotential  $\eta_{conc}$  caused by a difference in electroactive species concentrations between the bulk solution and the electrode surface, the ohmic loss  $\eta_{ohm}$  and the ionic loss  $\eta_{ion}$ . Hence, the cell voltage  $U_{cell}$  is then given by:

$$U_{cell}(t) = E(t) - \eta_{act}(t) - \eta_{conc}(t) - \eta_{ohm}(t) - \eta_{ion}(t) \quad [V] \quad (3.14)$$

Unfortunately, these overpotentials are difficult to identify, depend on

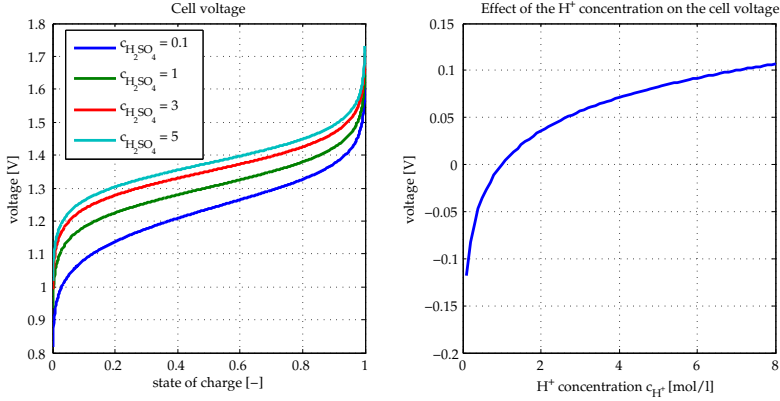


Figure 3.8.: On the left: cell voltage for four different sulphuric acid concentration of  $H_2SO_4$ ; the proton concentration increases as the battery is charged. The concentration of the vanadium species is ranging from 0 to 1 M depending on the state of charge. On the right: part of the cell voltage due to the proton concentration in the Nernst equation (2.29).

the electrolytes composition, the cell geometry, the material and the operating conditions. Moreover, they are seldom found in the literature and often applicable only to peculiar conditions. Therefore, (3.14) is not readily applicable to a practical model.

Indeed, for a given battery, the overpotentials mainly depend on the current  $i$ , the temperature  $T$  and the electrolyte flowrate  $Q$ ; the total overpotential, or internal loss<sup>1</sup>,  $U_{loss}$  is the difference between the equilibrium voltage  $E$  and the cell voltage  $U_{cell}$ :

$$U_{loss}(t) = |E(t) - U_{cell}(t)| \quad [V] \quad (3.15)$$

In the case where the temperature and the flowrate are considered constant, the internal losses are described by an equivalent resistance<sup>2</sup>  $R_{eq}$

<sup>1</sup>The internal losses are by definition always positive.

<sup>2</sup>Also by definition, the equivalent resistance and equivalent overpotential are positive.

and an equivalent overpotential  $\eta_{eq}$  [79]:

$$U_{loss}(t) = R_{eq,charge/discharge} |i(t)| + \eta_{eq,charge/discharge} \quad [V] \quad (3.16)$$

where:	$R_{eq,charge}$	=	charge equivalent resistance	[ $\Omega$ ]
	$R_{eq,discharge}$	=	discharge equivalent resistance	[ $\Omega$ ]
	$\eta_{eq,charge}$	=	charge equivalent overpotential	[V]
	$\eta_{eq,discharge}$	=	discharge equivalent overpotential	[V]

Note that when the flowrate  $Q$  is low, the concentration overpotential might increase and in consequence, the equivalent resistance  $R_{eq}$  might also change. Furthermore, the difference between  $R_{eq,charge}$  and  $R_{eq,discharge}$  is explained by the kinetics of the VRB reactions, in particular the cathodic reactions which are slower during the discharge, as it was seen in section 2.4.1.

The equivalent resistances are obtained experimentally for a particular stack; their values are determined from the slope of the voltage versus the current during the charge and during the discharge and are often expressed as cell area resistivities:

$$R_{eq} = \frac{R_A}{A} \quad [\Omega] \quad (3.17)$$

where:	$R_{eq}$	=	cell resistance	[ $\Omega$ ]
	$R_A$	=	Area resistivity	[ $\Omega \text{ cm}^2$ ]
	$A$	=	cell area	[ $\text{cm}^2$ ]

For example, Fig. 3.9 presents experimental data<sup>3</sup> for a 19 cells stack taken from the work of M. Skyllas-Kazacos and C. Menictas [76]. The correlation between the data and (3.16) is very good; the equivalent overpotential  $\eta_{eq}$  are seen on the y-axis at the origin.

---

<sup>3</sup>The experimental data of Fig. 3.9 have been measured at approximately 50% state of charge during 1 min. charge and discharge cycles. The values of the slopes are respectively 0.0370  $\Omega$  and  $-0.0390 \Omega$  for the charge and the discharge. This leads to the following average stack area resistivities:  $R_{A,charge} = 2.96 \Omega \text{ cm}^2$  and  $R_{A,discharge} = 3.12 \Omega \text{ cm}^2$  for a  $80 \text{ cm}^2$  cell. The charge and discharge equivalent stack overpotentials,  $\eta_{eq,charge}$  and  $\eta_{eq,discharge}$ , are respectively 0.36 V and 0.38 V (or 0.019 V and 0.020 V per cell).

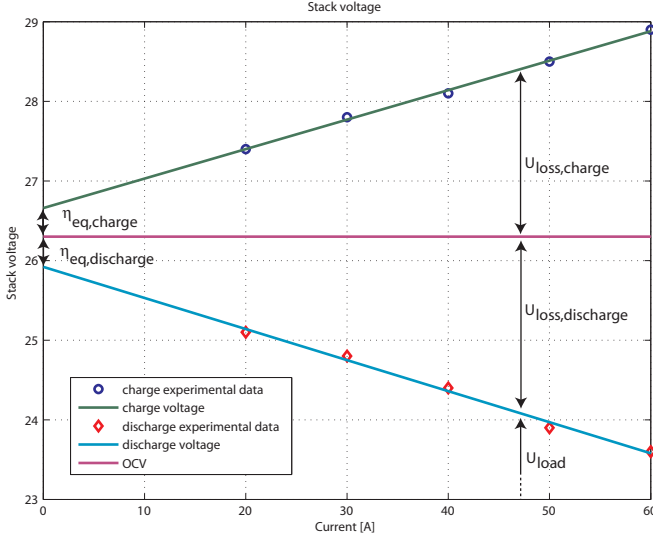


Figure 3.9.: Charge and discharge stack voltage versus current curves at approximately 50% state of charge for a 19 cells stack. The OCV voltage is 26.3 V. Experimental data are from [76].

### The Cell Voltage

During the discharge, the cell acts like a galvanic element: the cell equilibrium voltage  $E$  is split between the load voltage  $U_{load}$  and the internal loss  $U_{loss}$  due to the internal impedance [66]. The proportionality between the current and the loss  $U_{loss}$  explains the negative slope observed in Fig. 3.9. So, the cell voltage during the discharge  $U_{cell,discharge}$  is given by:

$$U_{cell,discharge} = E - U_{loss,discharge} \quad [V] \quad (3.18)$$

And during the charge, the voltage drop across the cell internal impedance is added to the equilibrium voltage  $E$ :

$$U_{cell,charge} = E + U_{loss,charge} \quad [V] \quad (3.19)$$

The internal loss model (3.16) is a linear function that describes accurately the battery behaviour when the current is above a certain threshold; but obviously an error is made whenever no current is flowing as the loss must be zero at that moment. This is represented in Fig. 3.10 where a simplified model is proposed: this second model simply discards the equivalent overpotential from (3.16):

$$U_{loss,simplified}(t) = R_{eq,charge/discharge} |i(t)| \quad [V] \quad (3.20)$$

Nevertheless, both models are a good approximation since they introduce only a small error (around 1.5%)<sup>4</sup>. Moreover, it has been found experimentally by M. Schreiber and al. that the overpotential  $\eta_{eq}$  might be ignored in practice and that the VRB may be taken to behave ohmically [46].

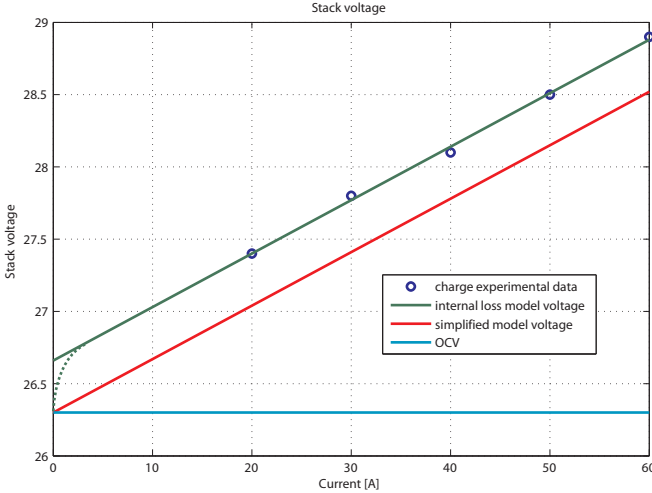


Figure 3.10.: Comparison of the internal loss model (3.16) and the simplified model (3.20) with the experimental data. The dashed line represents the expected behaviour of the battery.

<sup>4</sup>The same verification for the discharge leads to the same conclusion and the introduced error is also around 1.5%.



### 3.5. Response Time

The response time of any storage system is an important characteristic that determines the time necessary to the system to respond to a change in its reference operating point; in fact, this value determines the potential applications that the storage system will be able to fulfil. Furthermore, the response time is also an important variable for the definition of the control strategy.

In the VRB case, the electrochemical response time to a change from zero output to full output is very fast: it is under 0.5 ms. This was verified through experimental measurements by T. Kaizuka and al. [39]: they have found a response time of  $350\ \mu\text{s}$  for a 1.1 kW, 1 kWh battery. This electrochemical response time is two orders of magnitude faster than the response time of the power conversion system whose response time is typically within 10 to 20 ms [80].

In fact, the largest response time in the VRB is due to the flow of electrolyte; indeed, the time required to establish the flowrate in the electrolyte circuit is very large compared to the electrochemical time constant. Therefore, the electrochemical response time is not the limiting factor from a system point of view. For example, the start up time of the battery is limited by the time required to flow enough active species into the stack to sustain the electrochemical reaction rate and not by the reaction itself. In fact, the start up time depends upon the state of charge *SoC*; indeed, the flowrate  $Q$  must in some conditions be higher to compensate the small quantity of active species. In consequence, it takes more time to reach this larger flowrate.

### 3.6. Augmented and Simplified VRB Model

In the previous sections, we have discussed the vanadium and proton concentrations and established the relations that describe the concentrations inside the tank and the cell. With these relations, the electrochemical model introduced in the previous chapter (section 2.5 and Fig. 2.19) can be enhanced and simplified. This new stack model illustrated in Fig. 3.11 incorporates the new building blocks based on the relations introduced in the sections 3.2, 3.3 and 3.4.

The number of operating parameters defined in Tab. 2.1 has been reduced; all the concentrations have become internal parameters and the

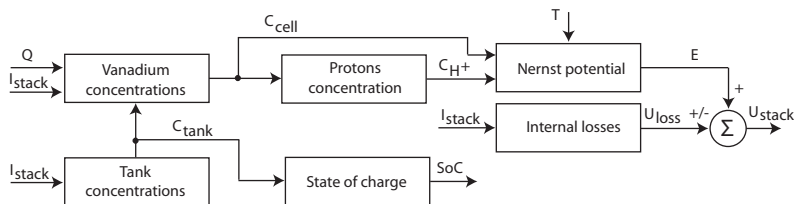


Figure 3.11.: Flowchart of the simplified VRB stack model.

only remaining control parameters are the current  $I_{stack}$  and the flowrate  $Q$ ; the temperature  $T$  is still an external parameter.

The change in the vanadium concentrations in the tank  $c_{tank}$  depends only on the current and is determined from (3.8);  $c_{tank}$  is then used to determine the state of charge  $SoC$  from (2.43) and the concentrations inside the cells  $c_{cell}$  from (3.11). The proton concentration  $c_{H+}$  is related to the  $V^{4+}$  concentration and is calculated with (3.13); the proton and vanadium concentrations are then fed into (2.29) to obtain the equilibrium voltage  $E$ . After the calculation of the internal losses  $U_{loss}$  from (3.16), the stack voltage  $U_{stack}$  is finally obtained from (3.18) and (3.19). The dependence of the variables on the operating conditions and other variables is shown in Tab. 3.2.

Variable	f(?)	$I_{stack}$	$T$	$Q$
$c_{tank}$		●		
$c_{cell}$	$c_{tank}$	●		●
$c_{H+}$	$c_{vanadium}$	○		○
$SoC$	$c_{tank}$	○		
$E$	$c_{cell}$ and $c_{H+}$	○	●	○
$U_{loss}$		●		
$U_{stack}$	$E$ and $U_{loss}$	○	○	○

Table 3.2.: Variables dependency on the operating conditions. ● denotes a direct dependence and ○ denotes an indirect dependence.  $Q$  is the electrolyte flowrate.

### 3.7. Energy Density

Before we discuss the use of the electrochemical stack model in the simulation of a small stand alone system and in a series of charge and discharge cycles, we need to introduce a few notions in the next two sections: the energy density and the efficiency. We know that the theoretical energy density of a battery is determined by the amount of active materials; in the case of the VRB, this material is dissolved in the electrolyte.

So, the theoretical capacity is expressed as the total quantity of electricity produced during the electrochemical reaction; this value is defined in terms of coulombs or ampere-hours. In the case of the VRB, this is defined by the number of vanadium ions dissolved in the electrolyte; thus the available charge  $Q_c$  depends on the total vanadium concentration  $c_{vanadium_{total}}$  and on the size of the tank  $V_{tank}$ :

$$Q_c = c_{vanadium_{total}} V_{tank} N A e \quad [C] \quad (3.21)$$

The energy stored in the electrolyte  $E_{electrolyte}$  is then determined by the product of the available charge  $Q_c$  and the cell voltage  $U_{cell}$ . But  $U_{cell}$  is not unequivocally defined as it depends on the operating conditions, therefore an average cell voltage  $U_{cell,av}$  of 1.35 V is used instead. To operate the battery, the redox reactions (2.1) and (2.2) must simultaneously occur in both half-cells; thus the energy stored in the battery is divided between the two electrolytes (Fig. 1.17) and  $E_{electrolyte}$  becomes:

$$E_{electrolyte} = \frac{1}{2} \frac{U_{cell,av} Q_c}{3600} \quad [Wh] \quad (3.22)$$

The energy density is the ratio of the amount of stored energy to the volume or mass. In our case, the electrolyte energy density  $U_{electrolyte}$  per volume unit is:

$$U_{electrolyte} = \frac{E_{electrolyte}}{V_{tank}} \quad [Wh/l] \quad (3.23)$$

Fig. 3.12 illustrates  $U_{electrolyte}$  as a function of the vanadium concentration  $c_{vanadium_{total}}$ . The energy density per mass unit will be easily derived from (3.23) with the electrolyte density introduced in the next chapter (section 4.3).

Note that the VRB system energy density  $U_{VRB,system}$  is in reality smaller than the electrolyte density  $U_{electrolyte}$  because the complete sys-

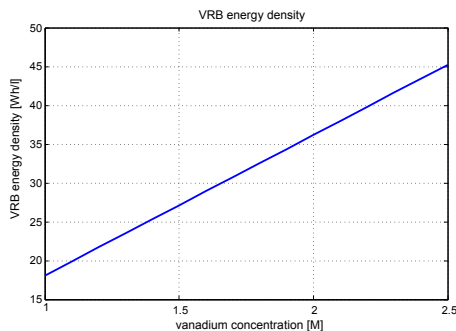


Figure 3.12.: Energy density for both VRB electrolytes together vs. the vanadium concentration.

tem also includes the pipes and pumps, the stack and the power converter that increase the system weight and volume. Furthermore, the energy density offered in practice is still lower due to the following reasons:

- The average voltage during the discharge is lower than the theoretical voltage, this voltage drop is due to the internal loss and depends on the operating condition.
- The battery is not discharged completely and all of the available capacity is not utilized.

Therefore, typical real applications have energy densities ranging from 15 to 25 Wh/l [81, 82].

### 3.8. Efficiencies

Efficiencies are one of the metrics used to assess the performance of storage systems. Basically, the definition of efficiency is simple, it is the ratio of the energy output  $E_{output}$  of the system to the energy input  $E_{input}$ :

$$\eta = \frac{E_{output}}{E_{input}} \quad [-] \quad (3.24)$$

Difficulties quickly appear when we try to compare different technologies or product from different suppliers. Indeed, the operating modes have a significant impact on the battery performance: a quick charge produces more losses than a gentle one. Many authors and datasheets do not precisely define how the efficiency was characterized, thus contributing to a great confusion. Hence, we want to introduce here a clear definition of the efficiency; we are going to discuss three types of efficiencies: the energy efficiency, the coulombic efficiency and the voltage efficiency.

### Energy Efficiency

The energy efficiency  $\eta_{energy}$  is defined as the ratio of the energy furnished by the battery during the discharge to the energy supplied during the charge:

$$\eta_{energy} = \frac{\int P_{discharge}(t)dt}{\int |P_{charge}(t)|dt} \quad [-] \quad (3.25)$$

where:	$P_{discharge}$	=	Stack power during the discharge cycle	[W]
	$P_{charge}$	=	Stack power during the charge cycle	[W]

### Coulombic Efficiency

The coulombic efficiency  $\eta_{coulombic}$  is a measure of the ratio of the charge withdrawn from the system during the discharge to the charge supplied during the charge and is always larger than the energy efficiency:

$$\eta_{coulombic} = \frac{Q_{discharge}}{Q_{charge}} = \frac{\int i_{discharge}(t)dt}{\int |i_{charge}(t)|dt} \quad [-] \quad (3.26)$$

where:	$Q_{disch./ch.}$	=	charge transferred	[C]
	$i_{disch./ch.}$	=	discharge and charge current	[A]

Losses in coulombic efficiency can be caused by side reactions such as oxygen or hydrogen evolution that might occur during the charge. The cross mixing of the electrolyte through the membrane due to ion transfer and unbalanced flowrates of the electrolytes are other sources of coulombic losses [73].

#### Voltage Efficiency

The voltage efficiency  $\eta_{voltage}$ , also named potential efficiency, is defined for a charge and discharge cycle at constant current. It is a measure of the ohmic and polarisation losses during the cycling.

Its value can be maximised by ensuring minimum contact, electrode, electrolyte and membrane resistances and by using an electrode material with good electro-catalytic properties for the reactions [73].

The voltage efficiency value is calculated as the ratio of the integral of the battery voltage  $U_{discharge}$  during the discharge to that of the voltage  $U_{charge}$  during the charge. Note that this ratio coincides with the ratio of the potential of the half-discharged solution to that of half charged solution.

Since by definition the current is held constant, the voltage efficiency is also expressed as a ratio of the energy efficiency (3.25), to the coulombic efficiency (3.26), so its expression becomes:

$$\eta_{voltage} = \frac{\int U_{discharge}(t)dt}{\int U_{charge}(t)dt} = \frac{\eta_{energy}}{\eta_{coulombic}} \quad [-] \quad (3.27)$$

### 3.9. Simulation of a Small Stand Alone System

To illustrate the possibilities of the VRB electrochemical model developed in the previous sections and summarized in Fig. 3.11, we propose to simulate here the behaviour of a small stand alone system and thereafter a series of charge and discharge cycles.

The stand alone system is composed of a 2 kW photovoltaic power source connected to a load and a 1.5 kW, 10 h VRB (Fig. 3.13); this system is simulated over a 24 h period. The load represents the power consumption of a small household and has two peak periods during the meal hours.

In detail, the considered VRB is composed of a 19 elements stack and two tanks filled with 200 l of electrolytes having a total vanadium concentration of 2 M; the electrolyte flowrate is maintained constant all the time. The initial concentration of each vanadium species is set at 1 M: the state of charge is therefore 0.5. Tab. 3.3 summarizes the parameters used in this simulation.

In this first approach, power profiles are used to characterize the exchanges between the different components of the system. Obviously, in

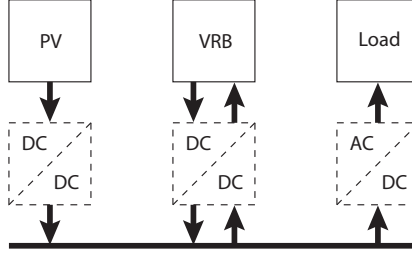


Figure 3.13.: Schematic of the simulated system: the power converter are represented (dashed) but not taken into account in the simulation. The arrows represent power flows.

in a real application, power converters will be needed to adequately match the voltage and current levels. It is one aim of this work to identify the constraints on these levels in order to have better specifications for the static converters. But for this example, their efficiencies have been set to 100%, so they have no effect on this simulation.

### Power Profiles

In this example, the power profile of the PV source  $P_{solar}$  during a sunny day and the power profile of a small household  $P_{load}$  during a 24 h period are known (see Fig. 3.14); what we want to know is how the VRB behaves under these conditions. Clearly, the battery stores the surplus of power available during the day and releases it whenever needed. Thus, the power exchanged by the VRB  $P_{VRB}$  is defined as:

$$P_{VRB} = P_{load} - P_{solar} \quad [W] \quad (3.28)$$

The power profile of the VRB is also represented in Fig. 3.14; at night, the VRB delivers all the power required by the load. In bright daylight, the PV source supplies the load and charges the battery; and when the lights are fading and the load is reaching its second peak, both the PV source and the VRB deliver power to the load. In accordance with the convention adopted in section 3.2.1,  $P_{VRB}$  is negative when energy is stored and

Name	Value
number of cells $N_{cells}$	19
$R_{charge}$	$0.037 \, \Omega$
$R_{discharge}$	$0.039 \, \Omega$
electrolyte flowrate $Q$	2 l/s
electrolyte vanadium concentration	2 M
tank size $V_{tank}$	200 l
initial concentration of vanadium species	1 M

Table 3.3.: the parameters of the simulation.

positive when energy is released.

The internal losses of the battery  $P_{loss}$  are also represented in Fig. 3.14; they are by nature always positive and grow with the current  $I_{stack}$ . Note that the losses from the auxiliaries are not taken into account in this simulation; the mechanical power required to flow the electrolytes is discussed in chapters 5 and 6.

### Stack Voltage and Current

The power converter controls the flow of power between the battery and the rest of the system; the converter automatically adapts the current to the instantaneous stack voltage to meet the power requirements set by (3.28). The electrochemical model determines the stack voltage that depends on the operating conditions: state of charge  $SoC$ , electrolyte flowrate  $Q$  and current  $I_{stack}$ . Both the stack voltage  $U_{stack}$  and the stack current  $I_{stack}$  are represented in Fig. 3.15.

A close observation of Fig. 3.15 reveals that that  $U_{stack}$  rises when the battery is in charge to compensate the internal losses  $U_{loss}$ ; this illustrates (3.19) and the discussion about the cell voltage in section 3.4. The voltage also increases due to the change in the vanadium concentrations: indeed the equilibrium voltage  $E$  (2.29) depends on the concentrations. Thus, the current must decrease to respect the power flow  $P_{VRB}$ ; this phenomenon is particularly remarkable in Fig. 3.15 around noon.

Similarly during the discharge,  $U_{loss}$  induces a voltage drop proportional



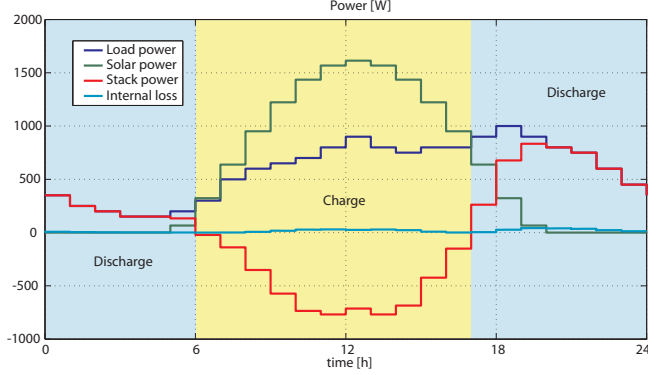


Figure 3.14.: Power profiles of the photovoltaic source, the load, the internal loss and the power furnished or stored by the VRB.

to the current (3.18). When the concentrations diminish, so does the equilibrium voltage  $E$ ; thus the current must increase to maintain the delivered power at its reference level. This is particularly obvious in the evening.

The stack voltage  $U_{stack}$  is maximal during the charge at high current and high state of charge  $SoC$ ;  $U_{stack}$  is minimal during the discharge at high current and low  $SoC$ .

#### Vanadium Concentrations

The variations of the vanadium concentrations inside the tank  $c_{tank}$  are represented in Fig. 3.16. We observe that the rate of the concentrations change is proportional to the stack current  $I_{stack}$  as it was expected from (3.8). At the end of the simulation, the state of charge of the battery has decreased because there was more power consumed by the load than delivered by the photovoltaic source.

#### System Efficiency

To conclude this section, we will discuss the efficiency of this system. But, as we have seen in Fig. 3.16, the state of charge of the battery has

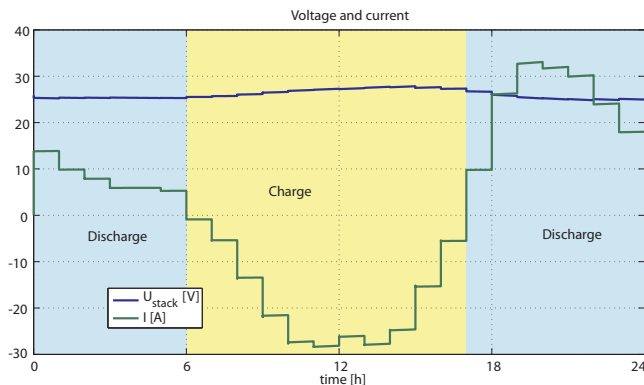


Figure 3.15.: Current and voltage of the stack.

decreased. Thus, the efficiencies introduced in section 3.8 would make no sense. Indeed, these relations are meant for a round trip, i.e. the battery should have reached its initial SoC at the end of its operation. Nevertheless, we can define two new efficiencies: a charge efficiency  $\eta_{charge}$  and a discharge efficiency  $\eta_{discharge}$ . They are given by:

$$\begin{aligned} \text{During the charge: } \eta_{charge} &= \frac{\int |P_{VRB}(t)| dt - \int P_{loss}(t) dt}{\int |P_{VRB}(t)| dt} \quad [-] \\ \text{During the discharge: } \eta_{discharge} &= \frac{\int P_{VRB}(t) dt}{\int P_{VRB}(t) dt + \int P_{loss}(t) dt} \quad [-] \end{aligned} \quad (3.29)$$

The charge efficiency  $\eta_{charge}$  is the ratio of the energy stored  $E_{stored}$  in the battery to the energy furnished  $E_{VRB}$  to the battery during the charge;  $E_{stored}$  corresponds to the difference between  $E_{VRB}$  and the energy lost in the battery  $E_{loss}$ .

Similarly, the discharge efficiency  $\eta_{discharge}$  is defined as the ratio of the energy furnished by the battery  $E_{VRB}$  to the energy extracted  $E_{extracted}$  from the electrolyte during the discharge;  $E_{extracted}$  is the sum between  $E_{VRB}$  and  $E_{loss}$ .

So, we found for this example with (3.29) that the charge efficiency

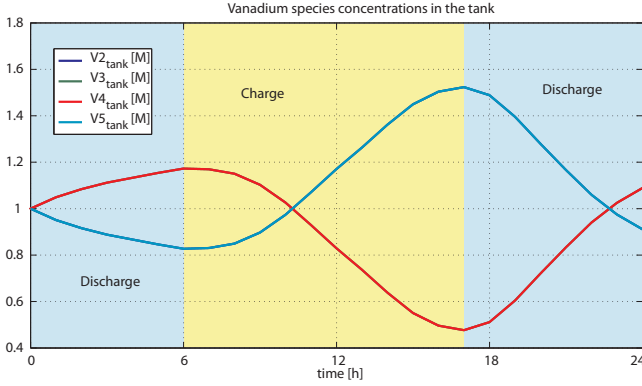


Figure 3.16.: Vanadium ion concentrations in the VRB. In this case, the concentration of  $V^{2+}$  is equal to the  $V^{5+}$  concentration, similarly, the concentration of  $V^{3+}$  has the same value than the  $V^{4+}$  concentration.

$\eta_{\text{charge}}$  and the discharge efficiency  $\eta_{\text{discharge}}$  are respectively 96.7% and 96.4%. These efficiencies are high because the battery always operates below its rated power; we will discuss in the next section the effect of the current on the VRB efficiencies in details. Also note that they do not take into account the auxiliaries losses which are discussed in chapters 5 and 6.

### 3.10. Charge and Discharge Cycles

We have seen in the previous example that the electrochemical model is able to predict the behaviour of the VRB in a stand alone system: it determines the stack voltage and current, the vanadium concentrations and the internal losses. But we were not able to determine the efficiency of the storage system because the battery has consumed more energy than it has stored. Thus, we propose to simulate a series of charge and discharge cycles in this section.

We will see that the operating conditions, among other factors, have a significant effect on the battery performance. Two different methods will be used to illustrate this influence: the battery is either cycled at constant current or at constant power. Then the effects on the stack voltage  $U_{\text{stack}}$ ,

### 3.10. CHARGE AND DISCHARGE CYCLES

Current [A]	Time [h]	$\eta_{charge}$ [%]	$\eta_{discharge}$ [%]	$\eta_{energy}$ [%]	$\eta_{voltage}$ [%]	$\eta_{coulombic}$ [%]
10	44.49	98.56	98.46	97.02	97.02	100
20	22.24	97.15	96.91	94.13	94.13	100
40	11.12	94.47	93.82	88.58	88.58	100
60	7.41	91.93	90.73	83.33	83.33	100
80	5.56	89.52	87.64	78.37	78.37	100
100	4.45	87.24	84.55	73.65	73.65	100

Table 3.4.: Cycle duration and efficiencies at various currents ranging from 10 to 100 A. The cycle starts at 2.5% SoC, the battery is charged until a 97.5% SoC and then discharged until a 2.5% SoC at a constant current.

the stack current  $I_{stack}$ , the stack power  $P_{stack}$  and the efficiencies are observed and discussed.

The battery put into operation in this series of charge and discharge cycles has the same characteristics as the battery used in the stand alone system (Tab. 3.3), except for the tank size<sup>5</sup> that has been downsized to 83 l to match the capacity of the experimental battery presented in [76]; indeed, this battery is used to compare the results of the electrochemical model to experimental data in order to assess its performance.

#### 3.10.1. Constant Current

The first method cycles the battery at constant current; a cycle starts from a 2.5% state of charge  $SoC$  until the battery reaches a 97.5%  $SoC$ , then it is discharged back to 2.5%  $SoC$ . During a cycle, the current is maintained constant and its magnitude has been ranged from 10 A to 100 A. At the end of every simulation, the charge efficiency  $\eta_{charge}$ , the discharge efficiency  $\eta_{discharge}$ , the energy efficiency  $\eta_{energy}$ , the voltage efficiency  $\eta_{voltage}$  and the coulombic efficiency  $\eta_{coulombic}$  are calculated with respectively (3.25), (3.26), (3.27) and (3.29); these results are summarized in Tab. 3.4 and represented in Fig. 3.17.

The coulombic efficiency  $\eta_{coulombic}$  is 100% because the model does not

<sup>5</sup>Note that the tank size has no influence on the efficiency, but only on the cycle duration.

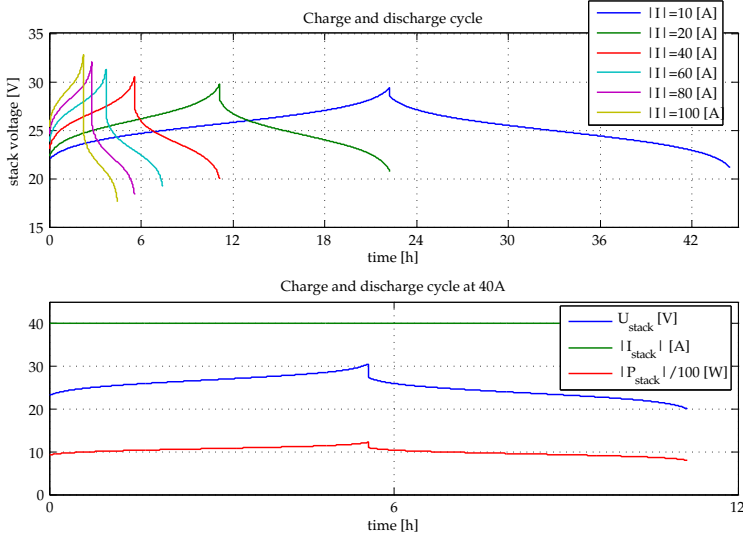


Figure 3.17.: Above: stack voltages during a cycle under diverse currents. Below: stack voltage, current and power at 40 A.

take into account any side reactions such as oxygen or hydrogen evolution nor any cross mixing of the electrolyte. Thus the equality between the energy efficiency  $\eta_{energy}$  and the voltage efficiency  $\eta_{voltage}$  is easily explained from (3.27). We remark also that  $\eta_{energy}$  is equal to the product of the charge and discharge efficiency:

$$\eta_{energy} = \eta_{charge}\eta_{discharge} \quad [-] \quad (3.30)$$

Manifestly, the efficiencies decrease when the magnitude of the current increases; these lower efficiencies are due to the internal losses that are proportional to the current. During the charge, the voltage applied to the stack  $U_{stack}$  has to compensate these voltage drops; similarly during the discharge, these same voltage drops reduce the available output voltage. We can observe these phenomena in Fig. 3.17, particularly when we compare the different  $U_{stack}$  or at the transition between the charge and the

discharge.

Obviously, the efficiency becomes maximal when the internal losses are kept minimal: this happens when the current is minimal. Thus, to augment the efficiency, the battery should be operated at low current: for example, the stack voltage is smaller during the charge at lower current, and so is the power necessary to store the same amount of charge into the battery. However, there is a drawback: the time required to charge the battery is inversely proportional to the current. So, there is a potential to increase the efficiency in some applications such as load leveling by fully exploiting the time allocated to the charge. But this is not possible when the battery is connected to a renewable power source, because the energy has to be stored immediately whenever it is available.

We can make a few more observations from Fig. 3.17: the duration of the cycles are unsurprisingly proportional to the current: a cycle is ten time longer when the current is ten time smaller. Furthermore, since the current is constant, it takes exactly the same amount of time to charge and discharge the battery. Finally, we remark in the second graph that the stack power is directly proportional to the stack voltage.

#### Verification and Validation

We have chosen the stack parameters to match the characteristics of the second stack presented by M. Skyllas-Kazacos and al. in [76] in order to compare the electrochemical model to an experimental battery; their results are summarized in Tab. 3.5. Experimentally, they have observed that the efficiency improves as the battery became conditioned; we can observe this in the three 100 A cycles that were carried out continuously.

The experimental coulombic efficiency is slightly below the simulated efficiency (100%), though the difference tends to decrease when the battery becomes conditioned. The fact that the lower efficiencies happened during the first cycles suggests that some incomplete side reactions were still occurring in the electrolyte; these reactions consumed some electrons that were intended to the vanadium redox reactions. Another source of imprecision might be the difficulty to determine precisely the beginning and the end of the charge and discharge cycle.

Furthermore, we observe that the simulated voltage efficiencies at 60 A and 100 A compare very well with the experimental values: the difference always stays below 2%. In the case of the energy efficiency, the results

Current [A]	Energy efficiency [%]	Coulombic efficiency [%]	Voltage efficiency [%]
60	78.3	94.6	82.8
100 (cycle 1)	68.0	94.0	72.3
100 (cycle 2)	70.8	96.1	73.0
100 (cycle 3)	73.1	98.7	74.0

Table 3.5.: Experimental results from M. Skyllas-Kazacos and C. Menictas presented in [76].

are not so good in the first cycles but improve as the battery becomes conditioned. The maximum difference between the experimental and simulated  $\eta_{energy}$  is around 8.3% for the first 100 A cycle. Nevertheless, this difference drops below 1% for the third cycle.

### 3.10.2. Constant Power

In this second series of charge and discharge cycles, we are interested to know how the battery behaves when it is cycled at constant power. Indeed, some storage applications supply their load with a constant power. Hence, we applied a constant power ranging from 250 W to 2500 W to the same battery and observe how the efficiencies change under these different conditions. The simulated efficiencies are presented in Tab. 3.6 and the curves are given in Fig. 3.18.

We can draw up a series of remarks similar to the constant current cycles: the energy efficiency equals the product of the charge and discharge efficiency (3.30). The coulombic efficiency is still 100% because the model does not take into account any side reactions; the efficiencies are maximal when the power is low but it takes more time to store the same quantity of energy.

But in the constant power cases, the voltage efficiency makes no sense because the current is not constant (see its definition in section 3.8); the current must constantly be adapted to the change in the stack voltage in order to maintain the power constant. For the same reason, the relation (3.27) between  $\eta_{voltage}$ ,  $\eta_{energy}$  and  $\eta_{coulombic}$  is not valid.

### 3.11. POWER DENSITY AND EFFICIENCY

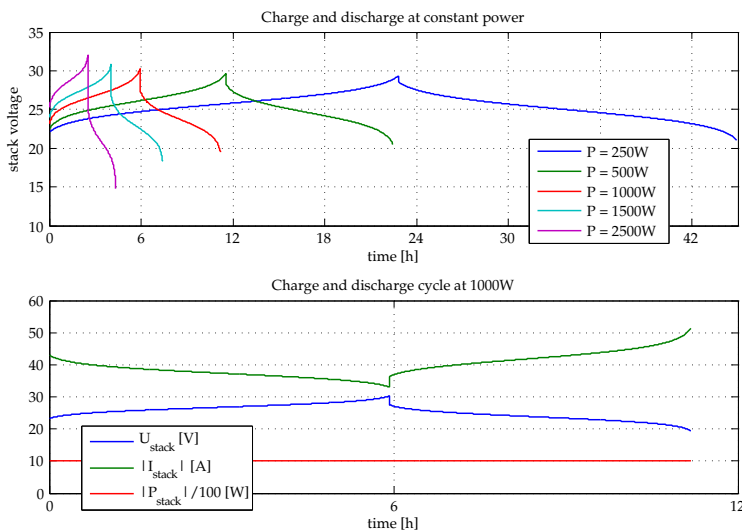


Figure 3.18.: Above: stack voltages during a cycle under diverse powers. Below: stack voltage, current and power at a power of 1000 W.

A second difference is that the charge and discharge durations are not equal anymore; to maintain the power constant, the current is increased to compensate the voltage drop, thus depleting faster the electrolyte. In the second graph of Fig. 3.18 we can observe the stack voltage  $U_{stack}$ , the stack current  $I_{stack}$  and the stack power  $P_{stack}$ ; the current is especially high when the state of charge is low and/or at high power.

To conclude this section, we remind that the auxiliaries losses are not taken into account in these simulations; they are discussed in chapters 5 and 6.

### 3.11. Power Density and Efficiency

The design of an electricity storage system has to meet many requirements: cost, efficiency, energetic capacity and power capacity. We have already discussed the VRB cost in section 1.4.2, the energetic capacity in section



Power [W]	Time [h]	Charge efficiency [%]	Discharge efficiency [%]	Energy efficiency [%]	Coulombic efficiency [%]
250	44.94	98.59	98.44	97.04	100
500	22.44	97.25	96.83	94.14	100
1000	11.18	94.78	93.42	88.49	100
1500	7.41	92.54	89.71	82.95	100
2500	4.36	88.61	80.88	71.56	100

Table 3.6.: Cycle duration and efficiencies at various power ranging from 250 to 2500 W. The cycle starts at 2.5% SoC, the battery is charged until a 97.5% SoC and then discharged until a 2.5% SoC at a constant power.

3.7 and some aspects of efficiency in sections 3.8, 3.9 and 3.10; moreover, the efficiencies of the overall storage system will be discussed in chapter 6. In this section, we will see how the energy efficiency  $\eta_{energy}$  affects the power capability of the battery [83].

As an illustration, we will use the same battery as in the two previous sections<sup>6</sup>, its characteristics are summarized in Tab. 3.3, except for the tank size  $V_{tank}$  that has been reduced to 10 l. We show in Fig. 3.19 the energy efficiencies  $\eta_{energy}$  for a series of charge and discharge cycles at constant currents (1-100 A) and constant powers (25-2500 W); in a cycle, we charge the battery from a 2.5% state of charge *SoC* until it reaches a 97.5% *SoC* and then discharge it until it reaches a 2.5% *SoC*.

We observe in Fig. 3.19 that the efficiency  $\eta_{energy}$  depends on the duration of the cycle and is independent of the operating method (constant current or constant power). The slight difference observed during short cycles, i.e. at high current or high power, is probably due to the difference between the equivalent charge and discharge resistances,  $R_{eq,charge}$  and  $R_{eq,discharge}$ , and to the asymmetry of the equilibrium voltage as a function of the state of charge (see Fig. 2.9); indeed, at high power and low state of charge, the current quickly increases to meet the power requirements and thus reducing further the overall stack voltage.

<sup>6</sup>Note that in section 3.9; the power capability (10 kW, 10 h) of the battery was underrated since this battery is able to provide 2.5 kW during 6 h.

### 3.11. POWER DENSITY AND EFFICIENCY

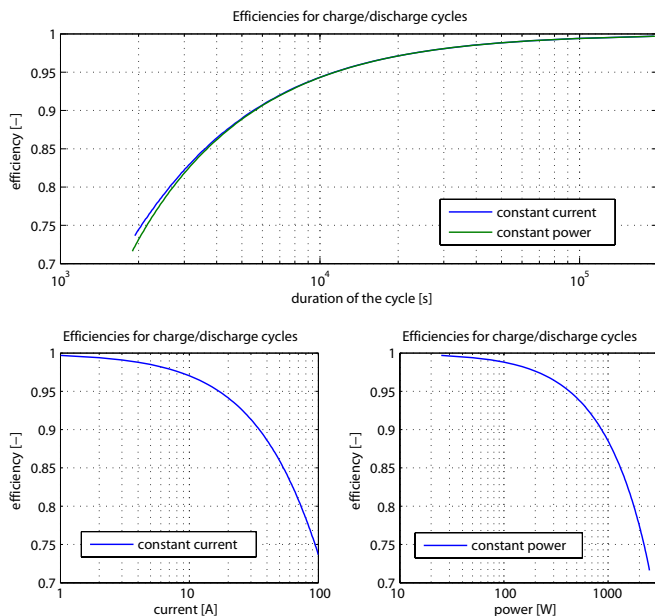


Figure 3.19.: VRB energy efficiencies  $\eta_{energy}$  for series of charge and discharge cycles at constant currents and constant powers. The top graph presents the efficiencies as a function of the duration of the cycles and the two graphs below present the same efficiencies as a function of the current and the power.

Furthermore, we can observe in the two bottom graphs of Fig. 3.19 that the energy efficiency  $\eta_{energy}$  decreases exponentially for both the current and the power. From these graphs, we can quickly assess the system efficiency at any operating conditions; in many cases, they will also give a good hint about the efficiency when the constant current or power are replaced with an average value. For example, if we consider this battery for an application requiring a 90% efficiency, we know from Fig. 3.19 that the power must be limited to 870 W, thus strongly reducing the rated power of the battery.

Hence, the power density  $P_{density}$  of the VRB depends on the desired efficiency; in any case,  $P_{density}$  depends on the maximal power deliverable by the system  $P_{max,system}$  and either on the volume of the system  $V_{system}$  or on the total mass of the system  $M_{system}$ :

$$P_{density} = \frac{P_{max,system}}{V_{system}} \text{ or } \frac{P_{max,system}}{M_{system}} \quad [W/m^3 \text{ or } W/kg] \quad (3.31)$$

To conclude this section, we have differentiated the charge cycle from the discharge cycle and determined the charge  $\eta_{charge}$  and discharge  $\eta_{discharge}$  efficiencies with (3.29). In the charge cycle, the battery is operated at constant current or power from 2.5% *SoC* to 97.5% *SoC*. The discharge cycle is simply the reverse cycle; the results are shown in Fig. 3.20. In that case, the efficiency is clearly a function of the cycle duration; thus, this is a good indication that the difference observed in Fig. 3.19 is due to the difference in equivalent resistances  $R_{eq,charge}$  and  $R_{eq,discharge}$  and to the asymmetry of the equilibrium voltage.

We also observe in the two bottom graphs of Fig. 3.20 that the discharge cycle is always less efficient than the charge cycle; the difference is greater at large constant power because of the large voltage drop at the end of the cycle (see Fig. 3.18). Again, the causes are the difference of equivalent resistances and the equilibrium voltage asymmetry.

### 3.12. Effects of the Operating Conditions

In this last section, we will observe the effects that the operating conditions (the current  $I_{stack}$  and the state of charge *SoC*) have on the battery behaviour. We will use three dimensional (3D) figures to illustrate the change in the stack voltage  $U_{stack}$ , the stack power  $P_{stack}$  and the internal losses  $P_{loss}$ .

For the simulations, the same battery as in the stand alone system was employed (section 3.9 and Tab. 3.3); the electrolyte flowrate was maintained constant at 2 l/s. The effects of the flowrate on the battery performance are discussed in detail in chapter 6.

#### Stack Voltage

The stack voltage  $U_{stack}$  is illustrated in Fig. 3.21 where we remark that  $U_{stack}$  varies greatly and depends on the operating conditions: the max-

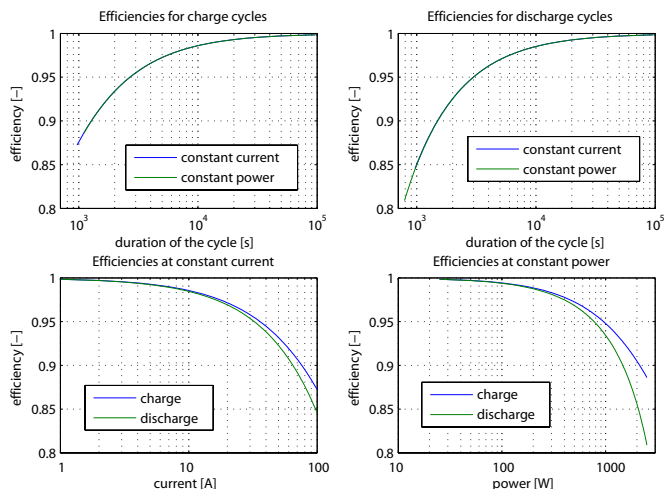


Figure 3.20.: Charge  $\eta_{charge}$  and discharge  $\eta_{discharge}$  efficiencies for series of charge or discharge cycles at constant currents (ranging from 1 to 100 A) and constant powers (ranging from 25 to 2500 W). The two top graphs present  $\eta_{charge}$  and  $\eta_{discharge}$  as a function of the duration of the charge or the discharge and the two bottom graphs present the efficiencies at constant current and power as a function of respectively the current and the power.

imal voltage occurs during the charge when the current  $I_{stack}$  and the state of charge  $SoC$  are maximal. This voltage is more than twice the minimal voltage that occurs during the discharge at maximal  $I_{stack}$  when the battery becomes totally depleted:  $SoC$  tends to zero.

We clearly recognize in Fig. 3.21 the characteristic shape of the equilibrium voltage  $E$  (2.29) that was illustrated in Fig. 2.5. Indeed, when there is no current, the two curves are equal; in all the other cases, the internal losses  $U_{loss}$  are either added or subtracted depending on the operating mode of the battery: charge or discharge (see section 3.4).

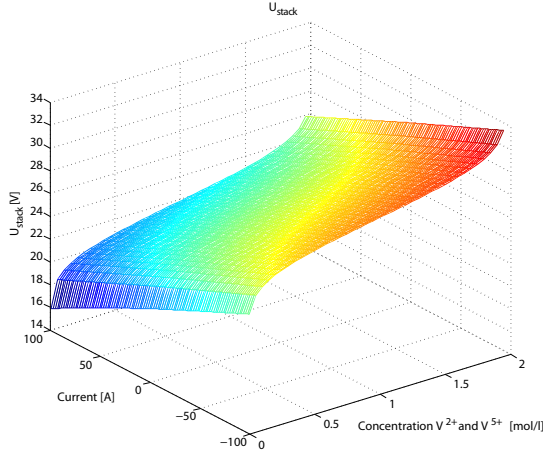


Figure 3.21.: Stack voltage  $U_{stack}$  of a 19 cells battery; when the current is negative, the battery is in charge and when it is positive, the battery is discharging. The electrolyte flowrate is 2 l/s.

### Stack Power

The power exchanged with the battery  $P_{stack}$  is controlled by the current  $I_{stack}$ ; the available power mainly depends on the state of charge  $SoC$ . In Fig. 3.22, we can see how  $P_{stack}$  changes as a function of  $I_{stack}$  and  $SoC$ ; by convention, the power is positive during the discharge and negative during the charge. Its absolute value is maximal at high  $SoC$  and high  $I_{stack}$ . For example, at 100 A, the deliverable power is ranging from 1577 W, when the battery is almost discharged, to 2570 W when it is fully charged. Obviously, the power drops to zero with no current.

### Internal Losses

In the electrochemical model presented in section 3.6, the internal losses  $P_{loss}$ , represented in Fig. 3.23, are proportional to the square of the current  $I_{stack}$  and independent of the state of charge  $SoC$ . However, in a more detailed model, like the stack electrochemical model presented in section

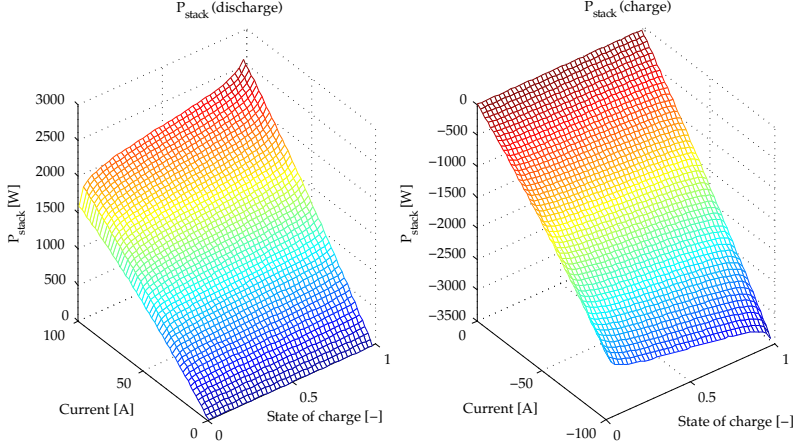


Figure 3.22.: Stack power  $P_{stack}$  as a function of the current  $I_{stack}$  and state of charge  $SoC$ . On the left, the battery is discharging and on the right it is in charge. The electrolyte flowrate is in both cases 2 l/s.

2.5, which takes into account the activation and concentration overpotential,  $P_{loss}$  depends also on  $SoC$ , especially at both extremities where the active vanadium species become depleted. In Fig. 3.23, we remark the symmetry between the charge and discharge; note that  $P_{loss}$  is positive by definition.

### 3.13. Summary

In this chapter dedicated to the electrochemical model of the VRB, we have first explained how to determine the vanadium ion and proton concentrations. The change in vanadium concentrations was explained from Faraday's law and depends on the electrochemical reactions rate; in other words, this change is proportional to the electrical current  $I_{stack}$ . In fact, the concentrations are not uniformly distributed in the battery; two important concentrations were defined: the tank concentration  $c_{tank}$  from which the battery state of charge  $SoC$  is derived, and the concentrations

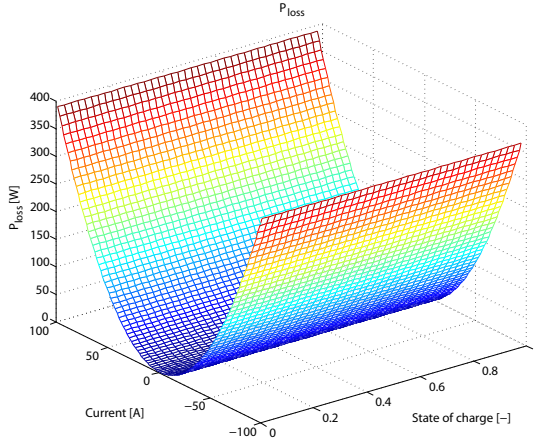


Figure 3.23.: Internal losses  $P_{loss}$  of a 19 cells stack; when the current is positive, the battery is in charge, otherwise, the battery is discharging. The electrolyte flowrate is 2 l/s.

within the cells  $c_{cell}$  used to calculate the equilibrium voltage  $E$ .

The operating conditions include the stack current  $I_{stack}$ , the electrolyte flowrate  $Q$  and the state of charge  $SoC$ ; their effect on the concentrations in the cells  $c_{cell}$ , and consequently on the cell voltage  $U_{cell}$ , were then discussed in detail. In fact, we have shown that there is a potential gain in performance when the flowrate is adjusted to the actual operating conditions. Thereafter, two methods were proposed to estimate the state of charge: the simplest measures the equilibrium voltage from a bypass cell and thus determines the state of charge from the Nernst equation.

In addition, the relation that describes the proton concentration  $c_{H^+}$  from the electrolyte composition was also introduced; they are derived from the full ionic equations. In fact, the proton concentration depends mainly on the sulphuric acid concentration and also on the state of charge: indeed, protons are produced during the  $V^{4+}$  oxidation.

Then, a simplified model of the internal losses was proposed; this model is based on an empirical approach that replaces the overpotentials by an equivalent resistance  $R_{eq}$  and an equivalent overpotential  $\eta_{eq}$ . Together

with the relations that describe the vanadium and proton concentrations, they form the augmented and simplified electrochemical model. This model predicts the stack voltage  $U_{stack}$ , determines the concentrations in the tank  $c_{tank}$  and in the cells  $c_{cell}$ , and the state of charge  $SoC$  from the stack current  $I_{stack}$  and the electrolyte flowrate  $Q$ . The response time and its main limiting factors were also briefly discussed.

In a second part, important notions such as the energy density and the battery efficiencies were introduced and commented. Indeed, the comparison of batteries has always been a source of confusion and therefore requires clear definitions of how the efficiencies are determined. We have introduced three main definitions: the energy efficiency  $\eta_{energy}$ , the coulombic efficiency  $\eta_{coulombic}$  and the voltage efficiency  $\eta_{voltage}$ .

In the third part of this chapter, the augmented electrochemical model was used to predict the behaviour of a 1.5 kW, 10 h VRB in a small stand alone system composed of a photovoltaic source and a small household over a 24 h period. The model determines the power exchanged with the battery from the power profiles of the source and the load; then it calculates the stack voltage  $U_{stack}$  and the stack current  $I_{stack}$ . Other internal variables such as the vanadium and proton concentrations, the internal losses, and the state of charge are also determined.

In order to accurately determine the battery efficiencies, we have performed a series of charge and discharge cycles at constant current and at constant power. The simulated results were commented and successfully compared to experimental data. Indeed, a good concordance between the model and the experimental battery was found. Finally, the effect of the efficiency on the power density was also discussed.

Then, the effect of the operating conditions on the battery, in particular on the stack voltage, the stack power and the internal losses were discussed and illustrated.

In conclusion, this chapter has proposed an electrochemical model that accurately describes the electrochemical behaviour of the stack; but this model still misses an important feature: the description of the mechanical loss required to flow the electrolyte from the tank to the stack. In the next chapters, we will investigate the electrolyte properties and introduce a mechanical model based on the fluid mechanics.



# Electrolyte Properties

---

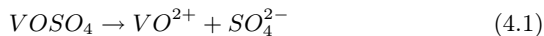
## 4.1. Introduction

In the first part of this work, we have established the electrochemical model of the VRB (see chapters 2 and 3); in order to have an overall model of the VRB storage system, we still need to propose a mechanical model of the electrolyte circuit. The principle aim of this mechanical model is to determine the power required to flow the electrolyte. But before we apply the fluid mechanics to the VRB in the next chapter and then assemble the overall multiphysics model in chapter 6, we will introduce in this brief chapter some important properties of the electrolyte: the density and the viscosity.

So, we will start this chapter with a short description of how to prepare the electrolyte from the preparation of a vanadyl sulphate solution to its electrolysis; the electrolysis then leads to the formation of the desired electrolyte solution. Thereafter, we will discuss the density and the viscosity: both are important variables of the mechanical model. Therefore, we will describe the characteristics of  $V^{2+}$ ,  $V^{3+}$ ,  $V^{4+}$  and  $V^{5+}$  solutions. Moreover, the effect of the temperature and the sulphuric acid concentration will also be commented. Finally, empirical models that predict the density and the viscosity as a function of the concentrations and the temperature will be presented.

## 4.2. Electrolyte Preparation

In this section, we introduce a method to prepare the electrolytic solutions; this method is based on the electrolysis of a vanadyl sulphate  $VOSO_4$  solution. This solution is obtained from the dissolution of  $VOSO_4$ :



The electrolysis reaction occurs in an electrolytic cell; this cell is composed of two compartments separated by a cation exchange membrane (Nafion for example). In addition, two electrodes are also immersed into the solutions as it is illustrated in Fig. 4.1. The nitrogen  $N_2$  minimises the contact with oxygen present in the atmosphere and prevents the oxidation of the  $V^{2+}$  solution.

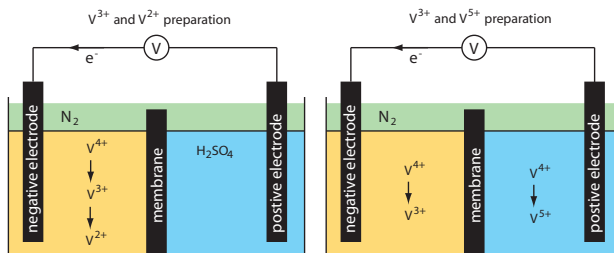
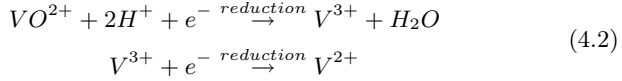


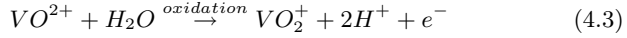
Figure 4.1.: Illustration of an electrolysis cell. The left cell presents the setup to obtain the  $V^{2+}$  and  $V^{3+}$  solutions from a vanadyl sulphate solution and the right cell presents how to obtain  $V^{5+}$  and  $V^{3+}$  solutions.

So the catholyte is obtained from an electrolytic oxidation of the  $VOSO_4$  solution and the anolyte from an electrolytic reduction. In more detail, the  $V^{2+}$  and  $V^{3+}$  solutions are obtained by placing the vanadyl sulphate solution into the negative compartment of the electrolysis cell (Fig. 4.1) and filling the positive compartment with a sulphuric acid solution with a sulphate concentration equivalent to the vanadium concentration in the negative compartment. These anolytic solutions are obtained from the

following electrolytic reduction [73]:

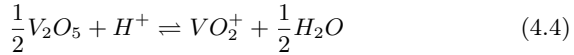


And to obtain the  $V^{5+}$  solution, both compartments are filled with the  $VOSO_4$  solution and an electrical current is applied to the electrodes; the electrolytic oxidation in the positive compartment produces the  $V^{5+}$  solution (4.3) and  $V^{3+}$  as a by-product in the negative compartment. In that case, the oxidation reaction is:



Note that a battery filled with  $V^{3+}$  and  $V^{5+}$  is not a functioning battery as they correspond respectively to a discharged and charged state; for example, a charged battery contains  $V^{2+}$  and  $V^{5+}$  solutions.

Of course, there are other ways to produce the electrolytes: for example, a  $V^{5+}$  solution is obtained from the dissolution of vanadium pentoxide  $V_2O_5$  into a sulphuric acid solution as described by the following relation:



### Reaction time

From Faraday's law (section 3.2.1), we quickly determine the time  $t$  necessary to perform the complete reaction:

$$t = \frac{c_V V n F}{I} \quad [s] \quad (4.5)$$

where:	$c_V$	=	vanadium concentration	$[M]$
	$V$	=	electrolyte volume	$[m^3]$
	$n$	=	number of electrons involved in the reaction	$[-]$
	$I$	=	constant current	$[A]$

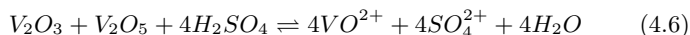
### 4.3. DENSITY

Name	molar mass [g/mol]	density [g/cm <sup>3</sup> ]
<i>V</i>	50.94	6.11
<i>VO</i>	66.94	5.76
<i>V<sub>2</sub>O<sub>3</sub></i>	149.88	4.87
<i>V<sub>2</sub>O<sub>5</sub></i>	181.88	3.35
<i>H<sub>2</sub>SO<sub>4</sub></i>	98.08	1.00 (0.5%) - 1.83 (100%)
<i>H<sub>2</sub>O</i>	18.02	1.00

Table 4.1.: Molar mass and density of diverse materials. For the sulphuric acid, the numbers in brackets are the mass of solute divided by the total mass of solution [43, 70].

#### Vanadyl Sulphate Solution Preparation

To conclude this section about the electrolyte preparation, we present here the preparation of the vanadyl sulphate solution; it is prepared by reacting a mixture of vanadium trioxide  $V_2O_3$  and vanadium pentoxide  $V_2O_5$  in a dilute sulphuric acid solution. The reaction is given by the following equation:



### 4.3. Density

In this section, we will discuss the electrolyte density; the density  $\rho$  of a fluid is simply defined as the ratio of its mass to its volume. It is one of the most basic properties of the material that indicates its inertia or resistance to an accelerating force [84]. We can relate the density to the attraction forces between the particles and their three dimensional arrangement in space. Hence, the density of the electrolytic solution depends on the force between the constituent of the solution, namely the water molecules and the solute molecules [73].

In Tab. 4.1 we give the molar mass and the density of some materials found in the electrolyte or necessary to its preparation. Although they are not used in the rest of this work, they give an order of magnitude of their individual contribution to the overall density.

### 4.3.1. Density of $V^{2+}$ and $V^{3+}$ Solutions

In this section, we will discuss the dependence of the density upon the composition of the electrolyte, in particular upon its vanadium concentrations and upon the total sulphate concentration: the density is related to the attraction forces between these particles and the water molecules. We will also see that the temperature has an influence on the density. All these effects are illustrated with  $V^{2+}$  and  $V^{3+}$  solutions; the density of  $V^{4+}$  and  $V^{5+}$  solutions will be discussed in section 4.3.4.

In Fig. 4.2, experimental densities are presented as a function of the vanadium concentration; these experimental data are from the work of A. Mousa [73]. The electrolyte solutions are either composed of  $V^{2+}$  or  $V^{3+}$  diluted in a 2 M solution of sulphuric acid  $H_2SO_4$ . We clearly see that the density increases with the vanadium concentration: in fact, the  $V^{3+}$  solution increases at a faster pace than the  $V^{2+}$  solution. Although the  $V^{2+}$  density is slightly smaller, the difference stays below 6% at vanadium concentration below 2 M.

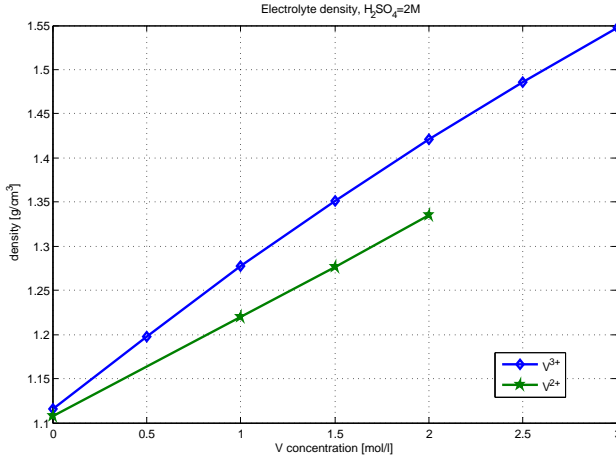


Figure 4.2.: Density of  $V^{2+}$  and  $V^{3+}$  electrolytes, in each case, the  $H_2SO_4$  concentration is 2 M at 25 °C. Experimental data are from [73].

### 4.3.2. Influence of the Sulphuric Acid Concentration and of the Temperature

We have seen in Fig. 4.2 that the density depends upon the vanadium concentration, but the sulphuric acid concentration and the temperature have also an influence on the density as it can be seen in Fig. 4.3. Indeed, the density increases with the  $H_2SO_4$  concentration, but its influence tends to decrease as the vanadium concentration increases: the vanadium concentration has a greater effect on the solution density than the  $H_2SO_4$  concentration.

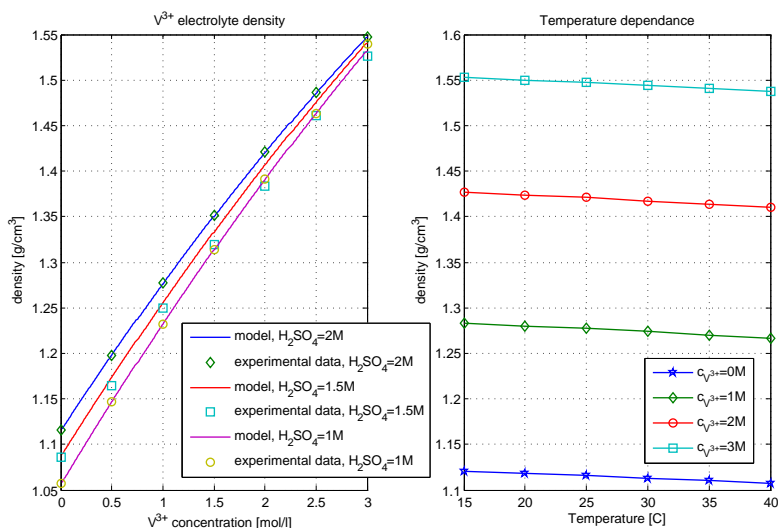


Figure 4.3.: Left: Experimental and simulated with the empirical relation (4.7) density of a  $V^{3+}$  solution as a function of the  $V^{3+}$  and  $H_2SO_4$  concentrations. Right: temperature dependence of the electrolyte density, the sulphuric acid concentration is  $c_{H_2SO_4} = 2$  M. Experimental data are from [73].

We know that many properties of matter change with the temperature [85]: the density is one among them. Indeed, when the temperature in-

Coefficient	Value	unit
A	1.00320	$\text{g}/\text{cm}^3$
B	0.08822	$\text{g}/\text{Mcm}^3$
C	0.00256	$\text{g}/\text{M}^2\text{cm}^3$
D	0.07363	$\text{g}/\text{Mcm}^3$
E	-0.00491	$\text{g}/\text{M}^2\text{cm}^3$
F	-0.00061	$\text{g}/\text{cm}^3$

Table 4.2.: Empirical coefficients for the equation (4.7) [73].

creases, the energy of the molecules, and their motions, increases too. Thus, most materials expand when their temperature increases<sup>1</sup>; in consequence, their density decreases. The density of a  $V^{3+}$  solution is illustrated in Fig. 4.3 as a function of the temperature; the density tends to decrease gently with the temperature: the slope is approximately  $-0.0006 \text{ g}/\text{cm}^3\text{K}$ .

#### 4.3.3. Empirical Model

The density depends on the attraction force between the particles and their arrangement in space; these complex relations depend themselves on the vanadium and sulphuric acid concentrations and on the temperature. A Mousa has proposed in [73] an empirical model for the density of the  $V^{3+}$  solution; this model is based on experimental data and employs empirical coefficients given in Tab. 4.2:

$$\rho = A + Bc_{V^{3+}} + Cc_{V^{3+}}^2 + Dc_{SO_4^{2-}} + Ec_{SO_4^{2-}}^2 + FT \quad [g/cm^3] \quad (4.7)$$

where A, B, C, D, E and F are empirical coefficients given in Tab. 4.2 and T is the temperature.

In Fig. 4.3, the empirical model (4.7) is shown and compared to the experimental data; the correlation between them is well within the experimental errors, the maximal difference being below 2%. It is expected that a similar empirical model should be applicable to other vanadium solutions if a sufficient amount of experimental data is available to determine the value of the empirical coefficients.

<sup>1</sup>Most materials expand when their temperature is raised, but not all. Water, for example, contracts with an increase in temperature in the range of 0 to 4°C [85].

#### 4.3.4. Density of $V^{4+}$ and $V^{5+}$ Solutions

Although no extensive study of the density of  $V^{4+}$  and  $V^{5+}$  solutions have been found in the literature, we expect their densities to react in a similar manner as the  $V^{2+}$  and  $V^{3+}$  solutions to a change in temperature and/or concentrations. Densities of 1.2 to 1.5 g/cm<sup>3</sup> for the  $V^{4+}$  and  $V^{5+}$  solutions have been reported by G. Oriji and al. who have investigated their properties. They have used vanadium concentrations ranging from 1 to 2 M and sulphuric acid concentrations ranging from 1 to 9 M [86]. The densities discussed in this section are all in the same order of magnitude; the effects of the density on the flow of the electrolyte will be discussed in the next chapter 5.

#### 4.4. Viscosity

Viscosity is also an important property that describes the *fluidity* of a fluid; it is a measure of its ability to resist deformation under shear stress. The viscosity is due to intermolecular attractions and may be thought of as internal friction between the molecules [5, 87]. The value of viscosity depends on the particular fluid and is often strongly affected by the temperature, decreasing rapidly when the temperature increases. For Newtonian fluids, the dynamic viscosity<sup>2</sup> is the ratio of the shearing stress  $\tau$  to the rate of shear strain (velocity gradient) [84]:

$$\tau = \mu \frac{dv}{dy} \quad [N/m^2] \quad (4.8)$$

The viscosity of a fluid might also be expressed as a kinematic viscosity, in that case, it is defined as the ratio of its dynamic viscosity to its density  $\rho$ :

$$\nu = \frac{\mu}{\rho} \quad [m^2/s] \quad (4.9)$$

But the usefulness of the viscosity is not limited to the VRB fluid mechanics that will be discussed in the next chapter 5, it also plays an important role in the kinetics of the electrochemical reaction. Indeed, when the viscosity becomes too high, the concentration overpotential increases, leading to a deterioration of the electrochemical performance [88]. Therefore,

---

<sup>2</sup>The SI unit for the dynamic viscosity is  $\frac{Ns}{m^2}$  or  $Pa \cdot s$ , but the centipoise (cP) is still commonly used.  $1cP = 1mPa \cdot s$



an optimal composition of the electrolyte has to be found that satisfies the need of a high energy density and good electrode reaction kinetics.

In the third part of this chapter, we will discuss in detail the viscosities of  $V^{2+}$ ,  $V^{3+}$ ,  $V^{4+}$  and  $V^{5+}$  solutions; as it was the case for the density, we will see that the viscosity depends on the vanadium concentration, the sulphuric acid concentration and on the temperature. We will also present an empirical model that describes the viscosity, and then discuss the influence of the concentrations and the temperature. In Tab. 4.3, we present the viscosity of some common liquids in order to have a point of comparison.

Name	viscosity $\mu$ [ $mPa \cdot s$ ]
Sulphuric acid	1.01 (0.1%) - 5.92 (60%)
Water	1.00
Gasoline	0.31
SAE 30 oil	380
Glycerine	1500

Table 4.3.: Viscosity of some common liquids at 20°C . For the sulphuric acid, the numbers in brackets are the mass of solute divided by the total mass of solution. For the gasoline and the oil, the viscosity may vary due to variation of the petroleum properties; for these two liquids, the values are given at 15.6°C . Sources: [70, 87].

#### 4.4.1. Viscosity of $V^{2+}$ and $V^{3+}$ Solutions

In a solution, the molecules are closely spaced, with strong cohesive forces between them, and the resistance to relative motion between adjacent layers of fluid is related to these intermolecular forces [87]. Hence, the VRB viscosity depends on the composition of the electrolyte. Today, no general analytical description of the viscosity of a given solution has been established, therefore the viscosity is still experimentally measured with a viscometer. Then, an empirical model of a particular solution can be built based on the experimental data.

In Fig. 4.4, we see that the viscosity of  $V^{2+}$  and  $V^{3+}$  solutions increases exponentially with the vanadium concentration. However, the  $V^{3+}$  solu-

## 4.4. VISCOSITY

tion is more sensible to the vanadium concentration than the  $V^{2+}$  solution. This reflects the difference in the behaviour of the  $V^{2+}$  and  $V^{3+}$  ions in the sulphuric acid solutions, in particular in the degree of ion pairing [73].

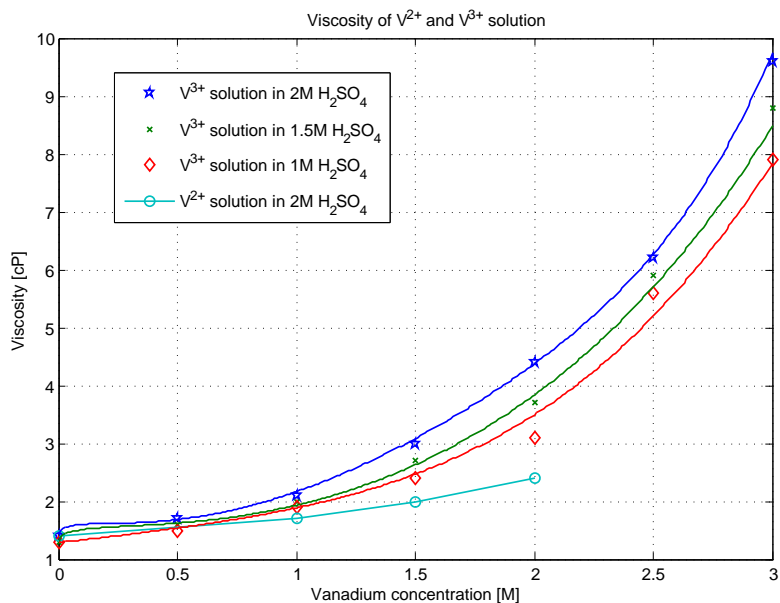


Figure 4.4.: Vanadium  $V^{2+}$  and  $V^{3+}$  at  $25^\circ\text{C}$ . For the  $V^{3+}$  solution, the continuous lines represent the value of the empirical model. Experimental data are from [73].

### 4.4.2. Viscosity of $V^{4+}$ and $V^{5+}$ Solutions

The viscosity of  $V^{4+}$  and  $V^{5+}$  solutions are presented in Fig. 4.5. As it was the case for the analytic solution, the viscosity increases exponentially with the vanadium concentration. Note that the  $V^{4+}$  viscosity is the kinematic viscosity ( $\text{mm}^2/\text{s}$ ) and that the dynamic viscosity (cP) can be retrieved with the solution density and (4.9).

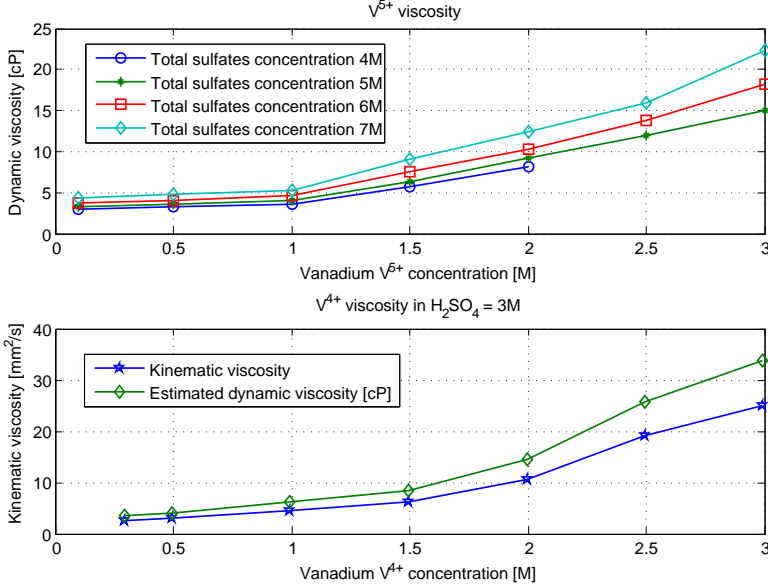


Figure 4.5.: On top: dynamic viscosity of vanadium  $V^{5+}$  solutions (0.1 to 3 M) in 4-7 M total sulphate concentrations at 20°C . Experimental data are from [89]. Below: kinematic viscosity and the corresponding estimated dynamic viscosity of vanadium  $V^{4+}$  solution (0.25 to 3 M) in a 3 M  $H_2SO_4$  solution at 20°C . Experimental data are from [88].

The  $V^{4+}$  solution has a greater viscosity than the  $V^{5+}$  solution and tends to increase faster at high vanadium concentration. As for the  $V^{3+}$  solution, the ions pairing seems to play a role in the increase of the viscosity, other causes might be the increase in ion size, a higher size to charge ratio and finally the effect of solute on the water [89].

#### 4.4.3. Empirical Model

Although attempts to fit the viscosity to polynomial equations usually show good results, these models are empirical and have no theoretical

#### 4.4. VISCOSITY

Coefficient	in 2M $H_2SO_4$	in 1.5M $H_2SO_4$	in 1M $H_2SO_4$	unit
A	0.8388	0.7818	-0.0585	$1/\sqrt{M}$
B	-1.3246	-0.8969	0.4503	$1/M$
D	1.1300	0.5737	-0.0266	$1/M^2$
E	-0.0969	0.0286	0.0866	$1/\sqrt{M^7}$
F	0.0013	0.0002	-0.00001	$1/M^7$

Table 4.4.: Empirical coefficients for the  $V^{3+}$  solution for the equation (4.10) at 25°C [73].

basis [73, 90]. An empirical model based on the Jones and Dole model has been proposed by A. Mousa:

$$\mu_r = \frac{\mu}{\mu_0} = 1 + A\sqrt{c} + Bc + Dc^2 + E\sqrt{c^7} + Fc^7 \quad [cP] \quad (4.10)$$

where:

$\mu_r$	=	relative viscosity	$[-]$
$\mu$	=	solution viscosity	$[cP]$
$\mu_0$	=	solvent viscosity	$[cP]$
$c$	=	vanadium concentration	$[mol/l]$
$X$	=	empirical coefficients, values for the $V^{3+}$ solution are given in Tab. 4.4	$[N.A.]$

The  $A$  coefficient is related to the ion-ion interaction and is a function of the charge and mobility of the ions and the  $B$  coefficient is related to the ion charge and size. No physical meanings have been reported for the others coefficients so far [73, 90]. Even if the model describes correctly the value of the viscosity, the empirical coefficients are dependent on the particular conditions (temperature, acid concentration). For example, Tab. 4.4 gives the coefficients for the  $V^{3+}$  solution for three sulphuric acid concentrations at 25°C .

In Fig. 4.4, we can visually compare the model to the experimental data and observe a good concordance. The difference between the model and the experimental data stays below 11.5% and its average value is around 2.6%. Note that this model is also applicable to the other vanadium solutions.

#### 4.4.4. Effect of the Temperature

In the introduction of this section, we have stated that the viscosity is strongly affected by the temperature; we verify here that it is also the case for the VRB electrolyte. The viscosity of the  $V^{3+}$  solution is shown in Fig. 4.6 at various temperature. We clearly see that the viscosity decreases as the temperature increases. This change is explained by the increase in the kinetic energy of the molecules that results in a reduction of the cohesive forces between the molecules and in consequence, the resistance against the flow is reduced. The Andrade equation is useful for the extrapolation of the viscosities at various temperatures for the same concentrations [73, 90]:

$$\mu = A \exp \frac{E_a}{RT} \quad [Ns/m^2] \quad (4.11)$$

where:	$A$	=	empirical parameter	$[Ns/m^2]$
	$E_a$	=	activation energy	$[J/mol]$

After the Arrhenius equation (2.49), S. Arrhenius makes here a second contribution to this work with the Arrhenius plot (Fig. 4.6) which is useful to determine the values of  $A$  and  $E_a$ : the  $A$  coefficient comes from the intersection with the y-axis and the activation energy  $E_a$  is given by the slope. These values depend on the vanadium and sulphuric acid concentrations.

#### 4.4.5. Effect of the Sulphuric Acid Concentration

Finally, we observe the effect of the sulphuric acid  $H_2SO_4$  concentration on the viscosity specifically in Fig. 4.7, but this might also be observed in Fig. 4.4 and 4.5. The viscosity increases exponentially with the sulphuric acid concentration, although the rate depends on the solute and its concentration. This observation confirms our previous statement that the viscosity is strongly related to the interactions between the ions dissolved in the solution.

### 4.5. Electrolyte Stability

We conclude this chapter with a discussion on an important property: the electrolyte stability. Indeed, a battery will lose some of its storage capac-

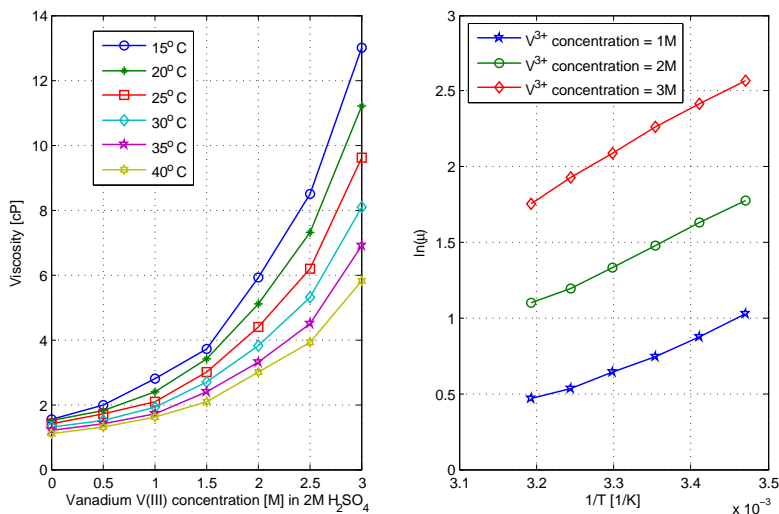


Figure 4.6.: Left: effect of the temperature on a vanadium  $V^{3+}$  (0 to 1.5 M) solution in 2 M total sulphates at various temperatures (15-40°C ). Right: Arrhenius plot for the  $V^{3+}$  viscosity. Experimental data are from [73].

ity if its electrolyte becomes degraded; the degradation of the electrolyte occurs when some vanadium ions undergo a thermal precipitation. For example, it has been stated in [73] that 2 M vanadium solutions are capable of maintaining an energy density of 25 Wh/kg at a temperature range of 10 to 35°C .

The stability depends on the temperature, the vanadium concentrations, the sulphuric acid  $H_2SO_4$  concentration and on the state of charge. In the catholyte, precipitations are observed when the fully charged electrolyte (100%  $V^{5+}$ ) is maintained at elevated temperatures for extended period. For example, it will take 7 days for a slight precipitate to appear in a solution of 2 M of vanadium and 3 M of  $H_2SO_4$  at a *SoC* of 1, but no precipitation is observed after 18 days at a *SoC* of 0.9 [91]. The precipitation

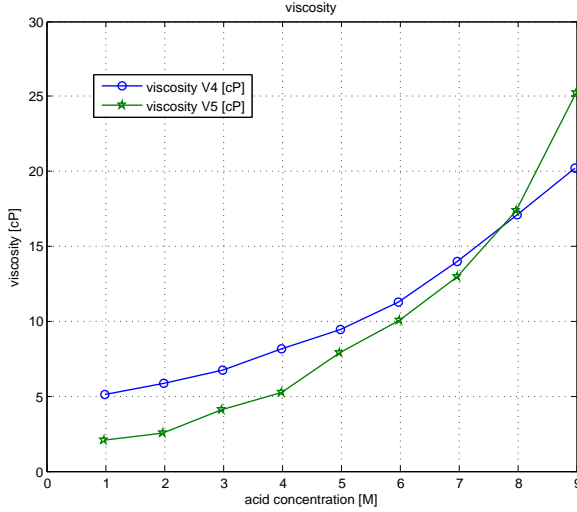
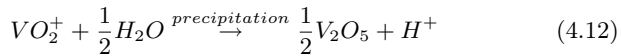


Figure 4.7.: Effect of the sulphuric acid concentration on the  $V^{4+}$  and  $V^{5+}$  solutions at  $25^{\circ}\text{C}$ . Experimental data are from [86].

reaction for the catholyte is:



Fortunately, the precipitation of  $V^{5+}$  is not irreversible because the  $V^{5+}$  precipitates are readily redissolved when the battery is discharged. Furthermore, a higher temperature range is achievable when the vanadium concentration is lowered, but this would lead to a significant decrease in the energy density.

The low temperatures also decrease the solubility:  $V^{4+}$ ,  $V^{3+}$  and  $V^{2+}$  sulphates start to precipitate at temperature lower than  $10^{\circ}\text{C}$  in solution containing 2 M of vanadium [92]. Furthermore, these temperatures also slow the rates of the reactions at the electrodes; operation at  $0^{\circ}\text{C}$  could result in significantly slower reaction rates, possibly around 3 to 5 times slower [93].

Some works have been done to increase the stability of the electrolyte either with the addition of precipitation inhibitors or with a heat treatment of the electrolyte. Potassium triphosphate and sodium hexametaphosphates were reported to be effective precipitation inhibitors for both  $V^{4+}$  and  $V^{5+}$  solutions, whereas ammonium sulphate and ammonium phosphate were reported to provide precipitation inhibition for  $V^{2+}$ ,  $V^{3+}$ ,  $V^{4+}$  and  $V^{5+}$  solutions [73, 89]. The exact mechanism through which additives enhance the stability is not fully understood; the additives can be classified into three categories: dispersion, complexing and threshold agents. Dispersion agents decrease the strength of the attraction forces between the particles, thereby reducing the chance of agglomeration, complexing agents form new complexes with one of the ions involved in the precipitation, thus reducing the ion activity and enhancing the stability and the threshold agents inhibit the precipitation of a certain compound [73].

The heat treatment boils the electrolyte for a few hours to remove the impurities; thus removing the nucleation sites that promote the precipitation process. For example, the thermal treatment of  $V^{2+}$  solutions presented in [73] heats the electrolyte at 55°C during 16 h. The stability can be further increased if the thermal treatment is repeated up to three times.

## 4.6. Summary and Outlook

At the beginning of this chapter, we have presented a method to prepare the electrolyte from a vanadyl sulphate solution; the electrolyte is either obtained from an electrolytic oxidation or an electrolytic reduction. Then we have introduced two important properties of the electrolyte: the density and the viscosity. Both properties are important parameters in the next chapter 5 where fluid mechanics is applied to the VRB.

We have presented the densities and the viscosities of  $V^{2+}$ ,  $V^{3+}$ ,  $V^{4+}$  and  $V^{5+}$  solutions and discussed the influence of the vanadium concentrations, the sulphuric acid concentration and the temperature. We have also introduced empirical models that describe the density and the viscosity as a function of the concentrations under specific conditions.

The solutions discussed in sections 4.3 and 4.4 contain only one vanadium species, either  $V^{2+}$ ,  $V^{3+}$ ,  $V^{4+}$  or  $V^{5+}$ : these conditions corresponds to a battery either fully charged or fully discharged. Thus for a given electrolyte, we know the density and the viscosity at the charged and dis-



charged states; but we do not know how they change in between (Fig. 4.8). In a first approximation, we might consider that they change linearly, but this is not necessarily the case. It will be very interesting to investigate further, especially the behaviour of the viscosity that has a greater influence on the fluid mechanics (see chapter 5).

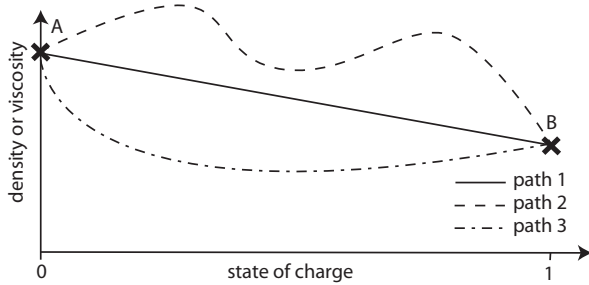


Figure 4.8.: Possible paths between the two known values, points *A* and *B*, of the viscosity or the density. Note that when the state of charge is 0 or 1, the concentration of one vanadium species is zero and the other is maximal (2.45), thus corresponding to the conditions of the electrolyte discussed in this chapter.

Finally, we have briefly discussed the stability of the electrolyte which depends on the composition of the electrolyte and its temperature. The stability is enhanced when the battery operates in optimal conditions: reduced thermal and *SoC* ranges have a positive effect on the stability. Furthermore, additives might be added to the electrolyte to improve the stability; a thermal treatment of the electrolyte also improves the stability.



# Fluid Mechanics Applied to the Vanadium Redox Flow Batteries

---

## 5.1. Introduction

This fifth chapter is dedicated to the mechanical aspect of the VRB modeling. Indeed, the mechanical power required to flow the electrolyte constitutes in fact a mechanical loss in the overall battery efficiency. In order to determine the performance, it is necessary to model the hydraulic circuit of the electrolyte; hence, the mechanical loss can be estimated under any operating conditions. We have discussed in the previous chapter the mechanical properties of the electrolyte: the density and the viscosity. These two parameters are important in the fluid mechanics of the VRB.

In a first part, we will briefly introduce the mechanical construction of the stack. There are two ways to flow the electrolyte throughout the stack: serial and parallel flows. We will also present the decomposition of the stack into single cells; these cells are made of bipolar and/or end plates, carbon felt electrodes and a membrane. The cells are then piled up to form a stack.

Then, we will propose an analytical model of the hydraulic circuit; unfortunately, the stack geometry is too complex to be analytically described and is therefore the subject of a later section. First, we will introduce some important generalities and principles about fluid mechanics: the

Reynolds number that determines the flow regime, the Bernoulli's principle that leads to the Bernoulli's equation, an expression of the law of energy conservation, the first law of thermodynamics that leads to the extended Bernoulli's equation from which the pressure drop is obtained, the head loss due to friction, and the minor losses that represent the head loss in bends, valves, etc.

The analytical model determines accurately the mechanical losses in the pipes, valves and in the tanks, but does not take into account the losses occurring in the stack. Therefore, a numerical approach is proposed to determine these losses; this approach will lead to the stack numerical model. This hydraulic model is based on a finite element method (FEM); but the analysis of some large stacks are very long, sometimes it takes weeks or months to obtain a result. Therefore, we propose an original method based on an analogy with the Ohm's law; this method determines a flow resistance from which the pressure drop across the stack is instantly obtained as a function of the flowrate.

To determine the stack flow resistance, we have divided it into smaller basic parts that are then reassembled to form a stack of any dimensions. This method is very fast compared to the FEM simulation of a complete stack and gives very good results. We will conclude this fourth part with a small discussion about the effects of the density and the viscosity on the flow resistance. Finally, we will summarize the principles and relations introduced in this chapter into an overall mechanical model of the VRB.

## 5.2. Construction of a Stack

Before we address the general principles of fluid mechanics, we introduce here a few notions about the construction of a stack. There are two main ways to flow the electrolyte throughout the cells: in series or in parallel. In Fig. 5.1, we can observe that the whole flow passes from one cell to the next in the serial connection; in a parallel topology, the flow is divided between the cells.

The intrinsic advantage of the serial topology is the limited leakage current  $I_{leak}$ , also called bypass current, flowing in the electrolyte. Indeed,  $I_{leak}$  can only flow between two adjacent cells; hence, the bypass potential  $U_{bypass}$  is limited to the potential of a single cell. On the contrary in a

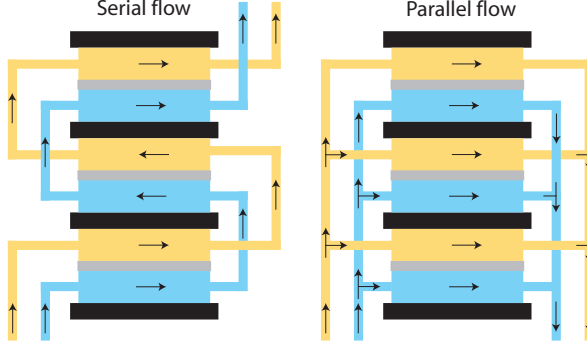


Figure 5.1.: Schematics of the electrolyte flow path. Left: serial flow path. Right: parallel flow path.

parallel flow, the leakage current might flow in between any cells<sup>1</sup>; in the worst case, the maximal bypass potential is the stack voltage  $U_{stack}$ .

But in a serial configuration, more power is needed to flow the electrolyte because each cell must sustain the whole flowrate  $Q$ ; on the contrary,  $Q$  is divided between the cells in the parallel configuration. We will see throughout the rest of this chapter (for example in sections 5.3.1 and 5.5.1) that the pressure drop  $\Delta p$ , and in consequence the power required to flow the electrolyte, is at least proportional to  $Q$ .

Note that the cell concentration  $c_{cell}$  as it was defined in section 3.2.2 is not valid as it is for the serial topology<sup>2</sup>. Indeed, the vanadium concentration changes from cell to cell as the active species are consumed; therefore, we must determine individually  $c_{cell}$ : the output concentration  $c_{out}$  of a cell being the input concentration  $c_{in}$  of the next cell. Thus, the cell voltage  $U_{cell}$  is not uniformly distributed inside the stack; in some case, this might lead to degraded operating conditions.

In this work, we have chosen the parallel topology for its advantages; it is also the conventional topology for the majority of VRB. In Fig. 5.2,

<sup>1</sup>A common technique to reduce the leakage current is to lengthen the electrolyte path in between the cell: this increases the ionic resistance  $R_{ionic}$  and thus diminishes the leakage current.

<sup>2</sup>But the cell concentration for the serial topology can easily be derived from the relations introduced in sections 3.2.1 and 3.2.2.

## 5.2. CONSTRUCTION OF A STACK

we present the decomposition of a stack; a cell is always composed of a *bipolar or end plate - carbon felt electrode - membrane - carbon felt electrode - bipolar or end plates*. The cells are then piled up to form a stack; two adjacent cells share a common bipolar plate; the bipolar and end plate are electrical conductors. To flow the electrolyte through the cell, channels have been drilled into the bipolar plates (Fig. 5.2), but other designs are possible: for example, flow frames and bipolar electrodes are used in the stack presented in [76]. Important issues are the prevention of electrolyte leakage or cross mixing and electrical isolation of the bipolar plates.

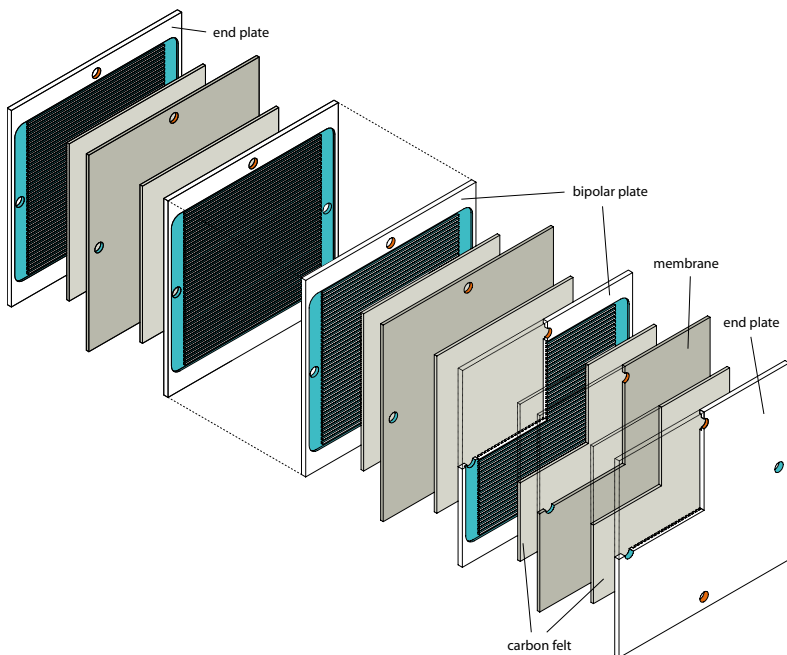


Figure 5.2.: View of the different components composing a VRB stack. The surfaces in contact with the catholyte are coloured in blue and in orange for the anolyte.

### 5.3. Generalities about Fluid Mechanics

The mechanical model developed in this chapter is composed of an analytical part that models the pipes, bends, valves and tanks and a numerical part that describes the more complex stack hydraulic circuit. We start this section with some generalities about fluid mechanics; the relations introduced are necessary to build the analytical part of the mechanical model.

To determine the power required to flow the electrolyte, we must first determine if this flow is laminar or turbulent; the Reynolds number is a famous criterion to distinguish this. Then, we will develop the Bernoulli's principle, a relation applicable only to steady and laminar flow with an incompressible and inviscid fluid, into the more general extended Bernoulli's equation; this equation includes the friction loss created by a laminar or turbulent flow, the minor losses that occur in bends, elbows, valves, etc., and the work done on the system by a mechanical machine. Evidently, we will also introduce the relations that describe the friction loss  $E_f$ , the minor loss  $E_m$  and the mechanical work  $W_{th}$ .

We will conclude this section with a short discussion about the pump power and its efficiency.

#### 5.3.1. Reynolds Number

The Reynolds number  $Re$  is undoubtedly the most famous dimensionless parameter in fluid mechanics. It is named in honour of Osborne Reynolds (1842-1912), a British engineer who first demonstrated that this combination of variables could be used as a criterion to distinguish between laminar and turbulent flow [87].

The Reynolds number is the ratio of inertial forces to viscous forces and is obtained from a combination of the geometrical characteristics of the conduit, the fluid flowrate and its properties:

$$Re = \frac{\rho V_s D}{\mu} = \frac{V_s D}{\nu} \quad [-] \quad (5.1)$$



Figure 5.3.: Osborne Reynolds 1842-1912 (source: [24]).

where:	$\rho$	=	density	$[kg/m^3]$
	$V_s$	=	fluid velocity	$[m/s]$
	$D$	=	characteristic length (equal to diameter if a cross-section is circular)	$[m]$
	$\mu$	=	(dynamic) viscosity	$[Ns/m^2]$
	$\nu$	=	kinematic viscosity	$[m^2/s]$

The Reynolds number is used to determine whether a flow will be laminar or turbulent: laminar flow occurs at low Reynolds numbers where viscous forces are dominant whereas turbulent flow occurs at large Reynolds numbers where viscous effects are small relatively to the inertial effects. Laminar flows are characterized by smooth, constant fluid motion whereas turbulent flows show an unsteady character which takes the form of eddies.

The laminar and turbulent regimes are separated by an intermediate regime: the transition regime where the flow is neither fully laminar nor fully turbulent. This regime occurs not at a specific Reynolds number but in a range which depends on the conduit configuration and must, in some case, be determined experimentally.

For example, it is generally accepted that a flow in a round pipe is laminar whenever the Reynolds number is below 2000 whereas it is usually turbulent at values greater than 4000. In the case of a horizontal pipe, the pressure gradient is directly proportional to the flowrate  $Q$  in the laminar regime and proportional to the square of the flowrate in the turbulent regime<sup>3</sup> [84]. This is summarized in Tab. 5.1.

---

<sup>3</sup>the exponent on  $Q$  depends on the roughness of the pipe (see Tab. 5.2).



Reynolds number $Re$	Flow regime	Pressure gradient $\Delta p$ proportional to
$< 2000$	laminar	$Q$
$2000 - 4000$	transition	variable
$> 4000$	turbulent	$Q^{1.8}$ to $Q^2$

Table 5.1.: Dependence of pipe flow regime and pressure gradient on Reynolds number [84]. Note that the proportionality between the pressure gradient and the flowrate is only applicable in the case of a horizontal pipe, in other case, the effect of gravity has to be taken into account.

### 5.3.2. Bernoulli's Principle

Bernoulli's principle, named in honour of the Swiss mathematician Daniel Bernoulli, applies to a steady and laminar flow, where the fluid is incompressible and inviscid, i.e. the viscosity is small enough to be ignored. In essence, this principle states that where the velocity of a fluid is high, the pressure is low, and where the velocity is low, the pressure is high [85].

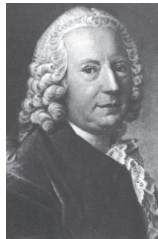


Figure 5.4.: Daniel Bernoulli 1700 - 1782 (source: [24]).

This leads to Bernoulli's equation, which is an expression of the law of energy conservation:

$$\frac{V_s^2}{2} + \frac{p}{\rho} + gz = \text{constant} \quad [m^2/s^2] \quad (5.2)$$

### 5.3. GENERALITIES ABOUT FLUID MECHANICS

---

where:	$g$	=	gravitational acceleration	$[m/s^2]$
	$z$	=	height	$[m]$
	$p$	=	pressure	$[Pa]$

Thus, in a general case where a fluid is flowing in a tube, as illustrated in Fig. 5.5, the velocities and pressures at both ends are related by:

$$\frac{V_{s,1}^2}{2} + \frac{p_1}{\rho} + gz_1 = \frac{V_{s,2}^2}{2} + \frac{p_2}{\rho} + gz_2 \quad [m^2/s^2] \quad (5.3)$$

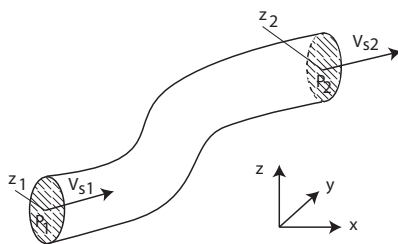


Figure 5.5.: General case of a fluid flowing in a tube.

#### 5.3.3. The First Law of Thermodynamics

The first law of thermodynamics is an expression of the law of conservation of energy and states that the change in internal energy of a closed system  $\Delta E_{int}$  is equal to the energy added to the system by heating minus the work done by the system. In its extended expression, it becomes for a system that has kinetic energy  $K$  and potential energy  $U_{en}$  [85]:

$$\Delta K + \Delta U_{en} + \Delta E_{int} = Q_{heat} + W \quad [J] \quad (5.4)$$

where:	$\Delta K$	=	change in kinetic energy	$[J]$
	$\Delta U_{en}$	=	change in potential energy	$[J]$
	$Q_{heat}$	=	heat added to the system	$[J]$
	$W$	=	work done to the system	$[J]$

In the case of an open system in steady state, for example the general case of Fig. 5.5, the first law can be expressed as [94]:

$$H_2 - H_1 + K_2 - K_1 + U_{en,2} - U_{en,1} = \Delta H + \Delta K + \Delta U_{en} = Q_{heat} + W \quad [J] \quad (5.5)$$

where  $\Delta H$  is the change in enthalpy. Then the kinetic energy  $K$ , potential energy  $U_{en}$  and enthalpy  $H$  are given by:

$$K = \frac{1}{2}mV_s^2, \quad U_{en} = mgz, \quad H = E_{int} + pV \quad [J] \quad (5.6)$$

where  $V$  is the volume. It is interesting to express these values per mass unit, the same unit as the Bernoulli equation (5.3):

$$k = \frac{1}{2}V_s^2, \quad u_{en} = gz, \quad h = e_{int} + \frac{p}{\rho} \quad [m^2/s^2] \quad (5.7)$$

Here, the internal energy refers to the thermal energy; in fact, the friction is a source of change in the internal energy. We can express the internal energy per mass unit  $e_{int}$  as a function of the specific heat capacity  $c$  and the temperature  $T$ :

$$e_{int} = cT \quad [m^2/s^2] \quad (5.8)$$

#### 5.3.4. The Extended Bernoulli's Equation

Often in practice, the viscosity is not negligible and creates friction loss  $E_f$  in the conduit; therefore, we should extend the Bernoulli equation (5.3) to include this loss. Furthermore, we should also include the minor losses  $E_m$  which occur in the bends and elbows or when the conduit is suddenly contracted or expanded, and the theoretical work done on the system  $W_{th}$  to impose the desired velocity and pressure [94]. We will discuss the friction loss  $E_f$  in the next section 5.3.5 and the minor losses  $E_m$  in section 5.3.6. Hence, we derive the extended Bernoulli equation from the Bernoulli equation (5.3) which becomes:

$$\frac{V_{s,1}^2}{2} + \frac{p_1}{\rho} + gz_1 - \frac{V_{s,2}^2}{2} - \frac{p_2}{\rho} - gz_2 = e_f + e_m - w_{th} \quad [m^2/s^2] \quad (5.9)$$

$$\begin{array}{lll}
 \text{where:} & e_f & = \text{friction loss per mass unit} & [m^2/s^2] \\
 & e_m & = \text{minor loss per mass unit} & [m^2/s^2] \\
 & w_{th} & = \text{theoretical work done on the system} & [m^2/s^2] \\
 & & \text{per mass unit} & 
 \end{array}$$

When we reformulate the expression of the first law of thermodynamics (5.5) and introduce (5.7) into it to express it per mass unit, we obtain:

$$\Delta e_{int} + \frac{\Delta p}{\rho} + \frac{\Delta V_s^2}{2} + g\Delta z = q_{heat} + w_{real} \quad [m^2/s^2] \quad (5.10)$$

$$\begin{array}{lll}
 \text{where:} & w_{real} & = \text{real work done on the system per} & [m^2/s^2] \\
 & & \text{mass unit} & \\
 & q_{heat} & = \text{heat transfer per mass unit} & [m^2/s^2]
 \end{array}$$

Since the efficiency of the pump is often around 80 to 90% [94], the real work  $W_{real}$  done on the system is always larger than the theoretical work  $W_{th}$  necessary to maintain the desired velocity and/or pressure; the difference in work  $W_{real} - W_{th}$  is transformed into heat. The rise of temperature  $\Delta T$  in the conduit is found by combining (5.9) and (5.10) with (5.8):

$$\Delta T = \frac{\Delta e_{int}}{c} = \frac{w_{real} - w_{th} + q_{heat} + e_f + e_m}{c} \quad [K] \quad (5.11)$$

In fluid dynamics, the hydraulic head is an important notion that defines either the energy dissipated through friction and turbulences or the energy brought to the system by the pump. These energies are expressed per weight unit; we can define three heads: the head losses due to friction  $h_f$ , the minor loss  $h_m$  and the work done on the system by the pump  $h_{w,th}$ . They are obtained when (5.9) is divided by the gravitational acceleration  $g$ :

$$\frac{V_{s,1}^2}{2g} + \frac{p_1}{\gamma} + z_1 - \frac{V_{s,2}^2}{2g} - \frac{p_2}{\gamma} - z_2 = h_f + h_m - h_{w,th} \quad [m^2/s^2] \quad (5.12)$$

where  $\gamma$  is the specific weight. Finally, in the general example of Fig. 5.5, the pressure drop  $\Delta p$  across the conduit is obtained by rearranging (5.12):

$$\Delta p = p_2 - p_1 = \gamma \left( h_{w,th} - \frac{\Delta V_s^2}{2g} - \Delta z - h_f - h_m \right) \quad [Pa] \quad (5.13)$$

### 5.3.5. Head Loss Due to Friction

The overall head loss for a hydraulic circuit consists of the head loss  $h_f$  due to viscous effect in the straight pipes and the head loss  $h_m$  in the various pipe components, often termed the minor loss [87]. We will introduce the head loss  $h_f$  due to friction in this section; we will see how it depends on the friction factor  $f$  which varies with the flowrate and depends on the flow regime: laminar or turbulent. The minor losses will be discussed in the next section.

The head loss due to friction  $h_f$  depends on the wall shear stress between the fluid and the conduit surface; it is obtained from the Darcy-Weisbach equation that determines its value  $h_{f,i}$  within a given segment of pipe:

$$h_{f,i} = f_i \frac{L_i}{D_i} \frac{V_{s,i}^2}{2g} \quad [m] \quad (5.14)$$

where:	$L$	$=$	length of the conduit	$[m]$
	$D$	$=$	diameter of the conduit	$[m]$
	$f$	$=$	friction factor	$[-]$

The total head loss due to the friction  $h_f$  in a hydraulic circuit (an example of hydraulic circuit is given in Fig. B.1) is the sum of each given segment of pipe  $h_{f,i}$ :

$$h_f = \sum h_{f,i} \quad [m] \quad (5.15)$$

### The Friction Factor

The friction factor is a dimensionless coefficient; Darcy and Nikuradse [94] have shown from experimental data that this factor depends mainly on the Reynolds number  $Re$  and on the relative roughness of the pipe wall  $\epsilon/D$ :

$$f = F(Re, \epsilon/D) \quad [-] \quad (5.16)$$

This factor can be evaluated from various empirical or theoretical relations that depend on the given geometry and on the conditions of the flow. Tab. 5.2 gives the value of the equivalent roughness  $\epsilon$  of some common new pipes.

pipe surface	$\epsilon$ [mm]
Plastic, glass, copper, lead	0
Commercial steel, wrought iron	0.05
Galvanized iron	0.15
Cast iron	0.25
Concrete	0.3-3

Table 5.2.: Equivalent roughness for new and clean pipes [84, 95].

### Laminar Flow

For a laminar flow ( $Re < 2000$ ), the friction factor is derived from the Poiseuille law [94] and does not vary with the roughness  $\epsilon$ . It is simply given by the following relation:

$$f_i = \frac{64}{Re_i} \quad [-] \quad (5.17)$$

### Turbulent Flow

For a turbulent flow in a smooth pipe ( $\epsilon = 0$ ), the friction factor  $f_i$  is obtained from the two following relations that depend on the Reynolds number  $Re$ . The Blasius equation is valid for Reynolds numbers in the 4000 - 10000 range:

$$f_i = 0.316 Re_i^{-1/4} \quad [-] \quad \text{for } 4000 < Re_i < 10000 \quad (5.18)$$

and the Von Karman and Nikuradze relation is applicable to Reynolds numbers greater than 10000:

$$\frac{1}{\sqrt{f_i}} = 2 \log(\sqrt{f_i} Re_i) - 0.8 \quad [-] \quad \text{for } 10000 < Re_i \quad (5.19)$$

In the case of turbulent flow in a rough pipe ( $\epsilon \neq 0$ ), the friction factor is given by the Colebrook equation that depends on the Reynolds number  $Re$  and on the relative roughness  $\epsilon/D$ :

$$\frac{1}{\sqrt{f_i}} = -2 \log \left( \frac{\epsilon_i}{3.7 D_i} + \frac{2.51}{Re_i \sqrt{f_i}} \right) \quad [-] \quad (5.20)$$

Finally, the friction factor for turbulent flow can also be obtained graphically from the Moody chart (Fig. 5.6).

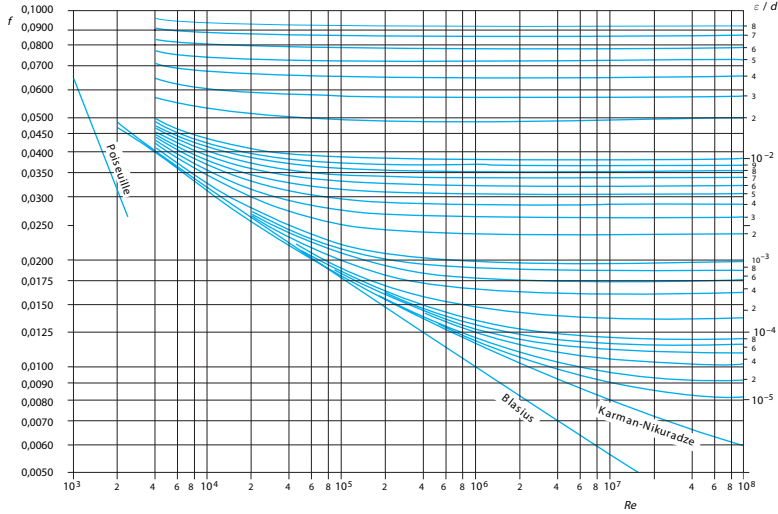


Figure 5.6.: Friction factor as a function of Reynolds number and relative roughness also known as the Moody chart [95].

### 5.3.6. Minor Losses

After the head losses  $h_f$  due to the viscous effects, the minor losses  $h_m$  are an important source of losses<sup>4</sup>; in the previous section, we have seen how the Darcy-Weisbach equation (5.14) enables the calculation of the head loss  $h_f$  in the straight sections of pipes as a function of the friction factor  $f$  and the flowrate  $Q$ . Here, we will see how to determine the minor losses  $h_m$ ; these losses occur in the components that connect the straight sections of pipe together: they might have the form of a bend, an elbow or a valve.

<sup>4</sup>The term *minor* loss is not always a wisely chosen name as it might become the largest source of loss when the system contains a large number of components and a relative short length of pipe.

But they also occur when the fluid flows from (or into) a reservoir into (from) a pipe or when the diameter of the pipe changes. We will discuss all of these cases in the following parts of this section. The total head loss  $h_m$  due to these various components is simply the sum of their individual contributions  $h_{m,i}$  [87, 94]:

$$h_m = \sum h_{m,i} \quad [m] \quad (5.21)$$

The minor losses  $h_{m,i}$  are described by a relation similar to the Darcy-Weisbach equation (5.14) where a loss coefficient  $k_L$  has been introduced to replace the friction factor  $f$ ; its value depends upon the geometry of the component. Hence the head loss  $h_{m,i}$  is given by:

$$h_{m,i} = k_{L,i} \frac{V_{s,i}^2}{2g} \quad [m] \quad (5.22)$$

#### Bends, Elbows and Tees

The most common components in the electrolyte circuit of a battery are the pipe fittings elements such as the elbows, the bends and the tees. Whenever the flow changes its direction, losses occur; their magnitude depends on the specific geometry of the component<sup>5</sup>. Some values of loss coefficients  $k_L$  are given in Tab. 5.3 for typical components; their values depend strongly on their shape. For example,  $k_L$  depends on whether the pipe joints are threaded or flanged. Practically, the loss coefficients  $k_L$  for such components are fairly independent of the pipe diameter  $D$ , the flowrate  $Q$  or the fluid properties [87].

#### Valves

The valves are also important elements of a flow battery; a minimal number is required for maintenance and security reasons, more sophisticated designs might include more valves to control precisely the flow. For example in a storage system composed of many stacks in parallel, an efficient control strategy might be to switch on only the minimal number of stacks required to satisfy the power need.

---

<sup>5</sup>Often, they are designed more for the ease of manufacturing and costs than to minimize the head loss [87].



Component	$k_L$ (flanged)	$k_L$ (threaded)
Regular 90° elbow	0.3	1.5
Long radius 90° elbow	0.2	0.7
Long radius 45° elbow	0.2	
Regular 45° elbow		0.4
180° return bend	0.2	1.5
Line flow tee	0.2	0.9
Branch flow tee	1	2

Table 5.3.: Loss coefficient  $k_L$  for diverse bends and elbows [87].

Similarly to the bends and elbows, the loss coefficient  $k_L$  of a valve depends on its geometry; typical loss coefficients are given in Tab. 5.4. Although the valves might control the flowrate  $Q$  by providing a means to adjust the overall system loss coefficient to the desired coefficient, we only consider here the fully open valve. Indeed, since we want to enhance the battery performance, it is not acceptable to control the flowrate with the system loss; hence the valves are only employed to open or close a section of pipe.

Component	$k_L$
Globe valve, fully open	10
Gate valve, fully open	0.15

Table 5.4.: Loss coefficient  $k_L$  for diverse valves [87].

### Sudden Expansion

The minor losses are not only caused by components introduced in between the straight section of pipe, they might also be due to changes in the pipe dimension. These changes are categorized in two parts: the sudden expansion and the sudden contraction. We will also examine the particular case where the flow either enters or exits the tank.

In sudden expansion, the fluid leaves the smaller pipe and initially forms a jet-type structure as it enters the larger pipe as illustrated in Fig. 5.7.

Within a few diameters downstream of the expansion, the jet becomes dispersed across the pipe, and fully developed flow becomes established again. In this process, a portion of the kinetic energy of the fluid is dissipated as a result of viscous effects [87]. In that case, the loss coefficient  $k_L$  can be obtained analytically [94]:

$$k_L = \left(1 - \frac{A_1}{A_2}\right)^2 \quad [-] \quad (5.23)$$

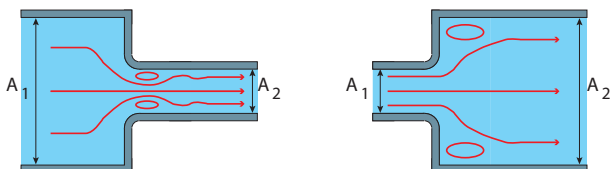


Figure 5.7.: Sudden contraction (left) and sudden expansion (right).

The dissipation of kinetic energy might be traced to the inefficient deceleration of the fluid; this phenomenon might be mitigated with a carefully designed expansion. Indeed, the losses are quite different if the expansion is gradual; for example, a diffuser<sup>6</sup> reduces the kinetic loss.

#### Sudden Contraction

The sudden contraction is the complementary change in flow condition to the sudden expansion (see Fig. 5.7). As it was the case above, the dissipation of kinetic energy might be mitigated if the contraction is gradual. The loss coefficient  $k_L$  is a function of the area ratio  $A_2/A_1$ ; some values are given in Tab. 5.5 for diverse ratios.

#### From a Reservoir into a Pipe

A fluid may flow from a reservoir into a pipe through any number of differently shaped entrance regions as sketched in Fig. 5.8. The majority of the loss is due to inertia effects that are dissipated by the shear stresses

---

<sup>6</sup>A device shaped to decelerate a fluid.

$A_2/A_1$	0.1	0.2	0.3	0.4	0.5	0.6	0.7	0.8	0.9	1
$k_L$	0.37	0.35	0.32	0.27	0.22	0.17	0.1	0.06	0.02	0

 Table 5.5.: Loss coefficient  $k_L$  for a sudden contraction [94].

within the fluid; only a small portion of the loss is due to the wall shear stress within the entrance region [87, 94]. Each geometry has an associated loss coefficient  $k_L$ ; these coefficients are given in Tab. 5.6. We remark in this table that an obvious way to reduce the head loss is to round the entrance region.

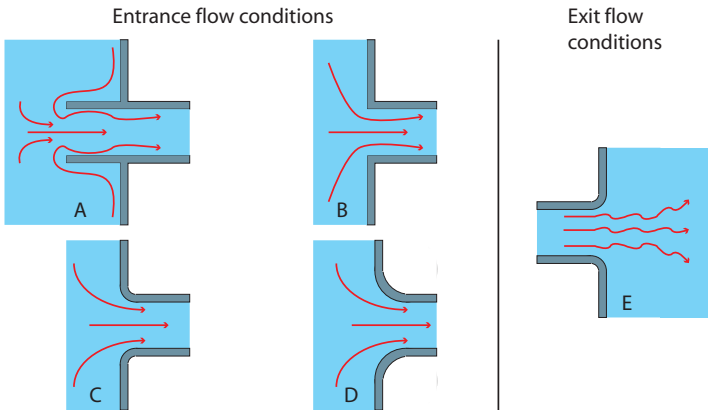


Figure 5.8.: Entrance flow conditions: A: reentrant, B: sharp-edged, C: slightly rounded and D: well-rounded. Exit flow conditions: E: the loss coefficient  $k_L$  equals 1 independently from the geometry.

### From a Pipe into a Reservoir

When a fluid flows from a pipe into a tank (see Fig. 5.8), a head loss (or exit loss) is also produced. In fact, this is a particular case of the sudden expansion, where  $A_2$  is very large compared to  $A_1$ ; therefore, we consider

	Type	$k_L$
A	Reentrant	0.8-0.9
B	sharp-edged	0.5
C	slightly rounded	0.2
D	well-rounded	0.04

Table 5.6.: Loss coefficient  $k_L$  for diverse entrance flow conditions [87, 94].

that the loss coefficient is equal to 1 according to (5.23). In that case, the entire kinetic energy of the fluid is dissipated through viscous effects as the stream of fluid mixes with the fluid in the tank and eventually comes to rest [87].

### 5.3.7. Pump Power

We know from the previous sections how to determine the pressure drop  $\Delta p$  that occurs in the pipes and others circuit elements; note that we will discuss in the specific section 5.5 the pressure drop in the stack: an element with a geometry too complex to be described by analytical relations. To conclude this section about the general notions of fluids mechanics, we need to introduce a relation that links the pressure drop  $\Delta p$  to the pump power  $P_{pump}$ .

In general, the pump family is divided in two main groups: the reciprocating positive displacement pumps and the centrifugal pumps; their main characteristic is to add energy to the fluid. In fact, they deliver a pressure across the hydraulic circuit that accelerates the fluid until the pressure drop  $\Delta p$  equals it. In this work, we are particularly interested by the pump power  $P_{pump}$ , a determinant variable that influences the battery performance. Unsurprisingly, the pump power is related to the head rise  $h_p$  supplied by the pump, to the fluid density  $\gamma$  and to the flowrate  $Q$ ; we can also relate it to the pressure drop  $\Delta p$  [84]:

$$P_{pump} = \gamma h_p Q = \Delta p Q \quad [W] \quad (5.24)$$

The nominal efficiency of the pump is often around 80-90% [94]; but the efficiency is not constant and decreases around its nominal flowrate as it is illustrated in Fig. 5.9. The actual performance of a pump can not

be accurately predicted analytically and is therefore determined experimentally; the results are presented as pump performance curves [87]. The overall efficiency  $\eta_{pump}$  is affected by three types of losses: the hydraulic losses in the pump, the mechanical losses in the bearings and seals and the volumetric losses due to leakages inside the pump. Therefore, the effective power required by the pump  $P_{mech}$  is given by:

$$P_{mech} = \frac{P_{pump}}{\eta_{pump}} \quad [W] \quad (5.25)$$

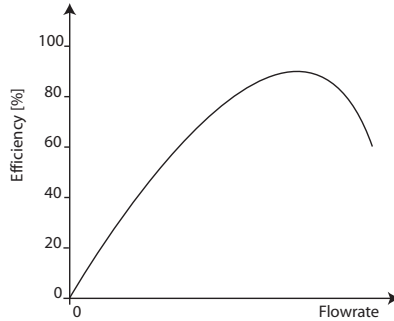


Figure 5.9.: Typical pump efficiency [87].

## 5.4. Analytical Model of the Hydraulic Circuit

In this section, we propose to establish the analytical model of the hydraulic circuit, with the exception of the stack circuit; indeed, the geometry of the stack is too complex to be analytically described and is the subject of section 5.5. This model summarizes the relations introduced in the previous sections; it determines the pressure drop  $\Delta p_{pipes}$  in the pipes and tanks, and the mechanical power  $P_{mech}$  required to flow the electrolyte in the pipes. An illustration of the hydraulic circuit is given in the appendix B.

First the model calculates the Reynolds number  $Re$  with (5.1) to de-

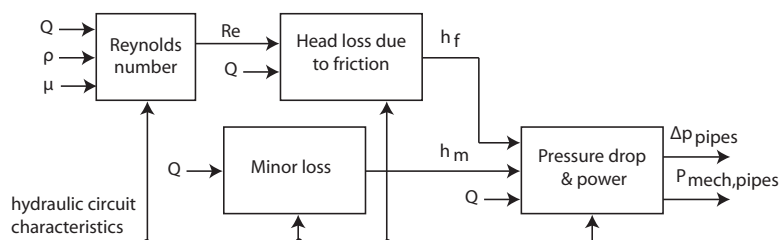


Figure 5.10.: Flowchart of the analytical model of the hydraulic circuit. Note that the model does not take into account the stack hydraulic circuit.

termine if the flow is laminar or turbulent<sup>7</sup>. With this information, the friction factor is determined with (5.17) for a laminar flow, and with either (5.18), (5.19) or (5.20) for a turbulent flow. Then, the head loss  $h_f$  due to friction is calculated with the Darcy-Weisbach equation (5.14) and (5.15); the minor head loss  $h_m$  is determined with (5.21), (5.22) and the loss coefficients  $k_{L,i}$  introduced in section 5.3.6. Finally, the pressure drop  $\Delta p_{pipes}$  is determined with the extended Bernoulli equation (5.13) and the corresponding mechanical power  $P_{mech,pipes}$  is calculated with (5.25).

Most of these relations depend directly on the geometrical dimension of the hydraulic circuit,  $D_i$  and/or  $L_i$ ; the extended Bernoulli equation (5.13) also depends on the difference in elevation  $\Delta z$ , but in most case, this difference should be zero. Furthermore, the head loss due to friction  $h_f$  depends on the pipe surface  $\epsilon$ ; all these parameters are summarized in the term *battery construction* in Tab. 5.7 where the dependence of the model variables on the operating conditions and on the battery construction is shown.

## 5.5. Stack Hydraulic Model

In the section 5.3, we have introduced the relations necessary to build the analytical model of the hydraulic circuit proposed in section 5.4; unfortunately, this model is not able to describe the hydraulic circuit of the stack

<sup>7</sup>In the case of a hydraulic circuit with different pipe diameters  $D$  and/or different flowrate  $Q$ ,  $Re$  must be calculated for each sections of the circuit. Indeed, the flow might be laminar in some parts and turbulent in others.

Variable	f(?)	$Q$	$\rho$	$\mu$	Battery construction
$Re$		•	•	•	•
$h_f$	$Re$	•	○	○	•
$h_m$		•			•
$\Delta p_{pipes}$	$h_f$ and $h_m$	○	•	○	•
$P_{mech,pipes}$	$\Delta p_{pipes}$	•	○	○	○

Table 5.7.: Variables dependency on the operating conditions. • denotes a direct dependence and ○ denotes an indirect dependence.

which is geometrically too complex. Therefore, we dedicate this section to the modeling of the stack circuit; once this task is completed, we will be able to model the overall VRB hydraulic circuit which is composed of three main parts: the tanks, the pipes and the stack.

There are two options to determine the mechanical power  $P_{mech,stack}$  required to flow the electrolyte in the stack: either build a VRB stack and experimentally measure the pressure drop  $\Delta p$  for a wide range of electrolyte flowrate  $Q$ , or use a numerical model of the stack. Practically, we have decided to use a finite element modeling tool since they are today widely available: we believe they are an adequate mean to create the numerical model of the stack circuit. The aim of this model is to determine the pressure drop  $\Delta p_{stack}$  as a function of the flowrate with the final purpose to determine the mechanical power  $P_{mech,stack}$ .

Quickly, we have discovered that the finite element method (FEM) is often a time and resources consuming method; in practice, the simulations of large stacks last a couple of weeks or even months on a dedicated server. Furthermore, we will see that the accuracy of the results depends on the mesh quality: a fine mesh add a supplemental burden on our limited resources. Therefore, we will introduce an original method that decomposes the stack into smaller parts, the *basic parts*, that are afterwards reassembled to form a stack of any dimensions. This method uses an analogy with Ohm's law to determine an equivalent hydraulic resistance  $\tilde{R}$ ; with this resistance, the model gives instantly the pressure drop  $\Delta p_{stack}$  and the mechanical power  $P_{mech,stack}$  as a function of the flowrate  $Q$  and the electrolyte properties  $\rho$  and  $\mu$ .

### The Hydraulic Circuit in the Stack

We have seen in section 5.2 how to build a stack from a set of basic components: the end plates, the bipolar plates, the membranes and the carbon felt electrodes (see Fig. 5.2). In fact, the VRB contains two hydraulic circuits: one for the catholyte and one for the anolyte. There are a multitude of possible designs to distribute the electrolyte from the manifolds to the surface of electrodes; in any case, this is done by some sort of distributing channels that are connected to the input and the output manifolds. Hence, the input manifolds are fed from an input pipe and the electrolyte is evacuated through the output pipe. The structure of a simple two cells stack is illustrated in Fig. 5.11; note that the electrodes, the membranes and the flow frames are not represented: the coloured segments represent the liquid electrolytes.

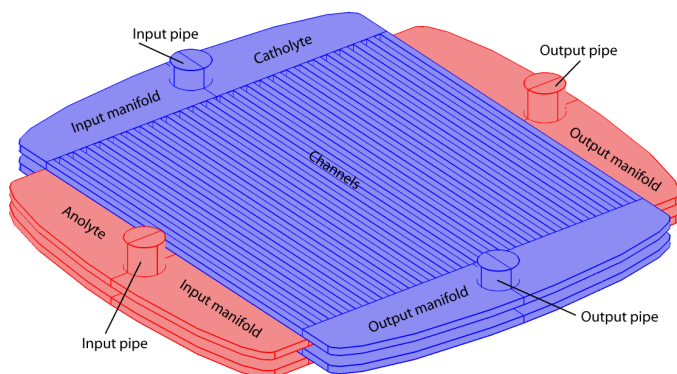


Figure 5.11.: Hydraulic circuit of a 2 cells stack. Note that the flow frames are not represented and that the coloured segments represent the electrolytes (liquid).

In the rest of this chapter, we will use the structure of Fig. 5.11 as an example to illustrate the principles governing the modeling of the stack hydraulic circuit. Of course, many more designs are possible that optimize either the cost, the ease of construction and/or the performance of the battery. We believe that the method introduced in the next sections is adaptable to any structure, although this might be more challenging in



some cases. Finally, a remarkable property of this structure is observed in Fig. 5.11 : the perfect identity between the anodic and the cathodic circuits.

### 5.5.1. The Flow Resistance, an Analogy with the Ohm's Law

The aim of the mechanical model developed in this chapter is to quickly assess the mechanical power  $P_{mech,stack}$  as a function of the operating conditions: in particular the flowrate  $Q$  and the electrolyte properties  $\rho$  and  $\mu$ . In order to quantify the effect of different control strategies on the VRB performance, the operating conditions need to be changed often. Unfortunately, it is unthinkable to run a new FEM simulation every time a parameter changes; indeed, FEM takes too much time and resources to be directly inserted into the VRB model. Therefore, a simple relation must be introduced to link the pressure drop  $\Delta p_{stack}$  and the mechanical power  $P_{mech,stack}$  to the operating conditions.

In fact, we can make an analogy between the flow of electrolyte in the stack and the flow of electrons in an electrical circuit. Indeed, there is an equivalence with Ohm's law ( $U = RI$ ) and fluid mechanics: a balance can be found in a fluid circuit between the pressure drop  $\Delta p$ , the flowrate  $Q$  and a flow resistance, or hydraulic resistance  $\tilde{R}$ :

$$\Delta p = Q\tilde{R} \quad [Pa] \quad (5.26)$$



Figure 5.12.: Georg Ohm 1789 - 1854 (source: [24]).

But because it is very difficult to simulate turbulent flow, in particular in

such a complex structure as a VRB stack, we must assume or demonstrate that the flow stays laminar in the stack. For example, we will discuss in chapter 6 the operations of the battery introduced during the simulation of the stand alone system in section 3.9 under various conditions; in that case, we can demonstrate that the flow stays laminar in the distributing channels even at maximal flowrate  $Q_{max}$ . Although the flow is turbulent in the pipes at this velocity, it should quickly become laminar due to the effect of the viscosity inside the manifolds. Finally, the fluid properties,  $\rho$  and  $\mu$  are introduced into (5.26) through the hydraulic resistance  $\tilde{R}$ ; we will see in sections 5.5.5 and 5.5.6 how they influence the pressure drop  $\Delta p$ .

### A Simple Method to Determine the Hydraulic Resistance

We have just seen that the pressure drop  $\Delta p$  is related to the flow resistance  $\tilde{R}$  with (5.26), but how do we determine this resistance? In fact, there is a simple method: first the geometrical characteristics of the conduit are introduced into the FEM software and then a series of FEM analysis is performed at either various pressures or flowrates<sup>8</sup>.

For example, the pressure drop  $\Delta p$  is illustrated in Fig. 5.13 as a function of the flowrate  $Q$  for some of the basic components introduced in the next section. Immediately, we observe that there is a linear relationship and that the flow resistance  $\tilde{R}$  is simply given by the slopes. Hence,  $\tilde{R}$  is quickly determined with any curve fitting method and (5.26).

### 5.5.2. Hydraulic Resistance of a Stack

We are now ready to determine the flow resistance of the stack  $\tilde{R}$  with the method introduced in the previous section. But often, the geometry of the stack becomes so large and complex that quickly the limited computing resources impose a very long simulation. This simulation time might be reduced with a coarser mesh, but this method is seldom satisfactory because it also reduces the accuracy of the solution. We have illustrated this phenomenon with a simple example in appendix A; in that case, the analytical and numerical model can be compared and the effects of the mesh size on the accuracy can be observed.

---

<sup>8</sup>We have observed that FEM simulation converges faster and more often when a pressure is applied across the conduit rather than when a flowrate is imposed.

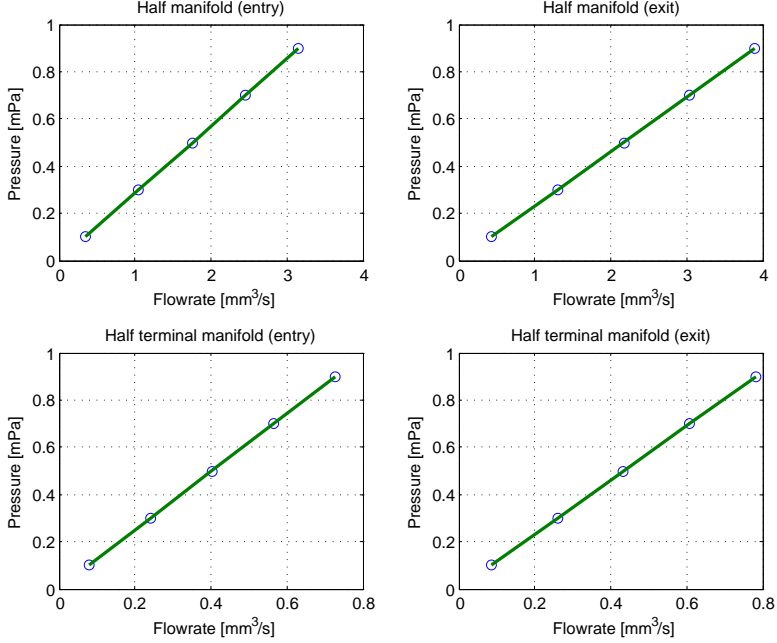


Figure 5.13.: Results of the FEM simulations for the different manifolds. Note that we have cut the manifolds in two parts to take advantage of their symmetry.

Therefore, we propose to develop a little further the analogy with the electrical circuits and to fractionate the stack into smaller parts that form a set of basic components; this set includes the manifolds and the flow plates. Their flow resistances  $\tilde{R}_i$  are quickly and accurately determined thanks to their small size and fine mesh. Then, we can assemble them in parallel and/or in series to form a stack of any number of cells. We have illustrated in Fig. 5.14 a method to construct a two cells stack from the basic components.

Then the second analogy with the electrical circuits is introduced: the flow resistance of the stack  $\tilde{R}$  can be determined from the Kirchhoff's

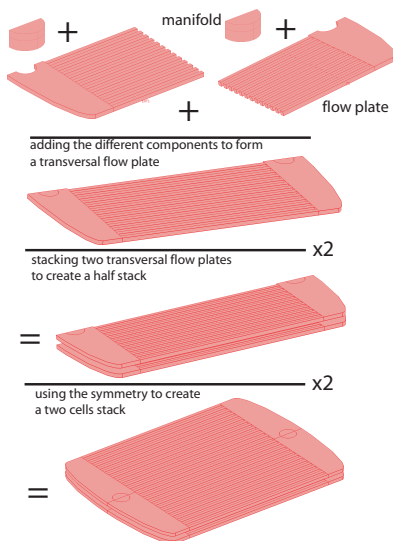


Figure 5.14.: Construction of a two cells stack using basic parts and the longitudinal symmetry of the design.

circuit laws. Indeed, the pressure  $P$  replaces the voltage  $U$  and the flowrate  $Q$  replaces the current  $I$ ; thus an equivalent hydraulic circuit is built with the flow resistance of the basic components  $\tilde{R}_i$  (see Fig. 5.16). Finally, the flow resistance  $\tilde{\mathbf{R}}$  is expressed in the form of a matrix (5.28) with Kirchhoff's laws; then the scalar flow resistance  $\tilde{R}$  is obtained by solving (5.27) which is derived from (5.26).

$$\begin{pmatrix} p \\ 0 \\ 0 \\ 0 \\ \vdots \\ 0 \\ 0 \\ 0 \end{pmatrix} = \tilde{\mathbf{R}} \cdot \begin{pmatrix} Q_1 \\ Q_2 \\ Q_3 \\ \vdots \\ Q_{N-1} \\ Q_N \end{pmatrix} \quad [Pa] \quad (5.27)$$

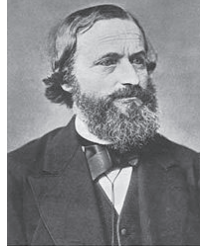


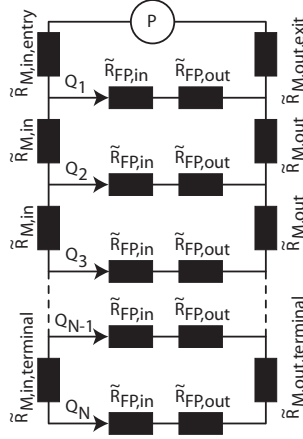
Figure 5.15.: Gustav Kirchhoff 1824 - 1887 (source: [24]).

where the matrix  $\tilde{\mathbf{R}}$  is:

$$\tilde{\mathbf{R}} = \begin{pmatrix} \tilde{R}_{ME} + \tilde{R}_{FP} & \tilde{R}_{ME} & \tilde{R}_{ME} & \dots & \tilde{R}_{ME} & \tilde{R}_{ME} \\ -\tilde{R}_{FP} & \tilde{R}_M + \tilde{R}_{FP} & \tilde{R}_M & \dots & \tilde{R}_M & \tilde{R}_M \\ 0 & -\tilde{R}_{FP} & \tilde{R}_M + \tilde{R}_{FP} & \ddots & \tilde{R}_M & \tilde{R}_M \\ \vdots & \ddots & \ddots & \ddots & \vdots & \vdots \\ 0 & 0 & 0 & \ddots & \tilde{R}_M + \tilde{R}_{FP} & \tilde{R}_M \\ 0 & 0 & 0 & \dots & -\tilde{R}_{FP} & \tilde{R}_{MT} + \tilde{R}_{FP} \end{pmatrix} \quad (5.28)$$

where:  $\tilde{R}_{ME}$  = Equivalent hydraulic resistance of the entry and exit manifolds  $[Pa \cdot s/m^3]$   
 $\tilde{R}_M$  = Equivalent hydraulic resistance of the two regular manifolds  $[Pa \cdot s/m^3]$   
 $\tilde{R}_{MT}$  = Equivalent hydraulic resistance of the two terminal manifolds  $[Pa \cdot s/m^3]$   
 $\tilde{R}_{FP}$  = Equivalent hydraulic resistance of the two flow plates  $[Pa \cdot s/m^3]$

With this method, the FEM analysis is reduced to the basic components that can be quickly and precisely simulated in order to determine the flow resistance of a  $N_{cell}$  cells stack; we will assess the accuracy of this


 Figure 5.16.: Equivalent hydraulic circuit of a  $N_{cell}$  cells stack.

method in section 5.5.4. Furthermore, we can reduce the size of the basic components by taking advantage of their axis of symmetry to reduce the simulation time and/or refine the resolution of the mesh. For example, in Fig. 5.14, we have taken advantage of the longitudinal symmetry of the stack to divide its size by two.

### The Resistance of the Basic Components

In order to determine the stack resistance  $\tilde{R}$  with the method introduced in the previous section, we must determine the flow resistances of the basic parts to solve (5.27) and (5.28). In this section, these basic parts will be identified and characterised. Practically, they were divided in two parts along their axis of symmetry to reduce their size; this smaller size speeds up the simulation while preserving the accuracy. Nevertheless, the resulting flow plates were still large and have therefore been divided in two more parts.

This section is dedicated to the characterization of the basic elements that compose the stack (see Fig. 5.11); in that structure, the electrolyte flows in parallel through the cells from a single input pipe. Therefore, two

types of manifolds were identified: the terminal manifolds that are on the top of the stack and have only one way out for the flow and the regular terminals with two ways out (one into the next manifold and one into the flow plate). These components are represented in Fig. 5.17 with the direction of the flow; we remark that the input and output components are geometrically identical, the only difference is the direction of the flow. Furthermore, we remark in Tab. 5.8 that it introduced a slight difference in the hydraulic resistances  $\tilde{R}_i$ .

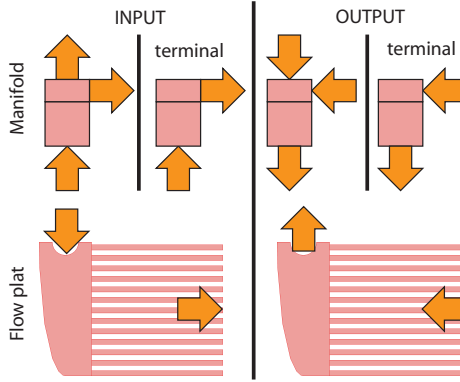


Figure 5.17.: Basic parts with the direction of the flow.

Then a series of FEM analysis was performed on these components; different pressures were applied and the corresponding fluid velocities were recorded. The data obtained were already represented in Fig. 5.13 to illustrate the method used to determine the flow resistance  $\tilde{R}$  (see section 5.5.1). Since we have simulated one half of the components, the slope of the pressure represents the flow resistance of only one half component  $\tilde{R}_{half}$ ; the total resistance  $\tilde{R}_{total}$  is equivalent to two half components in parallel. Therefore,  $\tilde{R}_{total}$  is given by:

$$\tilde{R}_{total} = \frac{\tilde{R}_{half}}{2} \quad [Pa \cdot s/m^3] \quad (5.29)$$

So, the hydraulic resistances  $\tilde{R}_i$  were determined from the FEM analysis

Name	max. mesh element size [mm]	$\tilde{R}$ [Pa · s/m <sup>3</sup> ]
input manifold	1	142'644
output manifold	1	115'770
terminal input manifold	1	620'027
terminal output manifold	1	576'055
input flow plate	1	33'670'584
output flow plate	1	34'098'014

Table 5.8.: The hydraulic resistance  $\tilde{R}$  and the max. element size of the basic parts.

with (5.29) and the results are represented in Tab. 5.8 with the maximal element size of the mesh used for the simulations. There is a criterion to assess the quality of the solution: if the resistance does not change when the mesh is refined, this can be interpreted as a sign of confidence in the accuracy of the solution [87]. In the case of the manifolds, the resulting resistances only change by 0.01% (around 1.3% for the flow plates) when the maximal element size is reduced from 1 mm to 0.5 mm. Therefore, we have a good confidence in the results of Tab. 5.8.

### 5.5.3. The Peclet Number and its Effects

We have seen in the previous sections that FEM analyses are a powerful tool when the geometry is too complex for an analytical description. Nevertheless, FEM analyses are also subject to instabilities that might prevent the solution from converging. We will see in the rest of this section why these instabilities occur and how to avoid them.

To understand this phenomenon, we should first look at what happens at the microscopic level of the fluid; for example, when the electrolyte flows through the VRB, the fluid experiences the effects of convection and diffusion. In a diffusive phenomenon, a change at one location affects in more or less equal measure in all directions around it; a convective phenomenon has an influence exclusively in the direction of the flow (see Fig. 5.18). A good image is the transport of colorant added to a river:



if the water is flowing quickly, the predominant form of transport will be convective and when the water is still, the colorant would simply disperse from its source in a diffusive manner.

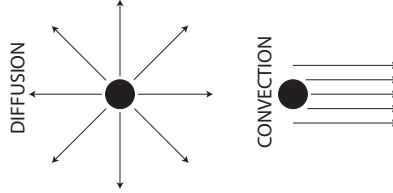


Figure 5.18.: Convection and diffusion.

Then we must know how the FEM solvers work; obviously FEM simulations require numerical solutions based on some kind of discretization. Unfortunately, the discretization of convection-dominated transport problems can introduce instabilities in the solution. These instabilities can take the form of oscillations that can be large enough to prevent the solution from converging. The details are beyond the scope of this work, the interested readers are referred to [96, 97].

But there is a method to circumvent this limitation in the form of the Peclet number  $P_e$ : a dimensionless number that describes the relationship between the convective and diffusive terms in a convection and diffusion equation. In fluid mechanics applications, the diffusive terms are introduced through the viscosity:

$$P_e = \frac{h_{mesh} \rho |V_s|}{\mu} \quad [-] \quad (5.30)$$

where  $h_{mesh}$  is the local mesh diameter. In fact, oscillations can occur when the Peclet number is greater than two; these problems result from the poor discretization, but there is, at least in theory, a mesh resolution beyond which the discretization is stable. But in reality, the mesh size is often limited by the available memory of the computer. So, for given values of density  $\rho$  and viscosity  $\mu$ , there are only two variables to maintain the Peclet number below two ( $P_e < 2$ ): the velocity  $V_s$  and the mesh size  $h$ . Often, the sole solution is to reduce the velocity.

To illustrate this phenomenon, we have performed a FEM analysis of

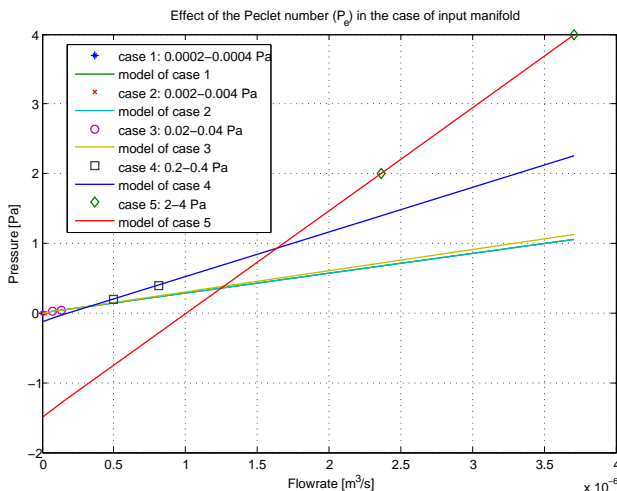


Figure 5.19.: Effect of the Peclet number  $P_e$  in the case of the input manifold. The Peclet numbers are respectively: 0.0072, 0.0725, 0.7047, 4.1768 and 19.1393 starting from case 1 to case 5. Note that the solid lines are extrapolations from the FEM points in the respective pressure ranges and that model 1 and 2 are superposed.

the input manifold with a fixed mesh size of 1 mm; in each case, we have changed the pressure applied to modify the fluid velocity and thus the Peclet number. We have shown in Fig. 5.19 the results of the FEM analysis where the Peclet numbers range from 0.0072 to 19.13. We clearly see a large difference between the curves with Peclet number below two and the curves above this value. The numerical results are summarized in Tab. 5.9 where we observe that the difference between the smallest  $P_e$  and the largest is well above 400%; in fact, the difference is already above 124% for a Peclet number equal to 4. We conclude that the accuracy of the solution is not acceptable when the conditions of the FEM analyses are ill-defined; therefore, the accuracy not only depends on the quality of the mesh (see the finite element analysis in appendix A), but also on the definition of the simulation conditions.

Case	Pressure range [Pa]	Max. Peclet number [-]	$\tilde{R}$ [Pa · s/m <sup>3</sup> ]	Difference [%]
1	0.0002-0.0004	0.0072	285'400	0
2	0.002-0.004	0.0725	283'800	0.59
3	0.02-0.04	0.7047	302'200	5.89
4	0.2-0.4	4.1768	639'500	124.04
5	2-4	19.1393	1'480'200	418.60

Table 5.9.: Numerical values of the Peclet number  $Pe$  and the hydraulic resistance  $\tilde{R}$  for various pressure ranges. These numbers apply to the input manifold, the mesh size is 1 mm.

#### 5.5.4. Validation of the Stack Decomposition

In this section, we will examine the validity of the stack decomposition method proposed in the section 5.5.2; this method determines the stack flow resistance  $\tilde{R}_{model}$ . Of course, the best way would have been to introduce  $\tilde{R}_{model}$  into (5.26) and to compare the result with experimental data; unfortunately, no experimental setup was available. Therefore, we have decided to simulate the whole stack on a powerful dedicated server; even with this large computational capacity, the simulations have taken many weeks, even months for the larger stack.

In order to perform the FEM analysis under the best conditions, we have taken advantage of the longitudinal symmetry to reduce the size of the stack; thus it was possible to improve the resolution of the mesh and in consequence increase the accuracy. The flow resistance  $\tilde{R}_{FEM}$  of stacks of different sizes were then determined with the method presented in section 5.5.1; the results are given in Tab. 5.10. As an illustration, the graphical result of the FEM analysis of a two elements stack is shown in Fig. 5.20.

Then the flow resistance  $\tilde{R}_{model}$  of a stack of  $N_{cell}$  elements was determined with the method proposed in section 5.5: the flow resistances  $\tilde{R}_i$  of the basic parts (given in Tab. 5.8) were introduced into (5.28) in order to determine  $\tilde{R}_{model}$  by solving (5.27). The results are given in Tab. 5.10 and shown in Fig. 5.21 where we can observe that the flow resistance decreases hyperbolically with the number of cells.

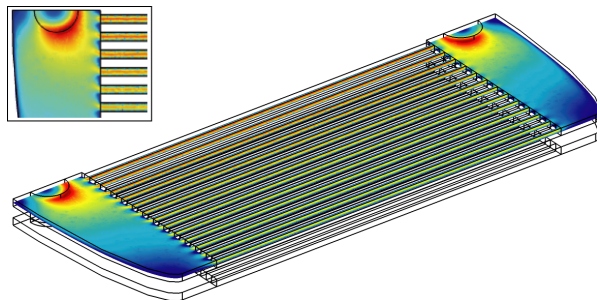


Figure 5.20.: Fluid velocities in the top cell of a two elements stack. In the corner, a view from above of the input manifold.

We can now compare the flow resistance  $\tilde{R}_{model}$  obtained with the method introduced in section 5.5.2 and the flow resistance  $\tilde{R}_{FEM}$  obtained from the FEM analysis of whole stacks. The maximal difference is around 2% (see Fig. 5.21 or Tab. 5.10), this give us a very good confidence in the accuracy of the method.

Note that we have carefully designed the distribution channels to maintain the flow laminar at the maximal flowrate  $Q_{max}$ . Although the flow might be turbulent in the pipe at these high velocities, the consequence should be negligible because the flow quickly becomes laminar in the manifolds. If the flow is turbulent in the major part of another type of stack, this method is not valid and the only option is to build a stack and experimentally determine the pressure drop  $\Delta p$  as a function of the flowrate  $Q$ . Furthermore, we have neglected in this section the effect of the structure of the carbon felt and considered its surface smooth.

### 5.5.5. The Effect of the Density on the Flow Resistance

In chapter 4, the properties of the electrolytes were investigated; in particular, we have seen that they are not constant and depend on the composition of the electrolyte. Hence the viscosity  $\mu$  and the density  $\rho$  depend on the state of charge  $SoC$ ; their influence on the flow resistance  $\tilde{R}$  will be discussed here and in the next section.

Since the shear stress  $\tau$  (4.8) is independent of the density in the case of

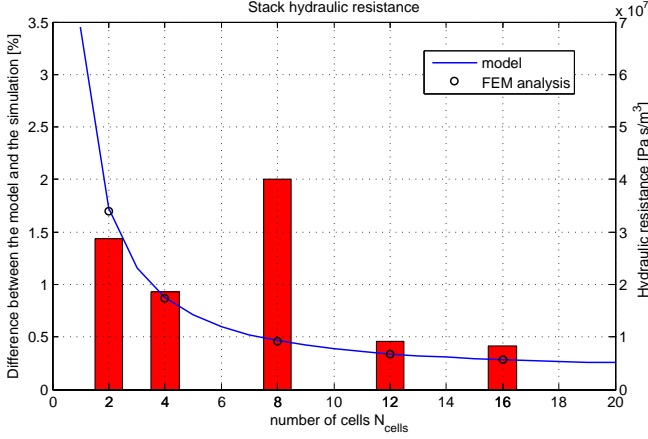


Figure 5.21.: Comparison between the flow resistance  $\tilde{R}_{\text{model}}$  obtained with (5.27) and the basic parts flow resistances  $\tilde{R}_i$ , and the flow resistance  $\tilde{R}_{\text{FEM}}$  obtained from the FEM analysis of whole stack.

a laminar flow, the flow resistance  $\tilde{R}$  should also be independent as long as the flow remains laminar. A series of FEM analysis of a two elements stack was performed to verify this independence; the simulations were made at different pressures (1, 5, 10 and 20 Pa) and different densities ranging from 1 to 1.6 g/cm<sup>3</sup> which correspond to possible densities of the electrolyte. The flow resistances  $\tilde{R}$  corresponding to each density were then calculated; the results are shown in Fig. 5.22.

Although it seems in Fig. 5.22 that the flow resistance  $\tilde{R}$  changes with the density, this is not the case; in fact this impression is due to the scale of the y-axis. In this example, the variation of the flowrate  $Q$  as a function of the density always stays below 0.1% and the difference between the flow resistances is also negligible: it is below 0.05%. Therefore, the flow resistance is clearly independent of the density. Nevertheless, the density  $\rho$  is important in fluid mechanics; indeed, the Reynolds number  $Re$  is directly proportional to  $\rho$ . Furthermore, the density also appears in the extended Bernoulli equation (5.13) where it becomes important whenever there is a change in elevation  $\Delta z$  between the two extremities of the conduit (see

Number of half cells	max. element size $h_{mesh}$ [mm]	$\tilde{R}_{model}$ [Pa · s/m <sup>3</sup> ]	$\tilde{R}_{FEM}$ [Pa · s/m <sup>3</sup> ]	Difference [%]
2	1	34'439'119	33'945'552	1.43
4	1	17'482'305	17'320'120	0.93
8	1	9'297'406	9'110'837	2.01
12	1	6'783'584	6'752'628	0.46
16	1	5'666'633	5'643'070	0.41

Table 5.10.: Mesh size and hydraulic resistance of the simulated stacks. These values are for a density  $\rho$  of 1620 kg/m<sup>3</sup> and a viscosity  $\mu$  of 0.008 Pa/s.

Fig. 5.5); although in most cases, the contributions of  $\Delta z$  cancel each other in the VRB hydraulic circuit.

### 5.5.6. The Effect of the Viscosity on the Flow Resistance

We have seen in section 5.3.5 that the friction factor  $f$  depends on the Reynolds number  $Re$  (5.16); we also know from section 5.3.1 that  $Re$  is inversely proportional to the dynamic viscosity  $\mu$  (5.1). Therefore the flow resistances must somehow be proportional to the viscosity; we can demonstrate this analytically with the Darcy-Weisbach equation (5.14) for a simple geometry or numerically through a FEM analysis of a complex structure.

The results of a FEM analysis of a two elements stack are shown in Fig. 5.23 with viscosities ranging from 2 to 20 cP; these values correspond to possible VRB electrolyte viscosities. The FEM analysis have been performed at three pressures (0.1, 0.5, 1 mPa) and the corresponding flowrates have been recorded; then the flow resistances  $\tilde{R}$  have been calculated at each viscosities. We observe in Fig. 5.23 that, according to our expectation, the flow resistance is proportional to  $\mu$ .

In the FEM analysis performed previously to determine the flow resistance  $\tilde{R}$ , the electrolyte properties were constant. Although we have seen in the previous section that the density  $\rho$  does not influence  $\tilde{R}$ , this is not the case for the viscosity  $\mu$ . Indeed the viscosity changes as the battery

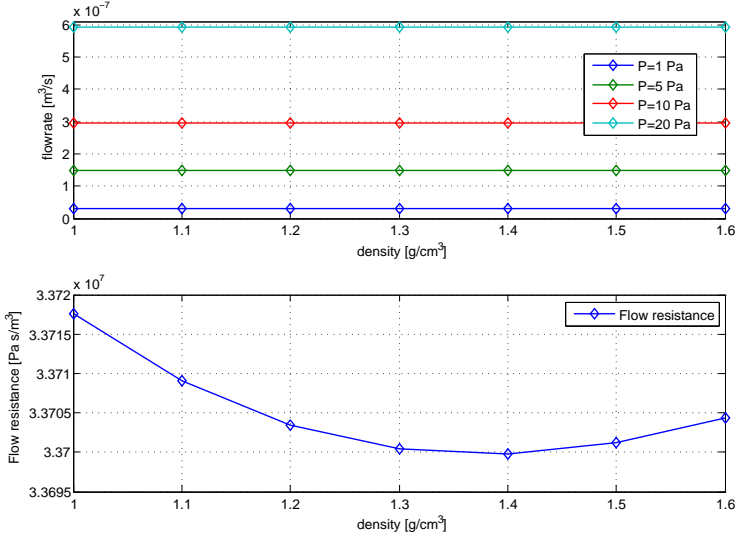


Figure 5.22.: Effect of the density on the flow resistance of a 2 elements stack. On top: the flowrate for a set of pressure as a function of the density. Below: the flow resistance as a function of the density.

is operating; therefore, a relation that links the viscosity  $\mu$  to the flow resistance is required. This relation is derived from the proportionality between the flow resistance and the viscosity observed in Fig. 5.23; hence, the flow resistance  $\tilde{R}$  at a given viscosity  $\mu$  is a function of the simulated resistance  $\tilde{R}_{simulation}$  at a fixed viscosity  $\mu_{simulation}$ :

$$\tilde{R} = \frac{\mu}{\mu_{simulation}} \tilde{R}_{simulation} \quad [Pa \cdot s/m^3] \quad (5.31)$$

## 5.6. Mechanical model of the VRB

We conclude this chapter with the presentation of the mechanical model of the VRB; this model is important to determine the mechanical power  $P_{mech}$  required to flow the electrolyte throughout the stack and is illus-

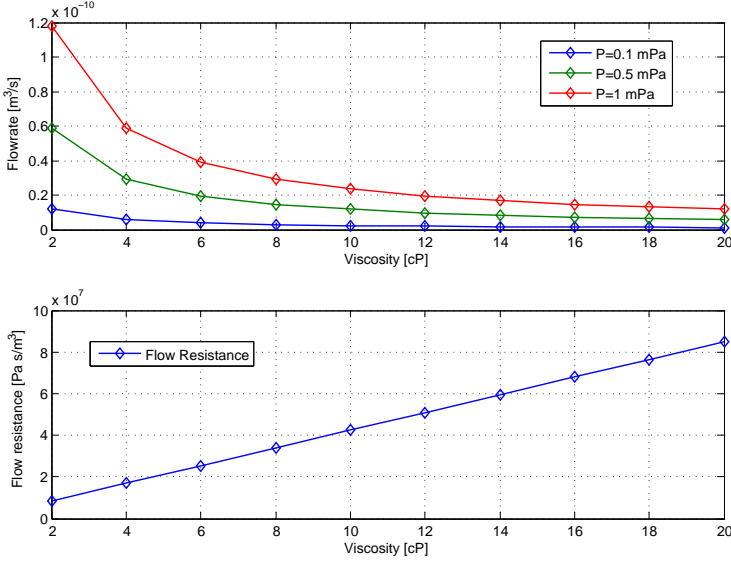


Figure 5.23.: Effect of the viscosity on the flow resistance of a 2 elements stack. On top: the flowrate for a set of pressure as a function of the viscosity. Below: the flow resistance as a function of the viscosity. In these examples, the density  $\rho$  is  $1620 \text{ kg/m}^3$ .

trated in Fig. 5.24. This model results from the combination of the analytical model proposed in section 5.4 and the principles and relations introduced in the previous section that describe the stack hydraulic circuit. Hence, we will be able to assess the battery performance with the electrochemical model (section 3.6) in the next chapter.

The analytical model was already described in section 5.4; therefore, it is not detailed here and is represented as a single block in Fig. 5.24. This analytical model determines the mechanical power  $P_{mech, pipes}$  as a function of the flowrate  $Q$  and the electrolyte properties.

The stack flow resistance  $\tilde{R}$  is determined with (5.28) and the equivalent resistances  $\tilde{R}_{ME}$ ,  $\tilde{R}_M$ ,  $\tilde{R}_{MT}$  and  $\tilde{R}_{FP}$ ; these equivalent resistances represent basic components that are assembled to form the hydraulic cir-



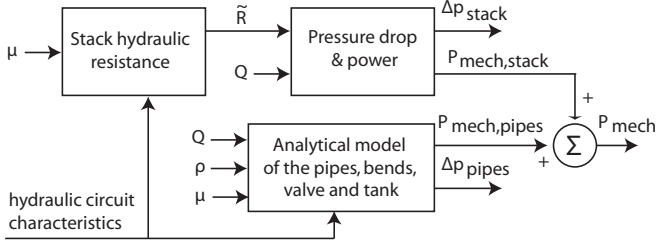


Figure 5.24.: Flowchart of the VRB mechanical model. The analytical model of the pipes, bends, valve and tank is described in more detail in Fig. 5.10.

cuit of the stack. They are obtained from a series of FEM analysis. The effect of the viscosity  $\mu$  is taken into account with (5.31). The pressure drop  $\Delta p_{stack}$  in the stack depends on the flowrate  $Q$  and the equivalent resistance of the stack  $\tilde{R}$ ; this relation is given by (5.26). Finally, the mechanical power of the stack  $P_{mech,stack}$  is found from (5.25).

Then, the overall mechanical power  $P_{mech}$  is simply obtained from the sum of the mechanical power of the stack  $P_{mech,stack}$  and the mechanical power of the pipes  $P_{mech,pipes}$ :

$$P_{mech} = P_{mech,stack} + P_{mech,pipes} \quad [W] \quad (5.32)$$

We have already shown the dependence of the analytical model variables on the operating conditions in Tab. 5.7; again, the term *battery construction* encompasses the geometrical dimensions of the overall hydraulic circuit. In conclusion, we show here the dependence of the numerical and overall models variables in Tab. 5.11.

## 5.7. Summary and Outlook

In the first part of this chapter, we have discussed the construction of a stack; we have seen that there are two ways to flow the electrolytes through the cells: the serial and the parallel flows. We believe that the parallel flow has more advantages, although the serial flow has minimal leakage current. We have also illustrated how to build a stack from basic

Variable	f(?)	$Q$	$\rho$	$\mu$	Battery construction
$\tilde{R}$			•	•	•
$\Delta p_{stack}$	$\tilde{R}$	•	◦	◦	◦
$P_{mech,stack}$	$\Delta p_{stack}$	•	◦	◦	◦
$P_{mech,pipes}$	$\Delta p_{pipes}$	•	◦	◦	◦
$P_{mech}$	$P_{mech,stack}$ and $P_{mech,pipes}$	◦	◦	◦	◦

Table 5.11.: Variables dependency on the operating conditions. • denotes a direct dependence and ◦ denotes an indirect dependence.

elements: the bipolar plates, the end plates, the membranes and the carbon felt electrodes.

The second part is dedicated to the principles of fluid mechanics that lead to the mechanical model of the hydraulic circuit in the pipes and tanks. This sections starts with some important generalities about fluid mechanics such as the Reynolds number that determines the flow regime, Bernoulli's principle and the first law of thermodynamics that lead to the extended Bernoulli's equation, an expression of the law of conservation of energy. Yet, we have defined an expression (5.13) that relates the pressure drop  $\Delta p$  across a conduit as a function of the fluid velocity  $V_s$ , the fluid specific weight  $\gamma$ , the geometry, the head losses due to friction  $h_f$ , the minor head losses  $h_m$  and the work done on the system  $h_w$ .

The head losses  $h_m$  are due to the viscous effects; they are defined by the Darcy-Weisbach equation (5.14) which depends on the conduit geometry, the fluid velocity  $V_s$  and the friction factor  $f$ . We have seen that the friction factor depends on the flow regime. If the flow is laminar:  $f$  is derived from the Poiseuille law and depends only on the Reynolds number<sup>9</sup>  $Re$  (5.17), otherwise  $f$  is determined from the Colebrook equation (5.20). In that case, the friction factor depends on  $Re$  but also on the diameter of the pipe  $D$  and on its roughness  $\epsilon$ .

The minor losses occur in the components that connect the straight sections of pipes together: they have the form of a bend, an elbow or

<sup>9</sup>Remember that  $Re$  is the ratio of inertial forces to viscous forces and is obtained from a combination of the geometrical characteristic of the conduit, the fluid flowrate and its properties.

a valve. Minor losses also occur when the fluid flows from (or into) a reservoir into (from) the pipe. The minor head losses  $h_m$  are determined by a relation (5.22) similar to the Darcy-Weisbach equation and depend on a loss coefficient  $k_L$ . We have discussed in section 5.3.6 the causes of these losses; we have also given tables (Tab. 5.3, 5.4, 5.5 and 5.6) from which the loss coefficients  $k_L$  might be retrieved. In the case of a sudden expansion,  $k_L$  is given by an analytical relation (5.23) from which the particular case of a fluid exiting a tank is derived.

In fact, we are particularly interested by the mechanical power  $P_{mech}$  required to flow the electrolyte; it depends on the flowrate  $Q$  and on the corresponding pressure drop  $\Delta p$  (5.24). Although the nominal pump efficiency is often around 80-90%, it is not constant and decreases around its nominal flowrate (see Fig. 5.9).

Then, we have summarized the principles and relations introduced in the section 5.3 into an analytical model that describes the hydraulic circuit of the pipes and tanks. This model represented in Fig. 5.10 determines the pressure drop  $\Delta p_{pipes}$  and the mechanical power  $P_{mech,pipes}$  in the pipes as a function of the flowrate  $Q$  and the electrolyte properties.

The fourth part of this chapter is dedicated to the modeling of the stack hydraulic circuit; indeed, the stack geometry is too complex to be described by the analytical relations of section 5.3. Therefore, we have proposed to make a FEM analysis; the other possibility would have been to build a stack and experimentally determine the pressure drop at different flowrates. Quickly, we have found out that FEM analyses are often a large consumer of time and resources; practically, it would not have been possible to run a FEM analysis in real time, even calculating a table of the pressure drops as a function of the flowrates did not seem reasonable.

Therefore, we have introduced an analogy with the Ohm's law; in that case, the flowrate  $Q$  replaces the electrical current  $I$ , the pressure drop  $\Delta p$  replaces the voltage  $U$  and the flow resistance  $\tilde{R}$  replaces the electrical resistance  $R$ . In consequence, a direct relation between  $\Delta p$  and  $Q$  is established (5.26). Then, we have proposed in section 5.5.1 a simple method to determine the flow resistance through a series of FEM analysis.

Because the FEM analysis of a stack is often very long, an original method to decompose the stack into smaller basic parts was proposed in section 5.5.2; these basic parts are then assembled to form a stack of any dimension (see Fig. 5.14). Indeed, the FEM analysis of the basic parts is fast and accurate. Another analogy with electrical circuits was made

to determine the equivalent hydraulic circuit with Kirchhoff's laws: this equivalent circuit is obtained by connecting the basic parts in parallel and/or series. Hence, it is possible to determine the stack resistance  $\tilde{R}$  with (5.27).

Then we have discussed the Peclet number, a dimensionless number that describes the relationship between the convective and diffusive terms. This number is important to avoid instabilities in the FEM solver that might prevent the solution from converging. The instabilities often take the form of oscillations caused by the discretization of convection-dominated transport problems. The instabilities might be avoided if the Peclet number is maintained below two; there are two available parameters to reduce  $Pe$ : the mesh size  $h_{mesh}$  and the fluid velocities  $V_s$ .

The flow resistance  $\tilde{R}_{model}$  determined from the stack decomposition method of section 5.5.2 and the flow resistance  $\tilde{R}_{FEM}$  obtained from the FEM analysis of a complete stack were then compared. We have observed very good concordance between these two methods: the maximal difference being around 2%. Note that these methods are only valid if the flow stays laminar in the stack; otherwise, the sole solution is to experimentally determine the relation between the flowrate  $Q$  and the pressure drop  $\Delta p$ .

This fourth part was concluded with a discussion about the effects of the density  $\rho$  and the viscosity  $\mu$  on the flow resistance  $\tilde{R}$ . Since the shear stress  $\tau$  is independent of the density in a laminar flow, the flow resistance is also independent; we have verified this statement through a series of FEM analysis at different densities: the results have shown that  $\tilde{R}$  is constant.

Furthermore, the linear relationship between the flow resistance  $\tilde{R}$  and the viscosity  $\mu$  was highlighted in section 5.5.6. This relation is demonstrated analytically through the Darcy-Weisbach equation (5.14), the friction factor  $f$  (see section 5.3.5) and the Reynolds number  $Re$  (5.1) for a simple geometry or numerically through a FEM analysis of a more complex structure (see Fig. 5.23). Then a relation was proposed to determine the flow resistance at any viscosity (5.31).

In the last part, a mechanical model that encompasses the principles and relations introduced in this chapter was proposed; this model determines the mechanical power  $P_{mech}$  as a function of the electrolyte properties and the fluid flowrate  $Q$ . It is based on the analytical model already discussed in section 5.4 and on flow resistance of the stack discussed in section 5.5. The mechanical power in the stack depends on the actual viscosity  $\mu$  and

on the flowrate  $Q$ .

In the future, it would be very interesting to complete this steady-state model with a dynamical model. Indeed, in order to implement sophisticated control strategies for the VRB storage system, it will be necessary to identify the time constant of the hydraulic circuit. In some applications such as an UPS, it is important to know the start up time of the battery: it represents the time required to establish the electrolyte flowrate.



# The Multiphysics Model and Energetic Considerations

---

## 6.1. Introduction

We have developed an electrochemical model of the VRB stack in chapter 3 and a mechanical model of the electrolyte circuit in chapter 5; in this last chapter, we will combine these two models into an overall multiphysics model of the VRB storage system. This final model summarizes the principles and relations previously introduced into a powerful means to understand the behaviour of the battery; furthermore, this knowledge will enable us to enhance the battery performance.

Of course, the battery never operates alone; it always links together a power source such as an array of photovoltaic panels, a wind turbine or simply the grid, and either a load or the grid (see Fig. 6.1). Power converters are required to adapt the voltages and currents; and thus ensure the power flows between these entities. In addition, a control system is necessary to supervise the battery operation and its interaction with the other system elements.

After the presentation of the multiphysics model in the first part of this chapter, we will discuss the battery performance at constant current  $I_{stack,ref}$  with a strong focus on the battery power  $P_{VRB}$ , the stack power  $P_{stack}$  and the mechanical power  $P_{mech}$  required to flow the electrolyte.

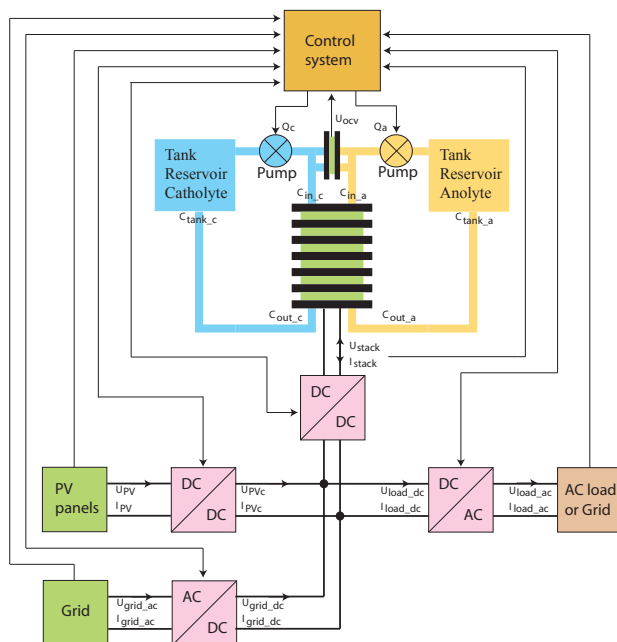


Figure 6.1.: Principles schematic of the VRB storage system.

First, we will examine the battery operation at a constant flowrate  $Q_{max}$  that supplies enough electroactive species under any operating conditions; in particular, the instantaneous battery efficiency  $\eta_{battery}$  will be determined and discussed.

Then, a second method that minimizes the mechanical power  $P_{mech}$  is introduced; in fact, this method finds the minimal flowrate  $Q_{min}$  required by the actual operating point. The relations necessary to determine  $Q_{min}$  are based on principles introduced in chapter 3. Although the minimal flowrate  $Q_{min}$  has a beneficial effect on the mechanical power  $P_{mech}$ , it also changes the vanadium concentrations within the stack. In consequence, the equilibrium stack voltage  $E_{stack}$  also changes and so does the stack voltage  $U_{stack}$  and the stack power  $P_{stack}$ . We will discuss in detail the



cause of this phenomenon.

In fact, we will see that the stack power  $P_{stack}$  decreases during the discharge when the battery is operated at minimal flowrate  $Q_{min}$ ; moreover,  $P_{stack}$  increases during the charge. At constant stack current  $I_{stack,ref}$ , the quantity of electrons  $e^-$  stored (or release) in (or from) the electrolyte does not depend on the stack power  $P_{stack}$ . Therefore, it is always better to charge the battery at minimal stack power  $P_{stack}$  and discharge it at maximal  $P_{stack}$ .

Intuitively, we feel that there should be an optimal flowrate  $Q_{opt}$  that optimizes the battery performance. Therefore, we will propose a method that finds this optimal flowrate  $Q_{opt}$  at any operating point. In these circumstances, the power delivered to the battery is minimized during the charge and the power supplied by the battery is maximized during the discharge. Then, we will assess the benefits of this new method compared to the two previous methods.

Then, we will perform the same series of charge and discharge at constant current as in chapter 3; but we will include this time the mechanical loss  $P_{mech}$ . So, the battery performances at the different flowrates  $Q_{max}$ ,  $Q_{min}$  and  $Q_{opt}$  can be compared with the voltage efficiencies  $\eta_{voltage}$  and the energy efficiencies  $\eta_{energy}$ . The importance of the internal loss  $U_{loss}$ , the stack voltage  $U_{stack}$ , the stack power  $P_{stack}$ , and the mechanical power  $P_{mech}$  will be discussed in this section; we will see that their importance depends on the operating conditions.

In the last section of this chapter, we will discuss the battery operation at constant stack power  $P_{stack,ref}$  and at constant battery power  $P_{VRB,ref}$ ; in these cases, there is a new control variable in supplement to the flowrate  $Q$ : the stack current  $I_{stack}$ . The optimal operating points,  $Q_{opt}$  and  $I_{stack,opt}$  will be determined and discussed for both operating conditions.

## 6.2. Multiphysics System Model

The combination of the electrochemical model described in section 3.6, the mechanical model described in section 5.6, and the electrolyte properties discussed in chapter 4 leads to the multiphysics VRB system model. The functions that determine the vanadium concentrations in the tank  $c_{tank}$  and the state of charge  $SoC$  have been separated from the electrochemical model in order to be incorporated into a new model named *reservoir and electrolyte model*; this model encompasses the electrolyte properties

and concentrations. A system control has also been added to supervise the battery operation; this system controls the flowrate  $Q$  and the stack current  $I_{stack}$ . This multiphysics system model, illustrated in Fig. 6.2, is a powerful means to understand the behaviour of the VRB, identify and quantify the sources of losses in this storage system; thus this multiphysics model is a good means to enhance the overall VRB efficiency.

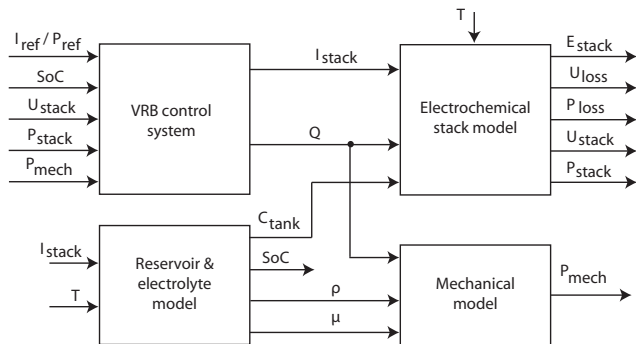


Figure 6.2.: Structured diagram of the multiphysics VRB system model.

This multiphysics model is composed of three main models and a control system:

- The **VRB control system** supervises the operation of the battery to meet the requirements set by the user or the application, and enhances the overall battery performance whenever possible. In basic operation, the user either sets the reference current  $I_{ref}$  or the reference power  $P_{ref}$  that the battery must provide or store; in more sophisticated applications which are not discussed in this work, the VRB control system might include other functions such as frequency control, power quality, peak shaving, load leveling, UPS etc. Furthermore, the control system also senses the internal variables and determines from these informations the appropriate current  $I_{stack}$  and flowrate  $Q$  adapted to the actual operating conditions<sup>1</sup>: the

<sup>1</sup>Note that some variables are redundant as they might be determined from the others.

state of charge  $SoC$ , the stack voltage  $U_{stack}$ , the stack power  $P_{stack}$  and the mechanical power  $P_{mech}$ .

- The **reservoir and electrolyte model** is fundamental to the electrochemical model because it determines the vanadium concentrations in the tank  $c_{tank}$  which are also the input concentrations of the stack  $c_{in}$ : in fact,  $c_{in}$  is the cornerstone of the equilibrium voltage  $E_{stack}$ . Besides, this model also determines the battery state of charge  $SoC$  and the actual electrolyte properties; the viscosity and the density are important variables in the mechanical model. The functions that determine the tank concentrations  $c_{tank}$  and the state of charge  $SoC$  were separated from the electrochemical model (section 3.6) and are respectively introduced in sections 3.2.2 and 2.3.4. The electrolyte properties are discussed in chapter 4.
- The **electrochemical stack model** is an important part of the overall model; it is based on the electrochemical principles and relations introduced in chapters 2 and 3 that were summarized into the augmented and simplified VRB stack model of section 3.6. Primarily, this electrochemical model determines the stack voltage  $U_{stack}$  as a function of the operating conditions: the flowrate  $Q$  and the current  $I_{stack}$  set by the control system, and the vanadium concentrations that depend on the actual battery state of charge. In addition, the electrochemical model also determines other internal variables useful to the control system or to determine the battery performance. These internal variables include: the stack equilibrium voltage  $E_{stack}$ , the stack internal losses  $P_{loss}$  and its corresponding voltage  $U_{loss}$ , and the stack power  $P_{stack}$ .
- The **mechanical model** is the last part of the multiphysics model; it is based on the fluid mechanical principles and relations introduced in chapter 5 that were summarized into the mechanical model of section 5.6. Its main purpose is to determine the mechanical power  $P_{mech}$  required to flow the electrolyte from the tanks to the stack. This value depends on the flowrate  $Q$ , the electrolyte properties and the structure of the hydraulic circuit that includes the pipes, the tanks and the stack.

### 6.3. Energetic Considerations at Constant Current

This section is dedicated to the performance of the VRB at constant current  $I_{stack,ref}$ <sup>2</sup>; the influences of different operating conditions will be discussed in detail. We will examine in particular the effects of the flowrate  $Q$  at different state of charge  $SoC$  and electrical current  $I_{stack}$ . First, the battery will be operated at constant flowrate  $Q_{max}$ : this constant flowrate carries enough electroactive species to fuel the electrochemical reactions at any operating point. An operating point is defined as the combination of a particular current  $I_{stack}$  with a given state of charge  $SoC$ .

Then, we will determine the minimal flowrate  $Q_{min}$  required at each operating point to sustain the battery operation: this flowrate depends only on  $I_{stack}$  and on  $SoC$ . From the comparison of the performances of these two methods, we will realize that there is an optimal flowrate  $Q_{opt}$  in between that maximizes the power performance of the battery; this optimal flowrate will be discussed in detail in section 6.3.3.

The power flows within the VRB storage system and with the external load and/or source are illustrated in Fig. 6.3. The power converters are necessary to adapt the stack voltage  $U_{stack}$  to the power source  $U_{grid}$  or to the load voltage  $U_{load}$ , and to supply the mechanical power  $P_{mech}$  required to operate the pumps; for simplicity reasons, they are considered lossless ( $\eta_{converter} = 1$ ).

It is important to remember that the stack voltage  $U_{stack}$  already includes the loss overpotential  $U_{loss}$  that is added to the equilibrium stack voltage  $E_{stack}$  during the charge, and subtracted during the discharge. This internal loss  $U_{loss}$  are discussed in detail in section 3.4;  $U_{loss}$  is directly proportional to the current  $I_{stack}$  and its sign depends on the operating mode of the battery. Furthermore, the equilibrium voltage  $E_{stack}$  depends solely on the vanadium concentrations within the stack  $c_{cell}$  and is determined from the Nernst equation (2.29). Hence, the electrochemical losses are already included in the stack power  $P_{stack}$  which is easily obtained from  $I_{stack}$  and  $U_{stack}$ :

$$P_{stack} = U_{stack}I_{stack} = (E_{stack} \pm U_{loss}) I_{stack} \quad [W] \quad (6.1)$$

The mechanical power  $P_{mech}$  is determined from the mechanical model proposed in section 5.6, and depends on the flowrate  $Q$ , the construction

---

<sup>2</sup>In fact, we consider that the current  $I_{stack,ref}$  is set by the user or by the application; therefore it might vary in time, but is a given value at each instant.

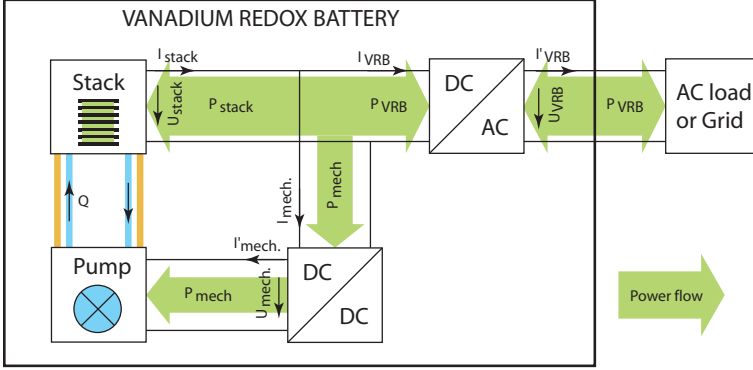


Figure 6.3.: Power flow in the VRB storage system. In this example, the power converters only adapt the currents and voltages, and are lossless.

of the hydraulic circuit and the electrolyte properties. Although these properties are not constant during the battery operation (see chapter 4), it was decided to maintain them constant in the rest of this work to simplify the discussion. Clearly, the mechanical power  $P_{mech}$  always flows in the direction of the pumps;  $P_{mech}$  is supplied by the stack during the discharge and from the grid during the charge.

In most stand-alone electricity storage system, the auxiliaries power  $P_{auxiliaries}$  includes the power converters loss and the power required to operate the control system that supervises the battery and measures the internal variables. In the VRB case, the mechanical power  $P_{mech}$  must be added to the auxiliaries power; in fact,  $P_{mech}$  is the only considered auxiliaries power in the rest of this work as the power converters are ideal and the power of the control system is neglected. Hence, the auxiliaries power is equal to  $P_{mech}$  and influences the power exchanged with the VRB  $P_{VRB}$ . This influence depends on the battery operating mode: during the charge, the mechanical power  $P_{mech}$  is provided from the external power source, and must therefore be added to the stack power  $P_{stack}$ :

$$|P_{VRB,charge}| = |P_{stack}| + P_{mech} \quad [W] \quad (6.2)$$

and during the discharge, the mechanical power  $P_{mech}$  is provided by the

stack and must this time be subtracted from the power furnished by the stack  $P_{stack}$ :

$$P_{VRB,discharge} = P_{stack} - P_{mech} \quad [W] \quad (6.3)$$

By convention, the battery power  $P_{battery}$  and the stack power  $P_{stack}$  are positive during the discharge and negative during the charge; the mechanical power is always positive. Therefore, (6.2) and (6.3) might be combined into:

$$P_{VRB} = P_{stack} - P_{mech} \quad [W] \quad (6.4)$$

#### VRB Characteristics

In order to discuss the performance of the battery, we should first describe its characteristics; we will continue to use the 2.5 kW, 15 kWh VRB introduced in the sections 3.9 and 3.10. Its electrochemical characteristics are summarized in Tab. 3.3.

The description of the hydraulic circuit is given in appendix B; the analytical model of the hydraulic circuit (see section 5.4) requires the dimensions of the pipes and tanks which are given in Tab. B.1 and B.2 for two possible tank sizes: 83 and 200 l. Of course, the energetic capacity of the battery depends on the tank size: the rating 2.5 kW, 15 kWh is for the 200 l tank. In addition, the hydraulic circuit of the stack has the form of the structure illustrated in Fig. 5.11; its flow resistance  $\tilde{R}$  is determined according to the method introduced in section 5.5.2 with the flow resistances  $\tilde{R}_i$  of the basic parts given in Tab. B.3. The flow resistance  $\tilde{R}$  of this 19 elements stack is then extracted from Fig. B.2; its value is 1'4186'843 Pa s/m<sup>3</sup>. As it was said before, the electrolyte properties are maintained constant for simplicity reasons.

##### 6.3.1. Maximal Flowrate

An efficient control strategy must optimize the power electrochemically exchanged with the stack  $P_{stack}$  while minimizing the losses: there is no point to have a battery that consumes more power than necessary. In this section, we will determine the maximal flowrate  $Q_{max}$  required to operate the stack under the worst operating conditions: low state of charge  $SoC$  during the discharge and high  $SoC$  during the charge. For both operating modes, the worst case occurs at high electrical current  $I_{stack}$ ;

at these moments, the electrochemical reaction rates are maximal whereas some electroactive species are scarce. Indeed, this high flowrate  $Q_{max}$  is required to provide enough electroactive vanadium ions to sustain the reaction rates.

Operating the battery constantly at this maximal flowrate  $Q_{max}$  is a very simple control strategy but its performance might not be optimal because of the constantly large mechanical power  $P_{mech}$ . In order to assess the battery performance at  $Q_{max}$ , we define an instantaneous battery efficiency  $\eta_{battery}$ :

$$\eta_{battery} = \frac{|P_{stack}|}{|P_{stack}| + P_{mech}} \quad [-] \quad (6.5)$$

Practically, the maximal flowrate  $Q_{max}$  of the 2.5 kW, 15 kWh VRB is around 1.97 l/s; this value depends on the maximal current  $I_{stack, Q_{max}}$  and on the *SoC* operating range. In fact,  $Q_{max}$  is proportional to  $I_{stack, Q_{max}}$  and depends exponentially on the maximal and minimal authorized *SoC*. At this flowrate, the mechanical power  $P_{mech, Q_{max}}$  required to flow both electrolytes is around 1720 W. The battery performance was then determined with (6.5) for every operating point; the results are shown in Fig. 6.4 as a function of  $I_{stack}$  and *SoC*; note that the stack power  $P_{stack}$  was already illustrated in Fig. 3.22.

Clearly, we observe that the battery performance is poor at constant flowrate  $Q_{max}$ ; therefore we come to the conclusion that constantly operating the battery at  $Q_{max}$  is not a wise strategy: the battery often consumes more power than necessary. Nevertheless, there is a method to improve this poor efficiency:  $Q_{max}$  might be reduced along with the corresponding mechanical power  $P_{mech, Q_{max}}$  simply by limiting the operating range of the battery: smaller current  $I_{stack, Q_{max}}$  and/or narrower *SoC* operating range. But this method also reduces the power rating and/or the energetic capacity of the battery while it increases the overall cost. In the next sections, we will discuss two different methods to enhance the battery performance.

### 6.3.2. Minimal Flowrate

We have just seen that operating the battery at constant flowrate  $Q_{max}$  is not efficient; therefore, we propose in this section another approach. This new method proposes to operate the battery at a minimal flowrate  $Q_{min}$

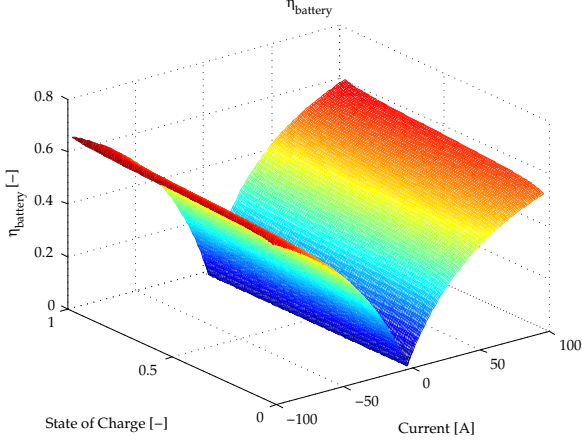


Figure 6.4.: The battery efficiency  $\eta_{battery}$  at constant flowrate  $Q_{max}$  as a function of the state of charge  $SoC$  and current  $I$ .

that is constantly adapted to the instantaneous operating point ( $SoC$  and  $I_{stack}$ ) in order to supply just enough electroactive materials to fuel the electrochemical reactions.

The vanadium concentrations  $c_{vanadium}$  are bounded between a minimal concentration  $c_{min}$  that is never less than zero, and a maximal concentration  $c_{max}$  that can not be larger than the total vanadium concentration  $c_{tot}$  in the electrolyte. Usually, the vanadium concentrations never reach these extreme limits; the boundaries are defined by design to let the battery operate in good conditions, and include safety margins as it is illustrated in Fig. 6.5.

Furthermore, the vanadium concentrations  $c_{vanadium}$  change within the stack proportionally to the electrical current  $I_{stack}$  (see chapter 3). Therefore, there are critical operating points where  $c_{vanadium}$  is close to its boundary; and in some cases, the variation of vanadium concentrations tends toward the limit values of the concentrations. These critical operating points are highlighted in Fig. 6.6 and depend on the operating mode of the battery. For example, when the  $SoC$  is close to zero (battery almost discharged) and the battery is still being discharged, the  $V^{2+}$  and  $V^{5+}$



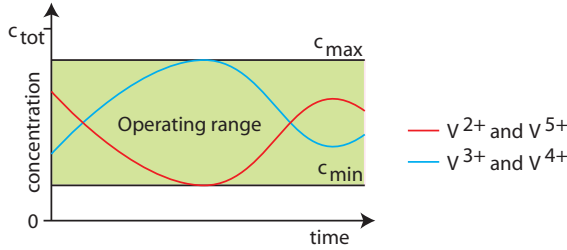


Figure 6.5.: The operating range of the vanadium concentrations  $c_{\text{vanadium}}$  is limited by the maximal concentration  $c_{\text{max}}$  and the minimal concentration  $c_{\text{min}}$ .

concentrations, which are already low, approach the minimal concentration  $c_{\text{min}}$ . At the same time, the  $V^{3+}$  and  $V^{4+}$  concentrations, which are already high, increase toward the maximal concentration  $c_{\text{max}}$ .

In these critical regions, the electrolyte flowrate  $Q$  must be larger to palliate the scarcity of electroactive vanadium ions; in fact, we can generalize this principle and determine a minimal flowrate  $Q_{\text{min}}$  for each operating point that supplies just enough active species to sustain the redox reactions. The necessary amount of active species is proportional to the reaction rate (see section 3.2.1); and in consequence, to the current  $I_{\text{stack}}$  according to (3.7). Of course, the minimal flowrate  $Q_{\text{min}}$  also depends on the input vanadium concentration  $c_{\text{in}}$ ; a value proportional to the state of charge  $SoC$ .

### Minimal Flowrate Determined by the Output Concentrations

In fact, there are two possibilities to define the boundaries of the vanadium concentrations: they can either be limited by the output concentration  $c_{\text{out}}$  or by the concentrations within the cells  $c_{\text{cell}}$ . In both cases, the maximal concentrations  $c_{\text{out,max}}$  or  $c_{\text{cell,max}}$  and minimal concentrations  $c_{\text{out,min}}$  or  $c_{\text{cell,min}}$  must be defined. In this section, we will determine the minimal flowrate  $Q_{\text{min}}$  from the output concentrations, and in the next, the concentrations within the cell  $c_{\text{cell}}$  will determine  $Q_{\text{min}}$ .

Rigorously, there are two cases that must be considered to determine  $Q_{\text{min}}$ : in the first case, the minimal flowrate  $Q_{\text{min},\downarrow}$  depends on the vana-

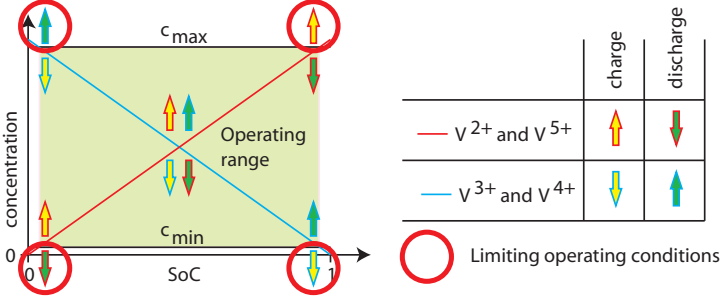


Figure 6.6.: Operating range and limiting operating conditions. The arrows represent the direction of the vanadium concentrations change as a function of the battery operating mode. The critical operating regions are highlighted in red; they represent the regions where the vanadium concentration  $c_{vanadium}$  tends to its limiting concentrations ( $c_{max}$  or  $c_{min}$ ).

dium species with decreasing concentrations  $c_{in,\downarrow}$ , and in the other, the minimal flowrate  $Q_{min,\uparrow}$  depends on the species with increasing concentrations  $c_{in,\uparrow}$ . Of course,  $Q_{min,\downarrow}$  and  $Q_{min,\uparrow}$  depend on the current  $I_{stack}$  and on the state of charge  $SoC$ . Their values are obtained by rearranging (3.10):

$$Q_{min,\downarrow}(t) = \frac{bN_{cell}i(t)}{F(c_{out,min} - c_{in,\downarrow}(t))} \quad [l/s] \quad (6.6)$$

$$Q_{min,\uparrow}(t) = \frac{bN_{cell}i(t)}{F(c_{out,max} - c_{in,\uparrow}(t))} \quad [l/s] \quad (6.7)$$

where  $b$  is the sign factor obtained from (3.9). In the case of well balanced vanadium concentrations, and equilibrated operating boundaries ( $c_{out,min}$  and  $c_{out,max}$ ), these two values are equal. Otherwise, the minimal flowrate  $Q_{min}$  is given by the greatest value of (6.6) and (6.7):

$$Q_{min}(t) = \max(Q_{min,\downarrow}(t), Q_{min,\uparrow}(t)) \quad [l/s] \quad (6.8)$$

### Minimal Flowrate Determined by the Cell Concentrations

Similarly, in the case where the limiting conditions are expressed with the vanadium concentrations within the cells  $c_{cell,max}$  and  $c_{cell,min}$ , the minimal flowrate  $Q_{min,av}$  is determined by introducing (3.10) into (3.11); after some rearrangements, the minimal flowrate  $Q_{min,av,\downarrow}$  for the species with decreasing concentrations  $c_{in,\downarrow}$  and the minimal flowrate  $Q_{min,av,\uparrow}$  for the species with increasing concentrations  $c_{in,\uparrow}$  are obtained from:

$$Q_{min,av,\downarrow}(t) = \frac{bN_{cell}i(t)}{2F(c_{cell,min} - c_{in,\downarrow}(t))} \quad [l/s] \quad (6.9)$$

$$Q_{min,av,\uparrow}(t) = \frac{bN_{cell}i(t)}{2F(c_{cell,max} - c_{in,\uparrow}(t))} \quad [l/s] \quad (6.10)$$

Again, these flowrates,  $Q_{min,av,\downarrow}$  and  $Q_{min,av,\uparrow}$ , should be equal if the vanadium concentrations are well balanced and the operating boundaries ( $c_{cell,min}$  and  $c_{cell,max}$ ) are equilibrate; otherwise the minimal flowrate  $Q_{min,av}$  is the largest value of (6.9) and (6.10):

$$Q_{min,av}(t) = \max(Q_{min,av,\downarrow}(t), Q_{min,av,\uparrow}(t)) \quad [l/s] \quad (6.11)$$

### Illustration of the minimal flowrate

The minimal flowrate  $Q_{min}$  is illustrated in Fig. 6.7 for a large number of operating points. We observe that the maximal values of  $Q_{min}$  occur in the critical regions that were highlighted in Fig. 6.6: low state of charge  $SoC$  and high current  $I_{stack}$  during the discharge, and high  $SoC$  and high  $I_{stack}$  during the charge. Moreover, the flowrate  $Q_{min}$  is, in comparison, very small in every other operating region; therefore, there must be a large benefit to operate the battery at  $Q_{min}$ . Finally, we remark that  $Q_{min}$  depends proportionally on  $I_{stack}$  and exponentially on  $SoC$ .

In addition, the corresponding mechanical power  $P_{mech,Qmin}$  required by a single pump to flow the electrolyte at  $Q_{min}$  is also illustrated in Fig. 6.7; we observe that  $P_{mech,Qmin}$  is very sensible to the state of charge  $SoC$  in the two critical regions and that it depends exponentially on the current  $I_{stack}$  and on the state of charge  $SoC$ .

Finally, we can retrieve in Fig. 6.7 the maximal flowrate  $Q_{max}$  and its corresponding maximal mechanical power  $P_{mech,Qmax}$  introduced in the previous section; these maximal values appear in both critical regions.

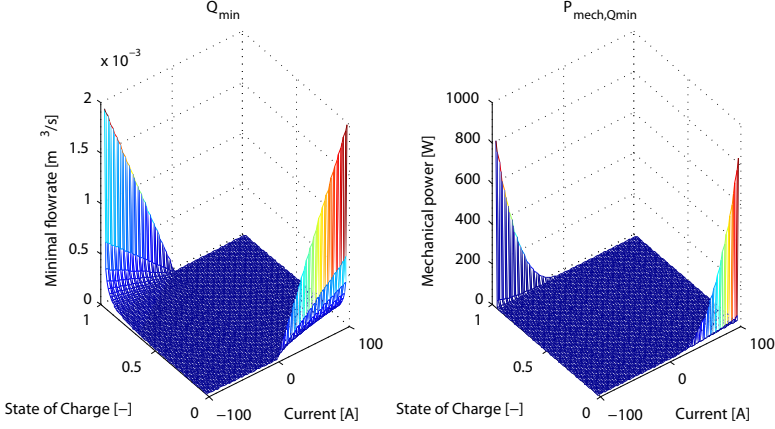


Figure 6.7.: Minimal flowrate  $Q_{min}$  and pump power  $P_{mech,Qmin}$  at minimal flowrate as a function of the  $SoC$  and the current  $I$ . Note that  $P_{mech,Qmin}$  represents here the mechanical power of a single pump.

Moreover, we can clearly imagine the effect that a limited operating range (smaller current  $I_{stack}$  and/or narrower  $SoC$  range) has on the maximal flowrate  $Q_{max}$  and its corresponding mechanical power  $P_{mech,Qmax}$ .

### Considerations on the Stack Power and on the Battery Power

We have just seen that the minimal flowrate  $Q_{min}$  has a beneficial influence on the mechanical power  $P_{mech}$ ; but we should also know that a change in flowrate  $Q$  does not only modify  $P_{mech}$  but also the stack voltage  $U_{stack}$ , and in consequence the stack power  $P_{stack}$ . Indeed, the vanadium concentrations within the stack  $c_{cell}$  determine the equilibrium stack voltage  $E_{stack}$  (see section 2.3.1); these concentrations are not constant and change as the battery operates (see section 3.2). In fact, the change in vanadium concentrations within the stack depends on the current  $I_{stack}$  and is inversely proportional to the flowrate  $Q$  (see (3.10)); therefore, the stack voltage  $U_{stack}$  becomes a function of the flowrate  $Q$ .

In fact, the change in concentrations within the stack is maximal at  $Q_{min}$ ; in consequence, we should also expect a variation of the stack equi-

### 6.3. ENERGETIC CONSIDERATIONS AT CONSTANT CURRENT

librium voltage  $E_{stack}$ , the stack voltage  $U_{stack}$  and the stack power  $P_{stack}$  between the operations at  $Q_{min}$  and at  $Q_{max}$ . This phenomenon is illustrated in Fig. 6.8 where the cell equilibrium voltage  $E$  is shown at minimal flowrate  $Q_{min}$  and at maximal flowrate  $Q_{max}$  for both the charge and the discharge. The equivalent state of charge  $SoC_{eq}$  represents the  $SoC$  of the electrolyte within the stack, and is also illustrated in Fig. 6.8 as a function of the flowrate  $Q$  and of the battery operating mode. We remark that the equivalent  $SoC_{eq}$  tends toward the battery  $SoC$  at high flowrate  $Q$ . Of course, the situations are different for each operating point, but the tendency is always the same.

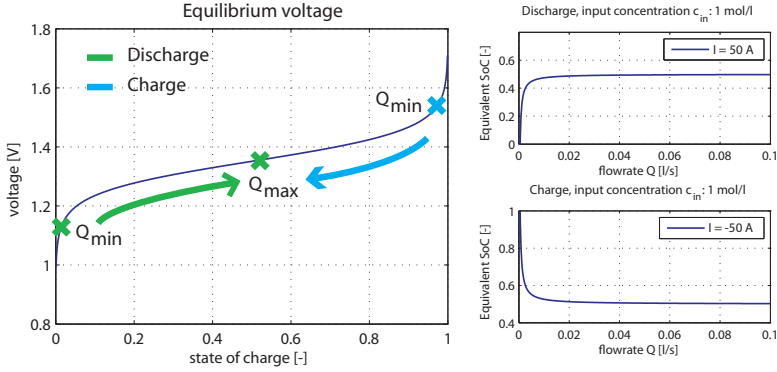


Figure 6.8.: Effect of the flowrate  $Q$  on the equilibrium voltage  $E$ . On the right, the variation of the equivalent state of charge  $SoC$  as a function of  $Q$  during the discharge and the charge. In this example, the battery  $SoC$  is 0.5, i.e. the input concentrations are 1 M for each vanadium species.

In addition, we observe that an increase of the flowrate  $Q$  has a beneficial effect on the equilibrium voltage  $E$ ; the direction of the change depends on the operating mode and its amplitude depends on the battery  $SoC$ . This phenomenon is important because the battery is operated at constant current  $I_{stack,ref}$ ; therefore the internal losses  $U_{loss}$  and  $P_{loss}$  are constant since they are only proportional to  $I_{stack,ref}$  (see section 3.4). In consequence, the stack power  $P_{stack}$  depends directly on the equilibrium stack voltage  $E_{stack}$  (see (6.1)).

Therefore, the stack power  $P_{stack}$  becomes larger when the flowrate  $Q$  is increased during the discharge; it reaches its maximal value at maximal flowrate  $Q_{max}$ : this value depends on the actual state of charge  $SoC$ . During the charge,  $P_{stack}$  is minimal at  $Q_{max}$ ; thus, from the strict point of view of  $P_{stack}$ , it is more interesting to operate the battery at maximal flowrate  $Q_{max}$ . Indeed, for the same amount of electrons  $e^-$  consumed (or stored) from (or in) the electrolyte, the stack power is maximal during the discharge and minimal during the charge. The difference between the stack power  $|P_{stack,Q_{max}}|$  at  $Q_{max}$  and the stack power  $|P_{stack,Q_{min}}|$  at  $Q_{min}$  is shown in Fig. 6.9.

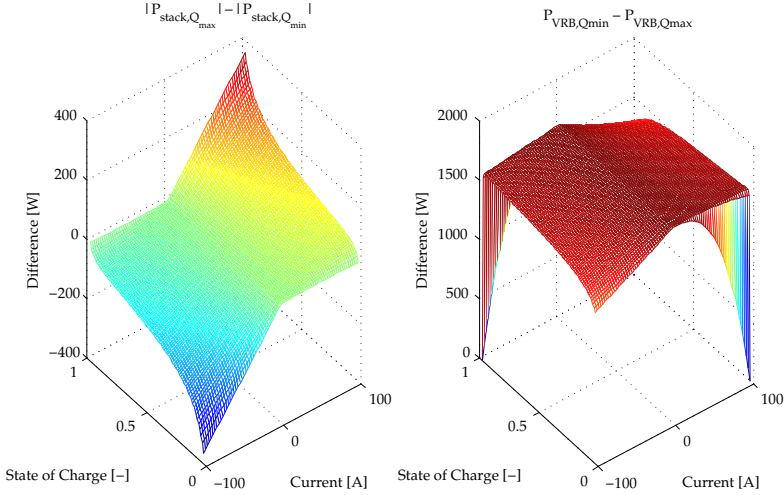


Figure 6.9.: Left: The difference between the stack power  $|P_{stack,Q_{max}}|$  at  $Q_{max}$  and the stack power  $|P_{stack,Q_{min}}|$  at  $Q_{min}$ . Right: the difference between the battery power  $P_{battery,Q_{min}}$  at  $Q_{min}$  and the battery power  $P_{battery,Q_{max}}$  at  $Q_{max}$ .

We observe in Fig. 6.9 that the difference is minimal in the critical regions defined previously in Fig. 6.6 where the minimal flowrate  $Q_{min}$  is close to  $Q_{max}$ ; logically, the difference is larger where the difference between the flowrates is also larger. In fact, the stack delivers more power

$P_{stack}$  for the same current  $I_{stack}$  during the discharge at maximal flowrate  $Q_{max}$  and consumes less power  $P_{stack}$  during the charge also at  $Q_{max}$ . Nevertheless, the stack power  $P_{stack}$  is not the only variable affecting the battery performance; indeed, the mechanical power  $P_{mech}$  greatly deteriorates its performance at maximal flowrate  $Q_{max}$ .

In fact, operating the battery at minimal flowrate  $Q_{min}$  has always an overall positive influence on the battery performance when compared to operations at  $Q_{max}$ . The gain in power exchanged with the battery  $P_{VRB}$  is shown in Fig. 6.9 where the gain during the discharge corresponds to a supplement of power delivered to the load and the gain during the charge corresponds to the power spared by the source. In this example, the average gain is around 1575 W; this is not negligible for a 2.5 kW, 15 kWh VRB!

Finally, the instantaneous battery efficiency  $\eta_{battery}$  (6.5) at minimal flowrate  $Q_{min}$  is illustrated in Fig. 6.10. Clearly, we observe again a large gain of performance when compared to the battery operations at constant flowrate  $Q_{max}$ . We conclude that operating the battery at minimal flowrate  $Q_{min}$  is always a better control strategy than operating it at constant flowrate  $Q_{max}$ . In section 6.3.3, we will introduce a method to find the optimal flowrate  $Q_{opt}$ .

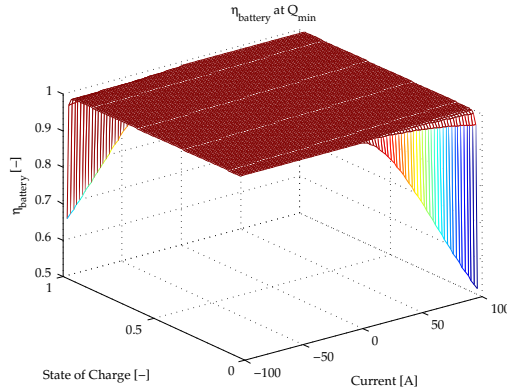


Figure 6.10.: The battery efficiency  $\eta_{battery}$  at minimal flowrate  $Q_{min}$  as a function of  $SoC$  and  $I_{stack}$ .

### 6.3.3. Optimal Flowrate

We have seen in the previous sections the advantages and disadvantages to operate the battery at either maximal flowrate  $Q_{max}$  or minimal flowrate  $Q_{min}$ . At  $Q_{max}$ , the stack power  $P_{stack}$  has the highest possible value but the mechanical power  $P_{mech}$  required to flow the electrolytes is also very large and thus deteriorates the battery performance. At minimal flowrate  $Q_{min}$ ,  $P_{mech}$  is reduced to the minimum, but  $P_{stack}$  is also reduced to a minimal value. Therefore, it should exist an optimal flowrate  $Q_{opt}$  somewhere between  $Q_{min}$  and  $Q_{max}$  that increases the stack power  $P_{stack}$  while maintaining the mechanical power  $P_{mech}$  at a small value. The method proposed in this section to determine the optimal flowrate at any operating point, whereas similar in many aspects, differs a little between the charge and the discharge.

#### Optimal Flowrate during the Discharge

This first section focuses on the method to determine the optimal flowrate  $Q_{opt}$  during the discharge: this flowrate should maximize the power delivered by the stack  $P_{stack}$  while minimizing the mechanical power  $P_{mech}$ ; when these conditions are met together, the power delivered by the battery  $P_{VRB}$  is optimized. We can express these conditions by the following relation:

$$\max_{f(U_{stack}, I_{VRB})}(\underbrace{P_{VRB}}_{f(U_{stack}, I_{VRB})}) = \max_{f(I_{stack}, Q, SoC)}(\underbrace{P_{stack}}_{f(I_{stack}, Q, SoC)} - \underbrace{P_{mech}}_{f(Q, \mu, \rho)}) \quad [W] \quad (6.12)$$

First, we must remember that we consider the stack current  $I_{stack,ref}$  constant in this section; therefore, the only control variable available to modify the battery performance is the flowrate  $Q$ . The case where the battery power  $P_{VRB,ref}$  is set by the user, and thus considered constant, is quite different and is discussed in section 6.4. The stack power  $P_{stack}$  is composed of two parts: the internal losses  $P_{loss}$  (see section 3.4) that depend only on the stack current  $I_{stack}$  and the equilibrium stack voltage  $E_{stack}$  that depends on the vanadium concentrations within the cells (see the Nernst equation (2.29)), on the flowrate  $Q$  and on the current  $I_{stack}$ . In consequence, the stack power  $P_{stack}$  is a function of  $I_{stack}$ ,  $Q$  and  $SoC$ ; but the only control variable able to modify  $P_{stack}$  in this case is the flowrate  $Q$ .



The mechanical power  $P_{mech}$  is determined from the mechanical model introduced in section 5.6;  $P_{mech}$  depends only on the flowrate  $Q$  and on the electrolyte properties  $\mu$  and  $\rho$ . Although these two properties depend on the state of charge, they are considered constant in this chapter. Therefore, the flowrate is also the only variable that influences the mechanical power  $P_{mech}$ . Therefore, the battery power  $P_{VRB}$  is also a function of  $Q$  and is determined by (6.4).

The battery power  $P_{VRB}$  is illustrated in Fig. 6.11 for a discharge current  $I_{stack}$  of 100 A as a function of the flowrate  $Q$  and of the state of charge  $SoC$ ; some curves at other discharge currents are given in appendix C. As it was expected, there is, in most cases, an optimal flowrate  $Q_{opt}$  in between  $Q_{min}$  and  $Q_{max}$  that maximizes the battery power  $P_{VRB}$ . At very low  $SoC$ , the optimal flowrate  $Q_{opt}$  is equal to  $Q_{min}$ ; this is due to the very small amount of electroactive species in the electrolyte. Furthermore, other curves such as the stack voltage  $U_{stack}$ , the equilibrium stack voltage  $E_{stack}$ , the stack voltage  $P_{stack}$ , the vanadium concentration  $c_{cell}$  within the cells, the equivalent  $SoC_{eq}$  and the mechanical power of a single pump are given in Fig. C.2 at a stack current  $I_{stack}$  of 100 A.

The shape of the curves of Fig. 6.11 can be generalized to other discharge currents  $I_{stack} > 0$  (see Fig. C.4 and C.5); although in some cases where the current  $I_{stack}$  is low, the battery power  $P_{VRB}$  might become negative at inappropriately high flowrate  $Q$ . Furthermore, there is a transition flowrate  $Q_{transition}$  between the laminar and the turbulent regimes; this flowrate is determined from the Reynolds equation (5.1) and is equal, for the 2.5 kW, 15 kWh VRB to 0.1551 l/s. In reality, there is an intermediate regime where the flow is neither laminar nor turbulent; in this model, this regime is neglected. Hence, there is a small discontinuity in the mechanical power  $P_{mech}$  at this flowrate  $Q_{transition}$ ; indeed,  $P_{mech}$  is larger for a turbulent regime than for a laminar regime. In consequence, this change of flow regime influences the optimal flowrate  $Q_{opt}$  in some operating points as it can be observed in Fig. C.5.

### Optimal Flowrate during the Charge

In many aspects, the method to determine the optimal flowrate  $Q_{opt}$  during the charge is similar to the method introduced in the previous section. The main difference is that the power furnished to the battery  $P_{VRB}$  should be minimized in that case. Indeed, at constant current  $I_{stack,ref}$ ,

### 6.3. ENERGETIC CONSIDERATIONS AT CONSTANT CURRENT

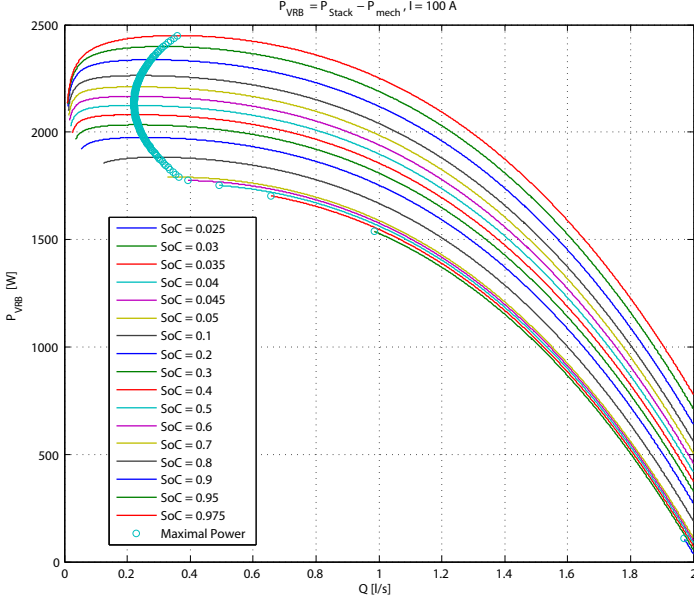


Figure 6.11.: Optimal flowrate  $Q_{opt}$  as a function of the flowrate  $Q$  and the state of charge  $SoC$ . Note that when  $SoC$  is low,  $Q_{opt}$  is equal to the minimal flowrate  $Q$ , and the discharge current is equal to 100 A.

the quantity of electrons  $e^-$  stored in the electrolyte does not depend on the stack power  $P_{stack}$  but solely on the stack current  $I_{stack}$ ; therefore, there is no reason to have a high  $P_{stack}$ . Hence, the optimal flowrate  $Q_{opt}$  is found when the sum of  $P_{stack}$  and the mechanical power  $P_{mech}$  are simultaneously minimal. This condition is expressed by the following relation<sup>3</sup>:

$$\min_{f(U_{stack}, I_{VRB})} \left( \underbrace{P_{VRB}}_{f(U_{stack}, I_{VRB})} \right) = \min_{f(I_{stack}, Q, SoC)} \left( \underbrace{P_{stack}}_{f(I_{stack}, Q, SoC)} + \underbrace{P_{mech}}_{f(Q, \mu, \rho)} \right) \quad [W] \quad (6.13)$$

<sup>3</sup>A close look at this relation reveals that it is the same as (6.12), although we believe that (6.13) is more intuitive for the charge.

### 6.3. ENERGETIC CONSIDERATIONS AT CONSTANT CURRENT

The battery power  $P_{VRB}$  is illustrated in Fig. 6.12 for a charge current  $I_{stack}$  of -100 A as a function of the flowrate  $Q$  and the state of charge  $SoC$ ; more curves at different charge currents are given in appendix C. Again, we remark that, in most cases, there is an optimal flowrate  $Q_{opt}$  between  $Q_{min}$  and  $Q_{max}$  that minimizes the battery power  $P_{VRB}$ . At very high  $SoC$ ,  $Q_{opt}$  is equal to  $Q_{min}$ ; this is due to the small amount of electroactive vanadium ions carried by the electrolyte. Furthermore, other curves such as the stack voltage  $U_{stack}$ , the equilibrium stack voltage  $E_{stack}$ , the stack voltage  $P_{stack}$ , the vanadium concentration  $c_{cell}$  within the cells, the equivalent  $SoC_{eq}$  and the mechanical power of a single pump are given in Fig. C.3 at a charge current  $I_{stack}$  of -100 A.

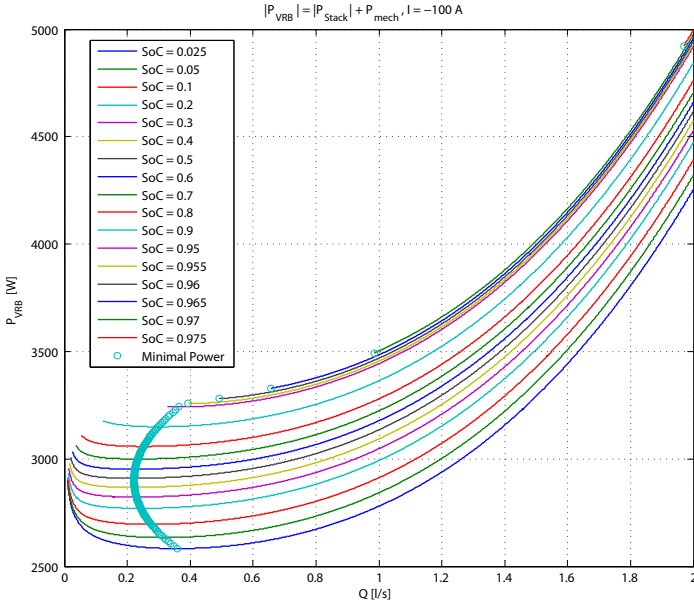


Figure 6.12.: Optimal flowrate  $Q_{opt}$  as a function of the flowrate  $Q$  and the state of charge  $SoC$ . Note that when  $SoC$  is high,  $Q_{opt}$  is equal to the minimal flowrate  $Q$ , and that the charge current  $I_{stack}$  is equal to -100 A.

The shape of the curves of Fig. 6.12 can be generalized to other charge currents  $I_{stack} < 0$  (see Fig. C.4 and C.5). Similarly to the discharge case, there is a small discontinuity in the mechanical power  $P_{mech}$  at the transition flowrate  $Q_{transition}$ . In consequence, the change of flow regime influences the optimal flowrate  $Q_{opt}$  in some operating points as it can be observed in Fig. C.5.

The optimal flowrate  $Q_{opt}$  is illustrated in Fig. C.1 and 6.13 as a function of the current  $I_{stack}$  and the state of charge  $SoC$ ; we observe that  $Q_{opt}$  is close to the minimal flowrate  $Q_{min}$  in the critical regions where there is a scarcity of electroactive species; moreover  $Q_{opt}$  tends to increase at both extremities of the  $SoC$  operating range. Furthermore, the optimal flowrate  $Q_{opt}$  is compared to  $Q_{min}$  in Fig. 6.13 at three different  $SoC$ ; we observe that  $Q_{opt}$  is always larger than  $Q_{min}$ , and grows exponentially with the stack current  $I_{stack}$  whereas the minimal flowrate  $Q_{min}$  increases linearly with  $I_{stack}$ . Clearly, the optimal flowrate  $Q_{opt}$  reaches a plateau when the flow regime becomes turbulent.

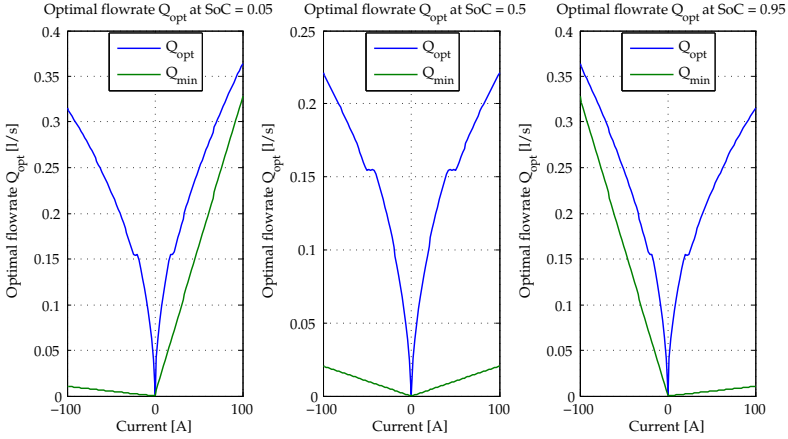


Figure 6.13.: Optimal flowrate  $Q_{opt}$  and minimal flowrate  $Q_{min}$  as a function of the current  $I_{stack}$  at  $SoC$  equal to respectively 0.05, 0.5 and 0.95.

### Assessment of the Benefits of the Optimal Flowrate

To conclude this section dedicated to the optimal flowrate  $Q_{opt}$ , we will assess the benefits of operating the battery at  $Q_{opt}$  in comparison with the previous operation at minimal flowrate  $Q_{min}$ . The difference between the battery power at optimal flowrate  $P_{VRB,Q_{opt}}$  and the battery power at minimal flowrate  $P_{VRB,Q_{min}}$  is illustrated in Fig. 6.14; this difference is not so impressive as the difference between  $P_{VRB,Q_{max}}$  and  $P_{VRB,Q_{min}}$  (see Fig. 6.9), but there is still a benefit to operate the battery at  $Q_{opt}$  during the charge and during the discharge. The average value of the difference is 57 W; furthermore, the energetic efficiency  $\eta_{energy}$  during a charge and discharge will be discussed in section 6.3.4.

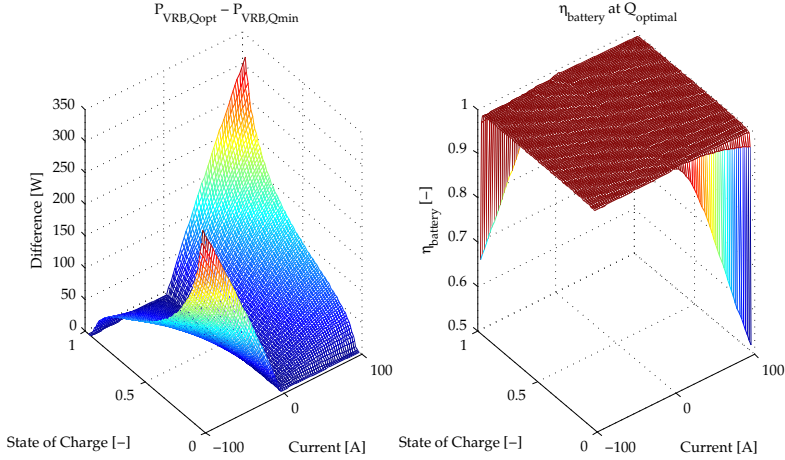


Figure 6.14.: Difference between the battery power  $P_{VRB,opt}$  at optimal flowrate  $Q_{opt}$  and the battery power  $P_{VRB,Q_{min}}$  at minimal flowrate  $Q_{min}$ .

In the critical regions, the difference is very small since the optimal flowrate  $Q_{opt}$  is equal or very close to the minimal flowrate  $Q_{min}$  whereas it becomes larger as the operating point is moved away from these regions. The instantaneous battery efficiency  $\eta_{battery,Q_{opt}}$  at optimal flowrate  $Q_{opt}$  is also shown in Fig. 6.14; although the difference with this metric between  $Q_{opt}$  and  $Q_{min}$  is very small,  $\eta_{battery,Q_{opt}}$  is always larger than

$\eta_{battery, Q_{min}}$ . Finally, note that the battery power  $P_{VRB}$  at optimal flowrate  $Q_{opt}$  is illustrated in Fig. C.1.

#### 6.3.4. Charge and Discharge Cycle at Constant Current

It is always difficult to assess the performance of a battery because it often depends on the operating conditions; in section 3.10, we have proposed a good method to assess the electrochemical performance of the stack that performs a series of charge and discharge cycles at constant current or at constant power. The energy efficiency  $\eta_{energy}$ , the voltage efficiency  $\eta_{voltage}$  and the coulombic efficiency  $\eta_{coulombic}$ , were defined in section 3.8 to compare the battery performances under different operating conditions.

We have seen in this chapter that the operating conditions, in particular the flowrate  $Q$ , influence the overall battery performance; indeed, even the stack voltage  $U_{stack}$  and the stack power  $P_{stack}$  are a function of the flowrate  $Q$  (see section 6.3.3). Hence, the efficiencies found in sections 3.10.1 and 3.10.2 are valid only at their respective electrolyte flowrate<sup>4</sup>. So, a new series of charge and discharge cycles at constant stack current  $I_{stack}$  has been performed to determine the overall VRB efficiency at the maximal flowrate  $Q_{max}$ , at the minimal flowrate  $Q_{min}$  and at the optimal flowrate  $Q_{opt}$ .

The energy efficiency was defined in section 3.8 as the ratio of the energy furnished by the battery during the discharge to the energy supplied during the charge (3.25); hence, the overall VRB energy efficiency  $\eta_{energy}$  which includes the mechanical loss  $P_{mech}$ , is given by:

$$\begin{aligned}\eta_{energy} &= \frac{\int P_{VRB, discharge}(t) dt}{\int |P_{VRB, charge}|(t) dt} \\ &= \frac{\int P_{stack}(t) - P_{mech}(t) dt}{\int |P_{stack}(t)| + P_{mech}(t) dt} \quad [-]\end{aligned}\tag{6.14}$$

The coulombic efficiency  $\eta_{coulombic}$  is a measure of the ratio of the charge withdrawn from the battery during the discharge to the charge supplied during the charge; it indicates the proportion of charges lost by side reactions such as oxygen or hydrogen evolution, or by cross mixing of the electrolyte. Since the multiphysics model developed in this work does not

---

<sup>4</sup>The flowrate  $Q$  was 2 l/s.

### 6.3. ENERGETIC CONSIDERATIONS AT CONSTANT CURRENT

Current [A]	$\eta_{voltage, Q_{max}}$ [%]	$\eta_{voltage, Q_{min}}$ [%]	$\eta_{voltage, Q_{opt}}$ [%]
10	97.02	87.74	96.69
20	94.13	85.11	93.70
40	88.58	80.09	88.03
60	83.33	75.31	82.69
80	78.37	70.78	77.68
100	73.65	66.46	72.94

Table 6.1.: Stack voltage efficiency  $\eta_{voltage}$  at constant maximal flowrate  $Q_{max}$ , at minimal flowrate  $Q_{min}$  and at optimal flowrate  $Q_{opt}$ .

take these losses into account,  $\eta_{coulombic}$  is always equal to 100% and will not be discussed further.

The voltage efficiency  $\eta_{voltage}$  is a measure of the ohmic and polarisation losses during the cycles; it is defined as the ratio of the integral of the battery voltage during the discharge to that of the voltage during the charge. In fact, the voltage efficiency is a metric of the electrochemical performance of the battery; therefore, only the stack voltage  $U_{stack}$  should be considered. Hence, the voltage efficiency  $\eta_{voltage}$  derived from (3.27) becomes:

$$\eta_{voltage} = \frac{\int U_{stack, discharge}(t)dt}{\int U_{stack, charge}(t)dt} \neq \frac{\eta_{energy}}{\eta_{coulombic}} \quad [-] \quad (6.15)$$

Because the energy efficiency  $\eta_{energy}$  includes the mechanical loss  $P_{mech}$ , the voltage efficiency  $\eta_{voltage}$  is not equal anymore to the ratio of the energy efficiency  $\eta_{energy}$  to the coulombic efficiency  $\eta_{coulombic}$ . And since the considered battery has the same electrochemical characteristics as the battery discussed in section 3.10, we should find the same voltage efficiencies  $\eta_{voltage}$  at maximal flowrate  $Q_{max}$ . The voltage efficiencies at maximal flowrate  $\eta_{voltage, Q_{max}}$ , at minimal flowrate  $\eta_{voltage, Q_{min}}$  and at optimal flowrate  $\eta_{voltage, Q_{opt}}$  are given in Tab. 6.1.

First, we observe that the voltage efficiencies  $\eta_{voltage}$  decrease when the current  $I_{stack}$  increases; this phenomenon was already observed in Tab. 3.4 and is caused by the internal losses  $U_{loss}$  that are proportional to  $I_{stack}$  (see section 3.4). Moreover, the highest voltage efficiencies occur at max-

### 6.3. ENERGETIC CONSIDERATIONS AT CONSTANT CURRENT

imal flowrate  $Q_{max}$ ; indeed, we have seen that a high flowrate always has a positive effect on the stack equilibrium voltage  $E_{stack}$  and consequently on the stack voltage  $U_{stack}$  independently of the battery operating mode (see Fig. 6.8 and (6.15)). Therefore, the worst voltage efficiencies  $\eta_{voltage,Qmin}$  occur at minimal flowrate  $Q_{min}$ ; furthermore, the voltage efficiencies  $\eta_{voltage,Qopt}$  at optimal flowrate is very close to the maximal possible efficiencies  $\eta_{voltage,Qmax}$ . In fact, the stack voltage  $U_{stack,Qmax}$  and  $U_{stack,Qopt}$  are also very close as it can be observed in Fig. 6.15, C.6 and C.7; but their difference with the stack voltage  $U_{stack,Qmin}$  at minimal flowrate  $Q_{min}$  is large.

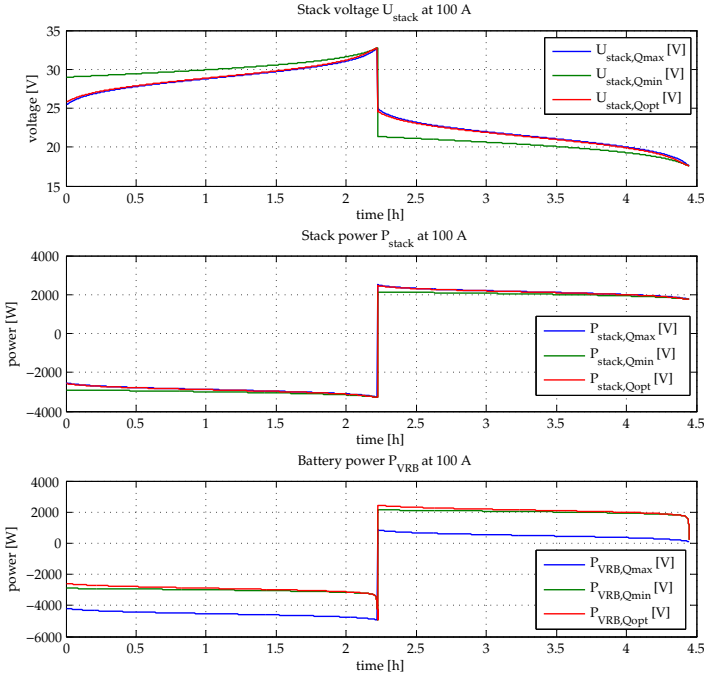


Figure 6.15.: Stack voltage  $U_{stack}$ , stack power  $P_{stack}$  and battery power  $P_{VRB}$  during a charge and discharge cycle at 100 A.



### 6.3. ENERGETIC CONSIDERATIONS AT CONSTANT CURRENT

Current [A]	Time [h]	$\eta_{energy, Q_{max}}$ [%]	$\eta_{energy, Q_{min}}$ [%]	$\eta_{energy, Q_{opt}}$ [%]
10	44.49	-73.42	87.73	96.54
20	22.24	-53.34	85.10	93.51
40	11.12	-25.65	80.04	87.77
60	7.41	-8.17	75.31	82.34
80	5.56	3.24	70.78	77.26
100	4.45	10.81	66.24	72.43

Table 6.2.: Overall VRB energy efficiencies  $\eta_{energy}$  at constant maximal flowrate  $Q_{max}$ , at minimal flowrate  $Q_{min}$  and at optimal flowrate  $Q_{opt}$ .

Then, we have also determined the overall VRB energy efficiencies with (6.14) at constant maximal flowrate  $\eta_{energy, Q_{max}}$ , at minimal flowrate  $\eta_{energy, Q_{min}}$  and at optimal flowrate  $\eta_{energy, Q_{opt}}$ ; the results are summarized in Tab. 6.2. Obviously, operating the battery at maximal flowrate  $Q_{max}$  is a terrible strategy: at some currents, the energy efficiencies  $\eta_{energy, Q_{max}}$  become negative. In fact, the battery does not deliver power to the load during the discharge at *small* currents but consumes more power to operate the pumps than the stack is furnishing (see Fig. C.6 and C.7). Of course, these efficiencies  $\eta_{energy, Q_{max}}$  might be improved if the flowrate  $Q_{max}$  is reduced; but this also limits the battery power rating and/or its energetic capacities.

The energy efficiencies  $\eta_{energy, Q_{min}}$  at minimal flowrate and  $\eta_{energy, Q_{opt}}$  at optimal flowrate are both reduced when the current  $I_{stack}$  increases; again, this is due to the internal losses  $U_{loss}$ . Although the relation (3.27) between the voltage efficiency  $\eta_{voltage}$  and the energy efficiency  $\eta_{energy}$  is clearly not applicable to the overall VRB storage system, their difference is small at both the minimal  $Q_{min}$  and optimal  $Q_{opt}$  flowrates. Therefore, the mechanical power  $P_{mech}$  at these two flowrates has only a limited influence on the energy efficiency  $\eta_{energy}$ .

But, the flowrate has a non-negligible effect on the stack power  $P_{stack}$  as it can be seen in Fig. 6.15, C.6 and C.7; in consequence, the battery power  $P_{VRB}$  is also influenced according to (6.2) and (6.3). Indeed, the difference between the energy efficiency  $\eta_{energy, Q_{min}}$  at minimal flowrate  $Q_{min}$  and the energy efficiency  $\eta_{energy, Q_{opt}}$  at optimal flowrate  $Q_{opt}$  is explained by

the difference in the stack powers  $P_{stack,Q_{min}}$  and  $P_{stack,Q_{opt}}$ .

In conclusion, we can state that the best strategy to operate the battery at constant current  $I_{stack,ref}$  is to find the optimal flowrate  $Q_{opt}$  at every operating point. During the charge and discharge cycles, the energy efficiency  $\eta_{energy}$  is increased by almost 10% between the minimal  $Q_{min}$  and optimal  $Q_{opt}$  flowrates; moreover, this difference tends to increase when the current  $I_{stack}$  is reduced.

## 6.4. Energetic Considerations at Constant Power

In the previous sections, we have discussed in detail the battery operation at constant current  $I_{stack,ref}$ ; we have introduced many principles that will also be useful in this last section dedicated to the battery operation at constant stack power  $P_{stack,ref}$  or constant battery power  $P_{VRB,ref}$ . In the previous sections, the only control variable was the flowrate  $Q$ ; a second control variable is available at constant power: the stack current  $I_{stack}$ .

Therefore, we will see how to determine the optimal operating point: this point is the combination of the optimal flowrate  $Q_{opt}$  and its corresponding stack current  $I_{stack,opt}$ . First, we will discuss the battery operation at constant stack power  $P_{stack,ref}$  and then at constant battery power  $P_{VRB,ref}$ .

### 6.4.1. Constant Stack Power

In this section, the battery is operated at constant stack power  $P_{stack,ref}$ ; similarly as in section 6.3.3 and from a power point of view, the optimal operating conditions should maximize the battery power  $P_{VRB}$  during the discharge:

$$\max(P_{VRB}) = \max(\underbrace{P_{stack}}_{\text{constant}} - \underbrace{P_{mech}}_{f(Q,\mu,\rho)}) \quad [W] \quad (6.16)$$

and it should minimize the battery power  $|P_{VRB}|$  during the charge:

$$\min(|P_{VRB}|) = \min(\underbrace{|P_{stack}|}_{\text{constant}} + \underbrace{P_{mech}}_{f(Q,\mu,\rho)}) \quad [W] \quad (6.17)$$

In these cases, there are two control variables that modify the operating

conditions: the flowrate  $Q$  and the current  $I_{stack}$ . Indeed, the mechanical power  $P_{mech}$  is a function of the flowrate  $Q$  and the electrolyte properties, although these properties are constant in this chapter; the stack power  $P_{stack}$  is the product of the current  $I_{stack}$  and the stack voltage  $U_{stack}$  that is a function of the flowrate  $Q$ , the state of charge  $SoC$  and  $I_{stack}$ . Hence, there are many control couples flowrate  $Q$  and current  $I_{stack}$  that produce the desired stack power  $P_{stack}$  as it can be observed in Fig. 6.16. The metric *ratio* used in Fig. 6.16 to assess the battery performance is defined as:

$$ratio = \frac{|P_{stack}|}{P_{mech}} \quad [-] \quad (6.18)$$

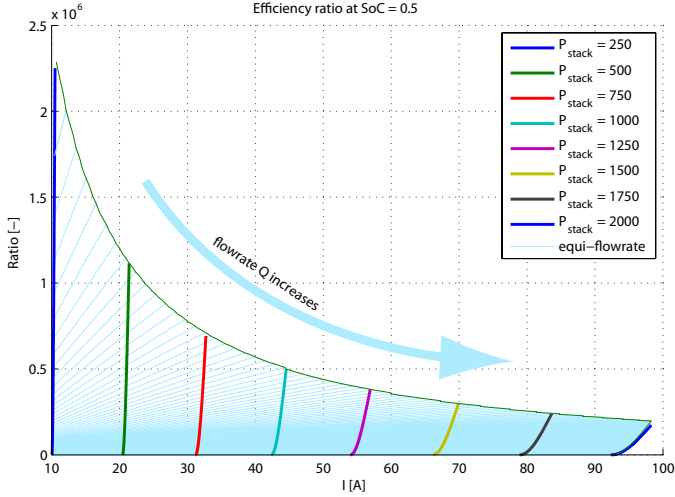


Figure 6.16.: Efficiency ratio at various stack powers  $P_{stack}$  as a function of the flowrate  $Q$  and the current  $I_{stack}$  during the discharge.

Since the stack power  $P_{stack}$  is constant, it is clear that the conditions (6.16) and (6.17) are met when the flowrate  $Q$  is minimal (see also Fig. 6.16). But at this minimal flowrate  $Q_{min}$ , the current  $I_{stack}$  is max-

imal because it must compensate the lower stack voltage  $U_{stack}$ . In consequence, more electrons  $e^-$  are necessary to sustain the larger reaction rates; and thus, the battery is discharged faster. Therefore, the battery performance must somehow be reduced; the optimal operating point is very difficult to find because there is no way to give a power or energetic value to an electron. Indeed, the power delivered depends on the discharge conditions: the electron energy is higher when the stack voltage is higher. The analysis of the charge at constant stack power  $P_{stack,ref}$  leads to similar conclusions.

### 6.4.2. Constant Battery Power

This last section focuses on the most probable operating conditions: the constant battery power  $P_{VRB,ref}$ . Indeed, most applications consume a more or less constant power.

$$\underbrace{P_{VRB}}_{constant} = \underbrace{P_{stack}}_{f(I_{stack}, Q, SoC)} - \underbrace{P_{mech}}_{f(Q, \mu, \rho)} \quad [W] \quad (6.19)$$

In that case, there are also two control variables: the flowrate  $Q$  and the current  $I_{stack}$ . The stack power  $P_{stack}$  is a function of the stack current  $I_{stack}$ , the electrolyte flowrate  $Q$  and the state of charge  $SoC$  and the mechanical power  $P_{mech}$  depends on the flowrate  $Q$  and the electrolyte properties. The optimal operating point should store as many electrons  $e^-$  as possible during the charge and should consume as few  $e^-$  as possible during the discharge. Hence, these conditions are expressed by the following relations:

$$\begin{aligned} \text{during the charge: } \max(|I_{stack}|) & \quad [A] \\ \text{during the discharge: } \min(I_{stack}) & \quad [A] \end{aligned} \quad (6.20)$$

### Optimal Operating Point during the Discharge

The battery power  $P_{VRB}$  during the discharge is illustrated in Fig. 6.17 as a function of the current  $I_{stack}$  and the flowrate  $Q$  at a state of charge  $SoC$  equal to 0.5. We observe that there is an optimal flowrate  $Q_{opt}$  that minimizes the discharge current  $I_{stack}$ ; at this optimal flowrate  $Q_{opt}$  the battery delivers the same power  $P_{VRB}$  but consumes less active vanadium ions and therefore the battery will operate longer and deliver more power.

The optimal flowrate  $Q_{opt}$  increases with the battery power  $P_{VRB}$  until it reaches a plateau due to the transition between the laminar and the turbulent regime; the transition flowrate is equal to 0.1551 l/s for the battery considered in this chapter.

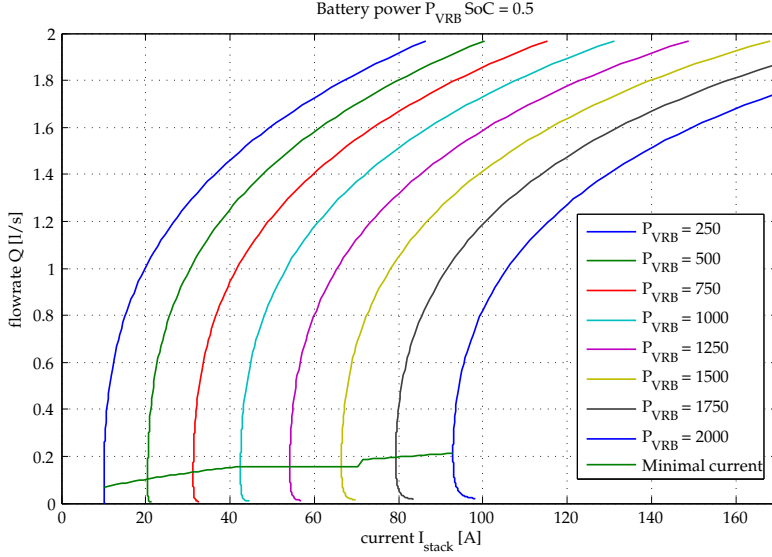


Figure 6.17.: Battery power  $P_{VRB}$  as a function of the discharge current  $I_{stack}$  and the electrolyte flowrate  $Q$  at a state of charge  $SoC$  equal to 0.5. The optimal operating points occurs when the current  $I_{stack}$  is minimal for a given battery power  $P_{VRB}$ .

In fact, the current  $I_{stack}$  above the optimal flowrate  $Q_{opt}$  increases to compensate the higher mechanical loss  $P_{mech}$ , i.e. the stack delivers more power  $P_{stack}$ . And the current  $I_{stack}$  also increases below  $Q_{opt}$ , this time to compensate the lower stack voltage  $U_{stack}$  due to the lower concentrations of active species (see Fig. 6.8). Furthermore, the shape of the curves shown in Fig. 6.17 might be generalized for other states of charge  $SoC$ ; some curves at different states of charge are given in Fig. C.8 and C.9. In some cases, there is no plateau because the optimal flowrate is above the

transition region.

### Optimal Operating Point during the Charge

The optimal operating points during the charge are illustrated in Fig. 6.18 where the battery power  $P_{VRB}$  is shown as a function of the current  $I_{stack}$  and the flowrate  $Q$  at a state of charge of 0.5. The optimal operating point maximizes the current  $|I_{stack}|$  delivered to the stack in order to store the maximum amount of electroactive species at a given power  $P_{VRB,ref}$ ; again, the optimal flowrate  $Q_{opt}$  increases with the battery power  $P_{VRB}$  until it reaches the plateau due to the flow regime transition.

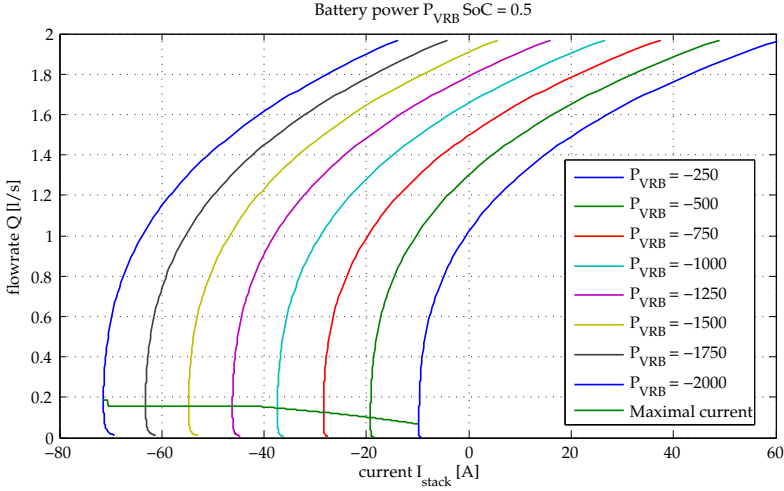


Figure 6.18.: Battery power  $P_{VRB}$  as a function of the charge current  $I_{stack}$  and the electrolyte flowrate  $Q$  at a state of charge  $SoC$  equal to 0.5. The optimal operating points occurs when the current  $|I_{stack}|$  is maximal for a given battery power  $P_{VRB}$ .

Interestingly, we observe in Fig. 6.18 that the stack current  $I_{stack}$  changes its sign at high flowrate  $Q$ ; in these unacceptable conditions, the stack is discharged while the battery is being charged. During the charge,

Power [W]	$\eta_{energy, Qmin}$ [%]	$\eta_{energy, Qopt}$ [%]
500	87.07	93.59
1000	81.04	87.78
1500	75.47	82.09
2000	69.91	76.39
2500	63.97	70.48

Table 6.3.: Overall VRB energy efficiencies  $\eta_{energy}$  for a charge and discharge cycle at constant power at either optimal flowrate  $Q_{opt}$  and minimal flowrate  $Q_{min}$ .

the stack current  $|I_{stack}|$  decreases above the optimal flowrate  $Q_{opt}$  to compensate the higher mechanical loss  $P_{mech}$ ; in consequence, less power is available to charge the stack (see (6.19)). Below the optimal flowrate  $Q_{opt}$ , the stack current  $|I_{stack}|$  also decreases because the stack voltage  $U_{stack}$  increases due the change in electroactive species concentrations within the cells  $c_{cell}$ ; note that the mechanical power  $P_{mech}$  is also reduced below  $Q_{opt}$ . Furthermore, the shape of the curves in Fig 6.18 might be generalized to other states of charge  $SoC$ ; some curves at different  $SoC$  are given in Fig. C.10 and C.11.

### Charge and Discharge Cycles at Constant Power

A new series of charge and discharge cycles at constant power has been performed to determine the energy efficiency at minimal flowrate  $\eta_{energy, Qmin}$  and at the optimal operating point  $\eta_{energy, Qopt}$ : this optimal operating point is constantly determined as a function of the actual state of charge. This optimal point is the combination of the optimal current  $I_{opt}$  and the optimal flowrate  $Q_{opt}$ . The efficiencies are given in Tab. 6.3.

We observe in Tab. 6.3 that the energy efficiencies at optimal flowrate  $\eta_{energy, Qopt}$  is always larger than the energy efficiencies at minimal flowrate  $\eta_{energy, Qmin}$ ; the gain in efficiency is 10% at 2500 W. Moreover, the efficiencies at optimal flowrate  $\eta_{energy, Qopt}$  are very close to the energy efficiencies  $\eta_{energy, stack}$  obtained in section 3.10.2 and summarized in Tab. 3.6. Note that these electrochemical efficiencies  $\eta_{energy, stack}$  do not take into account the mechanical losses  $P_{mech}$ ; therefore, the efficiencies ob-

tained at optimal operating points are very close to the maximal electrochemical efficiencies of the stack.

## 6.5. Summary

In the first part of this chapter, the multiphysics model of the overall VRB storage system was assembled from the electrochemical model introduced in chapter 3, the mechanical model of chapter 5 and the electrolyte properties discussed in chapter 4. This overall model is composed of four main parts: the VRB control system, the reservoir and electrolyte model, the electrochemical stack model and the mechanical model.

It is important to define the power flows within the battery in order to determine its performance; these power flows are the stack power  $P_{stack}$ , the mechanical power  $P_{mech}$  and the power exchanged  $P_{VRB}$  with the external load or source. In fact, there are two types of losses in the VRB: the mechanical losses  $P_{mech}$  required to flow the electrolytes and the electrochemical losses  $P_{loss}$  occurring within the stack. Actually,  $P_{loss}$  are already accounted for in the stack power  $P_{stack}$ . The losses are represented in Fig. 6.19 during a charge and discharge cycle; both the mechanical losses  $P_{mech}$  and the internal losses  $P_{loss}$  occur during the charge and during the discharge. In addition, a small storage loss might also occur, although the overall VRB model does not take this loss into account. This loss might be due to the auxiliaries power, to the cross-mixing of electrolytes, to the leakage current and to side reactions.

A large part of this chapter was dedicated to the battery operation at constant current  $I_{stack,ref}$ ; in that case, there is only one control variable: the electrolyte flowrate  $Q$ . First, the simplest control strategy was discussed in detail and its performance was determined. This strategy operates the battery at a constant flowrate  $Q_{max}$  that supplies enough electroactive species to fuel the electrochemical reactions under any operating conditions. We have found that the performance of this control strategy was poor due to the high mechanical power.

Therefore, we have proposed a new control strategy that operates the VRB at minimal flowrate  $Q_{min}$ ; so, the mechanical loss  $P_{mech}$  is reduced to the minimum in order to improve the efficiency. In that case, the minimal flowrate  $Q_{min}$  carries just enough active vanadium ions to sustain the redox reactions. Unfortunately, the vanadium concentrations  $c_{cell}$  within the cells depend on the flowrate, and at  $Q_{min}$ , the concentrations of elec-



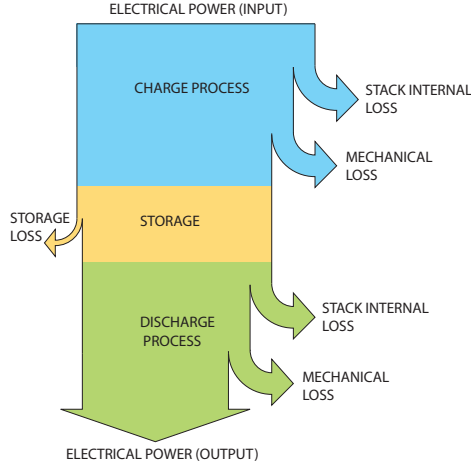


Figure 6.19.: Flowchart of the power during a charge and discharge cycle.

troactive species are reduced. In consequence, the stack power  $P_{stack}$  is lower during the discharge and larger during the charge.

We have then proposed a third control strategy that determines an optimal flowrate  $Q_{opt}$ ; at this flowrate, the battery power  $P_{VRB}$  is maximized during the discharge and minimized during the charge. The performance of this strategy was discussed in details and is always better than the two previous control strategies.

In order to determine and compare the battery efficiencies, we have then performed a series of charge and discharge cycles at constant current. The voltage efficiencies  $\eta_{voltage}$  and the energy efficiencies  $\eta_{energy}$  of the three control strategies were accurately determined. The highest voltage efficiency occurs at maximal flowrate  $Q_{max}$  because the electroactive vanadium ion concentrations within the cells are maximal; thus the stack voltage  $U_{stack}$  is high during the discharge and low during the charge. In fact, the voltage efficiency at optimal flowrate is very close to this value; but this is not the case for the minimal flowrate where the active species concentrations are low.

But, we have demonstrated that the energy efficiency  $\eta_{energy}$  at maximal

flowrate  $Q_{max}$  is unacceptable: often, the battery does not deliver power during the discharge because the mechanical losses are too large. The energy efficiency is always maximal at optimal flowrate  $Q_{opt}$  and decreases when the current  $I_{stack}$  increases. Finally, we have found that the energy efficiency  $\eta_{energy, Q_{opt}}$  at  $Q_{opt}$  is almost 10% higher than  $\eta_{energy, Q_{min}}$  at minimal flowrate  $Q_{min}$ .

In the last section of this work, we have discussed the battery operation at constant power; in fact, we have distinguished two cases, the constant stack power  $P_{stack, ref}$  and the constant battery power  $P_{VRB, ref}$ . In both cases, a new control variable was available in complement to the flowrate: the stack current  $I_{stack}$ . At constant stack power, it is difficult to find an optimal operating point because the energy associated with an electron depends on the operating conditions at the moment where it is consumed. But we have demonstrated that operating the battery at minimal flowrate  $Q_{min}$  is always a better strategy rather than operating it at maximal flowrate  $Q_{max}$ .

We have then proposed a method to determine the optimal operating point at constant battery power  $P_{VRB, ref}$ ; this method determines the optimal operating point that maximizes the quantity of electroactive species stored in the electrolyte during the charge at a given power  $P_{VRB}$  and minimizes this quantity during the discharge. Therefore, the battery can operate longer during the discharge and deliver more power. Finally, the energy efficiency  $\eta_{energy}$  at constant power were also established: the optimal operating point is 10% more efficient than the efficiency at minimal flowrate at nominal power.

---

# Epilogue

---

## 7.1. Overview and Contributions

Today, the electricity industries are facing new challenges as the market is being liberalized and deregulated in many countries. Unquestionably, electricity storage will play, in the near future, a major role in the fast developing distributed generations network as it has many advantages to offer: management of the supply and demand of electricity, power quality, integration of renewable sources, improvement of the level of use of the transport and distribution network, etc. Over the years, many storage technologies have been investigated and developed, some have reached the demonstrator level and only a few have become commercially available. The pumped hydro facilities have been successfully storing electricity for more than a century; but today, appropriate locations are seldom found. Electrochemical storage is also an effective means to accumulate electrical energy; among the emerging technologies, the flow batteries are excellent candidates for large stationary storage applications where the vanadium redox flow battery (VRB) distinguishes itself thanks to its competitive cost and simplicity.

But a successful electricity storage technology must combine at least three characteristics to have a chance to be widely accepted by the electrical industry: low cost, high reliability and good efficiency. A lot of works have already been done to improve the electrochemistry of the VRB and

to reduce its overall manufacturing cost. This thesis addresses primarily the battery performance and indirectly its cost; indeed, a good efficiency enhances the profitability and consequently reduces the operating cost.

In this ambitious work that encompasses the domains of electricity, electrochemistry and fluid mechanics, we have proposed a novel multiphysics model of the VRB. This model describes the principles and relations that govern the behaviour of the VRB under any set of operating conditions. Furthermore, this multiphysics model is a powerful means to identify and quantify the sources of losses within the VRB storage system; indeed, one of the purposes of this study is to propose strategies of control and operation for a greater effectiveness of the overall storage system.

Another important feature of this multiphysics model is to facilitate the integration of the VRB into the electrical networks. Indeed, power converters, whose properties and characteristics are known and efficient, are required in practice to interface the VRB with the network; the overall performance might improve if their control strategy takes into account the VRB characteristics.

### **Electrochemical Stack Model**

A good knowledge of the VRB chemistry is necessary to understand the principles that govern its behaviour. Through the detailed study of the VRB redox reactions and their associated overpotentials, we are able to determine the stack voltage under any operating conditions; furthermore, we also understand the factors and mechanisms that deteriorate and limit this voltage.

Then we have proposed an original model that constantly determines the vanadium concentrations, either in the reservoirs or within the cells; in addition, we have also developed a simplified model of the internal loss. Together with the electrochemical principles introduced in the first part, they form the electrochemical stack model.

We have also shown that this first model is already able to predict the behaviour of a VRB integrated into a stand-alone system. It has determined the stack voltage and current, the vanadium concentrations and the internal loss during a 24 hours period. Furthermore, the model was successfully compared with experimental data through a series of charge and discharge cycles at constant currents. We have also shown that the stack efficiency depends either on the current or on the power.

### **Electrolyte Properties**

The density and the viscosity are important characteristics of the electrolyte that were investigated in this work; in fact, they are both related to the attraction forces between the particles dissolved in the electrolyte and therefore they depend upon the electrolyte composition. Hence, we have discussed the effects of the temperature, the vanadium concentrations and the sulphuric acid concentration.

### **Mechanical Model**

In order to analyse the battery performance, it is necessary to know the mechanical power required to flow the electrolytes; therefore, we have developed a mechanical model from fluid mechanics principles. We have introduced the general principles that describe the pressure drops in the pipes and tanks and form the analytical part of the mechanical model. Then, we have proposed an original method to determine the mechanical loss within the stack; this numerical method is based on the finite element method (FEM). From a small set of basic parts, it is able to determine the flow resistance of a stack of any number of cells. Hence, the mechanical model predicts instantly the mechanical power from the actual flowrate and electrolyte properties.

### **Overall Multiphysics VRB Model**

The essential contribution of this thesis work is the original overall multiphysics model of the VRB; this model results from the combination of the electrochemical model and the mechanical model, it also integrates the electrolyte properties. This model provides a good insight of the battery operation and has highlighted some surprising phenomena.

Furthermore, we were able to analyse the battery operation at constant current and at constant power. In both cases, we have demonstrated that there exists an optimal operating point that maximizes the efficiency. For example, during a charge and discharge cycle, operating the battery at optimal flowrate rather than at minimal flowrate enhances the efficiency by 10%; moreover, this value increases when the stack current is reduced.

### 7.2. Perspectives and Future Developments

Although a lot of efforts have been devoted to the realization of this comprehensible model, there are still some opportunities to improve its performance with some additional features. For example, it would be very interesting to determine experimentally the limitations of the electrochemical model at extreme state of charge: it is probable that the concentration overpotentials are not negligible at these concentrations. Moreover, the study of the distribution of the vanadium ions and the reaction sites within the cells is another challenging field of investigation.

Furthermore, the analysis of the dynamical response of the electrolyte circuit will greatly enhance the mechanical model; indeed, this will open new perspectives in the definition of efficient control algorithms and strategies of the battery/network interface. In addition, the study of the variation of the electrolyte viscosity and density as a function of the battery state of charge will nicely complement the proposed mechanical model.

Another aspect that was not treated in this work is the thermal model of the VRB; indeed, heat is produced within the cells by the internal losses, and evacuated by the electrolyte flow. In addition, heat is also produced in the hydraulic circuit by the friction loss. This study might be done by a multifunction analysis of the flow: charge transport, heat transport and by-pass current.

Finally, the study of less conventional properties such as the simultaneous charge and discharge of elements operating in the same stack is an original theme for a future work. A special applications DC-DC transformer, or voltage adapter, might be an interesting option for an optimized photovoltaic conversion.

---

## Finite Element Analysis

---

### A.1. Simulation of a Channel

Since it is impossible to determine analytically the power required to flow the electrolyte through the stack, a finite element analysis was necessary. Quickly, the limited resources of the computer have imposed limits on the size of the mesh. The aims of this section are to assess the effects of the mesh size on the quality of the final result and to observe the limitations introduced by Peclet number. Two solutions are then proposed to circumvent these limitations.

In order to do so, an easily analysed and well known rectangular structure (Fig. A.1) has been simulated. The accuracy of the finite element model is obtained by comparing these results to the analytical ones.

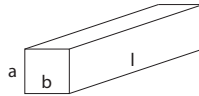


Figure A.1.: rectangular channel (2 mm x 2 mm x 10 cm).

### A.1.1. Analytical Model

The characteristics of the rectangular channel correspond to the ones that can be encountered in a small VRB. The velocity  $V_s$  is set at 1 m/s which corresponds to a flowrate  $Q$  of 4 cm<sup>3</sup>/s. The fluid is the VRB electrolyte and its properties are set to  $\rho = 1620$  kg/m<sup>3</sup> for the density and  $\mu = 0.008$  Pa/s for the dynamic viscosity. The pressure drop across the channel will be calculated with the formulas presented in the chapter 5.

In the case of a noncircular conduit, an equivalent hydraulic diameter  $D_h$  can be defined as four times the ratio of the cross-sectional flow area  $A$  divided by the perimeter  $P$  [87]. And for a rectangular pipe, it becomes:

$$D_h = 4 \frac{A}{P} = \frac{2ab}{a+b} \quad [m] \quad (\text{A.1})$$

$$\begin{aligned} \text{where: } a &= \text{height of the channel (2 mm)} & [m] \\ b &= \text{width of the channel (2 mm)} & [m] \end{aligned}$$

The flow stays laminar as long as the Reynolds number  $Re$  stays below 2000, remembering (5.1):

$$2000 > Re = \frac{\rho V_s}{\mu} D_h = 405 V_s \rightarrow V_s < 4.93 \quad [m/s] \quad (\text{A.2})$$

Therefore, the flow is laminar in the channel as long as the velocity stays below 4.93 m/s.

The friction factor  $f$  for a non-circular pipe is given by the following equation where the constant  $C$  depends on the particular shape of the pipe (see table A.1) [87]:

$$f = \frac{C}{Re} = \frac{C\mu}{\rho V_s D_h} \quad [-] \quad (\text{A.3})$$

Now that all the necessary variables are defined, the head loss  $h_l$  can be calculated using the Darcy-Weisbach equation (5.14):

$$h_l = \frac{1}{2} \frac{f l V_s^2}{g D_h} \quad [m] \quad (\text{A.4})$$

And from (5.13), assuming a horizontal channel ( $z_1 = z_2$ ), no minor head ( $h_m = 0$ ), a constant fluid velocity (because the section of the conduit is



$a/b$	$C$ [-]
0.05	89.9
0.1	84.7
0.25	72.9
0.5	62.2
0.75	57.9
1	56.9

Table A.1.: The constant  $C$  for a rectangular pipe. Data are from [87].

constant  $V_1 = V_2$ ) and no pump nor turbine ( $h_{w,th} = 0$ ), the pressure drop  $\Delta p$  across the channel becomes:

$$\Delta p = h_l g \rho = \frac{C \mu l V_s}{2 D_h^2} = 5690 \quad [Pa] \quad (A.5)$$

One can observe from (A.5) that the pressure drop is proportional to the velocity of the fluid for a given geometry of the pipe.

### A.1.2. Finite Element Model

The same channel is then simulated with a finite element software (Comsol). Since the analytical model assumes a fully developed flow, the pressure drop obtained analytically is applied across the channel. This method also eases the task of the solver.

Four resolutions of the mesh have been simulated and are defined by the maximum element size (respectively 0.5, 1, 1.5 and 2 mm). The accuracy of the solution depends on the quality of the mesh which is always a tradeoff between the complexity of the geometry and the limited resources of the computer. Simulation time is also affected exponentially by the resolutions.

The effects of the mesh resolution are illustrated in Fig. A.2. The quality of the resulting velocity field at a transverse section is increasing with the finesse of the mesh.

Table A.2 shows the number of elements of the mesh and the degrees of freedom for the four mesh sizes. The solution time and memory requirements are strongly related to the number of degrees of freedom in the

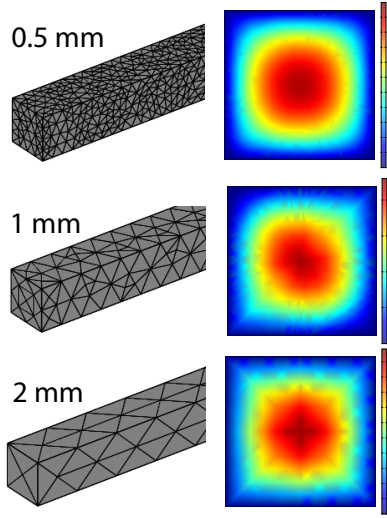


Figure A.2.: Effect of the mesh size: on the left, the mesh of a 2 mm x 2 mm x 10 cm canal with three max. element size of 0.5 mm, 1 mm and 2 mm and on the right the distribution of the velocity inside the channel. The fluid properties are  $\rho = 1620 \text{ kg/m}^3$  and  $\mu = 0.008 \text{ Pa/s}$ .

model. And unfortunately, this number increases very quickly when the mesh resolution is improved. The finest mesh size of Table A.2 (0.1 mm) is demanding an unsustainable amount of time and resources, and is therefore impracticable.

### Peclet Number Limitations

For the proposed operating conditions in the rectangular channel, in particular the 1 m/s velocity  $V_s$ , the Peclet number (5.30) is always greater than two, even with the finest mesh size (0.5 mm):

$$P_e = \frac{h\rho|V_s|}{\mu} = \frac{0.0005 \cdot 1620 \cdot 1}{0.008} = 101.25 > 2 \quad [-] \quad (\text{A.6})$$

Max. element size [mm]	Number of elements	Degrees of freedom
0.1	1207169	5984466
0.5	30294	166555
1	4026	25435
1.5	1656	11022
2	1200	7994

Table A.2.: Number of elements and degrees of freedom for the geometry of the channel (2 mm x 2 mm x 10 cm) for different mesh sizes with Comsol.

With such a high Peclet number, the simulation fails to converge and no solution is found. To comply with the *Peclet rule* ( $Pe < 2$ ), the mesh size should be smaller than  $10^{-5}$  m. These values are unfeasible with the available computer (this value is ten times smaller than the finest resolution presented in Tab. A.2). Therefore, because the density  $\rho$  and the viscosity  $\mu$  are given by the electrolyte composition, the only solution left is to change the velocity  $V_s$  by either:

- Reduce the maximal velocity  $V_{s,max}$  in the analytical model to comply with the Peclet rule, which is greatly smaller than the maximal laminar velocity (A.2),  $V_{s,max} = 0.0049 \ll 4.93$  [m/s].
- Determine the hydraulic resistance  $\tilde{R}$  (see section 5.5) of the channel at smaller velocities and then calculate the pressure drop with (5.26) and the relation  $V_s = Q/A$ .

With Comsol, the stationary solver automatically determines if the equation system is linear or not, and calls the linear or nonlinear solver. Fluid dynamics model are based on the Navier-Stokes equations which are nonlinear partial differential equations (PDE). Forcing the linear solver will yield the wrong result. But surprisingly in the channel example, this is not the case. The simulation results presented in Tab. A.3 show good correspondence with the analytical results found previously. This method was not used for other geometry due to the lack of confidence in the quality of the results, even if it also seems to give good results in the case of a stack.

Max. element size [mm]	Velocity [m/s]	Difference [%]
0.5	0.998	0.18
1	0.958	4.18
1.5	0.939	6.08
2	0.950	5.03

Table A.3.: Simulated velocity in the channel (2mm x 2mm x 10cm) for different mesh sizes with the linear solver of Comsol. The fluid characteristics are  $\rho = 1620 \text{ kg/m}^3$  and  $\mu = 0.008 \text{ Pa/s}$ . The input pressure is 5690 Pa and the theoretical velocity is 1 m/s.

### Reduced Velocity Method

To comply with the Peclet rule, the velocity  $V_s$  has to stay below the critical velocity  $V_{crit}$ :

$$P_e = \frac{h\rho|V_s|}{\mu} \leq 2 \rightarrow V_{crit} = 0.0049 \text{ [m/s]} \quad (\text{A.7})$$

The critical pressure drop  $\Delta p_{crit}$  is obtained by inserting  $V_{crit}$  in (A.5) and yields to  $\Delta p_{crit} = 27.88 \text{ Pa}$ . Tab. A.4 presents the simulated velocity in the channel for different mesh sizes obtained with the nonlinear solver. The input pressure used is 25 Pa and the theoretical velocity obtained from (A.5) is 0.0044 m/s.

Depending on the mesh resolution, the velocity varies from 4.39 to 4.13 mm/s and the maximal observed difference is around 6 %, it is clear that the numerical and analytical results agree quite well. Such a difference is acceptable to assess the power needed to flow the electrolyte through the channel whenever the velocity is below its critical value.

The quality of the results is almost the same with either the linear solver or the nonlinear solver.

### The Hydraulic Resistance Method

The hydraulic resistance method uses the principles introduced in section 5.5.1. First, the hydraulic resistance  $\tilde{R}$  is determined from a set of simulations and then the pressure drop  $\Delta p$  or the velocity  $V_s$  is determined

Max. element size [mm]	Velocity [m/s]	Difference [%]
0.5	0.00439	0.34
1	0.00421	4.33
1.5	0.00413	6.21
2	0.00417	5.17

Table A.4.: Simulated velocity in the channel (2mm x 2mm x 10cm) for different mesh sizes with the nonlinear solver of Comsol. The fluid characteristics are  $\rho = 1620 \text{ kg/m}^3$  and  $\mu = 0.008 \text{ Pa/s}$ . The input pressure is 25 Pa and the theoretical velocity is 0.0044 m/s.

from (5.26). This method is valid as long as the flow stays laminar.

In the case of the rectangular channel with a mesh size of 0.5 mm, the critical pressure drop is  $\Delta p_{crit} = 112.75 \text{ Pa}$  to comply with the Peclet rule. Above this pressure, the accuracy starts to deteriorate until the nonlinear solver fails to find a solution (around 500 Pa).

Simulations have been made with the nonlinear and linear solver, the results are presented in Fig. A.3. With the nonlinear solver, the pressure drop has been limited to 100 Pa to respect the condition  $P_e < 2$ . The hydraulic resistances  $\tilde{R}$  are given by the slopes. Both the linear and nonlinear solvers give the same value presented in Tab. A.5, the difference being less than 0.1 %.

Under the conditions given in the section A.1.1 , in particular  $V_s = 1 \text{ m/s}$ , the pressure drop is obtained from (5.26):

$$\Delta p = Q\tilde{R} = V_s A \tilde{R} \quad [Pa] \quad (\text{A.8})$$

The pressure drop found with the nonlinear and linear hydraulic resistances are given in Tab. A.5. The differences with the analytical solution are very small ( $< 0.3\%$ ).

## A.1. SIMULATION OF A CHANNEL

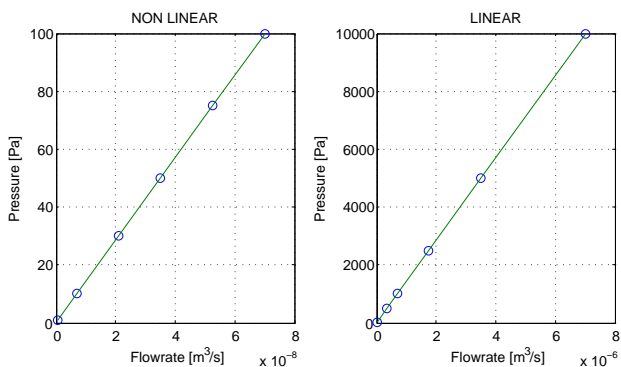


Figure A.3.: Simulation results of the rectangular channel for the nonlinear solver (left) and the linear solver (right). The fluid characteristics are  $\rho = 1620 \text{ kg/m}^3$  and  $\mu = 0.008 \text{ Pa/s}$ .

solver	$\tilde{R}$ [Pa · s/m <sup>3</sup> ]	$P_{e,max}$ [-]	Pressure at 1 m/s [Pa]	Difference [%]
nonlinear	1426463762	1.77	5705.84	0.28
linear	1425113465	177	5700.45	0.18

Table A.5.: Hydraulic resistance  $\tilde{R}$ , max. value of the Peclet number  $P_{e,max}$  and the pressure drop  $\Delta p$  at 1 m/s for the channel with the linear and nonlinear solver. The difference with the analytical pressure drop is also given.

# Vanadium Redox Flow Auxiliaries Hydraulic Circuit

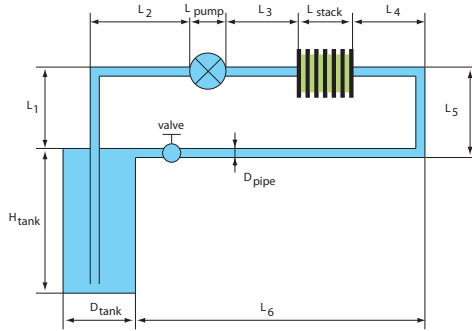


Figure B.1.: Schematic of the hydraulic circuit.

---

Name	Value [m]
$L_1$	1
$L_2$	0.5
$L_3$	0.5
$L_4$	0.25
$L_5$	1.02
$L_6$	1.19
$L_{pump}$	0.1
$L_{stack}$	0.1
$H_{tank}$	1
$D_{pipe}$	0.02
$D_{tank}$	0.5

Table B.1.: Dimension of the hydraulic circuit with a reservoir of 200 l.

Name	Value [m]
$L_1$	1
$L_2$	0.5
$L_3$	0.5
$L_4$	0.25
$L_5$	1.02
$L_6$	1.19
$L_{pump}$	0.1
$L_{stack}$	0.1
$H_{tank}$	1
$D_{pipe}$	0.02
$D_{tank}$	0.326

Table B.2.: Dimension of the hydraulic circuit with a reservoir of 83 l.



---

Name	$\tilde{R}$ [Pa · s/m <sup>3</sup> ]
input manifold	3321
output manifold	2901
terminal input manifold	772'134
terminal output manifold	987'790
flow plate	268'650'179

---

Table B.3.: The flow resistances  $\tilde{R}$  of the basic parts forming the stack of chapter 6.

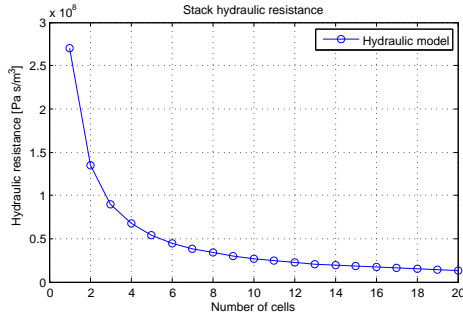


Figure B.2.: Flow resistances  $\tilde{R}$  for the stack of chapter 6. The flow resistance  $\tilde{R}$  for the 19 elements stack is 1'4186'843 Pa s/m<sup>3</sup>.



## Miscellaneous Graphs

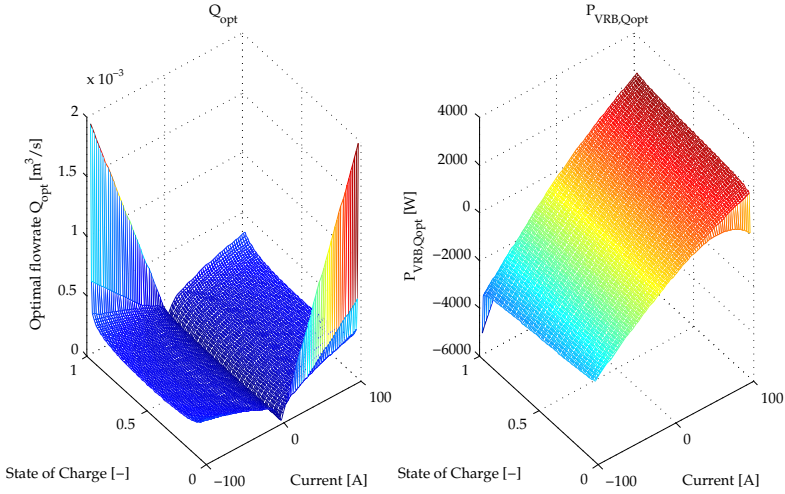


Figure C.1.: Optimal flowrate  $Q$  and battery power  $P_{VRB}$  as a function of the state of charge  $SoC$  and the current  $I_{stack}$ .

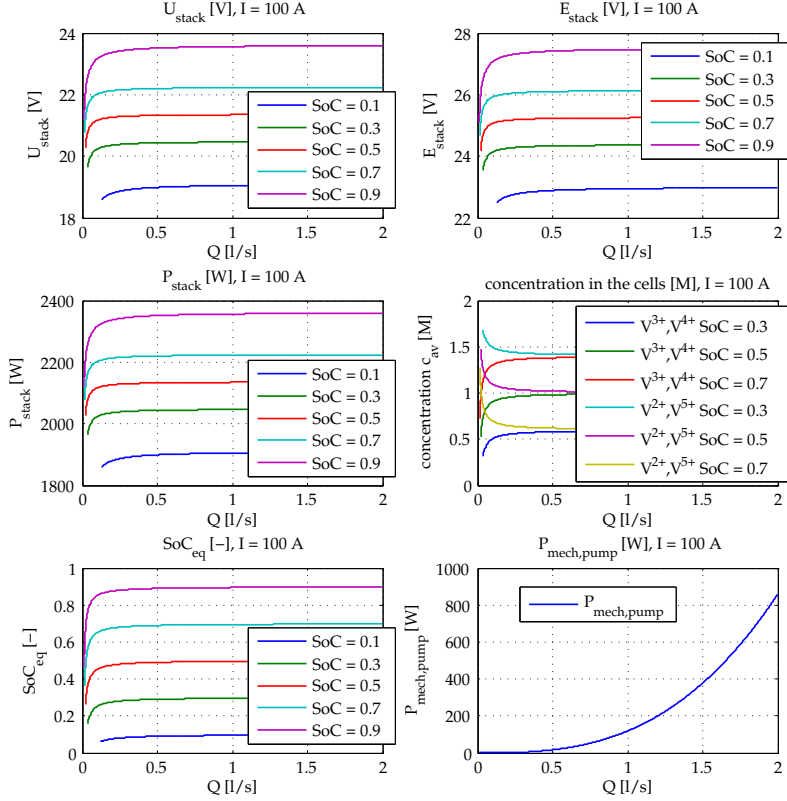


Figure C.2.: Stack voltage  $U_{stack}$ , stack equilibrium voltage  $E_{stack}$ , stack power  $P_{stack}$ , vanadium concentrations in the cells  $c_{av}$ , equivalent state of charge  $SoC_{eq}$  and mechanical power of a single pump  $P_{mech,pump}$  at a discharge current  $I_{stack}$  of 100 A as a function of the flowrate  $Q$ .

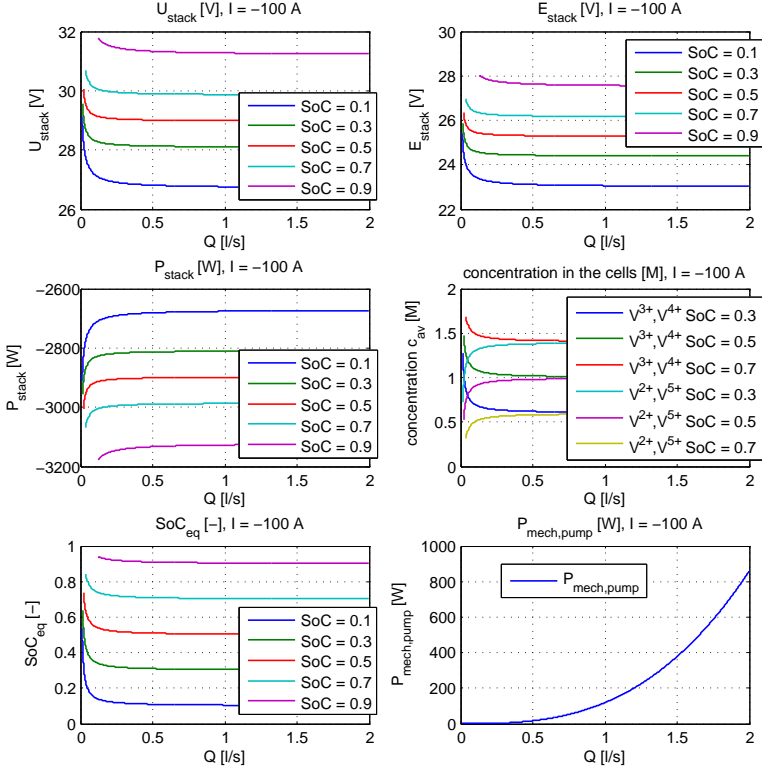


Figure C.3.: Stack voltage  $U_{stack}$ , stack equilibrium voltage  $E_{stack}$ , stack power  $P_{stack}$ , vanadium concentrations in the cells  $c_{av}$ , equivalent state of charge  $SoC_{eq}$  and mechanical power of a single pump  $P_{mech,pump}$  at a charge current  $I_{stack}$  of -100 A as a function of the flowrate  $Q$ .

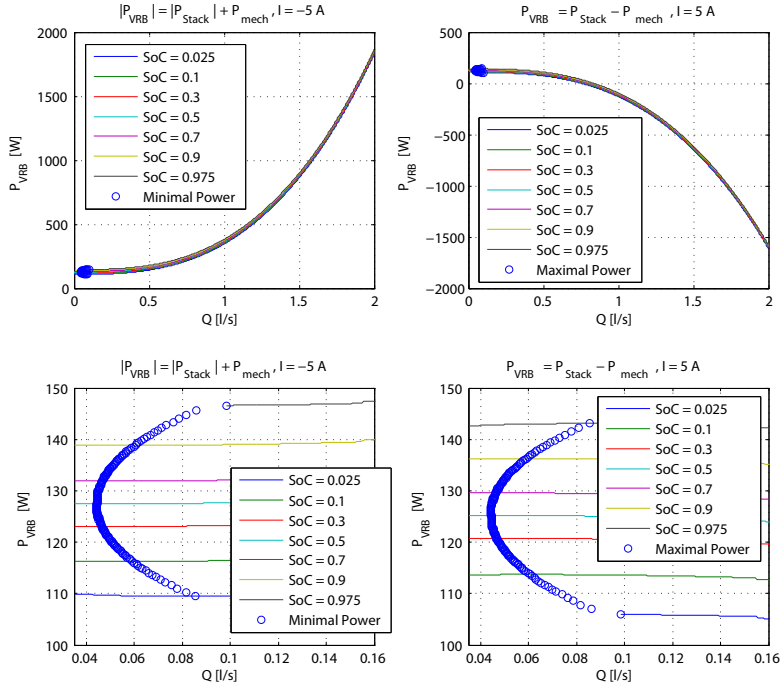


Figure C.4.: Optimal flowrate  $Q_{opt}$  as a function of the flowrate  $Q$  and the state of charge  $SoC$ . On the left,  $Q_{opt}$  for discharge current of 5 A. On the right,  $Q_{opt}$  for a charge current of -5 A. Note that the bottom graphs are a zoom of the top ones.

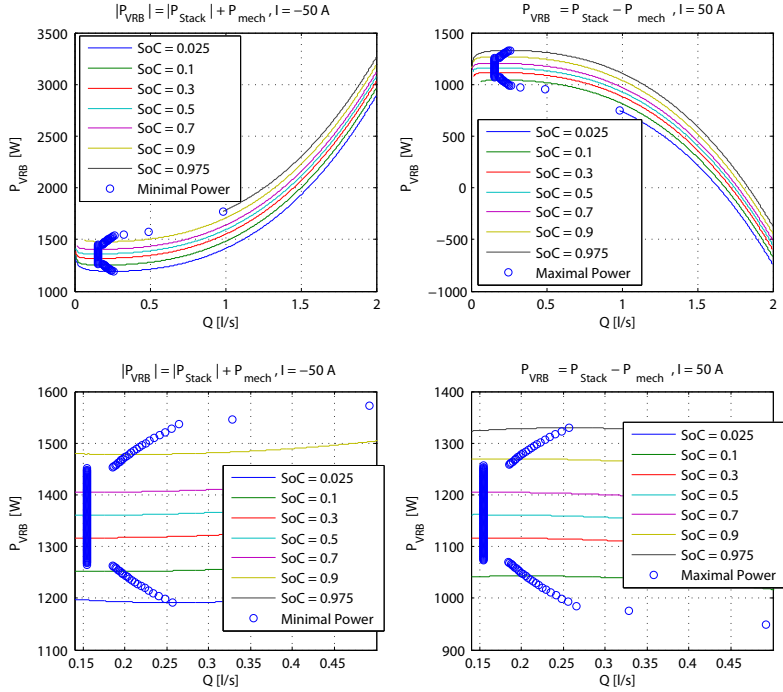


Figure C.5.: Optimal flowrate  $Q_{opt}$  as a function of the flowrate  $Q$  and the state of charge  $SoC$ . On the left,  $Q_{opt}$  for discharge current of 50 A. On the right,  $Q_{opt}$  for a charge current of -50 A. Note that the bottom graphs are a zoom of the top ones.

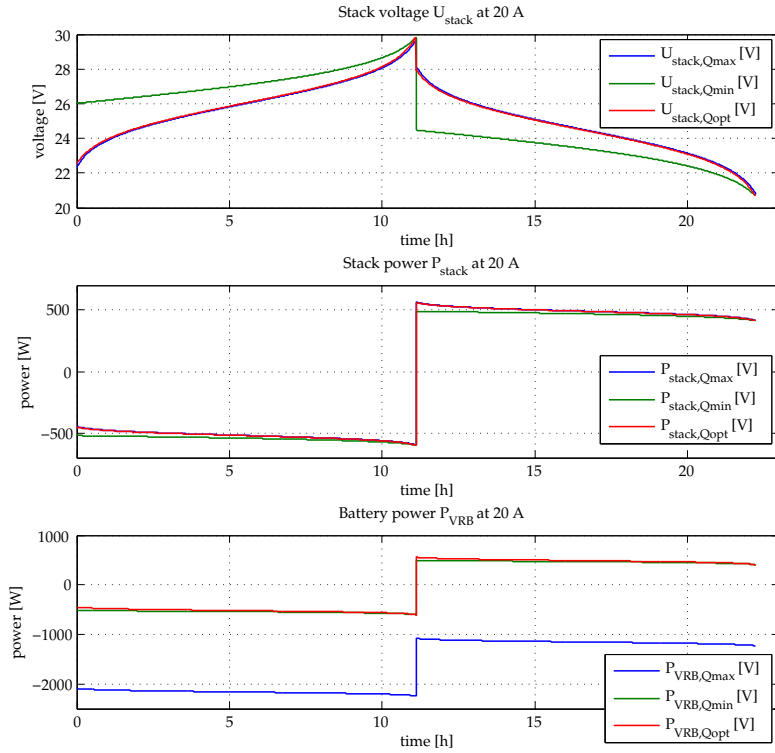


Figure C.6.: Stack voltage  $U_{stack}$ , stack power  $P_{stack}$  and battery power  $P_{VRB}$  during a charge and discharge cycle at 20 A.



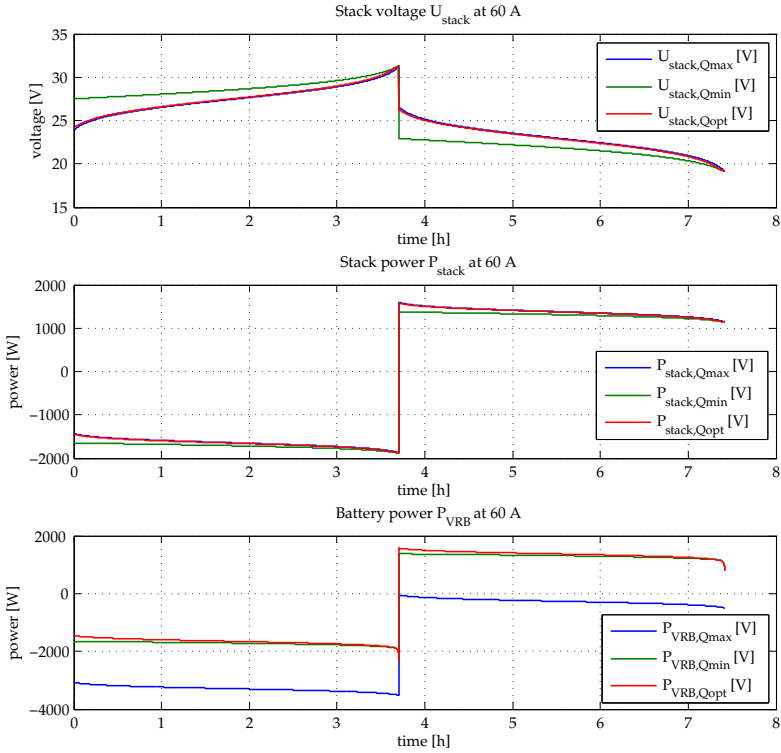


Figure C.7.: Stack voltage  $U_{stack}$ , stack power  $P_{stack}$  and battery power  $P_{VRB}$  during a charge and discharge cycle at 60 A.

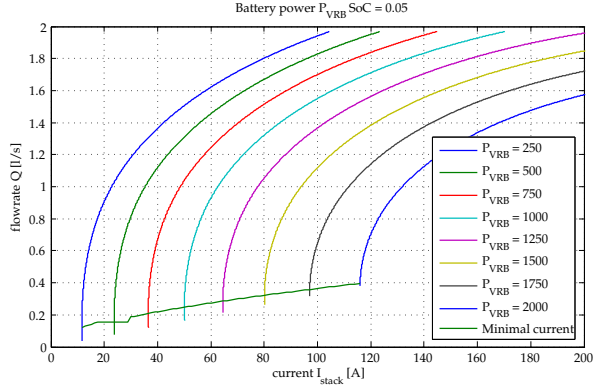


Figure C.8.: Battery power  $P_{VRB}$  as a function of the discharge current  $I_{stack}$  and the electrolyte flowrate  $Q$  at a state of charge  $SoC$  equal to 0.05. The optimal operating points occurs when the current  $I_{stack}$  is minimal for a given battery power  $P_{VRB}$ .

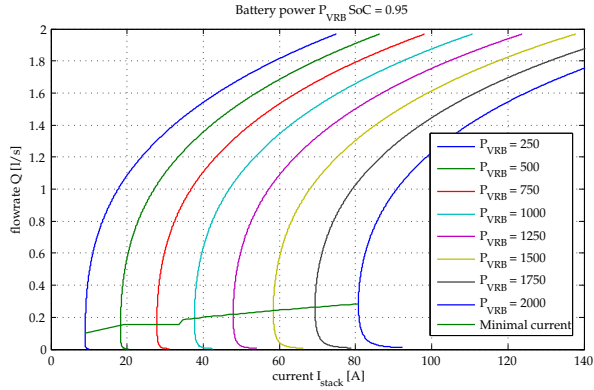


Figure C.9.: Battery power  $P_{VRB}$  as a function of the discharge current  $I_{stack}$  and the electrolyte flowrate  $Q$  at a state of charge  $SoC$  equal to 0.95. The optimal operating points occurs when the current  $I_{stack}$  is minimal for a given battery power  $P_{VRB}$ .

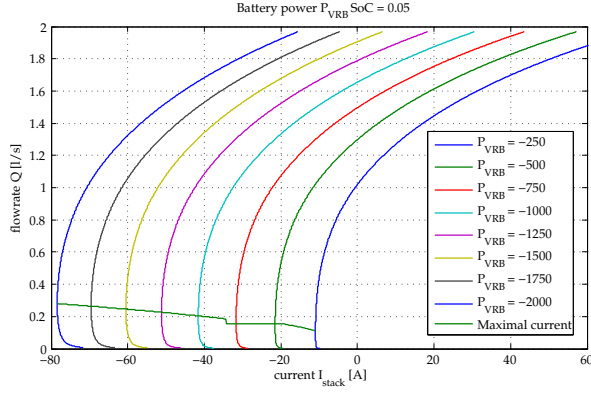


Figure C.10.: Battery power  $P_{VRB}$  as a function of the charge current  $I_{stack}$  and the electrolyte flowrate  $Q$  at a state of charge  $SoC$  equal to 0.05. The optimal operating points occurs when the current  $|I_{stack}|$  is maximal for a given battery power  $P_{VRB}$ .

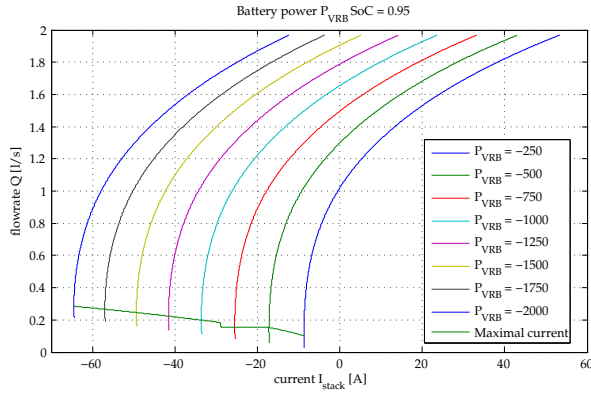


Figure C.11.: Battery power  $P_{VRB}$  as a function of the charge current  $I_{stack}$  and the electrolyte flowrate  $Q$  at a state of charge  $SoC$  equal to 0.95. The optimal operating points occurs when the current  $|I_{stack}|$  is maximal for a given battery power  $P_{VRB}$ .



---

## Bibliography

---

“ If I have seen further, it is by standing on  
the shoulders of giants. ”

— ISAAC NEWTON  
1643-1727

- [1] A. Rufer, “Benefits of short- and long-term energy storage in the context of renewable energies and sustainable management of energy resources,” *EVER 2007*, 2007.
- [2] J. Eyer, J. Iannucci, and G. Corey, “Energy storage benefits and market analysis handbook,” *Sandia Report*, vol. SAND2004-6177, 2004.
- [3] G. Bloch, “Le stockage d’énergie par air comprimé prêt à remplacer les batteries au plomb,” *Le Temps*, 24.06.2008.
- [4] A. Price, G. Thijssen, and P. Symons, “Electricity storage, a solution in network operation?,” *Distributech Europe 2000*, 2000.
- [5] “Encyclopædia britannica online,” 2008.
- [6] A. Rufer, P. Barrade, D. Hotellier, and P. Derron, “Supercapacitive energy storage: power electronic solutions and applications,” *ANAE* :

- Associazione Nazionale Azionamenti Elettrici, 13o Seminario Interattivo, Azionamenti elettrici : Evoluzione Tecnologica e Problematiche Emergenti*, 2002.
- [7] E. Hirst and B. Kirby, "Creating competitive markets for ancillary services," 1997.
  - [8] P. Fairley, "Can wind energy continue double-digit growth," *IEEE Spectrum*, March 2008.
  - [9] T. Sels, C. Dragu, T. Van Craenenbroeck, and R. Belmans, "Electrical energy storage systems: Existing systems versus newest systems - an overview," *International Conference Power Generation and Sustainable Development*, 2001.
  - [10] A. Hiratsuka, T. Arai, and T. Yoshimura, "Seawater pumped-storage power plant in Okinawa island, Japan," *Engineering geology*, vol. 35, 1993.
  - [11] Electricity Storage Association. [www.electricitystorage.org](http://www.electricitystorage.org).
  - [12] Beacon Power. [www.beaconpower.com](http://www.beaconpower.com).
  - [13] S. Lemofouet and A. Rufer, "Hybrid energy storage system based on compressed air and super capacitors with MEPT (maximum efficiency point tracking)," *IPEC 2005 : International Power Electronics Conference*, 2005.
  - [14] S. Lemofouet, "Investigation and optimisation of hybrid electricity storage systems based on compressed air and supercapacitors," *PhD thesis, EPFL*, 2006.
  - [15] W. Hassenzahl, "Superconducting magnetic energy storage," *Proceedings of the IEEE*, 1983.
  - [16] Accel Instrument. [www.accel.de](http://www.accel.de).
  - [17] W. Buckles and W. Hassenzahl, "Superconducting magnetic energy storage," *Power Engineering Review, IEEE*, 2000.

- 
- [18] L. Chen, Y. Liu, A. Arsoy, P. Ribeiro, M. Steurer, and M. Iravani, "Detailed modeling of superconducting magnetic energy storage (SMES) system," *IEEE Transactions on Power Delivery*, 2006.
  - [19] Maxwell Technologies. [www.maxwell.com](http://www.maxwell.com).
  - [20] A. Schnewly and R. Gallay, "Properties and applications of supercapacitors from the state-of-the-art to future trends," *PCIM 2000*, 2000.
  - [21] B. Destraz, P. Barrade, and A. Rufer, "Supercapacitive energy storage for diesel - electric locomotives," *SPEEDAM 2004 : Symposium on Power Electronics, Electrical Drives, Automation & Motion*, 2004.
  - [22] P. Barrade and A. Rufer, "The use of supercapacitors for energy storage in traction systems," *IEEE-VPP 04 : Vehicular Power and Propulsion Symposium*, 2004.
  - [23] A. Rufer, D. Hotellier, and P. Barrade, "A supercapacitor-based energy-storage substation for voltage-compensation in weak transportation networks," *IEEE Transactions on Power Delivery*, vol. 19, 2004.
  - [24] Wikipedia, "The free encyclopedia." [www.wikipedia.org](http://www.wikipedia.org).
  - [25] M. Farber De Anda, J. Boyes, and W. Torres, "Lesson learned from the Puerto Rico battery energy storage system," *Sandia National Laboratories*, vol. SAND99-2232, 1999.
  - [26] C. Rydh, "Environmental assessment of vanadium redox and lead-acid batteries for stationnary energy storage," *Journal of Power Sources*, vol. 80, 1999.
  - [27] D. Linden and T. Reddy, *Handbook of batteries*. 2002.
  - [28] W. Fischer, W. Haar, B. Hartmann, H. Meinhold, and G. Weddigen, "Der Natrium-Schwefel-Akkumulator," *BBC-Nachrichten*, 1978.
  - [29] NGK insulators ltd. [www.ngk.co.jp](http://www.ngk.co.jp).
  - [30] Y. Tachibana, "A new power supply system using nas (sodium sulfur) battery," *World Energy Council*, 1998.

- [31] M. Patel, *Spacecraft power systems*. 2005.
- [32] Kokam. [www.kokam.com](http://www.kokam.com).
- [33] M. Bartolozzi, "Development of redox flow batteries. a historical bibliography," *Journal of Power Sources*, vol. 27, 1989.
- [34] F. Abou Chacra, "Valorisation et optimisation du stockage d'énergie dans un réseau d'énergie électrique," *Thèse Supélec*, 2005.
- [35] L. Joerissen, J. Garche, C. Fabjan, and G. Tomazic, "Possible use of vanadium redox-flow batteries for energy storage in small grids and stand-alone photovoltaic systems," *Journal of Power Sources*, 2004.
- [36] E. Sum and M. Skyllas-Kazacos, "A study of the V(II)/V(III) redox couple for redox flow cell applications," *Journal of Power Sources*, vol. 15, 1985.
- [37] E. Sum, M. Rychcik, and M. Skyllas-Kazacos, "Investigation of the V(V)/V(VI) system for use in the positive half-cell of a redox battery," *Journal of Power Sources*, vol. 16, 1985.
- [38] C. Lotspeich, "a comparative assessment of flow battery technologies," *EESAT 2002*, 2002.
- [39] T. Kaizuka and T. Sasaki, "Evaluation of control maintaining electric power quality by use of rechargeable battery system," *IEEE*, 2001.
- [40] N. Tokuda, M. Furuya, Y. Kikuoka, Y. Tsutui, T. Kumamoto, and T. Kanno, "Development of a redox flow (rf) battery for energy storage," *IEEE PCC-Osaka*, 2002.
- [41] M. Skyllas-Kazacos, M. Rychick, and R. Robins, "US patent 4,786,567," 1988.
- [42] Mineral Information Institute. [www.mii.org](http://www.mii.org).
- [43] P. Atkins and L. Jones, *Chimie, Molécules, Matière, Métamorphoses*. 3ème ed., 1998.
- [44] EA Technology, "Review of electrical energy storage technologies and systems and of their potential for the UK," 2004.



- [45] M. Syllas-Kazacos, "The vanadium redox battery and fuel cell for large-scale energy storage," *19th World Energy Congress, Australia*, 2004.
- [46] M. Schreiber, A. Whitehead, M. Harrer, and R. Moser, "The vandium redox battery - an energy reservoir for stand-alone its applications along motor- and expressways," *IEEE Conference on Intelligent Transportation Systems*, 2005.
- [47] H. Bindner, P. Ahm, and O. Ibsen, "Vanadium redox-flow batteries - installation at Risø for characteristion measurements," *Risø International Energy Conference 2007*, 2007.
- [48] K. Yoshimoto, T. Nanahara, G. Koshimizu, and Y. Uchida, "New control method for regulation state-of-charge of a battery in hybrid wind power/battery energy storage system," 2006.
- [49] Energy Storage Association, "News letter," June 2005.
- [50] B. Williams and T. Hennessy, "Electric oasis," *Power Engineer*, 2005.
- [51] VRB Power Systems Inc, "Electricity storage for capital deferral," *Case Study*, available online: [www.vrbpower.com](http://www.vrbpower.com).
- [52] VRB Power Systems Inc. [www.vrbpower.com](http://www.vrbpower.com).
- [53] EN-o-DE, Energy on Demand Production and Sales GmbH. [www.en-o-de.com](http://www.en-o-de.com).
- [54] A. Whitehead, M. Harrer, and M. Schreiber, "Field test results for a 1 kw, 50 kwh vanadium redox flow battery," *EESAT 2005 Conference Proceedings*, 2005.
- [55] A. Price, S. Bartey, S. Male, and G. Cooley, "A novel approach to utility scale energy storage," *Power Engineering Journal*, 1999.
- [56] News Headlines, "Regenesys runs out of time," *Modern Power Systems*, 2003.
- [57] M. Thomas, "Persistence and progress - the zinc bromine battery in renewable energy systems," *Rega Forum*, 2003.

- [58] F. Grasser, "An analytical, control-oriented state space model for a PEM fuel cell system," *PhD thesis, EPFL*, 2005.
- [59] C. Rivas, "Etude, modélisation et propriétés d'un onduleur de courant à pulsion associé à une pile à combustible," *PhD thesis, EPFL*, 2003.
- [60] M. Rychcik and M. Skyllas-Kazacos, "Evaluation of electrode materials for vanadium redox cell," *Journal of Power Sources*, vol. 19, 1987.
- [61] H. Girault, *Electrochimie physique et analytique*. 2001.
- [62] D. Harris, *Exploring Chemical Analysis*. third ed., 2005.
- [63] J. Dick, *Analytical Chemistry*. 1973.
- [64] C. Hamann, A. Hamnett, and W. Vielstich, *Electrochemistry*. 2nd ed., 1998.
- [65] A. Heintz and C. Illenberger, "Thermodynamics of vanadium redox flow batteries - electrochemical and calorimetric investigations," *Ber. Bunsenges. Phys. Chem.*, vol. 102, 1998.
- [66] J. Van herle, *Electrochemical Technology, Fuel Cells and Batteries, postgrade course*. 2002.
- [67] A. Bard, R. Parsons, and J. Jordan, *Standard Potentials in Aqueous solution*. 1985.
- [68] C. McQuarrie, D. McQuarrie, and P. Rock, *Chimie générale*. 2003.
- [69] M. Gattrell, J. Park, B. MacDougall, J. Apte, and S. McCarthy, "Study of the mechanism of the vanadium 4+/5+ redox reaction in acidic solutions," *Journal of The Electrochemical Society*, vol. 151, 2004.
- [70] D. Lide, *Handbook of Chemistry and Physics*. 82 ed., 2002.
- [71] D. Skoog, D. West, and J. Holler, *Chimie analytique*. 7e ed., 1997.
- [72] A. Bard and L. Faulkner, *Electrochemical Methods, Fundamentals and Applications*. 2nd ed., 2001.

- 
- [73] A. Mousa, "Chemical and electrochemical studies of V(III) and V(II) solutions in sulfuric acid solution for vanadium battery applications," *PhD thesis, UNSW, Australia*, 2003.
- [74] G. Oriji, Y. Katayama, and T. Miura, "Investigation on V(IV)/V(V) and V(II)/V(III) redox reactions by various electrochemical methods," *Journal of Power Sources*, vol. 139, 2005.
- [75] C. Fabjan, J. Garche, B. Harrer, L. Jörissen, C. Kolbeck, F. Philippi, G. Tomazic, and F. Wagner, "The vanadium redox-battery: an efficient storage unit for photovoltaic systems," *Electrochimica Acta*, vol. 47, 2001.
- [76] M. Skyllas-Kazacos and C. Menictas, "The vanadium redox battery for emergency back-up applications," *Intelec 97*, 1997.
- [77] M.-H. Li, T. Funaki, and T. Hikiara, "A coupled dynamical model of redox flow battery based on chemical reaction, fluid flow, and electrical circuit," 2008.
- [78] Sumitomo Electric. [www.sei.co.jp](http://www.sei.co.jp).
- [79] M.-H. Li, T. Funaki, and T. Hikiara, "A study of output terminal voltage modeling for redox flow battery based on charge and discharge experiments," 2007.
- [80] Electric Power Research Institute, EPRI, "Epri-doe handbook of energy storage for transmission and distribution applications," 2003.
- [81] Energy on Demand (En-O-De), "Vanadium instant energy, white paper," 2005.
- [82] J. Hawkins, "The go with the (vanadium-redox) flow," *Presentation at ESA 2004*, 2004.
- [83] P. Barrade and A. Rufer, "Current capability and power density of supercapacitors: considerations on energy efficiency," *EPE 2003 : European Conference on Power Electronics and Applications*, 2003.
- [84] J. Wilkes, *Fluid mechanics for chemical engineers*. 2005.
- [85] D. Giancoli, *Physics for scientists & engineers*. 4th ed., 2008.

- [86] G. Oriji, Y. Katayama, and T. Miura, "Investigation on V(IV)/V(V) species in a vanadium redox flow battery," *Electrochimica Acta*, vol. 49, 2004.
- [87] B. Munson, D. Young, and T. Okiishi, *Fundamentals of Fluid Mechanics*. third ed., 1998.
- [88] Y. Wen, H. Zhang, P. Qian, P. Zhao, H. Zhou, and B. Yi, "Investigation on the electrode process of concentrated V(IV)/V(V) species in a vanadium redox flow battery," *Acta Physico-Chimica Sinica*, vol. 22, 2006.
- [89] N. Kausar, "Studies of V(IV) and V(V) species in vanadium cell electrolyte," *PhD thesis, UNSW, Australia*, 2002.
- [90] A. Horvath, *Handbook of aqueous electrolyte solutions*. 1985.
- [91] M. Kazacos, M. Cheng, and M. Skyllas-Kazacos, "Vanadium redox cell electrolyte optimization studies," *Journal of Applied Electrochemistry*, vol. 20, 1990.
- [92] F. Rahman and M. Skyllas-Kazacos, "Solubility of vanadyl sulfate in concentrated sulfuric acid solutions," *Journal of Power Sources*, 1998.
- [93] M. Gatrell, J. Park, B. MacDougall, S. McCarthy, and J. MacDonald, "The impact of low temperature on vanadium redox battery (VRB) performance," *Vanadium - Geology, Processing and Applications*, 2002.
- [94] S. Candel, *Mécanique des Fluides*. 2001.
- [95] M. Frelin, *Caractéristiques des Fluides*. [www.techniques-ingenieur.fr](http://www.techniques-ingenieur.fr), 1998.
- [96] COMSOL Multiphysics, *User's Guide*. 2006.
- [97] H. Versteeg and W. Malalasekera, *An Introduction to Computational Fluid Dynamics*. 1995.

---

---

## Curriculum vitae

---

## Christian Blanc

christian.blanc@a3.epfl.ch

## Education & Experience

- 2003 to date      Research Assistant & Ph.D. student  
*Laboratoire d'Electronique Industrielle, Ecole polytechnique Fédérale de Lausanne, Lausanne, Switzerland*
- Research work towards Ph.D. degree on the modeling of a vanadium redox flow battery electricity storage system.
  - Miscellaneous projects on SOFC fuel cells and active transformer quieting.
  - Education assistance for semester works and projects.
- 2002              Project Manager, motor drivers for space applications  
*ETEL, Môtiers, Switzerland*
- 1997-2002      Bachelor and Master of Science in Electrical Engineering  
*Ecole Polytechnique Fédérale de Lausanne, Lausanne, Switzerland*
- 1992-1997      High School Diploma  
*Collège Sainte-Croix, Fribourg, Switzerland.*
- 1994-1995      Honorary High School Diploma  
*Central High School, Norwood, Minnesota, USA*

## Publications

- C. Blanc and A. Rufer. *Multiphysics and Energetic Modeling of a Vanadium Redox Flow Battery*. In ICSET 2008 : IEEE International Conference on Sustainable Energy Technologies, 2008.
- C. Blanc and A. Rufer. *Modeling of a Vanadium Redox Flow Battery*. In PCIM 2007 : International Conference on Power Electronics, Intelligent Motion and Power Quality, 2007.
- C. Blanc and A. Rufer. *Modélisation d'un système de stockage de type électrolyseur réversible au vanadium*. In EPF 2006 : 11ème édition, Électronique de Puissance du Futur, 2006.
- C. Blanc, V. Chritin, E. Van Lancker, A. Rufer, B. Genevay, and M. Nicollérat. *Acoustic Mapping for Active Transformer Quieting Applications Based on a Modular DSP Platform*. In IECON 2005 : The 31st Annual Conference of the IEEE Industrial Electronics Society, 2005.
- J. Persson, C. Blanc, V. Nguyen, Y. Perriard. *Sensorless Position Estimation of a Voice-Coil Transducer*. In IAS 2001 : The 36th Annual Meeting of the IEEE Industry Applications Society, 2001.